Etude théorique de processus photoinduits sous contraintes

Laura Le Bras

PSL UNIVERSITÉ PARIS

THÈSE DE DOCTORAT
DE L'UNIVERSITÉ PSL

Préparée à Chimie ParisTech

Etude théorique de processus photoinduits sous contraintes

Soutenue par

Laura LE BRAS

Le 20 Septembre 2019

École doctorale n°388

Chimie physique et chimie analytique de Paris Centre

Spécialité

Physico-chimie

Composition du jury :

Karine COSTUAS Directrice de recherche, Université de Rennes 1	*Président*
Nicolas FERRE Professeur, Université d'Aix-Marseille	*Rapporteur*
Alfonso PEDONE Professeur, Université de Modène et de Reggio d'Émilie	*Rapporteur*
Isabelle NAVIZET Professeur, Université Paris-Est Marne-la-Vallée	*Examinateur*
Jean-Philip PIQUEMAL Professeur, Sorbonne Université	*Examinateur*
Nicolas PINEAU Ingénieur Chercheur, CEA DAM/DIF	*Examinateur*
Carlo ADAMO Professeur, Ecole Nationale Supérieure de Chimie de Paris	*Co-directeur de thèse*
Aurélie PERRIER Maitre de Conférences, Université Paris Diderot	*Directeur de thèse*

Chimie Paris ParisTech | PSL

À mon papy

Résumé

Au cours de ces travaux de thèse je me suis attachée à étudier, de façon théorique, des processus photoinduits sous contraintes. Les processus photoinduits, comme leur nom l'indique, résultent de l'interaction lumière/matière et correspondent à la réponse du matériau ou de la molécule suite à cette interaction. Les sciences qui s'intéressent à ces processus sont la photophysique et la photochimie. La première s'intéresse à la réponse de la molécule en terme de processus physiques parmi lesquels on retrouve entre autres les différents phénomènes d'émission que sont la fluorescence et la phosphorescence. La seconde s'intéresse elle aux transformations chimiques subies par la molécule suite à l'interaction avec la lumière et on pourra notamment mentionner l'exemple de la création/rupture de liaison induite par la lumière. Dans notre cas, nous allons nous intéresser à un processus photophysique et un processus photochimique.

Processus photophysique : la fluorescence

Quand une molécule passe de son état fondamental à un état excité (qu'elle absorbe un rayonnement lumineux), elle a deux possibilités pour relaxer vers son état fondamental. Elle peut soit se désexciter de façon radiative, il est alors possible d'observer de la fluorescence ($S_1 \rightarrow S_0$) ou de la phosphorescence ($T_1 \rightarrow S_0$). Si la molécule se désexcite de façon non-radiative, encore une fois, plusieurs possibilités s'offrent à elle. La molécule peut se désexciter via Conversion interne (CI), ce qui implique le passage d'un état S_{n+1} à un

état S_n, ou via un Croisement Intersystème (ISC), la relaxation se fait alors entre un état S_n et T_n. La désexcitation non-radiative peut également se faire de façon vibrationnelle. Le processus que nous proposons d'étudier est la fluorescence. Plus particulièrement, c'est la modulation de ce phénomène de fluorescence, due à l'environnement, qui a attiré notre attention. En effet, il a été démontré il y a maintenant plusieurs années que l'environnement pouvait modifier les propriétés émissives des molécules. De façon générale et ce depuis les travaux de Förster [56], il est admis que des molécules émissives dans un milieu dilué (en solution donc) ne l'étaient plus quand elles étaient sous forme d'agrégat. Cette caractéristique est d'ailleurs connue sous le nom d'$Aggregation - Caused\ Quenching$ (ACQ). Ce phénomène d'ACQ peut être un problème s'il est envisagé d'utiliser ces molécules pour des applications dans l'optoélectronique telles que les diodes électroluminescentes organiques ou OLEDs (Organic Light Emitting Diodes). En effet, les molécules vont alors se trouver sous forme de cristaux ou dispersés au sein de films mince et donc sous forme d'agrégat. En 2001, le groupe du Pr. Tang a mis en évidence un comportement contraire à l'ACQ, l'$Aggregation - Induced\ Emission$ (AIE). Le phénomène d'AIE correspond donc au comportement d'une molécule peu ou pas émissive en milieu dilué (solution) mais qui le devient fortement sous forme d'agrégat. Une variante de ce phénomène, qui concerne les cristaux et non plus l'agrégat, est également connue sous le nom de $Crystallization - Induced\ Emission$ (CIE). Outre le phénomène de fluorescence, nous nous intéressons donc principalement à la modulation de ce phénomène. Cette modulation peut être illustrée via une grandeur, le rendement quantique de fluorescence,Φ_F (Eq. 2):

$$\Phi_F = \frac{k_r}{k_r + k_{nr}} \ ; \ k_r = k_{fluo} + k_{phospho} \ ; \ k_{nr} = k_{CI} + k_{ISC} \tag{1}$$

Φ_F dépend de la constante de désexcitation radiative, k_r et de la constante de désexcitation non-radiative, k_{nr}. La première prend en compte la fluorescence et la phosphorescence (k_{fluo} et $k_{phospho}$) tandis que la seconde tient compte des phénomènes que sont la conversion interne (k_{IC}) et le croisement intersystème (k_{ISC}). Si le phénomène d'AIE est observé pour une molécule, cela implique soit qu'un chemin de désexcitation non-radiative présent en solution a été bloqué ou n'est plus accessible soit qu'un chemin de désexcitation radiative devient plus favorable en phase condensé. Pour étudier ces phénomènes, deux approches sont envisageables: (1) rester proche de la géométrie d'équilibre et considérer que tous les processus photophysiques ont lieu dans cette zone, ou (2) explorer la totalité de la

surface d'énergie potentielle. C'est le système et ses caractéristiques intrinsèques qui vont décider de l'approche qui est à utiliser. Plusieurs mécanismes ont été proposés afin d'expliquer ce phénomène d'AIE. On citera par exemple le transfert d'énergie vers les modes de vibrations/rotations de basses fréquences, qui favorise la désexcitation non-radiative. La restriction des rotations intramoléculaires (*Restricted Intramolecular Rotation*, RIR), des vibrations intramoléculaires (*Restricted Intramolecular Vibration*, RIR), des mouvements intramoléculaires (*Restricted Intramolecular Motion*, RIM) sont autant d'explications possibles au phénomène d'AIE et plus particulièrement au faible rendement de fluorescence observé en solution. Ces explications, intuitives, peuvent être supportées par des calculs théoriques. On citera notamment l'utilisation de la règle d'or de Fermi qui permet de calculer le taux de transition d'un état à un autre. Les facteurs de Huang-Rhys (HR) font également partie des outils théoriques à disposition pour la quantification des phénomènes d'AIE/ACQ. Ces facteurs rendent compte du couplage electron-vibration, que ce soit en absorption ou en émission, et représentent la variation d'un mode de vibration donné au cours de la transition d'un état à un autre. Ils sont calculés comme suit:

$$HR_j = \frac{\omega_j D_j^2}{2\hbar} \tag{2}$$

avec ω_j la fréquence de vibration du mode j et D_j le déplacement du mode de vibration j au cours de la transition électronique considérée. Pour chaque mode de vibration, il est possible de calculer une énergie de réorganisation correspondante, $E_{reorg,j}$. En sommant toutes ces énergies de réorganisation, l'énergie de réorganisation totale, $E_{reorg,totale}$, est accessible. $E_{reorg,totale}$ nous renseigne sur l'énergie qui est perdue sous forme de vibration pendant la réorganisation et donc sur l'importance des processus non-radiatifs et par extension, de façon qualitative, sur l'efficacité du phénomène de fluorescence, Φ_F.

La stratégie que nous avons adoptée pour étudier les systèmes présentant le phénomène d'AIE/CIE est la suivante:

(1) Comprendre et rationaliser le caractère émissif/non-émissif des molécules dans un milieu dilué (solution).

(2) Définir un protocole de calcul à même d'étudier les systèmes sous forme d'agrégat/cristal moléculaire.

(3) Etudier les processus de fluorescence des systèmes dans les environnements complexes.

Cette stratégie a été appliquée à trois systèmes présentant les phénomènes d'ACQ/AIE/CIE.

Une première molécule, le 4-fluorophenyl 4-((4-(octyloxy)phenyl)ethynyl)-benzoate (**FOEB**) a été considérée (Figure 1). En solution, **FOEB** présente un rendement de fluorescence modéré (26%, 49% et 30% respectivement dans le toluène [TLN], le tétrahydrofurane [THF] et l'acétonitrile [ACN]). Ce rendement augmente très fortement dans le cristal (60%) et diminue drastiquement quand la molécule est sous forme d'agrégat (Φ_F=9%). La molécule de **FOEB** présente donc à la fois un comportement de CIE et d'ACQ. Les isomères du dipyrrolyldiphenylethène (**DPYDPE**) ont ensuite été considérés. L'isomère **E-DPYDPE** est un AIEgène (Φ_F = 0.2% et 69% respectivement dans une solution de THF et sous forme d'agrégat) tandis que l'isomère **Z-DPYDPE** présente le phénomène de CIE (Φ_F = 10% et 89% respectivement dans une solution de THF et sous forme de cristal) et dans une moindre mesure le phénomène d'AIE (Φ_F = 37% dans l'agrégat). Les dérivés de la famille du tiazolo[5,4-b]thieno[3,3e]pyridine (**TTP**) ont finalement été étudiés afin d'expliquer le caractère globalement non-émissif des solutions de benzène contenant un des dérivés du **TTP** (Φ_F < 12%) puis le phénomène d'ACQ observé pour **TTP-0** (Φ_F = 1% dans le cristal) et enfin le phénomène de CIE que présentent les cinq autres dérivés de façon plus ou moins marquée (26% < Φ_F < 62%). Cette molécule présente également le phénomène de transfert de proton intramoléculaire à l'état excité ou ESIPT (*Excited state Intramolecular Proton Transfer*). Le but est donc dans un premier temps de proposer un protocole de calcul à même de prendre en compte les différentes phases évoquées précédemment (solution, agrégat, cristal). Ensuite, il va s'agir de d'étudier les phénomènes d'absorption et d'émission dans chacune des phases puis d'être capable d'expliquer la variations observées (1) entre différents solvants pour une même molécule, (2) entre différentes molécules (isomères ou dérivés) dans un même environnement et enfin (3) les variations entre différents environnements pour une même molécule. L'idée est donc de pouvoir apporter une explication théorique au phénomène d'AQ/AIE/CIE.

Processus photochimique : le photochromisme

Le photochromisme est la transformation réversible d'une molécule entre un isomère A et un isomère B suite à une irradiation lumineuse. Il est intéressant de noter que les photochromes et notamment ses isomères peuvent facilement être différenciés du fait qu'ils

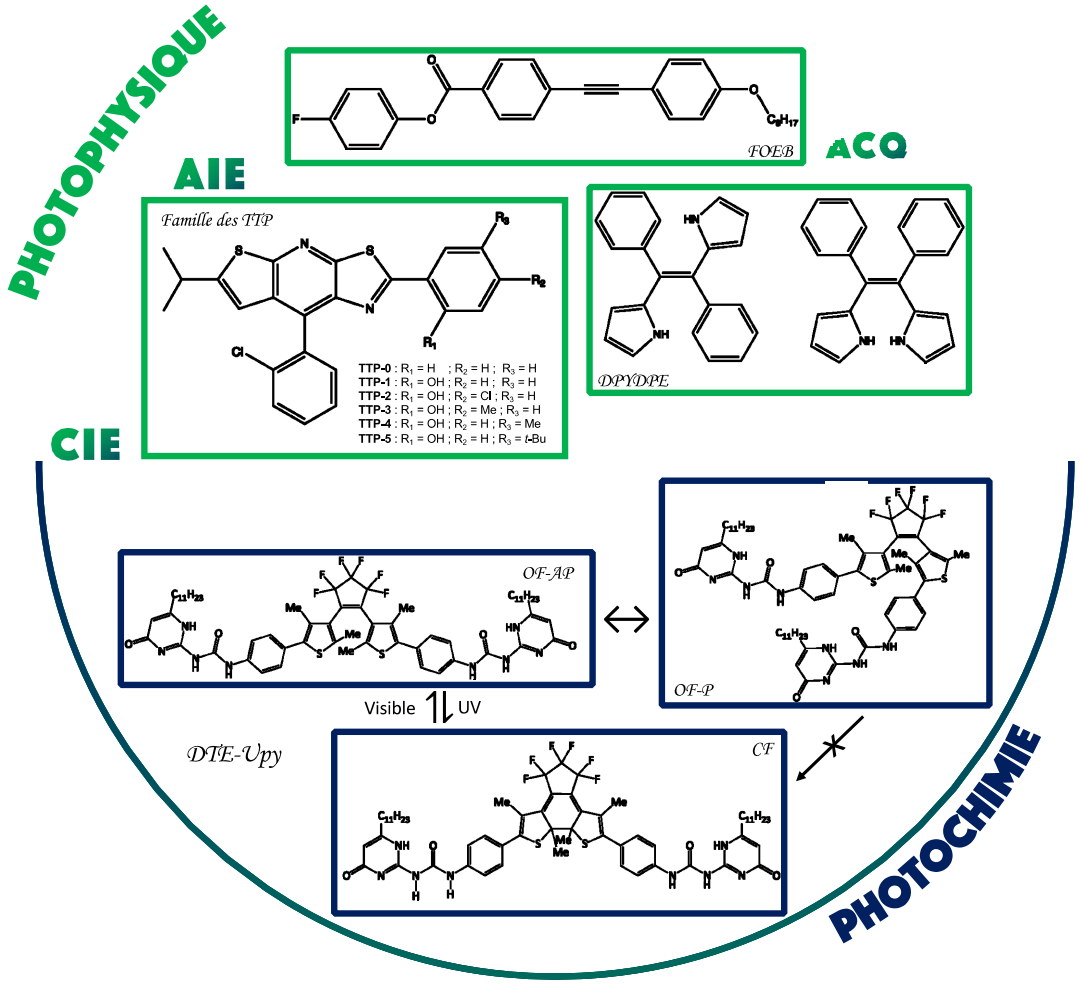

FIGURE 1 – Représentation schématique des processus étudiés lors de cette thèse, à savoir les processus photophysiques avec la modulation de la fluorescence *via* l'environnement et les réactions photochimiques avec l'étude d'un composé photochrome. Pour chaque cas, les structures des molécules étudiées ont été représentées.

possèdent un spectre d'absorption différent. Ce changement de couleur est souvent accompagné d'une modification structurale importante entre les deux isomères. Cette caractéristique a été notamment utilisée en chimie supramoléculaire puisqu'elle permet de contrôler la forme et/ou la taille des molécules avec la lumière et de transmettre cette modification à l'environnement pour induire une modification à une plus grande échelle. De nombreuses molécules photochromes sont aujourd'hui connues et étudiées. Des efforts, tant du point de vue de la caractérisation que de la synthèse, ont permis de mettre au point des molécules

photochromes aux propriétés d'absorption contrôlées ainsi que possédant une résistance à la fatigue (possibilité pour la molécule de réaliser de nombreuses fois la réaction photochimique et son retour sans perte d'efficacité) importante.

C'est un dérivé de la famille des dithiényléthène (**DTE**) qui a retenu notre attention. La molécule de **DTE** présente deux isomères, une forme ouverte (**FO**) ainsi qu'une forme fermée (**FF**). A noter que c'est **FO** qui est l'isomère le plus stable mais que les deux isomères sont stables thermiquement. Un troisième isomère, lui aussi de type "forme ouverte", existe. La différence entre les deux formes ouvertes réside dans l'orientation relative des deux carbones réactifs impliqués dans la réaction photochimique. Si les deux carbones sont orientés dans la même direction, alors il s'agit de la forme ouverte parallèle (**FO-P**) qui est non-photoactive. Si les deux carbones sont orientés dans des directions opposées, alors il s'agit de la forme ouverte parallèle (**FO-AP**). La réaction de cyclisation est induite par l'absorption de lumière dans l'ultra-violet (**FO-AP**→**FF**) et la réaction de cycloréversion est induite par l'aborption de lumière dans le visible (**FF**→**FO-AP**). Dans le cadre d'une collaboration avec le Pr. M. Takeshita de l'université de Saga au Japon et avec le Dr. S. Aloïse de l'université de Lille 1, nous nous sommes intéressés aux molécules de **DTE**, fonctionnalisées aux extrémités par des groupements uréidopyrimidinone (**Upy**). Ces groupements sont connus pour leur capacité à former des blocs de liaisons hydrogène, au nombre de quatre, permettant ainsi la formation d'édifices supramoléculaires. Les molécules de **DTE-Upy** ont fait l'objet d'études dans plusieurs environnements.

Dans le chloroforme, il a été montré grâce à la DLS (*Dynamic Light Scattering* ou diffusion dynamique de la lumière) que seuls des petits édifices de **FO**, d'une taille inférieure à 10 nm, sont présents. L'irradiation dans l'UV de **FO** (afin d'induire la réaction de photocyclisation) a conduit à une augmentation de la taille des particules, jusqu'à 650 nm. Cela indique qu'un assemblage supramoléculaire a pu se former suite à la réaction photochimique. Si la concentration initiale en **FO** est suffisante, il est même possible d'observer la formation d'un précipité bleu (la couleur traduisant la présence de **FF**).

Les mêmes molécules ont également été étudiées au sein de matrices polymères. Le polymère considéré présente lui aussi une fonctionnalisation en **Upy** à ses extrémités, permettant ainsi un assemblage supramoléculaire impliquant les extrémités **Upy** de **DTE-Upy** et du polymère. Un film mince contenant initialement à la fois **FF** et le polymère, est courbé

et de couleur bleue. Après irradiation dans le visible, le film s'aplatit instantanément et est suivi d'un retour lent à la forme initialement courbée. La réaction photochimique, qui a lieu à l'échelle moléculaire a donc un impact à l'échelle macroscopique puisqu'elle induit un changement de morphologie du matériau.

Suite à ces observations, les questions sont multiples :

- En solution, comment expliquer la formation d'un assemblage supramoléculaire uniquement pour la forme fermée, **FF** ?

- Au sein du polymère, est-on capable d'expliquer l'effet optomécanique observé ? Est-il possible, une fois la compréhension du phénomène optomécanique atteinte, d'améliorer le système afin d'associer à une forme d'une film mince (courbé, plat), un isomère de **DTE-Upy** (**FO**, **FF**) ?

Méthodes

Pour étudier l'ensemble de nos systèmes dans tous les environnements mentionnés plusieurs approches théoriques ont été considérées. La théorie de la fonctionnelle de la densité (DFT) ainsi que sa version dépendante du temps (TD-DFT) ont constitué un outil de choix pour l'étude des états excités (et donc des propriétés optiques) des molécules. En effet, à ce jour, la TD-DFT reste le meilleur compromis pour étudier de façon efficace des systèmes de grande dimension. Des approches de dynamique classique ont également été utilisées afin de rendre compte de la dynamique des systèmes en solution ou dans des matrices polymères. Des approches hybrides, combinant et des approches quantiques (DFT) et des approches de mécanique moléculaire (MM), QM/MM ont également été utilisées. Enfin, plusieurs outils d'analyse ont été considérés afin d'apporter des informations quantitatives aux phénomènes étudiés (calcul des facteurs HR, calcul du transfert d'énergie d'excitation, etc). Nous avons représenté de façon schématique la stratégie que nous avons adopté sur la Figure 2.

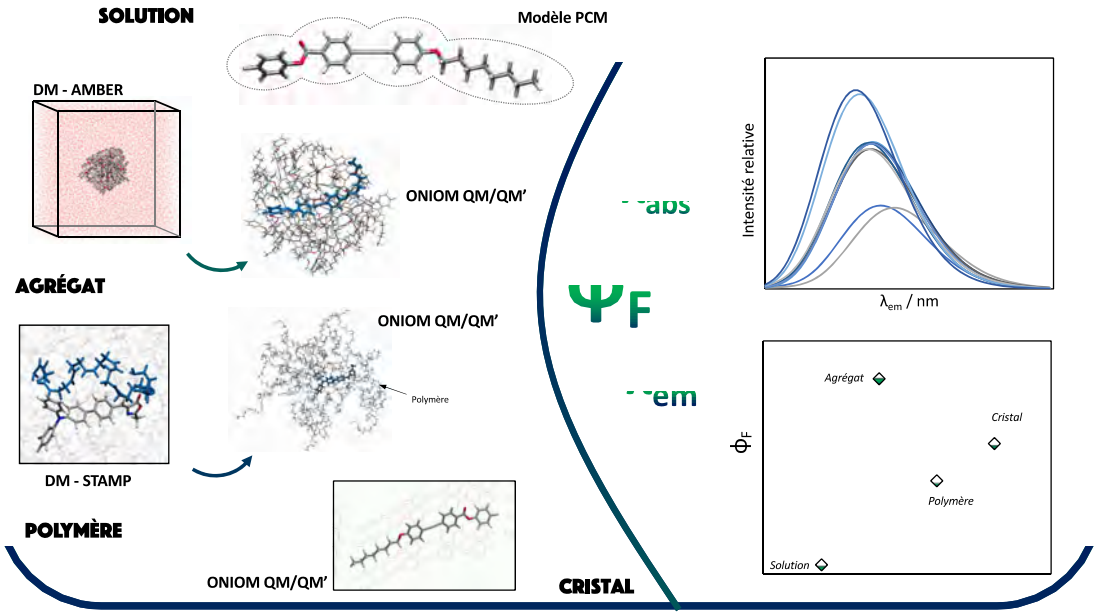

FIGURE 2 – Représentation schématique des schémas de calcul utilisés pour décrire les différents environnements (solution, agrégat, polymère et cristal) afin d'obtenir les propriétés optiques de chacune de ces phases.

Résultats

La fluorescence sous toutes ses formes

Pour les trois systèmes étudiés (la molécule **FOEB**, les isomères de **DPYDPE** et la famille des **TTP**), nous avons mis au point un protocole de calcul adapté à chaque environnement et capable de reproduire les propriétés optiques (absorption et émission) expérimentales.

Dans une première étape, l'étude des propriétés optiques en solution a permis de proposer une explication à la modulation de la longueur d'onde d'émission quand (1) la polarité du solvant est modifiée et/ou (2) quand différents isomères (**E-DPYDPE** and **Z-DPYDPE**) ou dérivés (**TTP** family) sont considérés. Nous montrons également que pour les trois systèmes étudiés, le faible à très faible rendement de fluorescence en solution est dû à une dissipation photophysique de l'énergie induite par des vibrations de basses fréquences, illustrée de façon qualitative par le calcul des facteurs HR. D'autres caractéristiques ont été étudiées. Par exemple, pour les isomères **DPYDPE**, en raison d'une forte réorga-

nisation structurelle le long du chemin de relaxation sur la surface d'énergie potentielle du premier état excité (S_1), nous avons recherché l'existence d'une éventuelle intersection conique. Cependant, aucun croisement S_0/S_1 n'a pu être trouvé. Nous avons également proposé une explication à la modulation de Φ_F. Par exemple, pour la famille **TTP**, la rigidification des structures observée suite à l'ajout d'une liaison hydrogène intramoléculaire a pour effet de diminuer le rendement de fluorescence (**TTP-1** et **TTP-3** à **TTP-5**), illustré par des valeurs de facteur HR plus grandes. Par conséquent, la rigidification de molécules via la mise en place de liaisons intramoléculaires faibles (liaison H, par exemple), qui est souvent utilisée pour limiter les mouvements de rotation et donc les possibles dissipations d'énergie, doit être considérée comme une stratégie risquée, car elle peut induire une dissipation d'énergie *via* des mouvement de vibrations de la molécule nouvellement rigidifiée. Les facteurs HR calculés fournissent des informations qualitatives utiles qui nous ont permis de toujours trouver une corrélation entre l'énergie de réorganisation totale calculée et la valeur expérimentale Φ_F.

Dans une deuxième étape, ce sont les études des phases plus denses, à savoir la phase cristalline (pour toutes les molécules) et/ou la phase agrégée lorsque cela était nécessaire (**FOEB** et **DPYDPE** uniquement), qui ont été entreprises. Nous avons dû faire face à différents phénomènes tels que l'ACQ (la molécule **FOEB** et le dérivé **TTP-0**), l'AIE (l'isomère **E-DPYDPE**) ou CIE (la molécule **FOEB**, l'isomère **Z-DPYDPE** ou les dérivés **TTP**). Nous avons montré que le phénomène d'ACQ trouve son origine dans la combinaison de deux processus contribuant à la désexcitation non radiative:

- La perte d'énergie due aux couplages excitoniques qui est due à l'agencement particulier des molécules entre elles et notamment l'empilement de type π-π.
- La dissipation d'énergie au cours du processus de conversion interne via le mode de vibration de basse fréquence identifié dans la solution. En effet, l'arrangement particulier des molécules **FOEB** et **TTP-0** ne limite pas ces vibrations. D'autre part, les comportements AIE et CIE ont été expliqués par le fait que la phase agrégée et/ou cristalline bloque le mode de vibration impliqué dans la faible efficacité du processus d'émission en solution, ouvrant ainsi les voies de désexcitation non radiative.

Néanmoins, une compétition subtile a été mise en évidence pour certaines molécules. Pour la molécule **TTP-1**, la voie de relaxation non radiative par couplage excitonique est éga-

lement possible et la compétition entre ces deux effets antagonistes (RIV et couplage excitonique) conduit finalement à un effet de CIE modéré. Un autre exemple d'effets subtils dans l'agrégat a été démontré pour la molécule **DPYDPE**. Pour les deux isomères, toutes les voies de désexcitation non radiatives sont bloquées, ce qui augmente l'efficacité du rendement quantique de fluorescence par rapport aux molécules isolées en solution. Il existe cependant une différence entre les deux isomères qui est due à une compétition entre des interactions intermoléculaires avec le solvant, avec d'autres molécules de **DPYDPE** et des interactions intramoléculaires entre les cycles pyrrole.

Par conséquent, la combinaison de stratégies théoriques adéquates permet une étude minutieuse des différents processus photophysiques à l'origine des effets d'ACQ/AIE/CIE, ainsi qu'une compréhension qualitative des observations expérimentales. Le développement de nouveaux AIEgènes et leur utilisation dans des dispositifs innovants de haute technologie peuvent ainsi tirer parti d'études théorique. La modélisation appropriée des effets environnementaux est cruciale pour ouvrir la voie au développement de nouveaux matériaux fonctionnels. Dans cette thèse, nous nous sommes particulièrement intéressés à la description de l'environnement, ce qui nous a empêché, en raison des modèles actuellement disponibles, une exploration plus poussée et des descriptions plus quantitatives (impliquant par exemple le calcul de la constante de temps associée aux désexcitation non radiatives, k_{nr}, ou les calculs de facteurs HR dans le modèle ONIOM). Cependant, ces approches qualitatives nous ont toujours permis de rationaliser les comportements relatifs de molécules appartenant à la même famille.

Le photochromisme dans tous ses états

À l'aide de simulations de dynamique moléculaire, nous avons étudié le comportement des monomères, dimères, hexamères et dimères empilés de **FO** et **FF** en solution. Notre objectif était d'expliquer la formation d'assemblages supramoléculaires uniquement pour les isomères **FF**. Nous avons montré que ce comportement peut être rationalisé par (1) la formation possible d'un dimère cyclique très stable pour les isomères **FO-P**; (2) la flexibilité relative des oligomères **FO** par rapport à leurs équivalents **FF**, comme le montre l'étude des hexamères en solution; (3) l'existence possible de dimères empilés impliquant

des interactions π qui ne présentent pas de groupements **Upy** libres pour le système **FO**. Ces résultats montrent systématiquement que la progression de l'assemblage supramoléculaire sera plus compliquée voire totalement empêchée pour les oligomères **FO**. En particulier, l'existence de structures cycliques très stables, sans groupements **Upy** libres, bloque l'auto-assemblage supramoléculaire. La formation de telles structures cycliques stables est systématiquement déclenchée par l'isomérisation de **FO-AP**/**FO-P**: la présence d'au moins un isomère de **OF-P** dans le système considéré est une condition nécessaire pour former ces agrégats cycliques. Sur la Figure 3 sont représentées de façon schématique la stratégie adoptée lors de cette étude ainsi que les résultats et conclusions importantes.

Toujours à l'aide de simulations de dynamique moléculaire, nous avons pu initier l'étude

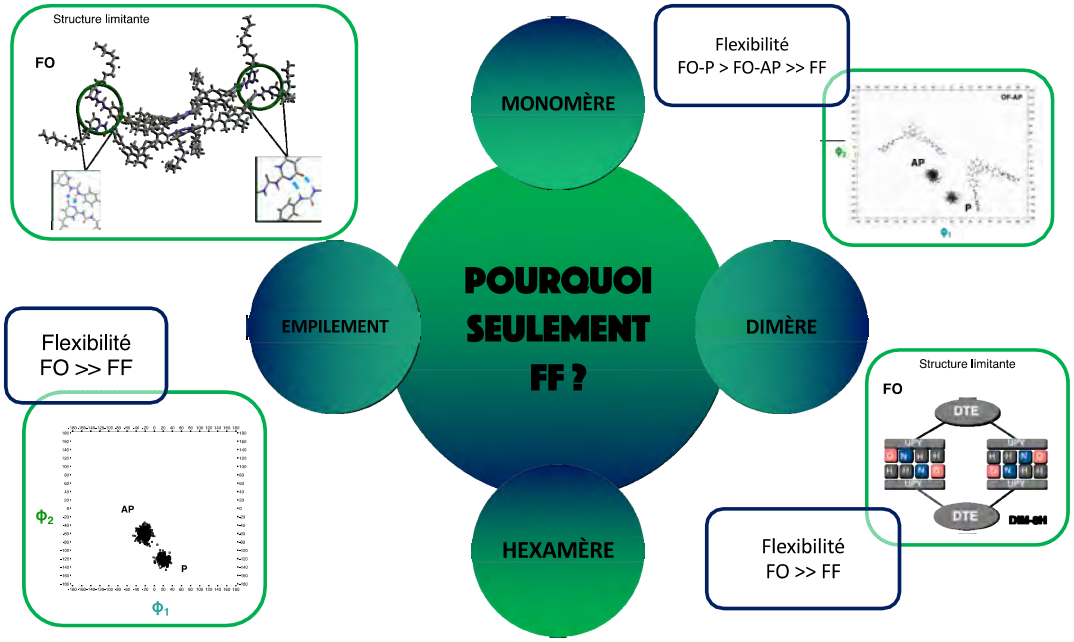

FIGURE 3 – Représentation de la stratégie adoptée, à savoir l'augmentation successive (monomère, dimère, hexamère et dimères empilés (π-*stacking*) du nombre de molécules considérées. Les résultats et conclusions associés à chaque étape apparaissent également.

des molécules de **DTE-Upy** au sein d'une matrice polymère. Il nous a d'abord fallu mettre en place les outils afin de pouvoir considérer à la fois le photochrome et la matrice polymère. Pour cela, dans le cadre d'une collaboration avec le CEA DAM/DIF, nous avons pu utiliser le logiciel STAMP qui permet entre autres de réaliser des simulations de dynamique moléculaire classique mais également de réaliser des étapes de polymérisation

in situ. Cette caractéristique est importance, car elle permet de générer un système ou la molécule d'intérêt est parfaitement imbriquée dans le polymère, puisque les chaînes se sont créées autour de la molécule. Elle est également novatrice puisque jusqu'ici, la procédure qui était utilisée, consistait à créer une cavité dans une matrice polymère et d'y insérer manuellement la molécule. A noter que pour une première approche, c'est un polymère modèle, le polybutadiène, sans extrémités **Upy**, qui a été considéré. Ensuite, deux aspects ont été abordés :

- L'impact de la matrice polymère sur le photochrome. Comme il a été démontré en solution que les systèmes étaient très flexibles et que cela avait un impact sur les propriétés optiques, l'idée est de voir si le fait d'insérer les molécules dans un environnement dense a dans un premier temps un impact structural. La grande flexibilité est-elle maintenue ? La réaction d'isomérisation est-elle encore possible ? Dans un second temps, les propriétés optiques ont été étudiées afin d'observer le possible impact de l'environnement sur ces dernières. Nous avons montré que, logiquement, la matrice polymère a un impact mécanique sur les molécules de **DTE-Upy**. En effet, la flexibilité, en particulier celle du coeur **DTE** et dans une moindre mesure celle des chaînes alkyles latérales est plus faible au sein du polymère.
- L'impact de la réaction de photocyclisation (**FO-AP**$\rightarrow$ **FF**) et de cycloréversion (**FF**$\rightarrow$ **FO-AP**) sur la matrice polymère. En effet, les deux réactions impliquent une grande modification structurale. La forme **FO-AP** est "décalée" tandis que **FF** est plane (du fait de la formation d'une liaison carbone-carbone). Si l'on considère la réaction de photocyclisation par exemple, notre stratégie a consisté à considéré la structure de **FO-AP** puis de modifier ses paramètres (Champ de force, types d'atomes, charges, matrice de connectivité) afin de lui imposer ceux de **FF**. Une étape de minimisation, avec les chaînes polymères fixes, a permis de relaxer la molécule de **DTE-Upy**. De cette façon, du point de vue du polymère, la réaction est instantanée et des contraintes sont donc apparues au niveau de l'interface polymère/**DTE-Upy** puisque chaque isomère occupe un espace, un volume qui lui est propre. Au cours de nos simulations, nous avons pu voir que la réaction de cycloréversion (ouverture) a plus d'impact que la réaction de cyclisation (fermeture). En effet, nous avons constaté qu'après 1 ns, le polymère essayait encore de répartir la pression localement élevée générée par le changement brutal de conformère **DTE-Upy**.

Perspectives

Concernant les perspectives associées à l'étude des phénomènes d'ACQ/AIE/CIE, l'objectif est d'adopter une approche plus quantitative avec par exemple le calcul des facteurs HR avec des approches ONIOM (pour les agrégats, cristaux et matrices polymères). On peut aussi mentionner le calcul de la constante de désexcitation non radiative, k_{nr}, qui donnera un paramètre objectif concernant le comportement émissif des molécules dans les différents environnements. L'utilisation du logiciel MOMAP, qui est un code qui permet le calcul des propriétés photophysiques, peut être envisagée pour atteindre cet objectif.
Concernant l'étude des molécules photochromes, le travail principal concerne le comportement au sein de la matrice polymère. En effet, dans le cadre d'une première approche, nous avons considéré une matrice modèle de polybutadiène.

Même s'il s'agissait d'un point de départ raisonnable pour mettre en place l'approche computationnelle et développer tous les outils d'analyse, ce n'est pas le polymère qui a été utilisé expérimentalement. L'évolution peut donc être d'envisager :
- Une fonctionnalisation, avec des fragments **Upy**, des chaînes polymères. L'idée est de créer un réseau de liaison H entre les molécules **DTE-Upy** et les chaînes polymères qui peuvent amplifier les modifications structurales photoinduites du matériau.
- La cinétique de la relaxation du polymère étant lente, des simulations plus longues peuvent être utiles. Pour le moment, nous avons systématiquement réalisé 1 ns de simulation.

Un autre projet a déjà été initié afin de décrire les AIEgènes dans les environnements polymères. Cette étude associe donc les deux "aspects" qui ont été développés lors de ce travaux. Ce type de système combinant des molécules émissives au sein d'un environnement polymère est particulièrement utilisé pour des applications telles que les concentrateurs solaires luminescents (LSC). L'étude de la modulation de l'efficacité d'émission avec l'environnement et le nouveau schéma de polymérisation *in situ* a été appliqué à une nouvelle molécule, le triphénylamine-(Z)-4-benzylidiène-2-méthyloxazol-5 (4H)-one (**TPA-BMO**), représenté sur la Figure 4.

L'intérêt de cette molécule réside dans la modulation de son efficacité de fluorescence

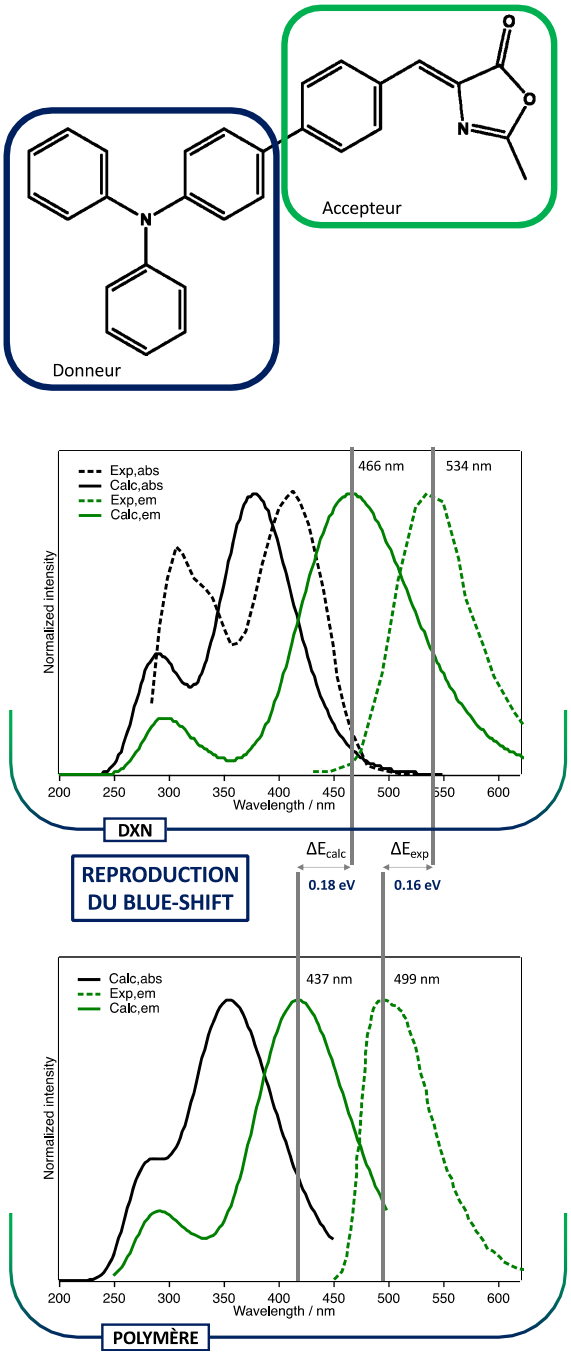

FIGURE 4 – Représentation de la structure du **TPA-BMO** (haut) et des spectres d'absorption et d'émission normalisés (convolués par une fonction gaussienne avec une largeur à mi-hauteur de 0.33 eV) pour le **TPA-BMO** dans le dioxane (milieu) et au sein de la matrice polymère (bas). Les spectres expérimentaux sont également représentés.

en fonction de l'environnement considéré (Tableau 1).

De façon générale, on peut observer une modulation du rendement quantique de fluo-

TABLE 1 – Propriétés expérimentales de la molécule de **TPA-BMO** dans différents solvants, sous forme d'agrégat, en phase cristalline et dans différentes matrices polymères. Les propriétés optiques (absorption et émission) sont données en nm. Le rendement quantique de fluorescence, Φ_F, est également fourni.

	Solution			Agrégat	Cristal	Polymère		
	DXN[a]	THF[b]	ACN[c]	-	-	PB[d]	PMMA[e]	PEG[f]
λ_{max}	406	407	408	425	-	-	-	-
λ_{em}	530	576	580, 700	574	635	499	525	567
Φ_F	0.62	0.51	0.03	-	0.46	-	-	-

[a] Dioxane. [b] Tétrahydrofurane. [c] Acétonitrile. [d] Polybutadiène. [e] Poly(méthyl méthacrylate). [f] Polyéthylène glycol.

rescence (Φ_F) et de la longueur d'onde d'émission (λ_{em}) avec la polarité du solvant et dans les différents environnements. Le **TPA-BMO** reste émissif dans l'agrégat et ne présente donc pas le phénomène d'ACQ. A l'intérieur d'une matrice polymère de polybutadiène, de poly(méthacrylate de méthyle) ou de polyéthylène glycol, la position de la bande d'émission se déplace vers les grandes longueurs d'onde à mesure que la polarité des chaînes polymères augmente. Cette caractéristique est un paramètre expérimental très important car elle peut être utilisée pour différencier et déterminer la nature des phases polymères mixtes. Suivant la procédure que nous avons développée et décrite précédemment, des calculs ont été effectués pour étudier le **TPA-BMO** dans tous les environnements mentionnés, c'est-à-dire :

- En solution et dans différents solvants. Le but est d'expliquer la modulation de Φ_F avec la variation de λ_{em} avec la polarité du solvant.
- En agrégat, pour expliquer la variation de λ_{max} et λ_{em}.
- Dans la phase cristalline, pour expliquer la variation λ_{em} et le léger effet CIE.
- Dans la matrice polymère, pour expliquer la modulation de λ_{em} dans différents polymères. Pour l'instant, seul le polymère PB est considéré. L'objectif est donc de pouvoir expliquer le décalage vers le bleu par rapport aux solvants non polaires (DXN).

La nouveauté de ce travail par rapport à ce qui a été fait précédemment réside dans la prise en compte des propriétés d'émission et donc de l'étude des états excités dans des

environnements complexes.

Nous avons représenté sur la Figure 4 quelques résultats préliminaires. La principale conclusion de ces résultats préliminaires est que, même si nous ne sommes pas en mesure de prédire avec précision la position des différentes bandes d'absorption et/ou d'émission, notre choix de protocole de calcul est capable de reproduire la tendance observée entre la solution DXN et la matrice polymère PB (tous les calculs ont été effectués en utilisant la fonctionnelle M06-2X et la base 6-311+G(d,p)). En effet, expérimentalement, un décalage vers le bleu de 0,16 eV (35 nm) est observé entre le λ_{em} en DXN (534 nm) et en matrice PB (499 nm). Avec nos calculs, nous obtenons un décalage vers le bleu de 0,16 eV (29 nm).

Comme il est maintenant possible de (1) considérer les molécules organiques dans une matrice polymère et (2) quantifier l'impact qu'elles ont les unes sur les autres, on peut imaginer d'imposer des contraintes externes (compression, étirement, cisaillement) et aller vers le mécanochromisme ou mécanofluorochromisme.

Le mécanochromisme est le changement de couleur d'un matériau lors de l'application d'une force extérieure. Le changement des propriétés d'émission lors de l'application de la force mécanique est connu sous le nom de mécanofluorochromisme, les molécules luminescentes voient alors leurs propriétés optiques modifiées (intensité et/ou couleur) par l'application de forces mécaniques externes. Les derniers sont particulièrement utilisés comme mécanocapteurs. Dans ce cas, les molécules mécanofluorochromiques sont utilisées comme "témoins" des contraintes qui peuvent être appliquées à un matériau. En effet, si le matériau est sollicité d'une manière particulière, la molécule mécanofluorochromique émettra de la lumière ou non et mettra en évidence la contrainte mécanique. Les approches développées dans le cadre de cette thèse peuvent naturellement être appliquées dans le contexte de la conception de nouveaux matériaux mécanochromiques.

Table of contents

Glossary

General introduction

1 Theoretical background **9**

1.1 Quantum mechanical methods 9

1.1.1 Wavefunction 10

1.1.1.1 Slater determinant 11

1.1.1.2 Atomic basis set 11

1.1.2 Hartree Fock 12

1.1.2.1 Method 12

1.1.2.2 Limitation 13

1.1.3 Density Functional Theory 14

1.1.3.1 Exchange correlation functional 15

1.1.3.2 Description of the used functionals 18

1.1.4 Time-dependent Density Functional Theory 19

1.2 Molecular mechanics based approaches 22

1.2.1 Force Field 22

1.2.1.1 Potential energy function 22

1.2.1.2 Classical Force Field 23

1.2.2 Molecular Dynamics . . . 23
1.2.2.1 Integration algorithms . . . 24
1.2.2.2 Time step . . . 25
1.2.2.3 Thermodynamics ensemble . . . 25
1.2.2.4 Periodic boundary conditions . . . 27
1.3 Hybrid approaches: QM/MM and QM/QM' . . . 29
1.3.1 Principle . . . 29
1.3.2 QM:MM and QM:QM' schemes . . . 30
1.3.3 Embedding schemes . . . 31
1.3.3.1 ONIOM(QM:MM)-EE model . . . 31
1.3.3.2 ONIOM(QM:MM)-PE . . . 31
1.3.3.3 ONIOM(QM:QM')-EE . . . 32
1.4 Modeling the environment . . . 32
1.4.1 Explicit model . . . 32
1.4.2 Implicit model . . . 33
1.5 Modeling photochemical processes . . . 35
1.5.1 Absorption and emission spectra . . . 36
1.5.2 Fluorescence quantum yield and Huang-Rhys factors . . . 37
1.5.3 Excitation Energy Transfer and electronic coupling . . . 38

2 To be emissive or not to be ? 43

2.1 Introduction: ACQ and AIE phenomena . . . 43
ACQ to AIE . . . 43
Explanation of the phenomena . . . 46
Design strategies . . . 51
Our strategy . . . 52
2.2 Computational details . . . 57
2.2.1 Solvated systems . . . 57
2.2.2 Crystalline phase . . . 63
2.2.3 Aggregated phase . . . 64
2.3 **FOEB** molecule . . . 67

2.3.1 At the beginning, molecules were solvated. . . . 67
2.3.2 Then, they turned into crystalline phase. . . . 74
2.3.3 They also formed aggregates. . . . 78
2.4 **DPYDPE** isomers . . . 81
2.4.1 Solution: a dark beginning. . . . 81
2.4.2 Crystal: one chance out of two . . . 86
2.4.3 Aggregation: stairway to AIE . . . 91
2.5 **TTP** family . . . 95
2.5.1 Solution: on the dark side . . . 95
2.5.2 Crystal: and there was light ! . . . 102
2.6 Conclusion . . . 111

3 To be colorful or not to be ? 113
3.1 Introduction: Photochromism . . . 113
3.1.1 Definition . . . 113
3.1.2 History . . . 114
3.1.3 Photochromic molecule: **DTE** derivatives . . . 116
3.1.4 Lucky dip! **DTE-Upy** . . . 117
Experimental features . . . 117
Previous study . . . 119
3.2 **DTE-Upy** in solution . . . 121
3.2.1 Computational details . . . 122
3.2.1.1 Molecular Dynamics . . . 122
3.2.1.2 QM calculations . . . 124
3.2.2 Results . . . 127
3.2.2.1 Monomer . . . 127
3.2.2.2 Dimer . . . 134
3.2.2.3 Hexamer . . . 140
3.2.2.4 π-Stacked dimers . . . 143
3.2.3 Conclusion . . . 146
3.3 **DTE-Upy** in polymer . . . 147

3.3.1 Computational details . . . 148
3.3.1.1 Molecular Dynamics . . . 148
3.3.1.2 Absorption properties: set up of the computational strategy 154
3.3.2 Impact of the matrix on the **DTE-Upy** properties . . . 156
3.3.2.1 Structural analysis . . . 156
3.3.2.2 Optical properties . . . 164
3.3.3 Impact of the photochemical reaction on the matrix . . . 166
3.3.3.1 Embedded photochemical reaction: How ? . . . 166
3.3.3.2 Minimization . . . 167
3.3.3.3 NVE production . . . 171
3.4 Conclusion . . . 174

General conclusion and perspectives **176**

Bibliography **185**

Appendices **197**

A-1 **FOEB** molecule: benchmark . . . 197
A-2 **FOEB** molecule: HR factors . . . 200
A-3 **FOEB** molecule: superposition of the structures . . . 201
A-4 **FOEB** molecule: important vibrational modes . . . 202
A-5 **DPYDPE** isomers: phenyl rotation . . . 203
A-6 **DPYDPE** isomers: optical properties of the aggregate . . . 204
A-7 **DPYDPE** isomers: structures superpositions . . . 205
A-8 **TTP** family: benchmark . . . 206
A-9 **TTP** family: HR factors . . . 208
A-10 **TTP** family: crystalline model . . . 210
A-11 **TTP** family: crystalline structures . . . 211
A-12 **DTE-Upy**: complementary analysis of the MD simulation of the dimers . . 212
A-13 **DTE-Upy**: complementary analysis of the MD simulation of **OF-P** dimer 213
A-14 **DTE-Upy**: complementary analysis of the MD simulation of **OF-P** cyclic dimer . . . 214

A-15 **DTE-Upy**: complementary analysis of the MD simulation of the π-stacked dimers 215
A-16 **OF-AP**: STAMP simulations 216
A-17 **OF-P**: STAMP simulations 217
A-18 **CF**: STAMP simulations 218

Glossary

— ACN: Acetonitrile

— ACQ: Aggregation-Caused Quenching

— AIE: Aggregation-Induced Emission

— AP: Antiparallel

— BTDN: Butadiene

— CF: Closed Form

— CIE: Crystallization-Induced Emission

— (TD-)DFT: (Time-Dependent-) Density Functional Theory

— DTE: Dithienylethene

— DPYDPE: Dipyrrolyldiphenylethene

— DXN: Dioxane

— EE: Electronic Embedding

— EET: Electronic Energy Transfer

— ESIPT: Excited State Intramolecular Proton Transfer

— FOEB: 4-fluorophenyl 4-((4-(octyloxy)phenyl)ethynyl)-benzoate

— HOMO: Highest Occupied Molecular Orbital

— HR: Huang-Rhys

— IC: Internal Conversion

— ISC: Intersystem Crossing

— IR: Infrared

— LUMO: Lowest Unoccupied Molecular Orbital

— MM: Molecular Mechanics

— OF: Open Form

— P: Parallel

— PES: Potential Energy Surface

— QM: Quantum Mechanics

— RIM: Restricted Intramolecular Motion

— RIR: Restricted Intramolecular Rotation

— RIV: Restricted Intramolecular Vibration

— THF: Tetrahydrofuran

— TLN: Toluene

— TPA-BMO: Triphenylamine-(Z)-4-benzylidiene-2-methyloxazol-5 (4H)-one

— TTP: Tiazolo[5,4-b]thieno[3,3e]pyridine

— Upy: Ureidopyrimidinone

— UV: Ultraviolet

— VR: Vibrational Relaxation

— Φ_F: Fluorescence Quantum Yield

General introduction

2015 was the International year of Light and Light-based Technologies, the United Nations thus recognized the great role of light in technological innovations, scientific discoveries and in life in general. One year after, the Nobel Prize in Chemistry was dedicated to J-P. Sauvage, F. Stoddart and B. Feringa for the "design and synthesis of molecular machines". Behind this work, the idea is to control photochemical and photophysical processes with light. In other words, to control the matter with light. Many examples can be cited such as:

- Molecular motors: they are constituted of molecules that have possible rotation motions around single or double bond. As a general rule, molecular motors involving rotation around simple bonds are chemically activated [1] whereas the ones involving rotations around a double bond are activated by light [2].
- Molecular photoswitch: a photoswitch corresponds to a molecule that can be reversibly shifted between two (or more) stables states by light [3, 4].
- Molecular shuttle: such a molecule is able to shuttle ions or other molecule from one location to another [5]. For example, the photoisomerization of azobenzene moiety is able to induce the movement of a macrocycle on the backbone of the molecule [6].

Concerning the emission process, one has to notice that the control of light emission (color and/or intensity) can be a target but light can also be part of the experimental conditions and can allow for example the excitation of a molecule at a particular wavelength

and the opening/closure of a particular photochemical and/or photophysical channel.
Photochemical and photophysical sciences study all the physico-chemical processes induced by the action of the light (from UV to near IR including visible light). Those processes concern the excited states of the atoms, molecules or systems under study. Photophysics concerns the physical processes that are induced by light while photochemical sciences are interested in photoinduced chemical transformation. As the boundary between those two domains is not always perfectly clear, they are considered as complementary. If one is interested by photophysical processes one needs to consider the chemical transformations that may be induced (photochemistry) while if one is interested in photochemical processes, one has to take into account the photophysical processes that are also involved. There is also sometimes a competition between these different processes.
Both photophysical and photochemical processes are involved in nature but also in high-technology applications. For the first one, one can cite for example the photosynthesis or the vision mechanism. Indeed, one has to notice that the first and the easiest way to find light source is the sun (the absorption wavelength, λ_{abs}, is between 380 and 750 nm). For the second one, the source of light can be the sun but also lamps or laser beams for which it is possible to control both the intensity and the type of light (position of λ_{abs}). The applications are numerous and one can cite photography developed at the beginning of the 19^{th} century (Numerical photographies are no longer using those processes), photodynamic therapy as an alternative to chemotherapy to cure cancer or the development of renewable energy (solar panels). With less immediate applications, one can also mention the possibility to use light and thus photochemical and photophysical processes to perform efficient and "clean" organic reactions (electrocyclic reactions, photoisomerization, radicals reactions, etc). We have represented on Figure I.1 some of the connexions that exist between photophysics/photochemistry and other scientific domains or applications. It illustrates the fact that photophysics and photochemistry are closely connected to other scientific domains. They are using data from spectroscopy studies, quantum mechanics and thermodynamics among others and provide useful information for applications in energy, materials and synthesis for example.
During this PhD I will be interested in the study of one photophysical and one photochemical process.

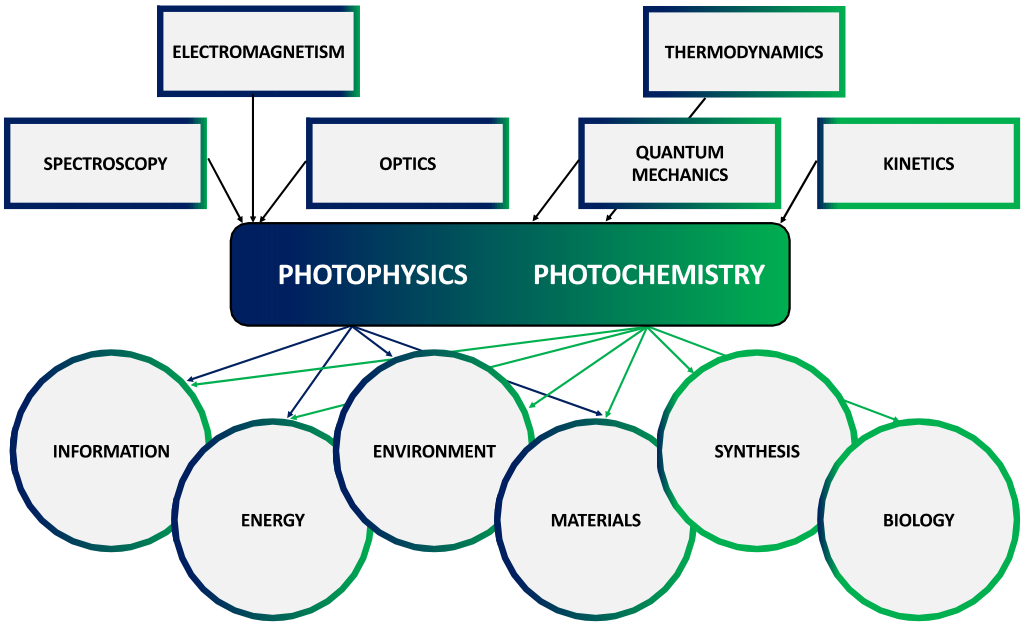

FIGURE I.1 – Connexions between photophysics/photochemistry and other scientific domains and with the different applications area [7].

Photophysics: fluorescence phenomena

Whether than only the fluorescence phenomena I will be more interested by the modulation of the fluorescence phenomena depending on the environment. Indeed, it has been shown that the fluorescence color and/or efficiency may be dependent of the environment. The modulation of emission efficiency is known in literature as Aggregation-Induced Emission (AIE), Crystallization Induced Emission (CIE) and Aggregation Caused Quenching (ACQ). The ACQ phenomenon corresponds to the behavior of molecules that are emissive in diluted medium (solution) but become poorly emissive when the molecules are aggregated (the aggregation process is often induced by adding a non-suitable solvent such as water in which emissive molecules, generally composed of aromatic moieties, are poorly soluble). The explanation of the non-emissive behavior in aggregate arises from the possible interaction between two molecules and the energy dissipation through excitonic couplings that will be in competition with the emission process. On the contrary, for AIE and CIE phenomena, molecules are poorly emissive in solution. This non-emissive behavior is generally attributed to an efficient energy dissipation achieved by almost free rotations of the substituents of the molecule in solution. When molecules are getting closer

(depending on the organization we face, whether an aggregate with no or low organization of the molecules between them, or a crystalline phase), they are also getting more emissive. It can be explained by the fact that in a dense environment, the movements of the substituents, that were responsible of the non-emissive behavior in solution, are no longer possible, may block the non-radiative pathway existing in solution and will thus induce the observed enhancement of emission. Understanding and being able to control either ACQ or AIE/CIE phenomena is of major importance as they can potentially be used for practical applications such as Organic Light Emitting diodes (OLEDs).

Photochemistry: photochromism phenomena

Photochromism is the reversible transformation of a chemical species between two isomers, A and B. This transformation can be induced in one or both directions by light irradiation. The interesting feature with photochromism molecules is that the two isomers can be differentiated *via* their different absorption spectra that are characteristic of each isomer. The color change is often correlated to a large structural difference between the two isomers. This parameter, the structural modification upon light irradiation, has been extensively used in supramolecular chemistry. The possibility that is given to reversibly control with light the size and the shape of the molecule means that they can be used to induce a shape change in their surrounding. Thus, photochromic molecules have been demonstrated to be good candidates as components of molecular switches or actuators. More generally, light-activated materials, which undergo macroscopic shape changes, are attractive targets in emerging photomechanical applications. In this context, light-driven actuators (actuator devices that use light as control signal or energy source) are capable of supplying energy in a non-contact manner with possible applications to industrial robots or micromachines used in the medical/nursing fields, artificial muscles or aerospace. Furthermore, if such devices are based on elastomer materials, performances improvement can be related with flexibility, light weight and noiselessness at the time of being driven. The most impressive demonstration of the huge abilities related with elastomeric light-driven devices has been reported recently with the first light-driven plastic motor running with UV-Visible light instead of electricity [8]. In order to develop promising devices able of converting light into mechanical work without the aid of batteries, electric wires or gears,

two conditions have to be fulfilled: (1) the response of theses systems should be rapid and (2) the deformed states should be thermally stable. Hence, a decisive step is the use of efficient bistable photochromic systems.

Importance of the environment

Up to now we briefly mentioned the impact of the environment, especially for ACQ/AIE/CIE phenomena, on both photophysics and photochemistry. Nevertheless, if one wants to consider a given molecule for practical application one needs to know if the desired property (fluorescence or photochromic reaction) will still be observed within a given environment. Indeed, the environment can modify the properties of the molecule (variation of the absorption and emission properties) but can also hinder or lessen some phenomena. One can cite the example of solvatochromism in which the environment (the solvent) has an impact on the optical properties. The presence of a crystalline or aggregated environment around a molecule may also modify its behavior as the movement of the molecule will be logically hindered (particular movement avoided, photochemical reaction no longer possible due to steric hindrance, etc). The comprehension of the interaction that exists between the molecule and its environment is thus of major importance if one wants to optimize the desired property of the considered molecule.

Aim of the thesis project

Throughout this work we propose to set up computational protocols that are adapted for the consideration of different environments. Indeed, it is necessary to adapt the tools that we will use as it is not possible to consider with the same methods a molecule in a diluted medium (solution) or a molecule embedded in a polymer matrix. In this thesis work, we will set up computational scheme to describe the photophysical and/or photochemical properties of molecules in solutions (with different solvents), aggregated molecules, molecular crystals and finally molecules embedded in a polymer matrix. Once those protocols are set up, we will consider photophysical and photochemical phenomena in all the previously cited environment. We will then systematically try to explain the observed phenomena (mainly absorption and emission properties) and provide theoretical insights to the experimental behaviors. We will carefully take into account the different environment in order

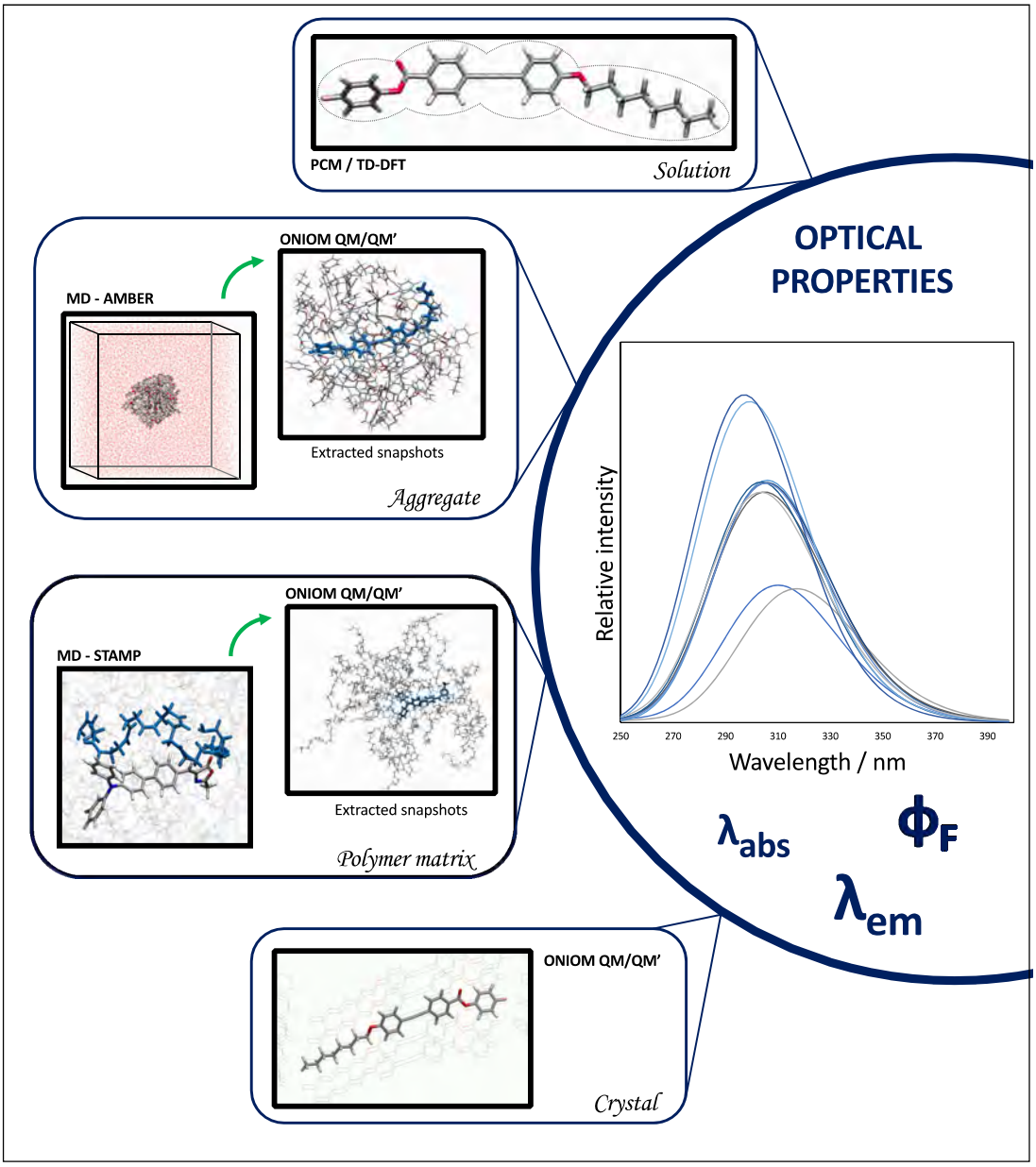

FIGURE I.2 – Sketch of the different approaches that will be used throughout this study.

to quantify as much as possible the impact, from a mechanical and/or electronic point of view, of the environment on the properties of the considered systems.

We have represented on Figure I.2 the different couples approach/environment that will be considered throughout this study. The different solvated system will be considered within an implicit solvent model. Molecular dynamics will be considered to study aggregates and systems embedded in a polymer matrix. Molecular crystals will be studied *via* hybrid approaches. Finally, the optical properties of all the molecules within those various envi-

ronments will be computed using whether quantum mechanical approaches (TD-DFT) or hybrid approaches (combining both quantum and molecular mechanics). All the methods presented on this Figure are going to be developed in Chapter 1. In Chapter 2 and 3 we will present the results we have obtained in the course of this PhD thesis. Chapter 2 will focus on the modulation of the fluorescence phenomenon depending on the environment. In Chapter 3, the behavior of a photochromic compound whether in solution or in a polymer matrix will be under study in order to rationalize the experimental features.

CHAPTER 1

Theoretical background

1.1 Quantum mechanical methods [1]

The molecular properties of one molecule can be retrieved through the resolution of the time-dependent Schrödinger's equation [9]:

$$H\Psi(r,t) = i\frac{\partial\Psi(r,t)}{\partial t} \tag{1.1}$$

where Ψ(r,t) is the time-dependent wavefunction and H is the polyelectronic Hamiltonian. For a stationnary system, Eq. 1.1 becomes:

$$H\Psi(r) = E\Psi(r) \tag{1.2}$$

where E is the energy of the stationary system and Ψ(r) the corresponding wavefunction, depending only on the spatial coordinates r of the N electrons and the M nuclei. The Hamiltonian can be written as the sum of the kinetic and the potential operators concerning both electrons and nuclei:

$$H = T_e + T_N + V_{Ne} + V_{NN} + V_{ee} \tag{1.3}$$

T_e and T_N are the kinetic energy operators of the electrons and the nuclei respectively:

$$T_e = -\frac{1}{2}\sum_{i=1}^{N}\nabla_i^2 \quad , \quad T_N = -\frac{1}{2}\sum_{A=1}^{M}\frac{\nabla_A^2}{M_A} \tag{1.4}$$

1. All the equations will be expressed using the atomic units

where M_A is the mass of the nuclei A. ∇^2 is the laplacian operator. V_{Ne}, V_{NN} and V_{ee} are the potential energy operators of the nuclei-electron electrostatic interaction, the electronic repulsion and the nuclear repulsion respectively:

$$V_{Ne} = -\sum_{i=1}^{N}\sum_{A}^{M}\frac{Z_A}{r_{iA}} \quad , \quad V_{ee} = -\sum_{i=1}^{N}\sum_{j>i}^{N}\frac{1}{r_{ij}} \quad , \quad V_{NN} = -\sum_{A}^{M}\sum_{A>B}^{M}\frac{Z_A Z_B}{r_{AB}} \tag{1.5}$$

with r_{iA}, r_{ij} and r_{AB} are the electron i - nuclei A, electron i - electron j and nuclei A - nuclei B distances respectively. Z_A and Z_B are the atomic numbers of the nuclei A and B. In the case of an interaction with the external environment such as an electric or magnetic field, Eq. 1.8 has a new term, V_{ext}, that accounts for the interaction potential of the electrons/nuclei with this external perturbation.

The Schrödinger's equation (Eq 1.2) can not be solved analytically for poly-electronic systems. It is thus necessary to introduce approximations to solve it. One of those approximations is the Born-Oppenheimer one [10]. It is based on the fact that the mass of an electron is smaller than the one of a nuclei (around 1836 times). As a consequence, the electrons will move faster than the nuclei. The approximation thus consists in considering the nuclei as fixed and the electrons as moving particles around the fixed nuclei. Eq. 1.8 can thus be simplified as T_N will be equal to zero and V_{NN} will be constant:

$$H_e = T_e + V_{Ne} + V_{ee} \tag{1.6}$$

This simplified Hamiltonian is the electronic Hamiltonian. One has to solve the following equation, for a fixed position of the nuclei:

$$H_e \Psi_e = E_e \Psi_e \tag{1.7}$$

with E_e the electronic energy. In the following, for the sake of simplicity, the electronic wavefunction $\Psi_e(x_1,...,x_N)$ will be noted as $\Psi(x_1,...,x_N)$ where x_i are the coordinates of the electron i.

1.1.1 Wavefunction

The Hartree-Fock method is a variational method that is used to solve the Schrödinger's equation and thus to calculate the energy of the system. The electronic wavefunction is defined as a single Slater determinant to describe the ground state of the system.

1.1.1.1 Slater determinant

The polyelectronic wavefunction (WF) has to respect the Pauli principle that imposes an antisymmetry condition. Indeed, when two electrons are inverted, the sign of the WF should change.

$$\Psi(x_1, x_2, ..., ..., x_i, ..., x_j, ..., x_N) = -\Psi(x_1, x_2, ..., ..., x_j, ..., x_i, ..., x_N) \tag{1.8}$$

In 1929, Slater proposed a simple wavefunction that fulfills this condition [11]. The polyelectronic wavefunction is expressed as a determinant composed of mono-electronic wavefunctions, ϕ_i(x):

$$\Psi(x_1, x_2, ..., x_N) = \frac{1}{\sqrt{N!}} \begin{vmatrix} \phi_1(x_1) & \dots & \phi_N(x_1) \\ \vdots & \ddots & \vdots \\ \phi_1(x_N) & \dots & \phi_N(x_N) \end{vmatrix} \tag{1.9}$$

The mono-electronic functions expressed in Eq. 1.9 are called spin-orbitals.

$$\phi_i(x) = \phi_i(r)\sigma(s) \tag{1.10}$$

The spin-orbital depends on spatial coordinates of one electron and on a spin coordinate, s. ϕ_r and σ_s are respectively the spatial orbital and the function describing the spin. One can also consider a wavefunction composed of a linear combination of several Slater determinants but for the methods presented hereafter, that are single-reference methods, the wavefunction of the ground state is composed of only one determinant.

1.1.1.2 Atomic basis set

The spatial orbitals, ϕ(r), are built as Linear Combinations of Atomic Orbitals (LCAO):

$$\phi_i(r) = \sum_{\mu} c_{\mu i}\chi_\mu(r) \tag{1.11}$$

where $c_{\mu i}$ is the coefficient of the atomic orbital χ_μ(r) in the OM ϕ_i(r) and χ_μ(r) are the atomic orbitals. The set of χ_μ(r) atomic orbitals constitutes the basis set.

In practice, the choice of the atomic basis set is of particular importance. Indeed, the more the basis set is extended, the more accurately the system is described but the longer the computational time is. Therefore selecting a basis set is therefore solving a dilemma

by taking into account the accuracy/effort balance.

In this work we have only considered Pople basis sets [12]. In Pople basis sets, core electrons are treated with one contracted basis function containing n Gaussian primitives, whereas the valence orbitals are treated with two (double-ζ) or three (triple-ζ) basis functions, each with a, b, c Gaussian primitives. The nomenclature for Pople basis sets is n-abcG with n=3 or 6, a=2 or 3, b=1 and c=0 or 1. Two special types of basis functions are usually added to complement the basis: polarization and diffuse functions. The former are added in order to give flexibility by providing functions with higher angular momentum. The nomenclature for including polarization functions is, for the case of 6-311G for example, 6-311G(d,p). The d indicates that an extra set of d function is added on "heavy" atoms like carbon and nitrogen, whereas the p indicates that polarization functions are added on the hydrogen atoms as well. The latter, diffuse functions, can be added to describe phenomena occurring "far" from the nuclei (H-bonds, delocalized electrons, excited states. . .). They possess the same angular quantum number as the valence basis functions but decay more slowly when going away from the nucleus. The nomenclature for adding diffuse functions to the 6-311G basis set is 6-311++G, where the first "+" indicates that extra functions are added to heavy atoms whereas the second "+" is dedicated to hydrogen atoms.

1.1.2 Hartree Fock

1.1.2.1 Method

One have to keep in mind three ideas when dealing with Hartree-Fock method. The first one is that in this model, the wavefunction is expressed as a single Slater determinant (see Eq. 1.9). Then, the variational principle is considered to retrieve the energy of the system.

$$W = \frac{\langle \Psi | H | \Psi \rangle}{\langle \Psi | \Psi \rangle} \geq E_{exact} \tag{1.12}$$

Finally, the interaction between the electrons is simplified by considering a mean-field approximation. It leads to a new expression of the polyelectronic Hamiltonian, composed by a set a mono-electronic Hamiltonians (F_i) named the Fock operators:

$$F_i = -\nabla_i^2 - \sum_A^M \frac{Z_A}{r_{iA}} + \sum_j^{N/2}((2J_j(r_i) - K_j(r_i)) \tag{1.13}$$

In Eq. 1.13, the first two terms are the kinetic energy of the electron i and the electron/nuclei interaction and represent the monoelectronic Hamiltonian, h_i. The last part of this equation contains bielectronic terms that express the mean electrostatic field undergone by the electron i arising from the other electrons.

$$J_j\phi_i = \int \frac{\phi_j^*\phi_j}{r_{ij}} dr\phi_i \ , \ K_j\phi_i = \int \frac{\phi_j^*\phi_i}{r_{ij}} dr\phi_j \tag{1.14}$$

J_j(i) accounts for the coulombic repulsion between the electron i and all the other ones, including itself. K_j(i) is the exchange term that ensures the Pauli principle. One has to solve a set of N Fock equations:

$$F_i\phi_i(r) = \epsilon_i\phi_i(r) \tag{1.15}$$

where ϵ_i is the energy of the spin orbital i and ϕ_i(r) the spatial orbital defined in Section 1.1.1.1. Those equations are iteratively solved to mimic the quantity W. Finally, one can obtain the total energy of the system as follows:

$$E_{HF} = \sum_i^N \langle\phi_i|F_i|\phi_i\rangle + \frac{1}{2}\sum_i^N\sum_j^N \langle\phi_j|J_i|\phi_j\rangle - \langle\phi_j|K_i|\phi_j\rangle \tag{1.16}$$

1.1.2.2 Limitation

Within the HF theory, the electronic correlation is partially taken into account because of the mean-field approximation. Löwdin defined a correlation energy, E_{corr}, that represents, within the limit of a complete basis set, the difference between the exact energy and the energy calculated within the HF method [13]:

$$E_{corr} = E_{exact} - E_{HF} \tag{1.17}$$

Correlation can be considered under two different aspects:
- Static correlation, related to the use of mono-determinantal wavefunction
- Dynamical correlation, related to the movement of the electrons that is not explicitely taken into account within the mean-field approximation.

Different approaches have been developed to account for this correlation effect. The results obtained with HF are considered as starting points and the new methods, called post-HF methods, correct this starting point by relying on the configuration interaction(CI) approach or by considering perturbative methods. These methodologies, that have not been used in the present work, are not presented in this methodological section.

1.1.3 Density Functional Theory

To solve the Schrödinger equation, one can also use the Density Functional Theory (DFT) approach. It is no longer the wavefunction that is considered to describe the ground state of the system but the density of particles ρ(r).

$$\rho(r) = N \int d^3r_2 \int d^3r_3 ... \int d^3r_N \Psi^*(r, r_2, ..., r_N)\Psi(r, r_2, ..., r_N) \tag{1.18}$$

DFT is based on two theorems, both proposed by Hohenberg and Kohn (HK) [14]. The first one consists in saying that for a ground state, it exists a direct relationship between the electronic density and the nuclear potential, ν(r), and between the Hamiltonian operator and the energy. All observables (in particular the energies) can be written as a functional of the electronic density. If one knows the density, ρ(r), then the value of the energy is accessible.

$$\rho(r) \rightarrow \nu[\rho(r)] \rightarrow \hat{H} \rightarrow E[\rho(r)]. \tag{1.19}$$

The second theorem can predict the density of a given system. Indeed, Hohenberg and Kohn demonstrated that the variational principle can be applied to the density:

$$E[\rho'(r)] \geq E[\rho_0(r)] \tag{1.20}$$

with ρ_0 the exact density, corresponding to the minimal value of the energy, of the ground state and ρ'(r) a test density for which one can define a potential V'_{ext}, a unique Ψ' and a unique Hamiltonian H'. In 1965, Kohn and Sham proposed an approach to circumvent the problem of considering interacting electrons [15]. In the Kohn-Sham (KS) formalism, the electrons are considered as non-interacting particles moving in an effective potential created by the others electrons. The novelty comes from the definition of an exchange-correlation (XC) functional. DFT can thus be considered as an exact theory as long as the XC functional is also exactly defined. Therefore, the HK-KS functional can be expressed as the sum of four terms:

$$E^{HK-KS}[\rho(r)] = T_s[\rho(r)] + V_{Ne}[\rho(r)] + J[\rho(r)] + \epsilon_{XC}[\rho(r)] \tag{1.21}$$

where T_s is the kinetic energy of the non-interacting electrons, V_{Ne} is the potential energy of the electron/nuclei interaction, J corresponds to the classical Coulomb repulsion and

ϵ_{XC} stands for the exchange-correlation functional (XCF). This last term cannot be determined exactly. When one use DFT methods, one has to choose properly the expression of the XCF.

1.1.3.1 Exchange correlation functional

To approximate the XCF part, we usually split the term into two parts. The first one (ϵ_X) concerns the exchange functional and accounts for the interaction between electrons with the same spin (Pauli principle) and the second part (ϵ_C) concerns the correlation effect not included in the first term.

$$\epsilon_{XC}[\rho(r)] = \epsilon_X[\rho(r)] + \epsilon_C[\rho(r)] \tag{1.22}$$

Hereafter are presented different families of XCF. They are all classified regarding their accuracy on a scale, the so-called Jacob's Ladder (Figure 1.1). One has to notice that a functional can be accurate for one given property and but provides poor results for another one. Therefore, one need to perform benchmark studies to decide which functional is the most appropriate for a given molecular system and a given property.

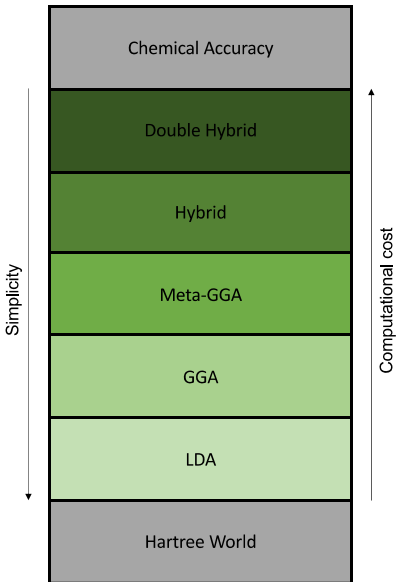

FIGURE 1.1 – Illustration of the Jacob's ladder adapted from Perdew's work [16].

Local Density Approximation

The first level of the Jacob's Ladder corresponds to the Local Density Approximation

(LDA). Within this model, the electronic density is considered as uniform as if it was an homogeneous gas model.

$$E_{XC}^{LDA}[\rho(r)] = \int \rho \ \epsilon_{XC}[\rho(r)]dr \tag{1.23}$$

The LDA approximation is still used for large systems where the electronic density is uniform. However, it gives poor results for organic molecules and other approximations are thus necessary.

General Gradient Approximation

The second level of the Jacob's ladder corresponds to the General Gradient Approximation (GGA). Usually, the electronic density of a molecule is not uniform leading to a limitation in the use of LDA approximation. To circumvent this problem of "uniformity" one can introduce the gradient of the local density.

$$E_{XC}^{GGA}[\rho(r)] = \int \rho \ \epsilon_{XC}[\rho(r), \nabla\rho(r)]dr \tag{1.24}$$

The new XCF is thus the XCF of the LDA approximation with a correction taking into account the inhomogeneity of the density. One has to notice that the XCF, as for LDA approximation, still depends on the density and its gradient at a given point inducing a "local" character for this approximation also.

$$\epsilon_{XC}^{GGA}[\rho(r), \nabla\rho(r)] = \epsilon_{XC}^{LDA}[\rho(r)] + \Delta\epsilon_{XC}\left[\frac{|\nabla\rho|}{\rho^{4/3}}\right] \tag{1.25}$$

GGA can be improved by considering also the second derivative of the electron density also known as the kinetic energy density, ∇^2. Those functionals are known as meta-GGA functionals.

$$E_{XC}^{meta-GGA}[\rho(r)] = \int \rho \ \epsilon_{XC}[\rho, \nabla\rho, \nabla^2\rho]dr \tag{1.26}$$

Hybrid Functional

Higher on the Jacob's ladder one can find the hybrid functionals. They have an explicit dependence on the occupied orbitals and include a fraction of exact HF exchange in the exchange part. Hybrid functionals thus combine both HF and DFT approaches to provide a better description of the systems. For the most simple approach, that is to say for global hybrid, the exact exchange is constant whatever the electronic distance is.

$$E_{XC}^{hybrid}[\rho(r)] = E_C^{DFT}[\rho(r)] + \lambda E_X^{HF} + (1-\lambda)E_X^{DFT}[\rho(r)] \tag{1.27}$$

where the mixture between DFT and HF is controlled by λ which controls the extent of the electron/electron interactions and ranges from 0 (no interaction) to 1 (exact, this is the adiabatic connexion). Hybrid XCF give better more accurate results than GGA or *meta*-GGA but strongly depends on the exact value of λ.

One of the major problem with this approach is that the description of the interaction when the inter-electronic distance, r_{12} is increasing fails and thus does not reproduce the correct asymptotic behavior ($\frac{-1}{r_{12}}$).

Range-separated Hybrid Functional

In 1996, Savin stated that at short distances, the dominant interaction is the dynamic correlation whereas at large distances, the non-Coulombic interaction (from the exchange part, nicely described within HF approach) is dominant [17]. Therefore, depending on the considered interaction (at short or long distance), the ratio of HF exchange should not be constant. New XCF has been developed taking into account the possibility for the ratio

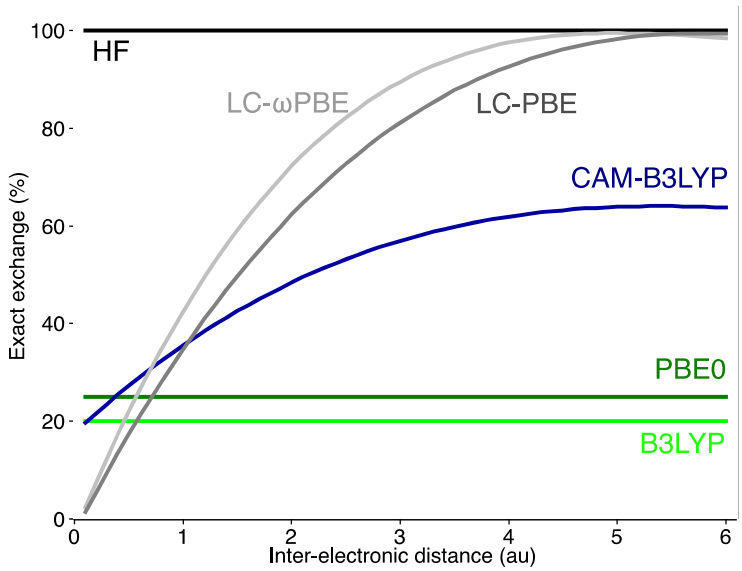

FIGURE 1.2 – Comparison of classical XC functionals with (CAM-B3LYP, LC-PBE, LC-ωPBE) or without (B3LYP, PBEO) long-range correction.

of HF exchange to change upon variation of the inter-electronic distance. They are known as range-separated hybrids (RSH). The percentage of HF exchange is thus varying if one considers short range (SR) or long range (LR) interaction. This is taken into account by

splitting the electron-repulsion operator into two parts:

$$\frac{1}{r_{12}} = \frac{1-[a+b\ erf(\gamma r_{12})]}{r_{12}} + \frac{a+b\ erf(\gamma r_{12})}{r_{12}} \tag{1.28}$$

where r_{12} is the inter-electronic distance and a and b are parameters and γ is an attenuation factor. A better asymptotic behavior is thus found when the inter-electronic distance is increasing. Benchmark studies have shown that RSH functionals provide accurate excitations energies for excitations presenting a charge transfer character [18, 19].

1.1.3.2 Description of the used functionals

Hereafter a short description of the functionals that have been used during this thesis is given.

B3LYP

B3LYP functional is a global hybrid functional that incorporates exact exchange from HF theory and exchange-correlation terms from DFT formalism. More precisely, this functional combines GGA (B88 [20] and LYP [21]) and LDA (VWN [22]) functionals and HF exchange.

$$\begin{aligned} E_{XC}^{B3LYP} = E_{XC}^{LDA}[\rho(r)] + a_0(E_X^{HF} - E_X^{LDA}[\rho(r)]) + a_x(E_X^{GGA}[\rho(r)] - E_X^{LDA}[\rho(r)]) \\ +a_c(E_C^{GGA}[\rho(r)] - E_C^{LDA}[\rho(r)]) \end{aligned} \tag{1.29}$$

where a_0=0.20, a_x=0.72 and a_c=0.81. One can see that the last two terms are used to correct both exchange and correlation GGA energies by subtracting the LDA energy.

PBE0

PBE0 functional is also a global hybrid functional. It combines GGA functional (PBE [23, 24]) and exact HF exchange.

$$E_{XC}^{PBE0}[\rho(r)] = E_{XC}^{PBE}[\rho(r)] + \frac{1}{4}(E_X^{HF} - E_X^{PBE}[\rho(r)]) \tag{1.30}$$

The PBE0 functional does not include experimental parameter and is thus considered as theoretical.

CAM-B3LYP

CAM-B3LYP is a range-separated hybrid functional. This functional is based on the Coulomb-attenuating method (CAM) along with the global hybrid B3LYP. It also considers a larger percentage of exact HF exchange for long-range (0.65) than for short-range (0.19) inter-electronic interactions. This functional is thus qualified of long range corrected functional. The parameters of the electronic-repulsion operator (Eq. 1.28) that are γ, a and b are set to 0.33, 0.19 and 0.46 respectively.

ωB97X-D

This functional is composed of the hybrid ωB98X functional that is taking into account long range (LR) and short range (SR) corrections, using the exact HF exchange (for both LR and SR) and GGA functional (B97 [25]).

$$E_{XC}^{\omega B97X}[\rho(r)] = \underbrace{E_X^{HF}}_{Long\ Range} + \underbrace{c_x E_X^{HF} + E_X^{B97}[\rho(r)]}_{Short\ Range} + E_C^{B97}[\rho(r)] \tag{1.31}$$

Empirical dispersions (Grimme's D2) are also added. The dispersion correction energy term is a function of the interatomic distance and it may contain adjustable parameters that are fitted to conformational and interaction energies computed at a high level of theory (CCSD(T)). The fitting is done for a given functional. D and D2 dispersion models consider all pairs of atoms while D3 dispersion model also considers triplets of atoms to account for three-body effects.

1.1.4 Time-dependent Density Functional Theory

The previously mentioned works of Hohenberg, Kohn and Sham have permitted to study the ground states of the systems. However, it is not possible to use those formalisms when the system is being perturbed by an external potential that time-dependent as this is the case for the light-matter interaction. The Time-Dependent version of DFT, TD-DFT, allows the description of such phenomenon. It has been proposed by Runge and Gross in 1984. According to TD-DFT formalism, when a polyelectronic system is perturbed by an external time-dependent potential, all the properties are determined thanks to the value of the time-dependent density at a time t, ρ(r,t). The Runge Gross theorems are the equivalent of the Hohenberg and Kohn's ones excepting the fact that this time the

external potential is time-dependent. It ensures a unique relationship between the external time-dependent potential ν_{ext}(r,t) and the time-dependent density, ρ(r,t).

Analogously to the KS equations, one can write time-dependent equations to solve the time-dependent Schrödinger's equation to retrieve the desired properties, $i.e$ the excited state electronic density:

$$H_{RG}\Psi_i(r,t) = i\hbar\frac{\partial}{\partial t}\Psi_i(r,t) \tag{1.32}$$

with

$$H_{RG} = T_s[\rho(r)] + \int \frac{\rho(r,t)\rho(r',t)}{r-r'}dr' + \nu_{ext}(r,t) + \nu_{XC}[\rho(r)](r,t) \tag{1.33}$$

and

$$\nu_{XC}[\rho(r)](r,t) = \frac{\partial A_{XC}[\rho(r)]}{\partial\rho(r,t)} \tag{1.34}$$

As in DFT, the A_{XC} functional is not analytically known. An approximation, called adiabatic approximation, allows us to write the functional as follows:

$$A_{XC}[\rho(r)] = \int E_{XC}[\rho_t(r),t]dt \tag{1.35}$$

E_{XC} represents the exchange-correlation energy introduced in the KS formalism and ρ_t(r) is the electronic density at a time t. This approximation is available only if the external potential is slowly varying with time. The exchange-correlation potential is calculated only for the density considered at the time t. It can thus be considered as a local approximation with respect to the time. The exchange-correlation potential is finally written as:

$$\nu_{XC}[\rho(r)](r,t) = \frac{\partial A_{XC}[\rho(r)]}{\partial\rho(r,t)} \approx \frac{\partial E_{XC}[\rho(r)]}{\partial\rho_t(r)} = \nu_{XC}[\rho_t(r)](r) \tag{1.36}$$

By applying the adiabatic approximation, the exchange-correlation potential that will be used is the one of time-independent DFT. However, one needs also to solve the equations proposed by Runge and Gross for a time-dependent (at any time) external potential. Within the Linear Response (LR) theory, one can write the time-dependent external potential as the sum of a time-independent and time-dependent term:

$$\nu_{ext}(r,t) = \nu^{(0)}_{ext}(r) + \nu^{(1)}_{ext}(r,t) \tag{1.37}$$

Based on the same approach, one can rewrite the electronic density:

$$\rho_{ext}(r,t) = \rho^{(0)}_{ext}(r) + \rho^{(1)}_{ext}(r,t) + ... \tag{1.38}$$

The first-order corrected density can be calculated using the the linear response function:

$$\rho_{ext}^{(1)}(r,t) = \int\int \chi(r,r',t-t')\nu_{ext}^{(1)}(r',t')drdt' \tag{1.39}$$

If the external perturbation is an oscillating electromagnetic field (as this is the case for light for example), with a pulsation ω, the pulsations for which the LR function is diverging (known as the poles of the function) correspond to the electronic transitions of the system, that is to say the absorption values.

In the case of a system containing non-interacting electrons, the LR function, χ, is a sum of fractional terms with at the denominator, the pulsation difference and the energetic gap between occupied and virtual orbitals. In this, the transitions are occurring at energies that correspond to the energetic gap between occupied and virtual orbitals.

$$\chi_s(r,r',\omega) = \sum_{i}^{occ}\sum_{j}^{virt} \frac{\Psi_i^*(r)\Psi_j(r)\Psi_i*(r')\Psi_j(r')}{\omega - \epsilon_j + \epsilon_i + i\eta} \tag{1.40}$$

where terms with i and j indices correspond to properties related to occupied and virtual orbitals respectively. However, in real systems, the electrons are in interaction and the LR function has a more general expression:

$$\chi(r,r',\omega) = \chi_s(r,r',\omega) + \int\int \chi_s(r,r_1,\omega)\kappa(r_1,r_2,\omega)\chi_s(r_2,r',\omega)dr_1dr_2 \tag{1.41}$$

The function $\kappa(\mathrm{r_1},\mathrm{r_2},\omega)$, the kernel, allows to take into account the electron-electron interactions. The transition energies are no longer the energetic differences between occupied and virtual orbitals. Casida, based on the general formulation of the LR and the kernel, proposed an eigenfunction whose eigenvalues are the excitation energies [26, 27]. The oscillator strengths of the transition (representing the intensity of this transition) between two electronic states, Ψ_0 and Ψ_1 characterized by the energy $\mathrm{E_1}$ and $\mathrm{E_0}$, are obtained as follows:

$$f = \frac{2}{3}(E_1 - E_0)|\left\langle \Psi_1|\vec{R}|\Psi_0\right\rangle|^2 \tag{1.42}$$

Benchmarks have indeed shown that TD-DFT's "accuracy" is typically of 0.15–0.30 eV [28].

1.2 Molecular mechanics based approaches

1.2.1 Force Field

In molecular mechanics all the interactions within the studied system are described by parameters that are gathered in a Force Field (FF). This FF allows us to calculate the potential energy of the system. One has to notice that contrary to quantum mechanics, in molecular mechanics one is interested only in the positions of the nuclei, the electrons being implicitly considered in the FF parameters. Two types of FF are known, the classical ones, CFF, and the polarizable ones, PFF. With a PFF one can take into account the response of the environment. In the course of our studies we have only considered CFF.

1.2.1.1 Potential energy function

The potential energy function of a CFF (Eq. 1.43), encompasses two types of terms. The one concerning the interactions between atoms that are bonded (V_{bonded}) and the one for non-bonded interactions ($V_{non-bonded}$).

$$V_{MM}(\mathbf{r}_N) = \underbrace{V_{bond} + V_{angle} + V_{torsion} + V_{improper}}_{V_{bonded}} + \underbrace{V_{vdW} + V_{el}}_{V_{non-bonded}} \tag{1.43}$$

The total potential energy, $V_{MM}(\mathbf{r}_N)$, depends of the position $\mathbf{r}$ of the N atoms that are present in the system. The terms concerning the bonds and the angles are usually described as harmonic oscillators (Eqs 1.44 and 1.45). The consequence of such a description is that there is no possibility to break or to form bonds.

$$V_{bond} = \sum_{bond} \frac{1}{2} k_r (r - r_0)^2 \tag{1.44}$$

$$V_{angle} = \sum_{angle} \frac{1}{2} k_\theta (\theta - \theta_0)^2 \tag{1.45}$$

The deviation with respect to the equilibrium position of one bond or one angle is expressed through ($\mathbf{r}$-$\mathbf{r}_0$) and (θ-θ_0). The force constant of the harmonic potential is characterized by k_r, for bond stretching, and k_0, to describe angle bending. One can note that it is possible to describe the bond and angle terms via a Morse or an anharmonic potential but both

models are more expensive. The two remaining terms have variable way to be defined but generally they are written as presented above:

$$V_{torsion} = \sum_{n=0}^{N} \frac{V_n}{2} [1 + cos(n\omega - \gamma)] \tag{1.46}$$

with n the multiplicity, ω the torsion angle and γ the phase angle.

$$V_{improper} = \frac{1}{2} k_\theta (\theta - \theta_0)^2 \tag{1.47}$$

Improper torsions are used to constraint the geometries of the molecule, for example to impose planarity to a moiety such as a phenyl ring.

For the non-bonded interaction, the van der Waals term, V_{vdW}, is calculated via a 12 - 6 Lennard Jones (LJ) potential:

$$V_{vdW} = 4\epsilon \left[\left(\frac{\sigma}{r} \right)^{12} - \left(\frac{\sigma}{r} \right)^{6} \right] \tag{1.48}$$

ϵ stands for the depth of the well, σ is the distance for which the energy is equal to zero and r the distance between the atoms. ϵ and σ are constants that depend on the two considered particles A and B. The first part of the LJ potential, varying in r^{-12}, is the repulsive part while the one varying in r^{-6} is the attractive one.

Finally the electrostatic term is a sum over all the interactions between the ponctual charges corresponding to the atoms A and B via the Coulomb's law.

$$V_{el} = \sum_{A>B} \frac{q_A . q_B}{4\pi\epsilon_0 r_{AB}} \tag{1.49}$$

1.2.1.2 Classical Force Field

During our studies only one CFF has been used, namely the General Amber Force Field (GAFF) [29]. It is derived from AMBER force field, which has been developed for the study of protein and nucleic acid and has thus only few parameters for organic molecules. GAFF is filling the gap by allowing the study of most of the organic molecules containing the following atoms: C, N, O, H, S, P, F, Cl, Br and I. The charge method used in GAFF is HF/6-31G* RESP charges.

1.2.2 Molecular Dynamics

Molecular dynamics (MD) is used to follow the evolution of a system along the simulation time. One can thus obtain a trajectory that gathers many structures hereafter

called snapshots. Each snapshots is representative of the system at a time t. To obtain the trajectories, one needs to solve the Newton's equation of the movement:

$$m_i \frac{d^2 x_i}{dt^2} = \mathbf{F}_{\mathbf{x_i}} = -\frac{d}{dx_i} V(x_i) \tag{1.50}$$

with m_i the atomic mass, x_i the displacement coordinate, $\mathbf{F}_{x_i}$ the force applied on the nuclei and $V(x_i)$ the potential. To start one need to know the initial conditions of the system that is to say positions and velocities at a time t_0. Most of the algorithms that are used to integrate the equation of the movement are based on Taylor's development. Different recurrence algorithms can be considered.

1.2.2.1 Integration algorithms

The Verlet algorithm

The most used integration method is the one adopted by Verlet [30]. The method is based on the positions $x(t)$, the accelerations $a(t)$ and the positions of the previous step $x(t-\delta t)$.

$$x(t+\delta t) = 2x(t) - x(t-\delta t) + a(t)\delta t^2 \tag{1.51}$$

One can notice that the velocities do not appear in the previous equation. They have been eliminated by addition of the equation obtained by Taylor expression of the position.

$$x(t+\delta t) = x(t) + v(t)\delta t + \frac{1}{2}a(t)\delta t^2 + ... \tag{1.52}$$

$$x(t-\delta t) = x(t) - v(t)\delta t + \frac{1}{2}a(t)\delta t^2 + ... \tag{1.53}$$

One can thus conclude that velocities are not necessary to compute the trajectory. However they remain important to evaluate the kinetic energy and more generally the total energy of the system. Velocities can be calculated through the following formula:

$$v(t) = \frac{r(t+\delta t) - x(t-\delta t)}{2\delta t} \tag{1.54}$$

The leap-frog scheme

Modifications of the Verlet algorithm have been proposed. One of the integration algorithm is the "leap-frog" scheme, developed hereafter:

$$x(t+\delta t) = x(t) + v(t+\frac{1}{2}\delta t)\delta t \tag{1.55}$$

$$v(t + \frac{1}{2}\delta t) = v(t - \frac{1}{2}\delta t) + a(t)\delta t \tag{1.56}$$

As for Verlet algorithm, the positions and the accelerations are necessary but, contrary to the verlet algorithm, the mid-step velocities, v(t - $\frac{1}{2}$ δt), are also needed.

The Velocity Verlet algorithm

In both Verlet and leap-frog schemes, the velocities are not or only partially taking into account. An approach storing at the same time the positions, the velocities and the accelerations has been proposed [31]. This "Velocity Verlet" algorithm is expressed as follows:

$$x(t + \delta t) = x(t) + \delta t\ v(t + \frac{1}{2}\delta^2 a(t)) \tag{1.57}$$

$$v(t + \delta t) = v(t) + \frac{1}{2}\delta t[a(t) + a(t + \delta t)] \tag{1.58}$$

This is the integration algorithm used in AMBER and thus the one that we used.

1.2.2.2 Time step

The first thing to do is to define a time step, δt corresponding to the integration's frequency of the equation of the movement. In an ideal case, one will want to use an as large as possible δt in order to perform long time simulation. Indeed, considering a very small time step will be inefficient as it will take a long (real) time of simulation. However, it is not possible to increase infinitely the time step as it will provide unstability in the integration algorithms. The unstability arises from the fact that, when a large time step is considered, due to the truncation in the integration process, the total energy of the system is increasing. Due to large time step, the position of two particles within the system can be nearly overlapping, inducing strong repulsion and the increase of the total energy. Strong (abnormal) modifications of the structures can also occur. Thus, the choice of the δt is a compromise between numerical stability (small time step) and the possibility to run long simulations (large time step).

1.2.2.3 Thermodynamics ensemble

In the course of MD simulation conditions will be imposed to the system by defining parameters that can be controlled and that are: the quantity of atoms, molecules (N) or the chemical potential (μ), the energy (E) or the temperature (T), the volume (V) or

the pressure (P). One usually decides to combine many parameters thus defining a thermodynamic ensemble aiming to reproduce the experimental conditions of the considered system.

- Microcanonical (NVE) ensemble where the number of particles, the volume and the energy are constant.
- Canonical (NVT) ensemble where the quantity of material, the volume and the temperature are constant.
- Grand canonical (μVT) ensemble where the chemical potential, the volume and the temperature are constant.
- Isobaric-isothermal ensemble (NPT) ensemble where the quantity of material, the pressure and the temperature are constant.

The thermodynamics ensembles used along this study are: the NPT and NVT ensemble. In order to control the temperature in these two ensembles, the Berendsen thermostat is considered. It is an algorithm that is used to re-scale the velocities of particles along the trajectory. Within this approach the system is coupled to an external heat bath with a fixed temperature, T_0. At each time step, the velocities are scaled so that the rate of change of temperature remains proportional to the difference in temperature:

$$\frac{dT(t)}{dt} = \frac{1}{\tau}(T_0 - T(t)) \tag{1.59}$$

where τ determines the strength of the coupling between the system and the bath. The change in temperature between two steps is expressed as follows:

$$\Delta T = \frac{\delta t}{\tau}(T_0 - T(t)) \tag{1.60}$$

In practice, τ is an empirical parameter. This value has to be chosen with care. When τ is large ($\tau \to \infty$), the thermostat becomes inactive and the system in considered as a microcanonical ensemble. The temperature can thus fluctuate and will reach the desired value, maintaining small fluctuations. The Berendsen thermostat is particularly efficient and used to reach a particular temperature.

1.2.2.4 Periodic boundary conditions

The success of a MD simulation remains on the good description of the interactions that are occurring in our system (i.e the potential energy function, see Section 1.2.1). However, the systems we are considering in the course of MD simulations are often smaller than the real systems, to keep a reasonable calculation time. One possibility to allow the comparison between the model system considered in MD and the macroscopic real system is to introduce periodic boundary conditions (PBC). To consider an infinite system, one has to replicate to infinity the box along the three directions of the space and to thus to use the concept of PBC. A schematic representation of this principle is provided in Figure 1.3. The initial box is called "primitive box" while the replicated ones are called "image box". As soon as a particle, initially in the primitive box, is leaving through one face of the box,

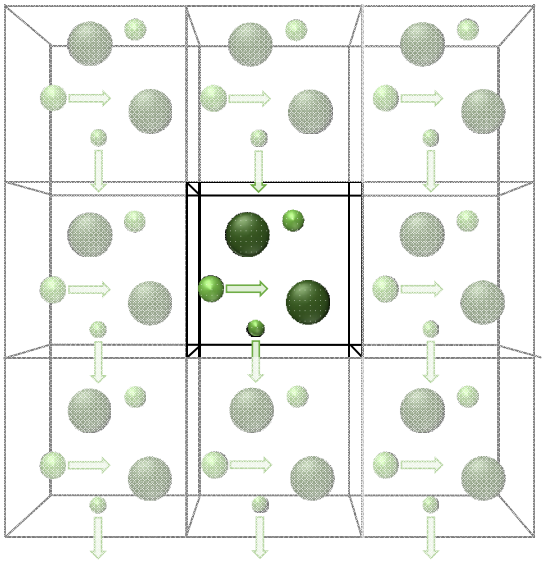

FIGURE 1.3 – Schematic representation of the Periodic Boundary Conditions.

it is immediately replaced by its own image, arriving from the opposite face, with the same velocity. The particles are thus not only interacting with particles inside the primitive box but also with the particles present in the image boxes. It leads to an infinite number of particles and thus an infinite number of particle-particle interactions to calculate. To avoid this time-consuming step, one introduces the cut-off radii notion, $r_{cut-off}$. This distance

represents the threshold beyond which the interactions will no longer be calculated.
When the PBC are considered, the coloumbic interaction cannot be written as in Eq. 1.49. Indeed, one has to consider the fact that, if there is a point charge q_i at the position r_i, then it also exists a point charge at r_i + ax + by + cz where a, b and c are integers such that ax + by + cz = nL (L is the characteristic length of the primitive box, L = |x| = |y| = |z|). The new coulombic potential can thus be expressed as follows:

$$V_{el} = \frac{1}{4\epsilon_0\pi}\frac{1}{2}\sum_{n}\sum_{i=1}^{N}\sum_{j=1}^{N}{}' \frac{q_i q_j}{r_{ij}+nL} \tag{1.61}$$

where the ' symbol is introduced to exclude the term $j = i$, if and only if n = 0. The $\frac{1}{2}$ factor has been added to avoid a double counting of each term). As this method is slowly converging and is an infinite series (sum over n), one can consider faster methods such as the Ewald sum method. Ewald sum is based on the splitting of Eq. 1.61 into two series that are:
- The fast variation part for small r which is supposed to decay fast and will become negligible beyond a cutoff distance.
- The smooth part for all (large) r such that its Fourier transform can be represented by only a few terms.

$$\frac{1}{r} = \frac{f(r)}{r} - \frac{1-f(r)}{r} \tag{1.62}$$

with f(r) = erfc(αr), α being the Ewald splitting parameter. To obtain this equation, one has to write first the delta functions of the charge density distribution of a point charges system that is splitted into two terms, corresponding to short and long range, and an additional gaussian distribution (G).

$$\rho_i(r) = \rho_i^S(r) + \rho_i^L(r) \tag{1.63}$$

$$\rho_i^S(r) = q_i\delta(r-r_i) - q_i G(r-r_i)\ ;\ \rho_i^L(r) = q_i G(r-r_i) \tag{1.64}$$

By solving the Poisson equation one will realize that the short range potential is singular while the long range one is not, meaning that it cannot be directly computed by a sum in real space. The basic idea of the Ewald sum is to transform this into a sum in the reciprocal space. Even if Ewald sum is a very good improvement of the direct sum (Eq. 1.61), it is still not so efficient when the size of the system is increasing. The Particle Mesh

Ewald (PME) has been introduced to circumvent this issue. Instead of using the implicit fourier transform to evaluate the sum in the reciprocal space, one will use the fast fourier transform (FFT). The time needed will thus decrease. One has to notice that the speed but also the accuracy depends on the mesh size.

1.3 Hybrid approaches: QM/MM and QM/QM'

In the previous sections we have presented:
- Quantum mechanics (QM) methods that are computationally expensive but essential to study phenomena involving electrons (electronic excitations for example). Because of the computational cost, QM methods are suitable for small to medium size molecules.
- Molecular mechanics (MM), thanks to the definition of force field in which all the parameters are gathered, allows the study of large systems along with dynamical description thanks to MD simulations. However, within the MM scheme, it is not possible to retrieve the electronic properties of the system.

It is possible to consider both approaches in one model in order to use their respective strenghts. This hybrid model is denoted as QM/MM (or QM/QM'). It consists in dividing the whole system into two parts with one being treated at a high QM level (the part of interest) and the other one at a lower level that can be either MM or QM' (QM' is a quantum mechanical level, lower and thus less computationally expensive than QM). One can for example study the emission properties of molecules, treated at a QM level, within a protein, treated at a MM level [32]. In the course of our study, we will use those methods only for "static" calculations on structures extracted from MD simulations to retrieve their optical properties.

1.3.1 Principle

As for the previously mentioned approaches, the main goal is to be able to calculate the total energy of the global system **G** by separating the system in two parts, the system of interest (**I**), the system whose photochemical properties or reactivity interest us, and the environment (**E**) (see Figure 1.4). One has to note the importance of the notation that is used when dealing with QM/MM approach. For the general case, one can use QM/MM

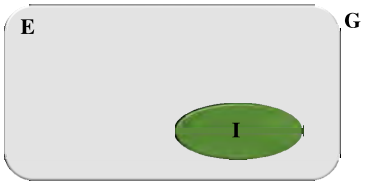

FIGURE 1.4 – Schematic representation of the sub-systems within a QM/MM (or QM/QM') approach. **G** is the global system, **E** is the global environment (treated at the MM or QM' level) of **I**, the part we are interested in (treated at a QM level).

denomination. As soon as there is a covalent link between **E** and **I**, it should be written as QM-MM (QM-QM'), if **E** and **I** are not linked, one should use QM:MM (QM:QM') notation. In our case, **E** and **I** will not be linked by covalent bonds and we will thus use QM:MM and QM:QM' schemes.

1.3.2 QM:MM and QM:QM' schemes

The calculation of the total energy can be done by considering either a soustractive or additive scheme.

Additive scheme

Within the additive scheme, the system **G** is divided into two sub-systems **I** and **E**, treated at a high level (QM) and a low level (MM or QM') respectively. The total energy is the sum of the energy of **I** (high level) and **E** (low level) but also of the energy corresponding to the interaction between **I** and **E**. This new term is of fundamental importance and should be considered with care. The Hamiltonian can be written as follows:

$$H_{total} = H^{\mathbf{E}}_{low} + H^{\mathbf{I}}_{high} + H^{\mathbf{G}}_{high-low} \tag{1.65}$$

Soustractive scheme

Within the soustractive scheme, the energy of **G** is obtained after three steps. The first one is a calculation on **G** at the low level, then the energy of **I** at the high level is calculated. At this point, the energy of **I** is taken into account twice at the low and high level. The energy of **I** has thus to be soustracted from the total energy. This model has

been the first one to be used and can be found in ONIOM (Our own N-layered Integrated Molecular Orbital and Molecular mechanics) model, available in Gaussian package. The Hamiltonian of the system can be written as follows:

$$H_{total} = H^{\mathbf{G}}_{low} + H^{\mathbf{I}}_{high} - H^{\mathbf{I}}_{low} \tag{1.66}$$

This is the model that we used in our studies. Hereafter are presented the embedding schemes, that is to say how we can improve the description of the whole system when considering different levels of theory.

1.3.3 Embedding schemes

All the schemes that are used to compute the total energy of the hybrid system, $E_{QM/MM}$, have been categorized into three groups [33]:
- Mechanical Embedding (ME)
- Electronic Embedding (EE)
- Polarizable Embedding (PE)

1.3.3.1 ONIOM(QM:MM)-EE model

Let's consider the example of the additive scheme within the QM:MM approach. The electrostatic embedding adds a term to the mechanical embedding, that is to say, $H^{elec}_{QM:MM}$. The interactions between the charge density of the N atoms of the QM part and the ponctual charges (q_B) of the MM part are taken into account. This new term will polarize the wavefunction of the QM part and is expressed as follows:

$$H^{elec}_{QM:MM} = \sum_{i}^{N} \sum_{B \in MM} -\frac{q_B}{|R_i - R_B|} \tag{1.67}$$

Electrostatic embedding can improve the description of the interaction within large system described by a QM:MM approach. It is for example appropriate when hydrogen bonds between **I** and **E** are observed in the system.

1.3.3.2 ONIOM(QM:MM)-PE

The polarizable embedding has been developed by Caprasecca et al [34, 35] and is available within the Gaussian package [36]. This scheme uses the fixed charges of the MM

part along with the induced dipoles. The wavefunction of the QM part can be polarized by both MM charges and induced dipoles, at the same time, the MM dipoles can also be affected by the electronic density of the QM part and it can lead to the formation of new induced dipoles. The wavefunction of the QM part and the induced dipoles of the MM part are mutually and self-consistently polarizing each other.

1.3.3.3 ONIOM(QM:QM')-EE

Within this model, the level of theory used for the QM part is more accurate and more computationally more demanding than the one used for the QM' part. The ONIOM(QM:QM')-EE has been developed by Raghavachari and co-workers [37, 38, 39]. The wavefunction of the QM part (**I**) can be polarized by the low-level QM charge distribution of the surrounding (**E**). The atomic charges (Mulliken) of the real system (**G**), calculated at the QM' level, are used to build the embedding potential. The complexity of this model arises from the fact that, unlike the ONIOM(QM:MM)-EE model, the charges are not fixed, the implementation and the derivation of analytic gradient is thus depending on the variable charges of **G**. The expression of the gradient is built using a set of coupled-perturbed equations. Then, by applying the z-vector method of Handy and Schaefer [40], the equations are reduced to a single set of SCF (Self Consistent Field) response equations [41].

1.4 Modeling the environment

Taking into account the environment in which the molecules are is of major importance for the calculation of the molecular properties. When molecules are solvated, one needs to consider the solvent effect in the calculation. Two different approaches are possible to mimic the effects of the environment, the solvent can be treated implicitly or explicitly.

1.4.1 Explicit model

The solvent molecules can be treated explicitly that is to say that the molecules are atomically described. It allows the description of specific solute-solvent interactions (hydrogen bonds for example). Because the solvent molecules have to be explicitly positioned, the polarity around the solute is more realistic. A dynamic study can be necessary to consider

a reliable configuration of the solvent molecules around the solute. The explicit solvation model can then be combined with the previously mentioned QM/MM or QM/QM' approach. One can thus consider specific interaction explicitly and still have a reasonable calculation cost by playing on the level of theory used for each system.

1.4.2 Implicit model

Within the implicit model, the solvent is described as an homogeneous medium, characterized by a dielectric constant. This constant is defined for all the usual solvents (see Table 1.1).

TABLE 1.1 – Dielectric constant (ϵ , F.m^{-1}) of the solvents that have been considered in our studies.

Solvent	ϵ	Solvent	ϵ
Benzene (BZN)	2.27	Toluene (TLN)	2.37
Tetrahydrofuran (THF)	7.43	Acetonitrile (ACN)	35.69

Molecules are thus not described in this approach. We present here the Polarisable Continuum Model (PCM) that has been used during our studies [42]. The solvatation free energy, ΔG equivalent to all the average solute/solvent interactions, can be written as follows:

$$\Delta G = \Delta G_{el} + \Delta G_{cav} + \Delta G_{dr} \tag{1.68}$$

where:

- ΔG_{el} is the electrostatic contribution. It corresponds to the interaction between the charges of the solute and the charges of the solvent, created by the continuum at the solute-solvent interface.

- ΔG_{cav} the cavitationnal energy. This is the energy that is necessary to create the cavity of the solute in the continuum.

- ΔG_{dr} the dispersion-repulsion energy. It represents the interaction between molecules that have instantaneous polarization.

Within the PCM method both nuclear and electronic degrees of freedom of the solute in its ground state are in equilibrium with the solvent (this is the equilibrium limit) [43]. When a system is interacting with an external field, as this is the case upon UV-

Vis irradiation, the polarization of the interacting system is modified accordingly to the frequency of the applied field. When the frequency is low (slow process), the solvent molecules have time to orient themselves in the direction of the applied field. When the frequency is increasing (fast process), only the electrons are reactive enough to adapt themselves to the external field. Considering an electronic transition from a ground state (GS) to an excited state (ES), two different mechanisms for the solute-solvent interaction can be used:

- The equilibrium (eq) limit. In this case, the solvent has time to adapt itself to the new electronic configuration of the solute (the ES).
- The non-equilibrium (neq) limit. Here, only the electrons of the solvent have time to adapt to the electronic configuration of the ES.

Within the Franck-Condon approximation, a transition between two electronic states is so fast that it is considered as vertical. Therefore, it should be computed within the "neq" limit. For absorption, the solvent is in equilibrium with the GS but in non-equilibrium with the ES. For emission, the solvent is in equilibrium with the ES but in non-equilibrium with the GS.

In addition, different levels of refinement exist to simulate how the PCM cavity is polarized in the excited state:

- The Linear-Response (LR) model [43, 44] this is the most straightforward scheme, in which the change in the PCM charges is calculated in terms of the transition densities.
- The State-Specific (SS) approaches. One can cite for example the corrected LR (cLR) scheme [45] that rely on the change of total dipole moment upon transition to model the solvent response to the change of state or the approach due to Improta, Barone, Scalmani and Frisch (IBSF) [46] .

The LR formulation is generally well-suited for strongly dipole-allowed transitions characterized by a small change of the electron density, i.e., for local ES, whereas the SS is more suited for charge transfer cases, in which the oscillator strength is small but the change of dipole is large [42, 47].

1.5 Modeling photochemical processes

Light (incident photon) can interact with the matter and gives rise to various phenomena after excitation. One can represent the energy level of a molecular system *via* the so-called Jablonski diagram, represented in Figure 1.5.

At the beginning, the molecule is in its ground singlet state (S_0). The first process consists

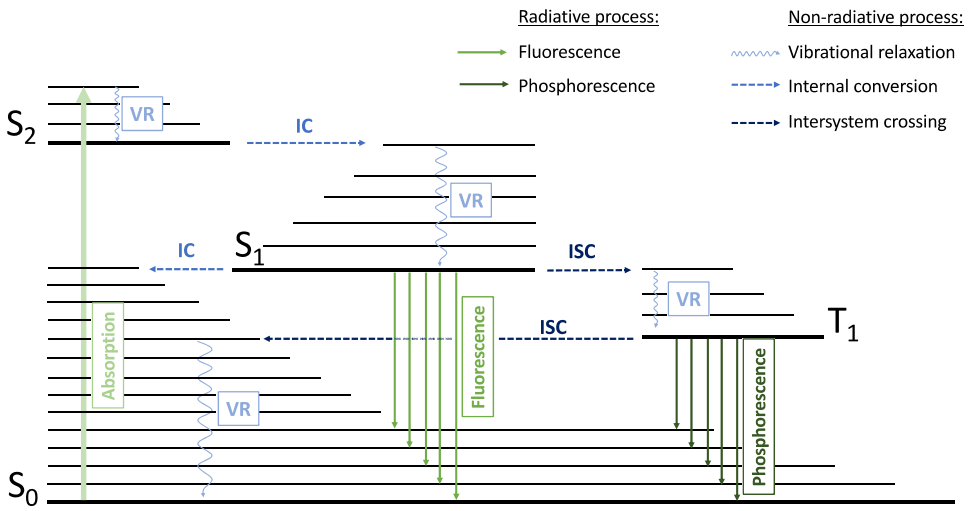

FIGURE 1.5 – Simplified Jablonski's diagram with the possible photophysical processes occurring after the absorption process.

in absorbing light. The molecule is excited from its ground state (GS) to a higher energetic excited state (ES) of the same spin multiplicity denoted as S_n. The ES that is reached depends on the energy of the incident photon and on the transition rules selection. This transition being really fast (fs) it does not allow nuclear displacement. Indeed, according to the Franck-Condon (FC) principle, the characteristic time for molecular vibration is about the picosecond [48, 49]. The transition is thus considered as vertical, as depicted on Figure 1.5.

After the absorption process, the system in the S_n state, will release the excess of energy by relaxing on a lower singlet excited state, for instance the S_1 [50, 51] . Two different processes can then be considered: (1) the non-radiative process through the internal conversion (IC) mechanism and (2) the radiative process through light emission (fluorescence). The IC process happens in a picosecond timescale while the fluorescence is a much slower pro-

cess (nanosecond). The Kasha principle states that, for most of the organic compounds, the emission of light can only be seen from the S_1 state. It is also possible to populate a triplet state through non-radiative process known as Intersystem crossing (ISC). The ISC often occurs because of spin-orbit coupling effects that are due to the presence of "heavy" atoms. It can be followed by the emission of light, the phosphorescence. Our molecules being only constituted of elements of the first three rows of the Periodic Table, no ISC process will be considered.

1.5.1 Absorption and emission spectra

In the following chapters, we are interested in the optical properties (absorption and emission) of the molecules under investigation. After a geometry optimization process, we systematically computed the absorption properties of the studied systems. The different steps and transition energies that we have considered are represented on Figure 1.6.

The approach that is used to model the absorption spectrum is based on the calculation

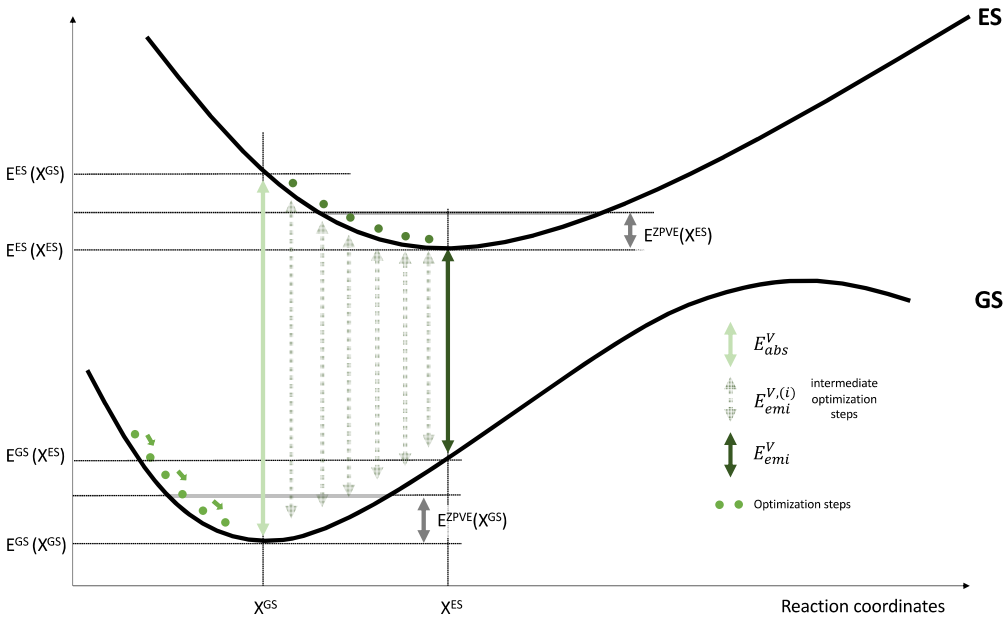

FIGURE 1.6 – Simplified energetic diagram to define the computed transition energies.

of the vertical transition energies, E^V_{abs}. It corresponds to the energy difference between the excited state (ES) and the ground state (GS), calculated at the GS optimized geometry.

$$E^V_{abs} = E^{ES}(X^{GS}) - E^{GS}(X^{GS}) \tag{1.69}$$

Usually we do not compute only one excited state but N excited states, leading to N vertical transition energies. Each vertical transition energy has its own intensity, given by the oscillator strength, f. The approximation that is made says that the larger the f is, the more the absorption process is efficient or in other words, the more the molar extinction coefficient (ϵ) is large. ϵ is one of the parameter of the Beer-Lambert law that rules the light absorption behavior of a solute, namely the molar attenuation coefficient.

$$A = \epsilon l c \tag{1.70}$$

where A is the absorbance of the solute, l is the path length of the beam light and c the concentration of the solute.

Having N vertical transition energies, one can simulate the global absorption spectrum by convoluting the N E^V_{abs}/f couples with Gaussian broadening functions. The influence of temperature, pressure and disorder are empirically modelled by the choice of the full width at half maximum (FWHM).

We systematically compared E^V_{abs} to the experimental λ_{max}. The limitation of this approach are: (1) the zero point vibrational energy (ZVPE) is not considered and (2) neither is the vibronic coupling.

We were also interested in the computation of the emission properties. To do so, we optimized the GS and calculated the absorption properties of each optimization step. Finally, we obtained the emission value as follows:

$$E^V_{emi} = E^{ES}(X^{ES}) - E^{GS}(X^{ES}) \tag{1.71}$$

1.5.2 Fluorescence quantum yield and Huang-Rhys factors

Being able to reproduce absorption and emission properties thanks to computational chemistry is the first step in order to rationalize experimental behaviors. However, being able to justify the efficiency of the previously mentioned processes may also be important. To this purpose, we introduced a new parameter, called the Huang-Rhys factor [52, 53, 54, 55]. This dimensionless constant accounts for the electron-vibration coupling value and represents, for the absorption or the emission process, the variation of the jth vibrational mode during the transition from one state to another. It is calculated as follows :

$$HR_j = \frac{\omega_j D_j^2}{2\hbar} \tag{1.72}$$

where ω_j is the vibrational frequency and D_j is the displacement along normal mode j between the equilibrium positions of the two electronic states of interest. The displacement D_j is given by:

$$D_j = \sum_n L_{jn}(q'_n - q_n) \tag{1.73}$$

where q' and q are the mass-weighted cartesian coordinates at equilibrium geometries of ES and GS respectively. L is the transformation matrix, calculated via frequency analysis using Gaussian package. For each mode j, the reorganization energy, $E_{reorg,j}$, is defined as the product of the HR factor and the corresponding vibrational energy. The total reorganization energy, $E_{reorg,total}$, is the sum of all the reorganization energies for each mode.

$$E_{reorg,j} = HR_j.\omega_j \tag{1.74}$$

$$E_{reorg,total} = \sum_j E_{reorg,j} \tag{1.75}$$

HR factors are proportional to the non-radiative decay constant, k_{nr}.

$$k_{nr} = \sum_n \frac{1}{\hbar^2}(\frac{\omega_n}{2\hbar}|R_n(fi)|^2)FC_n \tag{1.76}$$

where i corresponds to the initial state (excited state), usually S_1 state and f is the final state, that is to say $S_0.\omega_n$ is the frequency of the nth normal mode, R_n is the electron coupling term and FC is the Franck-Condon term defined as follows:

$$FC_n = \sqrt{\frac{2\pi}{\sum_j HR_j\omega_j^2(2\bar{n}_j+1)}} exp\left(-\frac{(\omega_{fi}+\omega_n+\sum_j HR_j\omega_j)^2}{2\sum_j HR_j\omega_j^2(2\bar{n}_j+1)}\right) \tag{1.77}$$

withω_{fi} is the gap between the initial and final state, $\bar{n}_j$, HR_j and ω_j are the mean of the Boltzmann photons, the HR factor and the frequency of the jth state respectively.

1.5.3 Excitation Energy Transfer and electronic coupling

The photosynthesis is the most famous example of a Excitation Energy Transfer (EET) process. A part of the plant is collecting the incident photon (light) to carry it to a reactive center where the photosynthesis process will be activated with a very high efficiency. From an experimental and synthetic point of view, it is not yet possible to reach this same efficiency. Theoretical tools, aiming at better understanding EET phenomena, have thus been developed with the idea to be able to control EET processes. In the course of our

study, EET calculations are undergone to quantify the energy that is exchanged, after excitation, between two molecules that are close enough (typically within a crystalline or aggregated environment). Indeed, the more the EET phenomenon is important, the more the non-radiative behavior will be predominant. We present hereafter the elements of the theory on which the calculation of EET is based.

The EET can arise from two different types of mechanism even if in each case, the electronically excited donor D^* transfers its energy to the acceptor A:

- The Coulombic Förster-like mechanism [56]. The initially excited state of a donor (D*) goes back to the ground state localized on D. At the same time, the excited state of A is promoted.

- The electron exchange Dexter-like mechanism [57]. It corresponds to an exchange of electrons between D and A along with an energy transfer process (Figure 1.7). The rate

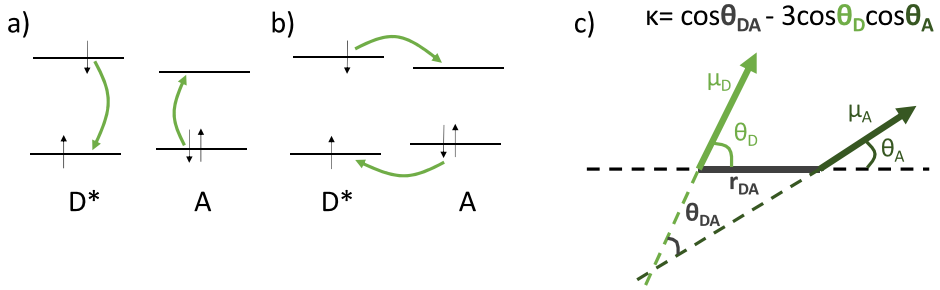

FIGURE 1.7 – Schematic representation of a four-orbital model for singlet electronic coupling between an excited donor (D*) and an acceptor (A). a) Coulomb coupling (Förster-type) and (b) exchange coupling (Dexter-type). c) Expression of the orientation factor, κ, with a representation of the transition dipole moments of D and A.

constant of the energy transfer within the two approaches are defined as follows:

$$k_{EET}^{Forster} \propto J_{DA}\frac{\kappa^2\Phi_D}{n^2 r_{DA}^6 \tau_D} \; ; \; k_{EET}^{Dexter} \propto J_{DA} exp\frac{-2r_{DA}}{L} \tag{1.78}$$

where J_{DA} is the spectral overlap integral and r_{DA} the distance between the donor and the acceptor. Φ_D and τ_D are the emission quantum yield and the lifetime of the donor respectively. κ is the orientation factor as defined on Figure 1.7. It will account for the relative alignment of the transition dipole moments of A and D. L is the sum of the Van der Waals radii of A and D. The Dexter-like expression shows an exponential decrease depending on r_{DA}. It means that, if the D and A are separated by a large distance, the

electron exchange will be negligible. In other words, within the Dexter formalism, only the electron exchange occurring at short distances will be considered.

As stated before, it is assumed that there is a weak electronic coupling between D and A. The electronic coupling is considered as weaker than the coupling of D and/or A with its own vibrations. The electronic coupling we are interested in can thus be considered as localized on only one site at a time. The EET is expressed *via* the Fermi Golden Rule formalism:

$$k_{EET} = \frac{2\pi}{h}|V_{DA}|^2 J_{DA} \tag{1.79}$$

where J_{AD} is the spectral overlap between the absorption spectra of A and the emission spectra of D. V_{DA} is the electronic coupling between D and A. It is this value that we will compute to have an idea of the importance of the excitation energy transfer process between two molecules, process which is in direct competition with the emission process. The direct coupling approach is the one that we will use in this thesis within the Gaussian16 package [58, 59] to compute V_{DA}. One can also use the fragment difference approach. The main advantage of the direct coupling approach consists in considering both donor and acceptor as separated (this is not the case within the fragment difference approach where the whole system is considered). It makes the computational cost affordable as one only need one TD-DFT calculation for each component of the whole system. Within the TD-DFT framework, one can rewrite the Casida's equation in a simpler way as:

$$\mathcal{A}\mathbf{X} = \omega\mathcal{I}\mathbf{X} \tag{1.80}$$

where

$$\mathcal{A} = \begin{pmatrix} A & B \\ B^* & A^* \end{pmatrix} \; ; \; \mathbf{X} = \begin{pmatrix} X \\ Y \end{pmatrix} \; ; \; \mathcal{I} = \begin{pmatrix} 1 & 0 \\ 0 & -1 \end{pmatrix} \tag{1.81}$$

The orbitals of D and A usually overlap, the overlap matrix is thus denoted as $\mathcal{S}_{DA}$. Eq. 1.80 can thus be rewritten as:

$$\begin{pmatrix} \mathcal{A}_{DD} & \mathcal{A}_{DA} \\ \mathcal{A}_{AD} & \mathcal{A}_{AA} \end{pmatrix} \begin{pmatrix} \mathbf{X}_D \\ \mathbf{X}_A \end{pmatrix} = \omega \begin{pmatrix} \mathcal{I} & \mathcal{S}_{DA} \\ \mathcal{S}_{AD} & \mathcal{I} \end{pmatrix} \begin{pmatrix} \mathbf{X}_D \\ \mathbf{X}_A \end{pmatrix} \tag{1.82}$$

The elements that constitute the off-diagonal of the matrix of the electronic Hamiltonian between the excited states is called the electronic coupling. It represents the interaction between two excited states localized either on D or A. One can thus express the

coupling V_{DA} as:

$$\langle D^*A|H_e|DA^*\rangle \tag{1.83}$$

where H_e is the total electronic Hamiltonian. $\langle D^*A\rangle$ and $\langle DA^*\rangle$ are the localized excited states. Considering a first order perturbation expansion, the electronic coupling, composed of three different terms, can be expressed as follows:

$$V_{DA} = \underbrace{\int \rho_D^{tr*}(r)\frac{1}{|r-r'|}\rho_A^{tr}(r')drdr'}_{V_{Coul}} + \underbrace{\int \rho_D^{tr*}(r)f_{XC}(r,r')\rho_A^{tr}(r')drdr'}_{V_{XC}} - \underbrace{\omega_0 \int \rho_D^{tr*}(r)\rho_A^{tr}(r)dr}_{V_{Ovlp}} \tag{1.84}$$

V_{Coul} is the Coulomb interaction between the transition densities (ρ^{tr}) of D and A, which is the dominant term [60]. As we are using TD-DFT formalism, V_{XC} corresponds to the exchange interactions that are occurring between transition densities of D and A with f_{XC} the exchange correlation kernel of the used XC functional. The last contribution allows to take into account the overlap between the D and A transition densities. ω_0 is the average resonance transition energy of the considered ensemble.

CHAPTER 2

To be emissive or not to be ?

2.1 Introduction: ACQ and AIE phenomena

ACQ to AIE

Materials or molecules that are able to undergo luminescent processes are now widely used in high-tech devices. The deep understanding that has been achieved the last years about light emitting processes has allowed the development of various applications with a social impact. One can cite for example the 2008 Nobel Prize in Chemistry that has been rewarded to O. Shimomura, M. Chalfie and R. Tsien for the discovery of green fluorescent proteins (GFP) and the protocol set up to use them. These proteins, when illuminated with blue light, are able to emit a green fluorescence light allowing the visualization of never seen biochemical structures and processes when it is embedded in a biological environment. This discovery permitted an extraordinary breakthrough in the knowledge that we have nowadays concerning the biological pathways and promoted the development of numerous fluorescent probes.

Depending on the application, the luminescent materials are incorporated in different environments. For the previously mentioned fluorescent probe or for biological applications in general, the luminophores are in an aqueous media. Even if efforts are made to increase

the miscibility of such molecules with water-like environments by adding polar moieties, the aromatic parts (responsible of the interesting emissive properties) often lead to the formation of aggregates. However, for most of the applications the luminophores are dispersed in condensed phases. In the field of optoelectronic devices which leads for instance to various applications like Organic Light-emitting diodes (OLEDs) [61, 62], the emissive molecules are found as crystals or solid thin films.

This effect of aromatic luminophore aggregation, which is directly linked to the concentration, has been rationalized in the last century. In 1954, Förster observed that a quenching of the emission, that is to say a decrease of the fluorescence intensity, was occurring when pyrenes molecules were aggregated [63, 64]. This phenomenon, also known as **Aggregation-Caused Quenching (ACQ)**, has then been extensively studied. Some general rules were highlighted [65]: it is now commonly admitted that aromatic luminophores often undergo ACQ effect when moving from dilute solution to a more concentrated phase, i.e aggregates or clusters. During the aggregation process, molecules are getting closer and a π-π interaction between the aromatic parts (the aromatic rings generally) is possible. The corresponding excited state of this assembly goes back to the ground state non radiatively. Indeed, the formation of absorption complex or excimer species in the excited state can be followed by various processes. For excimer species (association of two identical molecules, one being in its ground state and the other one in its excited state) a releasing of heat, due to the dissociation of the two molecules, can for example be observed. A more complex pathway is also possible, where the potential energy surface of the first excited state of the excimer will cross with the one of the ground state of the dissociated molecules, illustrating what is called conical intersection [66]. In both cases, it results in a quench of the emission process and thus to an ACQ phenomenon. So, whenever an emissive molecule involving aromatic rings for which π-π stacking is feasible, is considered, one may expect to observe ACQ. This phenomenon also depends on the solubility of the molecules in the considered solvent. It thus leads to a large number of examples where ACQ is encountered. However, the comprehension of the mechanisms leading to ACQ is important if one want to either control or avoid it (see Figure 2.1).

In 2001, Tang and his collaborators highlighted a new photophysical process dea-

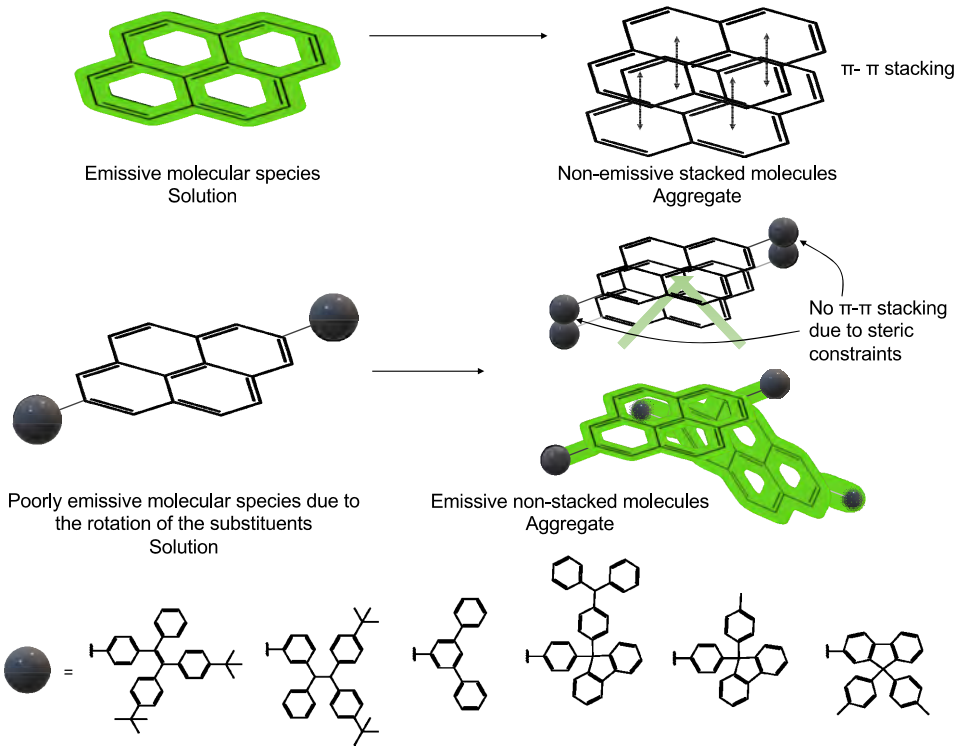

FIGURE 2.1 – Illustration of ACQ and AIE phenomena occuring for pyrene molecules. The introduction of bulky groups, due to the possible rotation between the substituent and the pyrene, decreases the emission efficiency in solution but increases it in the aggregate by avoiding π-π and blocking the rotations previously mentioned [67].

ling with aggregation and emission efficiency, called **Aggregation-Induced Emission (AIE)**. Contrary to what is observed with ACQ, molecules that are not emissive as isolated molecular species in solution are found to be emissive after the formation of an aggregate (called AIEgens hereafter). The first molecule reported as an AIEgen is the hexaphenylsilole (HPS) [68, 69], represented in Figure 2.2. In tetrahydrofuran (THF) solvent, HPS is not emissive (see Figure 2.4). When water - considered as a "bad" solvent, in which molecules with aromatic rings are not soluble - is gradually added to THF, molecules are starting to aggregate. When the volume of added water is close to 80%, the emission is turned on due to strong aggregation process of HPS in water. Since then, numerous studies have been undertaken to investigate this new feature. One of the most referenced molecule exhibiting AIE is the tetraphenylethene (TPE) in which a central carbon-carbon double bond is surrounded by four phenyl rings (see Figure 2.2). This molecule is poorly emissive

in solution and this behavior has been attributed to the non-radiative energy dissipation induced by the almost free rotations of the rings. However, when molecules are aggregated, two cooperative effects can be observed. First the twisted molecular conformation does not allow any intra- or intermolecular π-π stacking interaction and thus no excimer formation. Second, the rotations of the rings are blocked or at least hindered, disabling the non-radiative pathway previously mentioned. The restriction of intramolecular rotation (RIR) is at the origin of most of the reported AIE activity.

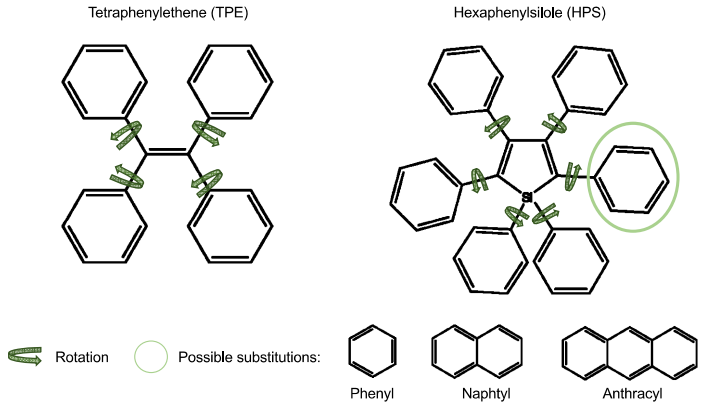

FIGURE 2.2 – Representation of the structures of HPS and TPE. Free rotations and possible substitution moieties for HPS are also represented.

Explanation of the phenomena

With the sake to better understand the expanding and promising field of AIEgen and their potential applications, a real effort has been made, from the theoretical and computational point of view, to provide explanations and models to explain AIE. The fundamental concept is the fluorescence quantum yield Φ_F. This quantity is related to the radiative (k_r) and non-radiative (k_{nr}) rates as illustrated in Eq 2.1.

$$\Phi_F = \frac{k_r}{k_r + k_{nr}} \tag{2.1}$$

Among the radiative processes one can find fluorescence (k_{Fluo}) and phosphorescence (k_{Phos}). Non-radiative processes include internal conversion (IC) and intersystem-crossing (ISC) to the ground state (see Figure 2.3).The k_r and k_{nr} rates can thus be defined as

follows:

$$k_r = k_{Fluo} + k_{Phos} \tag{2.2}$$

$$k_{nr} = k_{IC} + k_{ISC} \tag{2.3}$$

On Figure 2.3 are displayed the previously mentioned phenomena. When AIE effect is encountered it may be due to a restriction of non-radiative mechanisms or an increase of the probability for the system to emit. Two different approaches can be considered, the one that consists to remain near to the equilibrium geometries or the one that will consider the global PES and it is the physics of the system that will decide which approach is the most appropriate.

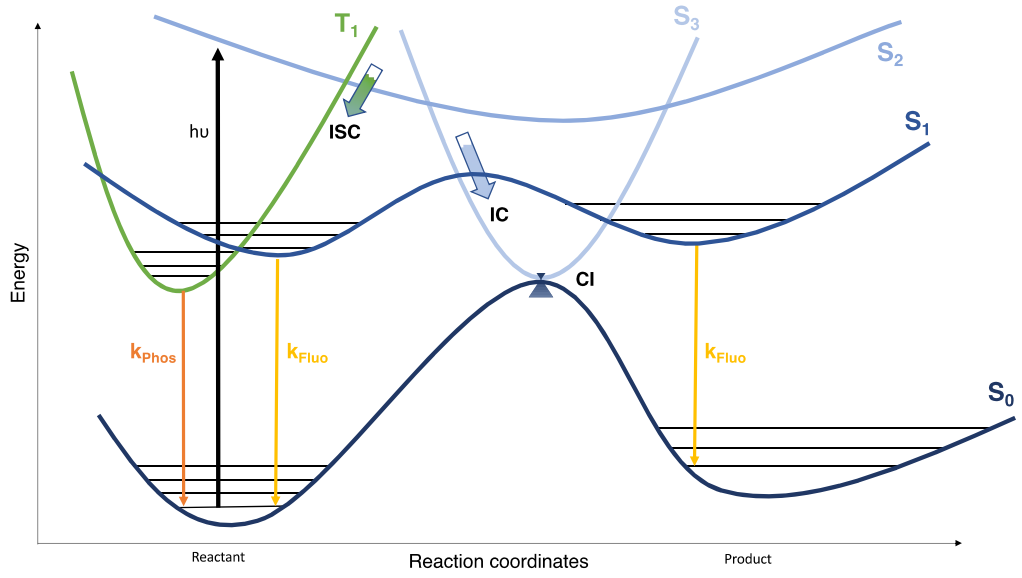

FIGURE 2.3 – Schematic representation of the potentiel energy surfaces with radiative and non-radiative processes.

As previously mentioned, different types of mechanisms have been proposed as explanations for the AIE effect. In a dilute solution, the transfer of the electronic excitation energy to low-frequency vibrational or rotational modes is possible and can lead to a non-radiative decay channel. The first type than can be cited includes restricted intramolecular rotation (RIR), restricted intramolecular vibration (RIV) and restricted intramolecular motion (RIM) mechanisms in a more global concept known as intramolecular restriction model (IRM) and supported by Fermi Golden Rule (FGR) calculations. The second type

concerns the global PES of the molecules with the restricted access to a conical intersection (RACI) model. They are both discussed in the following parts.

Intramolecular restriction model and FGR based calculations

Restricted intramolecular rotation. As suggested by the name, the aggregated phase can block the rotation of some moieties, suppressing the non-radiative pathway and thus increasing the quantum yield. As previously stated, it has been proposed after the study of first reported AIEgen, namely the HPS [70]. As depicted on Figure 2.4, the C-H$\cdots\pi$ interactions, in addition to stabilizing the aggregate and avoiding π-π interactions, are able to prevent possible rotations. One has to notice that intra- and intermolecular interactions are observed, doubling its benefits.

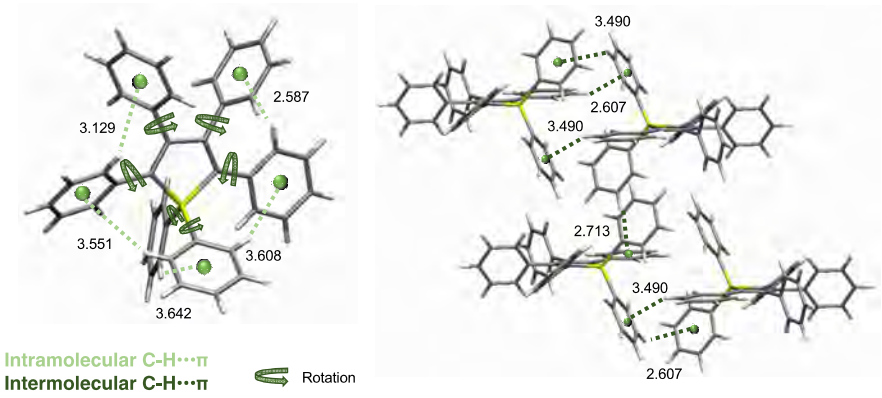

FIGURE 2.4 – Representation of the crystalline structure of HPS. On the left are represented the C-H$\cdots\pi$ interactions along with the simple carbon-carbon bond that are able to easily rotate in dilute solution. On the right part are represented the intermolecular C-H$\cdots\pi$ interactions.

Other ways to induce RIR have then been proposed. One can cite the increase of the viscosity of the environment, the decrease of the temperature or the increase of the pressure [70, 71]. For the latter case nevertheless, some studies showed that it can also lead to ACQ because it can promote π-π interactions between molecules [71]. Pressure has thus to be carefully considered if the aim is to induce the RIR mechanism. It is also possible to introduce bulky substituents so as to hinder rotations [72]. Playing on the length of the electronic conjugation path (moving from phenyl to naphtyl and anthracyl, as represented

on Figure 2.2, for example), has been tried with an effective increase of Φ_F [73, 74]. One has to be careful with the increase of the conjugation because it may lead to a possible stacking in the aggregated phase. More sophisticated way to induce RIR mechanism are available such as (1) the design of host-guest system, the AIEgen being able to form a complex with an host molecule that will block its rotations [75]; (2) the use of DNA hybridization process, the AIEgen being first incorporated in a simple DNA strand and then in a double strand that will totally block possible rotations [76]; (3) finally, simply adding a covalent bond between the rotors may be the most effective and simple way to activate RIR mechanism [77].

Restricted intramolecular vibration. Every AIE activity cannot be explained by the RIR mechanism. Indeed, some molecules that do not have rotors still present an AIE behavior. This is the case for example of the 10,10,11,11-tetrahydro-5,5-bidibenzo[a,d][7]- annulenylidene molecule (THBA) which is non-emissive in solution but strongly luminescent in the aggregated environment [78, 79]. THBA does not show free rotations as the phenyl rings are blocked with an alkyl bridge (see Figure 2.5). The explanation of the AIE behavior arises not from the restriction of rotations but from the restriction of intramolecular vibrations (RIV). The electronic to vibrational conversion decreases the emission efficiency. Being able to block those vibrations and the corresponding non-radiative decay channel can lead to AIE.

Restricted intramolecular motion. With the RIR and the RIV mechanisms, one can explain the behavior of most AIEgens. However, a combination of RIR and RIV, known as RIM (restriction of intramolecular motion), may also be an explanation. This is particularly useful in the case of a molecule containing both rotors and vibratable moieties as represented on Figure 2.5 [80]. The aggregation process, without any efficient π-π stacking, may thus induce RIM mechanism and lock the non-radiative pathway by stopping rotations and vibrations and finally leads to the increase of emission efficiency and to AIE activity.

The FGR approach. The previously mentioned mechanisms can be supported by theoretical calculations using the Fermi Golden Rule (FGR). This formula allows to predict an approximate decay rate between two states with the rate being proportional to strength of

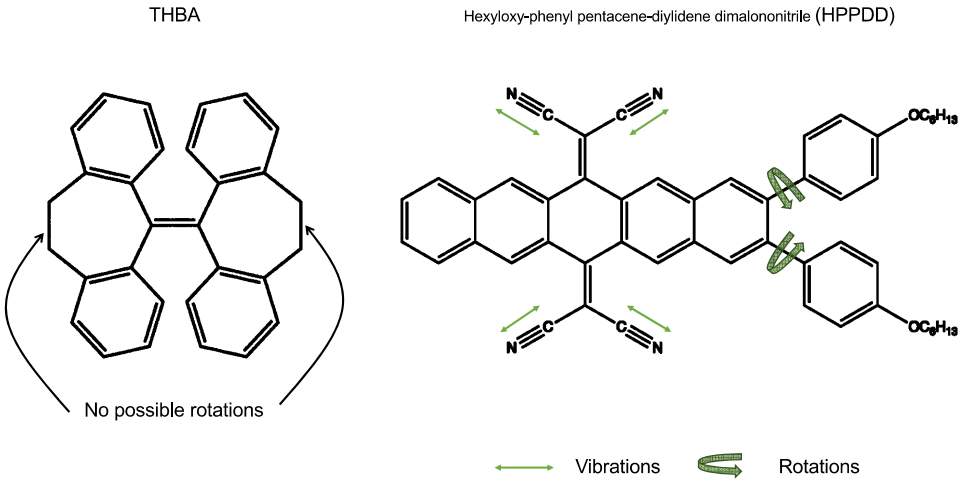

FIGURE 2.5 – Illustration of THBA and HPPDD molecules for which AIE activity is explained by RIV and RIM mechanisms respectively.

the coupling between them. The first and the simplest model is built as follows: the PES of the excited state is obtained by a displacement of the PES of the ground state. This model is assigned to the concept of the displaced harmonic approximation. The Huang-Rhys (HR) factors along with the derived reorganizations energies are suitable tools for the semi-quantitative study of AIE phenomena. Indeed, the identification of the normal modes mainly involved in the non-radiative process in solution (they belong to the IC processes and thus have an impact on k_{IC} and hence k_{nr}) is possible and their disappearance due to the steric hindrance of the aggregate is at the origin of the AIE effect. Other more refined approaches consider the mix between the ground and the excited state vibrations. To this purpose the Duschinsky rotation matrices are considered along with path integral framework [81]. Those approaches are both available in MOMAP software [82]. By calculating transition dipole moments, non-adiabatic couplings and spin-orbit couplings it is possible to have an estimation of k_r and k_{nr} constants [82, 83]. In the following, we will consider the HR factors to capture a semi-quantitative rationalization of AIE.

Exploration of the global PES

Restricted access to conical intersection. AIE can also arise from a more global phenomenon involving the entire PES. With FGR approach, only the coupling between states that

are close to the equilibrium geometries are taken into account. However, the excited state relaxation often involves various states and can occur far from the equilibrium geometry. The coupling between the states thus become highly anharmonic and the calculations of non-adiabatic couplings may not be sufficient to describe the non-radiative processes.
As it is illustrated on Figure 2.3, one of the possible non-radiative pathway driving the photochemical/photophysics process is the presence of conical intersection (CI). The CI is characterized by a crossing point where the PES of an excited state encounters the PES of the ground state, leading to a maximal probability of non-radiative decay. One has to notice that this phenomenon mainly occurs far from the ground state equilibrium geometry (known as as the Franck-Condon (FC) region) but can remain energetically accessible. In the **restricted acces to conical intersection** (**RACI**) model, the CI is proposed to explain the deactivation that lead to a non-radiative behavior in solution. When molecules are in the aggregate phase, the PES of both the ground and the excited state are modified and the energy of the CI can increase due to steric hindrance, making it energetically unreachable. The RACI model has been considered to explain the AIE behavior of various conjugated organic molecules including for example boranes [84] and molecules exhibiting excited-state proton transfer (ESIPT) [85]. Excited state dynamics calculations with the trajectory surface hoping (TSH) [86] is also used for its capability to directly give the decay to the ground state.

Design strategies

The AIE effect, because of its quite novelty, has been less studied than ACQ. While the mechanisms of ACQ is now well understood thanks to more than 50 years of studies, there is still a challenge to better understand AIE. Previously, because of the well know ACQ, when a molecule was already poorly emissive in solution people usually think that there is no need and no interest to use and study it in the solid state, the performance being generally inferior to what is observed in solution. With AIE, new possibilities can be considered and a new field of research is now open. In order to design new molecules with AIE features, many strategies have been considered.
ACQphores decoration. The first possibility consists in attaching directly an AIE moiety

to a ACQ core. For example, TPE (Figure 2.2) has been extensively used in this way so as to induce AIE properties. Indeed, due to its particular shape, when molecules with TPE moieties are aggregating, no π-π interaction is possible due to steric hindrance induced by TPE, preventing non-radiative decay channels [87, 88, 89]. One has to notice that whatever is the ratio between ACQphores and TPE, the ACQ to AIE transformation is always achieved.

AIEgens decoration. A non-intuitive way to design new AIEgen molecules is to decorate an already existing AIEgen with moieties exhibiting ACQ properties. It is believed that this strategy preserves the AIE effect of the starting molecule and combines it with the functional properties of ACQphores. Once again, TPE has been studied using this strategy [90]. One of its rings has been replaced by various substituents known for having ACQ effect (triphenylamine or carbazoles) and the final result is always the observation of AIE effect [91].

Rational design. With the two previous mentioned strategies, one is able to find the important features that are necessary to observe AIE effect. Indeed, having rotors that are able to dissipate energy in the isolated state (solution) and a non-planar system are key parameters. By taking this into account, it is possible to design new AIEgen. The common strategy consists in connecting stators to rotors via single bonds that are able to rotate [92, 93].

Our strategy

Therefore, what are the parameters we have to study when dealing with AIE ? As a first step, it is necessary to understand the non-radiative behavior of molecular species in solution. Then, the study of photophysical processes in the aggregated phase, more appropriate for applications, is necessary. Once again, the number of studies and thus the knowledge of emission process in solution is larger than what is available in the aggregate. Once the lack of knowledge on those two aspects will be fulfilled, the creation and the design of new systems with unique properties and utilities will be achieved. Hereafter we propose a study of three types of molecules presenting either ACQ or AIE/CIE (Crystallization Induced Emission, similar phenomenon as AIE but in this case it is the crystalline

phase that is considered instead of the amorphous aggregated phase).

Once upon a time there were ACQ and AIE.

As a first case of study of ACQ/AIE/CIE phenomena we propose a complete study of a linear molecule namely the 4-fluorophenyl 4-((4-(octyloxy)phenyl)ethynyl)-benzoate, hereafter abbreviated as **FOEB** (Figure 2.6) [94]. The central part of **FOEB** is a diphenylethynyl group also known as tolane. At each extremities of the core a donor (octyloxy) or an acceptor (ester) moiety is added.

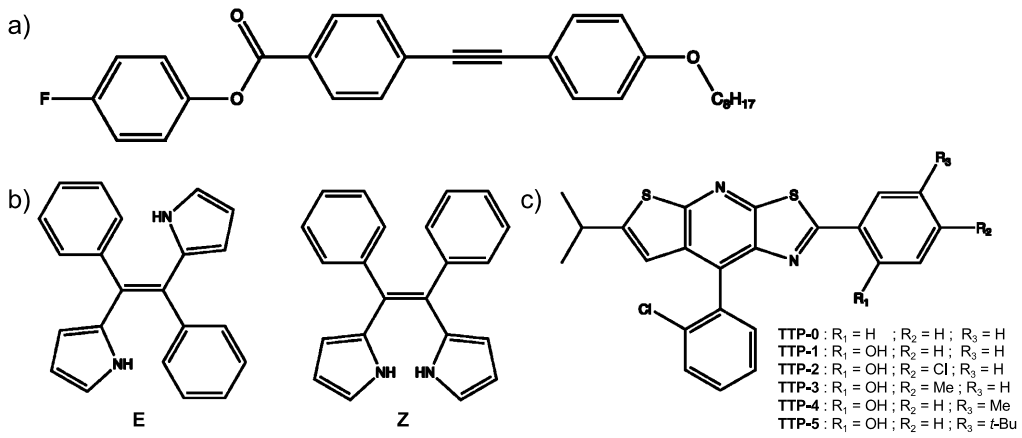

FIGURE 2.6 – Representation of the structures of (a) **FOEB** molecule, (b) **E-DPYDPE** and **Z-DPYDPE** isomers and (d) **TTP** family.

The optical properties of this molecule has been fully characterized in various environments highlighting the fact that its emission efficiency is varying with the surrounding. First, the quantum yield (Φ_F) is always lower than 50% in solution with a variation upon modification of the solvent polarity (see Table 2.1 for all the experimental properties). We decided to consider only three of the solvents that were used experimentally but we make sure to have a good representation of the solvent polarity amplitude. Indeed we used toluene (TLN) which is a non-polar solvent (ϵ=2.4), tetrahydrofuran (THF), a solvent with moderate polarity (ϵ=7.6) and finally acetonitrile (ACN) which is a polar solvent (ϵ=37.5). The study of the amorphous phase, i.e the aggregate, demonstrated that the emission process was less efficient than in solution, Φ_F being only 9%. However, when

FOEB was in its crystalline phase, the quantum yield increased a lot up to 60%. **FOEB** is thus exhibiting both ACQ and CIE phenomena.

TABLE 2.1 – Experimental absorption (λ_{abs}) and emission (λ_{em}) wavelength (in nm) along with quantum yields Φ_F (%) for **FOEB** molecule [94], isomers of **DPYDPE** [95] and the **TTP** family [96, 97] in solution, crystalline and aggregated phases.

	Solution			Crystal			Aggregate		
	λ_{abs}	λ_{em}	Φ_F	λ_{abs}	λ_{em}	Φ_F	λ_{abs}	λ_{em}	Φ_F
	325	386	26[a]						
FOEB	325	412	49[b]	-	388	60	280	420	9
	325	440	30[c]						
E-DPYDPE	357	461	0.2[b]	-	396	10	-	475	69
Z-DPYDPE	340	470	10[b]	-	489	89	-	450	37
TTP-0	360	387	10[d]	394	452	1			
TTP-1	373	545	2[d]	374	550	26			
TTP-2	375	530	12[d]	393	530	55			
TTP-3	373	545	4[d]	400	532	60			
TTP-4	377	570	4[d]	400	550	60			
TTP-5	376	656	4[d]	402	555	62			

[a] Toluene (TLN). [b] Tetrahydrofuran (THF). [c] Acetonitrile (ACN). [d] Benzene (BZN).

AIE or CIE? Choose the right isomer.

In a second step, we focused on a propeller-shape molecule which is a TPE derivative, namely the dipyrrolyldiphenylethene (**DPYDPE**). This molecule is composed of a central vinyl moiety surrounded by two phenyls and two pyrrole rings. It has been successfully synthesized and its two different isomers were separated and characterized [95]. The two isomers, **E-DPYDPE** and **Z-DPYDPE**, differ from the position of the different rings around the central double bond (Figure 2.6). Besides their structural differences, **E-** and **Z-DPYDPE** do not have the same behavior concerning their emission process depending on the environment that is considered. Indeed, there is a modulation of emission efficiency

in the same phase (solution, crystal or aggregate) between the two isomers but also, for the same isomer, between the three different phases. The different experimental quantum yields (Φ_F) are gathered in Table 2.1. Both isomers are weakly emissive in solution but become strongly emissive in different environments. **E-DPYDPE** has the characteristics of an AIEgen ($\Phi_F = 69\%$ in aggregate) while **Z-DPYDPE** has a more pronounced CIE behavior ($\Phi_F = 89\%$ in the crystal). One has to notice that no photoisomerization process between **E-DPYDPE** and **Z-DPYDPE** has been found under UV irradiation. So, by synthesizing and separating properly two isomers, one can observe whether CIE or AIE phenomena.

ACQ and CIE: let's play with substituents.

In the last part we will be interested in a family of molecules with a common central core, namely the thiazolo[5,4-b]thieno[3,2-e]pyridine (**TTP**) moiety. This family is composed of either positions isomers or derivatives with different substituted groups (see Figure 2.6). The molecules from which **TTP-2** to **TTP-5** are derived, namely **TTP-0** and **TTP-1** were first synthesized and it has been demonstrated that they exhibit interesting luminescent properties [96]. As presented in Table 2.1, **TTP-0** is weakly emissive in solution with a quantum yield efficiency of only 10% and is even less emissive in the solid state ($\Phi_F = 1\%$), leading to an ACQ behavior. The introduction of an intramolecular bond (see Figure 2.6) for **TTP-1** leads to a decrease of the emission efficiency in solution ($\Phi_F = 2\%$) but to a clear increase of Φ_F in the crystalline phase (26%). Based on the structure of **TTP-1** and its CIE behavior, other molecules were synthesized with various substitution schemes (position or nature of the group) schemes [97]. The resulting numerous **TTP** family is, moreover, able to emit all along the visible spectra with a λ_{em} ranging from 403 to 655 nm. We focused our study on 4 structures of this pool of molecules because of their particularly strong CIE behavior with an emission efficiency systematically higher than 55% in the solid state and lower than 12% in solution. One can notice that there is also an important Stokes shift for **TTP-1** to **TTP-5** which is attributed to an excited intramolecular proton transfer (ESIPT) phenomenon.

After the definition and the presentation of the detailed computational protocol for

each of the systems in all the considered phases, the results concerning the explanation of the ACQ/AIE/CIE phenomena will be presented for succesively **FOEB**, **DPYDPE** and the **TTP** family.

2.2 Common computational approach

Here will be presented the common computational approach that has been used for the cases presented in 2.3, 2.4 and 2.5.

2.2.1 Solvated systems

To study solvated systems we systematically used the Gaussian 09 [98] and Gaussian 16 [36] packages. The density functional theory (DFT) and its time-dependent counterpart (TD-DFT) methods were employed for the modeling of the absorption properties of the ground (GS, S_0) and the emission properties of the excited (ES, S_n) states. The approach we used in solution was to define a small set of exchange-correlation (XC) functionals that will be used for both optimization of the structures and the calculations of the optical properties. Only one extended basis set, with polarization and diffuse functions, has been used (the exact definition of the chosen basis set, slightly different for each molecule, will be provided in the following sections). The benchmark thus consisted in testing the n XC functionals for the two steps of calculation leading to (n!) $TD_i//Opt_j$ calculation schemes with i and j (i,j = 1...n) being a XC functional.

Choice of an XC functional: an illustration

For instance, for the **DPYDPE** molecule, three XC functionals were tested along with the extended 6-311+G(d,p) basis set. We considered the global hybrid functional PBE0 [99] and the two range-separated hybrid (RSH) functionals namely CAM-B3LYP [100] and ωB97X-D [101]. One has to notice that empirical dispersion corrections are included in the latest mentioned functional.

The first step consisted in optimizing the GS for the two isomers, **E-DPYDPE** and **Z-DPYDPE** with the three different XC functionals. A careful analysis of the obtained structures leads to the following conclusions:

(1) The structures obtained with CAM-B3LYP and ωB97X-D present small deviations (see Table 2.2).

(2) The main difference between PBE0 structure and the two others arises from the bond length of the central vinyl moiety (bond 7 on Figure 2.7). Indeed, while those values are equal to 1.356 (1.358) Å and 1.358 (1.359) Å for **E-DPYDPE** (**Z-DPYDPE**) with CAM-

B3LYP and ωB97X-D respectively, it increases up to 1.372 (1.371) Å with PBE0.
(3) The Bond Length Alternation (BLA), defined as the difference between the average lengths of the single bonds and the double bonds along the linear π-conjugated backbone, highlights the fact that PBE0 functional leads to the most conjugated structure with a value of 0.030 Å for **E-DPYDPE** (**Z-DPYDPE**) compared to 0.043 (0.041) Å and 0.041 (0.039) Å with CAM-B3LYP and ωB97X-D respectively.

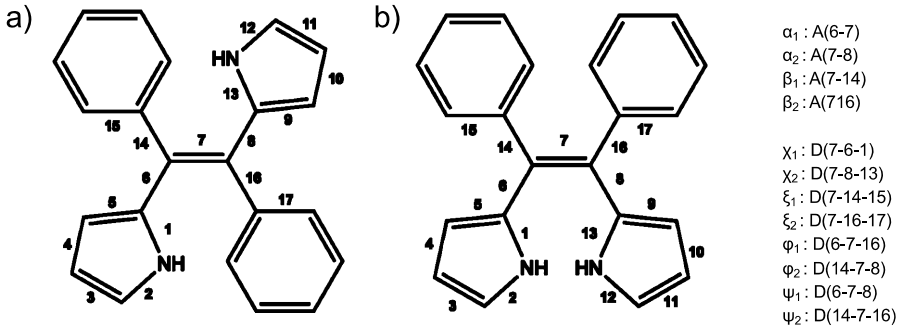

FIGURE 2.7 – Representation of the structures of (a) **E-DPYDPE** and (b) (a) **Z-DPYDPE** molecule. The bond denomination along with the definition of important angles and dihedrals are also provided.

The second step consisted in performing TD-DFT calculations using the previously optimized structures with each of the considered XC functionals to determine the maximum absorption wavelength (λ_{max}) of the two isomers. All the results obtained with the nine possible combinations within the LR approach are presented in Table 2.3 and on Figure 2.8. We introduce here the $\Delta E_{exp-calc}$ value which represents the energetic difference between experimental (λ_{exp}) and calculated (λ_{max}) values of λ, calculated as follows:

$$\Delta E_{exp-calc} = E_{abs,exp} - E_{cal} = hc(\frac{1}{\lambda_{exp}} - \frac{1}{\lambda_{max}}) \tag{2.5}$$

where h and c are the Planck constant and the speed of the light respectively. Our benchmark is based on the approximation consisting in the comparison of the λ_{exp} and the calculated vertical absorption (λ_{max}). A more refined benchmark model could be considered, taking into account the vibronic structure of the electronic absorption. We

TABLE 2.2 – Selected geometrical parameters calculated for the isomers **E-** and **Z-DPYDPE**. The Bond Length Alternation (BLA) parameter is also given. The distances and BLA are in Angstroms, the dihedral angles are in degrees. The bond numbering is provided on Figure 2.7.

	E-DPYDPE			**Z-DPYDPE**		
	PBE0	CAM-B3LYP	ωB97X-D	PBE0	CAM-B3LYP	ωB97X-D
Bonds						
1	1.375	1.375	1.374	1.374	1.374	1.373
2	1.362	1.363	1.363	1.360	1.363	1.363
3	1.382	1.374	1.376	1.379	1.374	1.376
4	1.415	1.416	1.417	1.414	1.417	1.418
5	1.394	1.384	1.385	1.389	1.381	1.382
6	1.460	1.466	1.466	1.461	1.469	1.468
7	1.372	1.356	1.358	1.371	1.358	1.359
BLA[a]	0.028	0.041	0.039	0.030	0.043	0.041
Dihedral						
Φ_1	14	11	12	-162	-165	-166
Φ_2	14	11	12	-162	-165	-166
Ψ_1	-165	-169	-167	18	15	15
Ψ_2	-166	-170	-170	17	14	14
χ_1	25	25	27	36	39	39
χ_2	25	25	27	36	39	37
ξ_1	-124	-117	-121	-135	-130	-131
ξ_2	-124	-117	-121	-135	-131	-130

[a] BLA, in Å is defined as follows:

$$BLA = \frac{\sum_{i=1}^{N} d_i}{N} - \frac{\sum_{j=1}^{M} d_j}{M} \tag{2.4}$$

where d_i (d_j) is the length of the simple (double) bond and N (M) the number of simple (double) bond considered.

also defined $\Delta E_{exp(E-Z)}$ which stands for the energetic difference between the λ_{max} of **E-DPYDPE** and **Z-DPYDPE** isomers:

$$\Delta E_{E-Z} = E_{abs,E} - E_{abs,Z} = hc(\frac{1}{\lambda_E} - \frac{1}{\lambda_Z}) \quad (2.6)$$

Considering ωB97X-D XC functional for TD-DFT calculations provides really similar results for both CAM-B3LYP and ωB97X-D optimized structures. As it was pointed out in the first part, the structures show trifling deviations and it thus leads to a difference between the λ_{max} smaller than 7 nm (0.08 eV) for the two structures. Nevertheless, the PBE0 geometry shows a red-shift with respect to the other geometries, +25 (+23) nm and +18 (+20) nm when compared to CAM-B3LYP and ωB97X-D geometries for **E-DPYDPE** (**Z-DPYDPE**). This trend is also reproduced for TD-PBE0 and TD-CAM-B3LYP with a systematic red-shift of the λ_{max} for the geometry optimized with PBE0 for both isomers but in a larger extent for **Z-DPYDPE** for which the $\Delta E_{exp-calc}$ is systematically larger than 0.27 eV. This is in line with the calculated BLA values presented before. PBE0 is thus not a suitable choice for geometry optimization.

Choosing PBE0 for the calculation of the absorption properties can also be questioned. One can observe that, whatever the XC functional used for geometry optimization, TD-PBE0 systematically provides a red-shifted absorption value for both isomers. **Z-DPYDPE** is particularly impacted with, for example for CAM-B3LYP structure, a $\Delta E_{exp-calc}$ of 0.40, 0.06 and 0.04 eV for TD-PBE0, TD-CAM-B3LYP and TD-ωB97X-D respectively. As a conclusion, TD-PBE0 can also be excluded from our possible computational scheme.

At this point, four possible computational schemes are remaining involving both CAM-B3LYP and ωB97X-D for the two steps of the protocol. Looking carefully at the calculated λ_{max} value allows us to say that there is no functional surpassing the other in the course of the geometry optimization because the most accurate results, independently from the TD-DFT functional, are obtained with ωB97X-D for **E-DPYDPE** and CAM-B3LYP for **Z-DPYDPE**. Moreover, experimentally, there is a blue-shift ($\Delta E_{exp(E-Z)}$ = -0.17 eV, see Eq. 2.6) of the absorption spectrum of **Z-DPYDPE** with respect to the **E-DPYDPE** one. Our calculations were not able to reproduce this blue-shift with values of $\Delta E_{exp(E-Z)}$ always positive. The best agreement, that is to say the smallest positive value of $\Delta E_{exp(E-Z)}$, is obtained for the ωB97X-D geometry. Therefore, we kept ωB97X-D for the geometry op-

timization process with the two remaining possibilities for TD-DFT calculation, that is to say CAM-B3LYP and ωB97X-D. The results we obtained for CAM-B3LYP//ωB97X-D and ωB97X-D//ωB97X-D being really close, 346 (350) nm and 343 (347) nm respectively for **E-DPYDPE** (**Z-DPYDPE**). To lighten the computational protocol we decided to select the ωB97X-D XC functional also for the calculation of the optical properties and we have finally selected the ωB97X-D//ωB97X-D calculation scheme. We also reported, for the best computational scheme, the results obtained with solvent correction, namely cLR and SS. For the previously selected computational scheme (TD-ωB97X-D//ωB97X-D), the λ_{max} values that we calculated with the cLR model are in closer agreement with the experiments. Indeed, the $\Delta E_{exp(E-Z)}$ is only 0.05 eV while it increases up to 0.11 eV for the SS model for an experimental value of -0.17 eV. The $\Delta E_{exp-calc}$ is -0.21(-0.24) eV and 0.02 (0.04) eV for **E-DPYDPE** and **Z-DPYDPE** within the cLR (SS) model respectively. As a conclusion, the TD-cLR-ωB97X-D//ωB97X-D has been retained for the study. Optimizations were carried out with the LR PCM model.

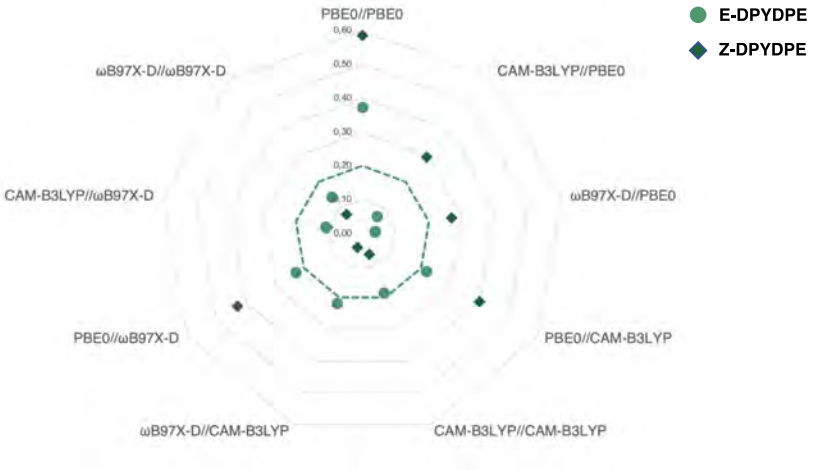

FIGURE 2.8 – Representation of the energy difference between the experimental and calculated excitation energies| $\Delta E_{exp-calc}$ | in eV as a function of the TD//Optimization calculation scheme for **E-** and **Z-DPYDPE** isomers.

Emission efficiency investigation Once the absorption and the emission properties were calculated thanks to the chosen computational scheme, a further analysis was done in order to gain more insights into the (non-)radiative process. The calculation of the analytical frequencies of both the GS (S_0) and ES (S_n) was performed. Then, we relied on

TABLE 2.3 – Maximum absorption wavelength λ_{max} (in nm) calculated for **E-** and **Z-DPYDPE** with different TD//Optimization computational schemes and within the LR-PCM solvent model. λ_{max} calculated with the cLR and SS models for the chosen calculation scheme are also presented. The energy difference between the experimental and calculated excitation energies $\Delta E_{exp-calc}$ is given as well as the variation of the excitation energy between the E and Z isomers ΔE_{E-Z}.

	E-DPYDPE		**Z-DPYDPE**		
TD//Opt	λ_{max}	$\Delta E_{exp-calc}$	λ_{max}	$\Delta E_{exp-calc}$	ΔE_{E-Z}
Exp[95]	357		340		-0.17
PBE0//PBE0	400	0.37	405	0.59	0.04
PBE0//CAM-B3LYP	381	0.22	382	0.40	0.01
PBE0//ωB97X-D	382	0.23	385	0.43	0.03
CAM-B3LYP//PBE0	364	0.07	370	0.30	0.06
CAM-B3LYP//CAM-B3LYP	339	-0.18	346	0.06	0.07
CAM-B3LYP//ωB97X-D	346	-0.11	350	0.10	0.04
ωB97X-D//PBE0	361	0.04	367	0.27	0.06
ωB97X-D//CAM-B3LYP	336	-0.22	344	0.04	0.09
ωB97X-D//ωB97X-D	343	-0.14	347	0.07	0.04
Solvent correction					
cLR-ωB97X-D//ωB97X-D	337	-0.21	341	0.02	0.05
SS-ωB97X-D//ωB97X-D	334	-0.24	344	0.04	0.11

the calculation of the Huang-Rhys (HR) factor [52, 53, 54, 55]. This dimensionless constant accounts for the electron-vibration coupling value and represents, for the absorption or the emission process, the variation of the jth vibrational mode during the transition from one state to another. It is calculated as follows :

$$HR_j = \frac{\omega_j D_j^2}{2\hbar} \tag{2.7}$$

where ω_j is the vibrational frequency and D_j is the displacement along normal mode j between the equilibrium positions of the two electronic states of interest. For each mode j, the reorganization energy, $E_{reorg,j}$, is defined as the product of the HR factor and the corresponding vibrational energy. The total reorganization energy, $E_{reorg,total}$, is the sum

of all the reorganization energies for each mode.

$$E_{reorg,j} = HR_j.\omega_j \tag{2.8}$$

$$E_{reorg,total} = \sum_j E_{reorg,j} \tag{2.9}$$

2.2.2 Crystalline phase

To mimic the crystalline environment, one needed to define a model. The strategy we employed to do so consisted in the extraction, from the experimental crystal supercell (X-Ray structure), of a large number of molecules to define a cluster. We then relied on the ONIOM QM/QM' method to determine the excited states properties of the crystalline phase (Figure 2.10). The system is divided as follows:

- The central molecule constitutes the high-level part, treated at a QM level.
- The surrounding remaining molecules compose the low-level region, treated at a QM' level of theory.

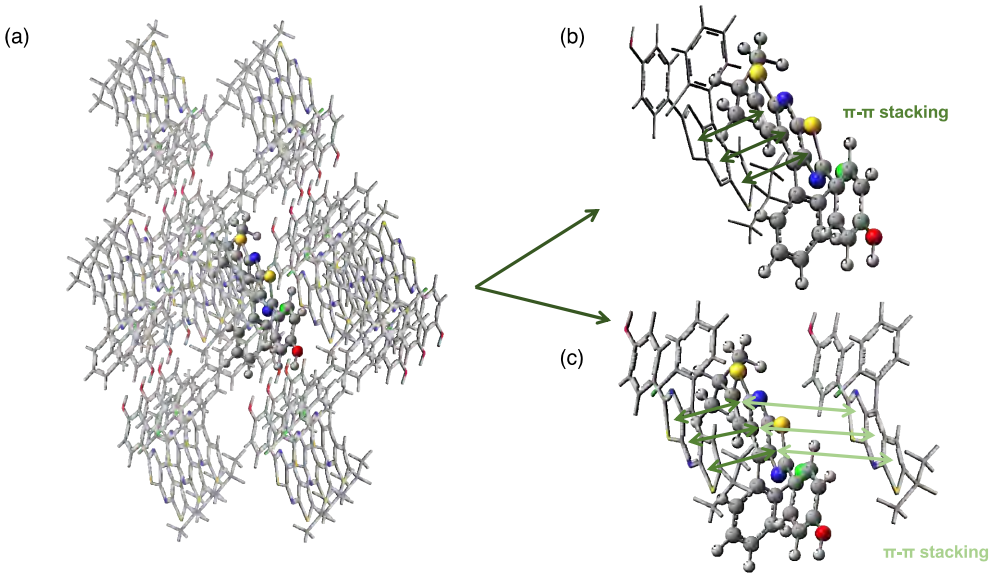

FIGURE 2.9 – Representation of the (a) QM/QM' model based on the crystalline packing (example of a cluster of 26 **TTP-0** molecules) and structures of a possible (b) dimer and (c) trimer for which the calculation of excitonic couplings are possible.

During the two steps of optimization of both the ground and the excited states, only the structure of the central molecule was relaxed, the others being kept frozen. The computational scheme for the optimization process and the absorption/emission calculations ($TD_j//Opt_j$) of the central molecule was the same as the one defined in solution. As previously reported [102, 103, 104], the low-level part of the system was treated at the Hartree-Fock (HF) level, with the 3-21G basis set. An electronic-embedding scheme [41], available within the Gaussian 16 package, was also considered. At this stage, our model was tested to verify its validity. In particular, the structure of the optimized central molecule and the distances between it and its surrounding are carefully check to see if our computational scheme and our model does not modify the crystal structure.
For the optimized structures, both the ground and the excited one, analytical frequencies calculations were performed. The electronic energy transfer (EET) between the central molecule and the neighboring ones (Figure 2.10), depending on the particular packing of each considered case, was analyzed. This approach consists in performing a TD-DFT excited-state calculation on each considered molecule, at the same level of theory previously defined, in gas phase. All the couplings between each state of each pair of molecule are then computed.

2.2.3 Aggregated phase

The aggregated phase that we defined as an amorphous phase was modeled using the AMBER16 package [105]. The starting configurations were obtained thanks to the PACKMOL package [106]. For the following protocole, the exact number of molecules and the different sizes of the box are provided in Table 2.4. A sufficiently large number of molecules was considered and placed in a cubic box. Systematically, so as to circumvent possible interference with the boundaries, a pure layer of water (5 Å width) was added, thus increasing the final size of the box. During our calculations, we did not simulate the aggregation process, that is to say that the molecules were not distributed uniformly. Indeed, to avoid this time-consuming step, the molecules were concentrated at the center of the simulation box.
In order to describe the atom types and the interaction parameters of our systems we relied on the General Amber Force Field (GAFF) [29]. The solvent, i.e water molecules, was

treated explicitly through the TIP3P model [107]. A systematic validation of the chosen force field was performed, consisting in two different steps. The first one is a comparison of the structures of the molecules after an optimization procedure in vacuum by DFT methods and with GAFF and the second one consists in comparing the corresponding optical properties of both optimized structures.

An example of the validation of the GAFF parameters

Hereafter is explained the scheme that is used to validate the force field for **FOEB** case of study. The comparison of the structures obtained after (1) a minimization step in vacuum with GAFF and (2) an optimization process at a QM level (CAM-B3LYP/6-311+G(d,p)) in vacuum also was done. The structures were then superposed and we looked carefully at some important structural parameters (see Figure 2.10). The first conclusion was that there were only minor differences between the two structures. The resulting structure obtained with GAFF appeared to be less planar (ϕ = 165° instead of 180°). The central triple bond, d_{cc}, is also different with values of 1.191 and 1.211 Å for GAFF and QM-Vacuum structures respectively. The optical properties were also investigated in order to investigate the impact of the small structural modifications on the λ_{max} value. The maximum absorption wavelengths, calculated at the CAM-B3LYP/6-311+G(d,p) level, reach 304 and 306 nm for the GAFF and the QM-Vacuum optimized structures respectively. The differences between the two structures being triffling, the same absorption signature was obtained. As a conclusion, the investigation of the structural and optical properties has allowed us to validate the use of GAFF for the study of **FOEB** within the aggregate.

The Coulomb interaction effects in the whole system was modeled via the Particle Mesh Ewald (PME) method [108, 109]. After a minimization step using the steepest descent algorithm, a simulation was first done in the NPT ensemble for 1 ns with a 1-fs time step. The atmospheric pressure (1 bar) and the temperature (300 K) were both incorporated by the Berendsen method [110]. Once this step has been done, we verified if the simulation box was at equilibrium. Small variations of the simulation box were found (see Table 2.4). Consequently, we modified the size of the cubic box and performed a new MD simulation in the NVT ensemble for 10 ns. The analysis of the trajectories were done with CPPTRAJ

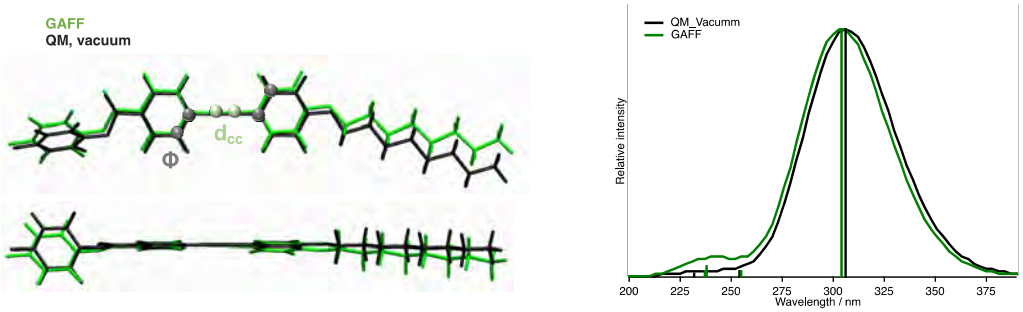

FIGURE 2.10 – (a) Superposition of the structures obtained after a QM optimization in vacuum or with GAFF. (b) Superposition of the corresponding absorption spectra obtained at the CAM-B3LYP/6-311+G(d,p) level of theory (gaussian function convolution with a FWHM of 0.33 eV). The central triple carbon carbon bond is defined by the green dots and the dihedral angle is defined by the four grey dots.

TABLE 2.4 – Parameters for the set up of the simulation box for **DPYDPE** and **FOEB** molecules. Values for the size of the box are given in nm.

Parameters	DPYDPE	**FOEB**
Number of molecules	21	25
Number of water molecules	21000	21000
Size of the box	3.0	7.5
Size of the box with the layer of water	4.0	8.5
Size of the box after NPT	4.10 (4.12)[a]	8.52
Volume variation (%)	+2.7 (+2.9)[a]	+0.3

[a] Sizes of the simulation box are different for **E-DPYDPE** and **Z-DPYDPE**. Values between parentheses are the ones corresponding to **Z-DPYDPE**.

software [111] within the AMBER16 package.

Snapshots were then extracted randomly from the MD trajectories in order to analyse both geometries and optical properties (with the same computational scheme as the one used in solution). The detailed procedure will be presented in the corresponding section of **DPYDPE** and **FOEB**.

2.3 Once upon a time there were ACQ and CIE: the story of FOEB molecules

Following the procedure presented in Section 2.2.1, we tested three XC functionals, namely PBE0 [99], B3LYP [112] and CAM-B3LYP [100] along with a unique basis set (6-311+G(d,p)) in toluene. Looking carefully at the computed maximum absorption wavelength (λ_{max}) and to the resulting $\Delta E_{exp-calc}$, it appears that the LR-PCM(TD-CAM-B3LYP//CAM-B3LYP) computational scheme is the most appropriate one to retrieve the experimental absorption properties ($\Delta E_{exp-calc}$ = 0.06 eV). Once the protocol has been set up we used it in order to study **FOEB** molecule, represented on Figure 2.11, in toluene (TLN), tetrahydrofuran (THF) and acetonitrile (ACN) and also for the study of the crystalline and the aggregated phase as discussed hereafter.

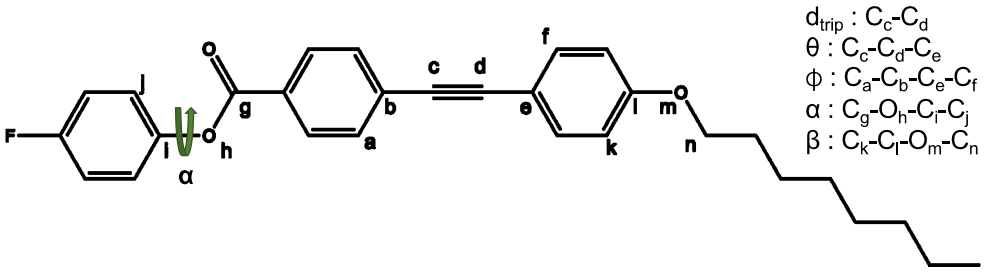

FIGURE 2.11 – Representation of the structure of **FOEB** molecule. The atom numbering along with the definition of important bonds, angles and dihedrals are also provided.

2.3.1 At the beginning, molecules were solvated.

Ground state study: structural and absorption properties

In Table 2.5 are gathered the results we obtained for the calculated maximum absorption wavelength (λ_{max}) in the three different solvents. A nice agreement is found between our calculations and the experimental results with $\Delta E_{exp-calc}$ values of 0.06, 0.17 and 0.13 eV in TLN, THF and ACN respectively. The first and main absorption band always corresponds to a transition from the highest molecular orbital (HOMO) to the lowest unoccupied molecular orbital (LUMO). As depicted on Figure 2.12, both orbitals are centered on the central part of the molecule that is to say the triple carbon-carbon bond and the two

neighboring phenyl groups. There is no delocalization on the fluorophenyl moiety.

TABLE 2.5 – Calculated absorption (λ_{max}, nm) and emission wavelength (λ_{em}, nm), oscillator strengths (f) and electronic excitation assignments for **FOEB** in different environments along with experimental absorption and emission wavelength and fluorescence quantum yields [94].

	Absorption				Emission			
Environment	λ_{max}	f	Assignment	$\lambda_{max,exp}$	λ_{em}	f	Φ_F	$\lambda_{em,exp}$
				Solution				
TLN	320	1.658	HOMO→LUMO	325	374	1.806	26	386
THF	311	1.642	HOMO→LUMO	325	391	1.871	30	412
ACN	314	1.613	HOMO→LUMO	325	400	1.896	49	440
				Crystal				
	310	1.605	HOMO→LUMO	-	378	1.668	60	388
				Aggregate				
	282	0.914	HOMO→LUMO	280	400	0.050	9	420

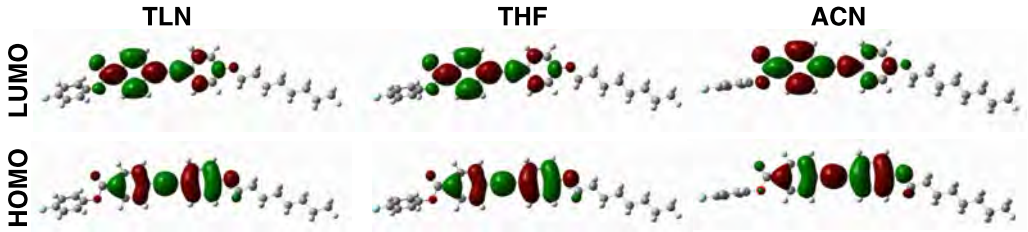

FIGURE 2.12 – Molecular frontier orbitals of **FOEB** in TLN, THF and ACN (isodensity = 0.025 a.u.).

From a structural point of view, Table 2.6 shows that changing the solvent polarity only leads to a modification of the orientation of the fluorophenyl group with respect to the central tolane core. Indeed, the value of the α dihedral angle slightly decreases from -57° in TLN to -92° in ACN, that is to say that the fluorophenyl moiety becomes orthogonal to the **FOEB** core. This structural modification has a minor impact on the absorption properties with computed λ_{max} values of 320, 311 and 314 nm in TLN, THF and ACN

respectively (Table 2.5) for an experimental $\lambda_{abs,exp}$ value of 325 nm for all the solvents [94]. As previously discussed, the fluorophenyl group is actually not involved in the electronic density variation observed upon the $S_0 \rightarrow S_1$ transition (Figure 2.12). Besides, for all the solvents, the two phenyl rings around the central acetylene axis are planar with a ϕ dihedral angle of 180°. Starting the geometry optimizations with a twisted configuration of the tolane moiety (ϕ =90°) systematically led to the planar equilibrium structure.

TABLE 2.6 – Selected structural parameters obtained for **FOEB** for the FC geometry (S_0) and for the S_1 optimized geometry for the three different solvents, the aggregated and the crystalline phases. The distances are in Angstroms, the angles and dihedral angles are in degree. The bond numbering and angle definition are provided in Figure 2.11.

	X-Ray	**TLN**		**THF**		**ACN**		**Agg.**		**Cry.**	
		S_0	S_1	S_0	S_1	S_0	S_1	S_0	S_1	S_0	S_1
Bond											
d_{trip}	1.205	1.204	1.239	1.204	1.241	1.204	1.241	1.202	1.292	1.216	1.232
Angle											
Θ	180	180	180	180	180	180	180	177	141	176	174
Dihedral											
ϕ	173	-180	179	-179	-180	180	-180	-64	-69	177	176
α	-60	-57	-45	-77	-54	-92	-92	41	40	-43	-41
β	3	-1	0	1	0	0	0	22	14	0	0

First excited state study: structural and emission properties

The first excited state of **FOEB** molecule in the three solvents was optimized. In the following, the corresponding structures are denoted as S_1. To investigate the structural modifications upon excitation we gathered the structural parameters in Table 2.6.

The first thing to notice is that in ACN solvent, there is almost no modification upon excitation and after relaxation, the central part is remaining planar (ϕ= 180° for S_0 and S_1) while the lateral fluorophenyl moiety is still perpendicular to the tolane (α= -92°). On the other hand, in both TLN and THF, after relaxation on the first excited state,

the main structural modification concerns this fluorophenyl group. While this moiety was tilted with respect to the central part in the GS (α= -57°and -77°for TLN and THF respectively), it tends to be less tilted in the excited state (α= -45°and -54°for TLN and THF respectively). **FOEB** is thus more planar when going from the GS to the ES in TLN and THF. In a non polar solvent (TLN), the orientation of the fluorophenyl is more guided by the electronic interaction with the central conjugated core than with the solvent. In a polar solvent (ACN), the main interaction occurs with the solvent and induce the perpendicular orientation of the lateral part. For THF, a moderately polar solvent, there is a competition between the two previously mentioned effect. Finally, except if one look at α, the three structures are similar and one can observe an increase of the length of the central triple bond, d_{trip}, when compared with the ground state.

As previously stated, no solvatochromic effect was observed for the absorption process for TLN, THF and ACN. Nevertheless, for the emission process, a red-shift is observed when the solvent polarity increases ($\lambda_{em,exp}$= 386, 412 and 440 nm in TLN, THF and ACN respectively, see Table 2.5). Our calculations nicely reproduced this red-shift with λ_{em} = 374, 391 and 400 nm leading to a difference with experimental values of 0.10, 0.16 and 0.28 eV. Because the optimized S_1 structures present triffling deviations, the bathochromic shift cannot be explained by structural considerations but should be due to solvatochromic effect.

In this context, the Lippert-Mataga equation can model this red-shift, while the solvent polarity increases, as follows:

$$\Delta\nu = \nu_{GS} - \nu_{ES} = \frac{2\Delta f}{hca^3}(\mu_{ES} - \mu_{GS})^2 + (\nu^0_{GS} - \nu^0_{ES}) \tag{2.10}$$

where, $\Delta\nu$ is the difference between the maximum absorption and emission wavenumbers ν_{GS} and ν_{ES}, namely the Stokes shift, μ_{GS} and μ_{ES} are the dipole moments in the excited and ground states, respectively, and h, c, and a stand for the Planck constant, the celerity and the Onsager solvent cavity radius, respectively. ν^0_{GS} and ν^0_{ES} are the absorption and emission values calculated in vacuum (at the CAM-B3LYP/6-311+G(d,p) level). The orientation polarizability, Δf, is calculated as follows:

$$\Delta f = \frac{\epsilon - 1}{2\epsilon + 1hca^3} - \frac{n^2 - 1}{2n^2 + 1} \tag{2.11}$$

where, ϵ and n are the static dielectric constant and the optical refractive index of the

solvent, respectively.

In Table 2.7 one can observe that the Lippert-Mataga model can reproduce the Stokes shift. It thus confirms that the effect of the solvent is predominant, increasing the emission wavelength when the dielectric constant of the solvent is also increasing. A polar solvent, like ACN, will better stabilize the excited state with a charge transfer character than less polar solvents like TLN and THF. This stabilization, by decreasing the energetic gap will increase the wavelength.

TABLE 2.7 – Stockes shift $\Delta\nu$ (in 10^3 cm^{-1}) calculated in TLN, THF and ACN with the Lippert-Mataga equation ($\Delta\nu_{LM}$) and compared with the calculated ($\Delta\nu_{calc}$) value.

Solvent	μ_{ES}[a]	μ_{ES}[a]	$\Delta\nu_{LM}$[b]	$\Delta\nu_{calc}$[c]
TLN	15.91	6.57	4.62	4.51
THF	17.70	6.94	5.70	6.58
ACN	18.55	7.19	6.11	6.85

[a] Calculated with Gaussian 16. [b] Calculated from Eqs 2.10 and 2.11. [c] Obtained from the calculated values of λ_{max} and λ_{em} given in Table 2.5.

Emission efficiency

The HR factors previously defined in Section 2.2.1 are used as indicators to measure the importance of some vibrational modes in the non-radiative relaxation decay channel. One of the parameters that influence the non-radiative decay is the internal conversion (IC) which is directly related to the HR factors. On Figure 2.15 are represented the calculated HR factors in the three solvents. The first thing to notice is that only few vibrational modes have a non negligible HR factor. A list with all the HR factors is reported in Appendice A-2. The main conclusions after the careful analysis of those HR factors are the following:

- In TLN (ACN) three (two) modes are found with large HR factors. The first vibrational mode with a wavenumber of 7 cm^{-1} (9 cm^{-1}) and a HR factor equal to 0.7 (0.2) corresponds to a global bending of the molecule out of the plane. The representation of this vibrational mode is provided in Figure 2.13. The two (one) following vibrational modes, ω= 23 and 28 cm^{-1} (20 cm^{-1}) with HR= 0.9 and 0.9 (2.4), corresponds to vibrations

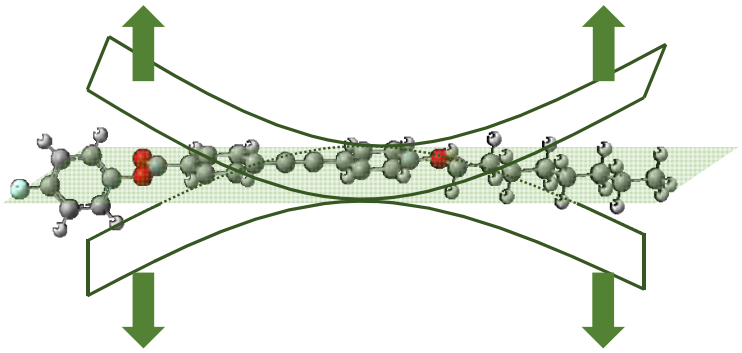

FIGURE 2.13 – Schematic representation of the vibrational mode corresponding to the largest HR value (ω= 7 cm^{-1}, HR = 0.70 for **FOEB** in TLN).

of the lateral moieties, whether the fluorophenyl group (ω= 20 cm^{-1} in ACN) or both fluorophenyl and alkyl chain (ω= 23 and 28 cm^{-1} in TLN). All the representations of the vibrational modes are depicted in Figure 2.14.

- In THF, all the previously mentioned vibrational modes cannot be retrieved. The first

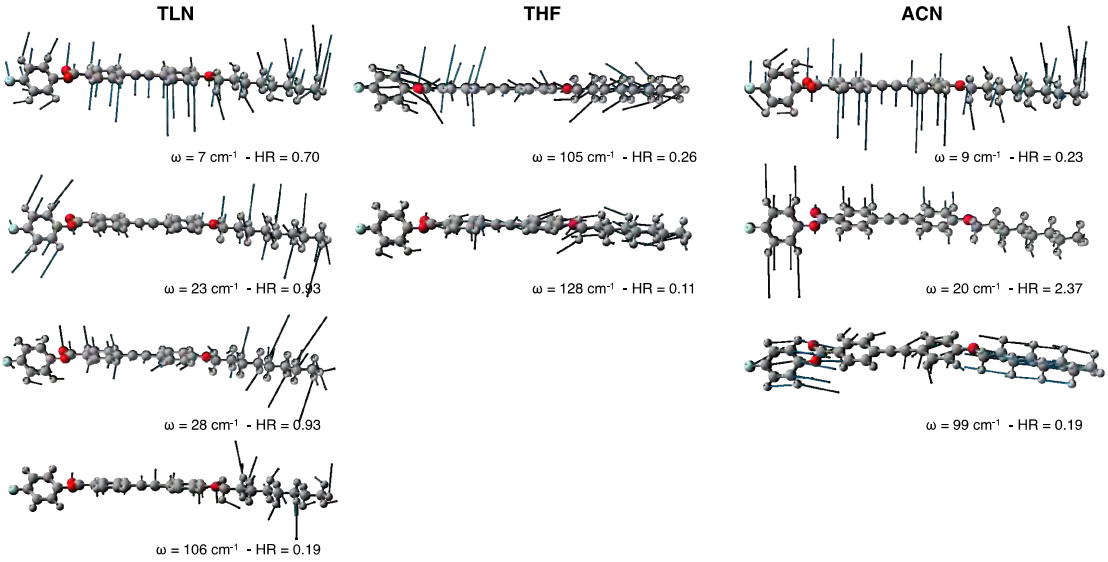

FIGURE 2.14 – Representation of the vibrational modes with important HR factors in TLN (left), THF (center) and ACN (right).

modes with non negligible HR factors (0.26 and 0.11) are found at larger wavenumbers (ω= 105 and 128 cm^{-1}). Unlike what is observed in TLN and ACN, in THF the vibrations are mainly in the plane of the molecule and consist in a stretching of the molecule.

As a conclusion, the fact that we found low frequency vibrational modes with relatively

large HR factors allows us to say that **FOEB** molecule, independently of the considered solvent for the moment, should be moderately emissive. This is confirmed by the experimental quantum yield with Φ_F= 0.27, 0.50 and 0.30 in TLN, THF and ACN respectively.

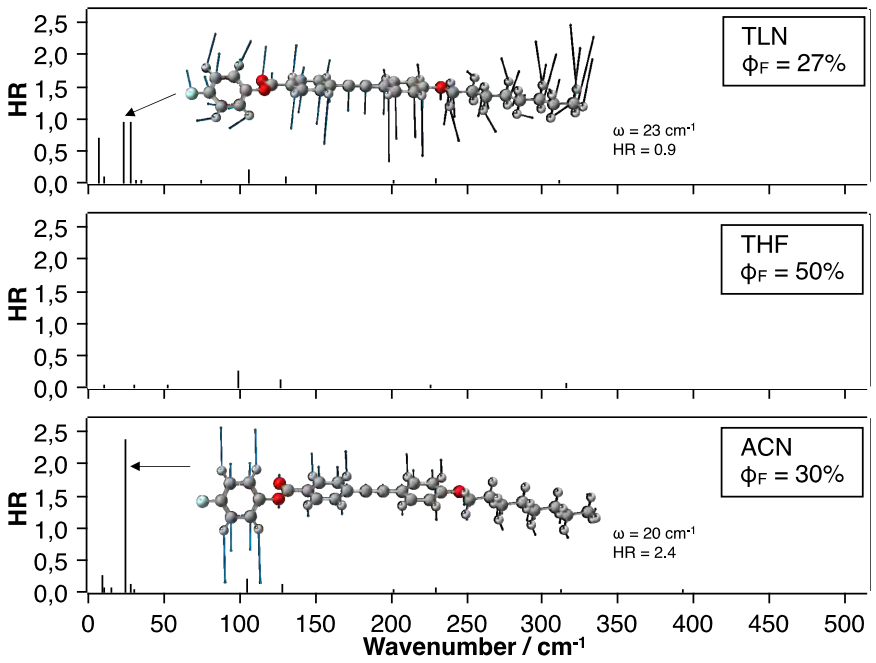

FIGURE 2.15 – Calculated HR factors versus the normal-mode wave numbers (ω in cm^{-1}) in the S_1 state for **FOEB** in TLN (top), THF (middle) and ACN (bottom). Vibration modes yielding the largest HR factors are also represented.

A modulation of the emission efficiency is observed when changing the solvent. This can be rationalized by the calculation of the total reorganization energies (Eq. 2.9) which is correlated to the number of vibrational modes with large HR factors (Eq. 2.8). The calculated values are the following: 72, 42 and 68 cm^{-1} in TLN, THF and ACN respectively. The higher the total reorganization energy ($E_{reorg,total}$) is, the stronger the quenching of the emission process should be due to large photophysical energy dissipation *via* vibrational movements. Hence, the emission process should be less efficient in TLN than in THF and in a lesser extent in ACN and should be evidenced by a smaller value of Φ_F for TLN and a larger value for THF. As shown in Table 2.5, this hypothesis is in qualitative agreement with the experimental fluorescence quantum yield.

Therefore, the low quantum yield in highly polar solvent should not be attributed to the

existence of a twisted intramolecular charge-transfer (TICT) state acting as a non radiative decay channel, as supposed by Tang *et al* in their experimental work [94], but to a RIV mechanism. The variation of Φ_F can actually be rationalized through the competition between two effects, (1) the increase of the conjugation while relaxing on the S_1 PES which is accompanied by a stretching of the central ethylenic bond and a tilt of the fluorophenyl group leading to a more planar structure, and (2) the interaction with the solvent. For non-polar (TLN) and weakly polar (THF), the first effect is predominant and increases with the solvent polarity. Then, in THF, the structural reorganization is more pronounced than in TLN and the HR factors become smaller (and even close to zero for the out-of-plane vibrations). On the opposite, for highly polar solvent, the competition between these two effects is dominated by the influence of the solvent polarity and there is no tilt of the fluorophenyl group. The structural reorganization is less pronounced while the vibrational modes are more similar and HR factors are thus non negligible.

2.3.2 Then, they turned into crystalline phase.

Ground state study: structural and absorption properties

We started by checking the validity of our model, as developed in Section 2.2.2. The molecular packing, extracted from the experimental X-ray structure [94], is represented on Figure 2.16. No clear π-π stacking is observed, the phenyl moieties of two neighboring **FOEB** molecules being nearly orthogonal. However, one can observe CH-π interactions, represented on Figure 2.16.

The optimized structures in solution and within the crystalline environment were compared. No major differences are observed when both molecules are in their ground states. The core of the molecule is planar in each case (Φ is close to 180°). The difference arises from the lateral fluorophenyl group. In the crystalline phase, this moiety slightly tends to align with the central part (α = -43° in the crystal while it varies between -57 and -92° in TLN, THF and ACN respectively). The calculated λ_{max} value is close to the one obtained is solution (see Table 2.5) as it was expected due to the minor structural differences between the two geometries.

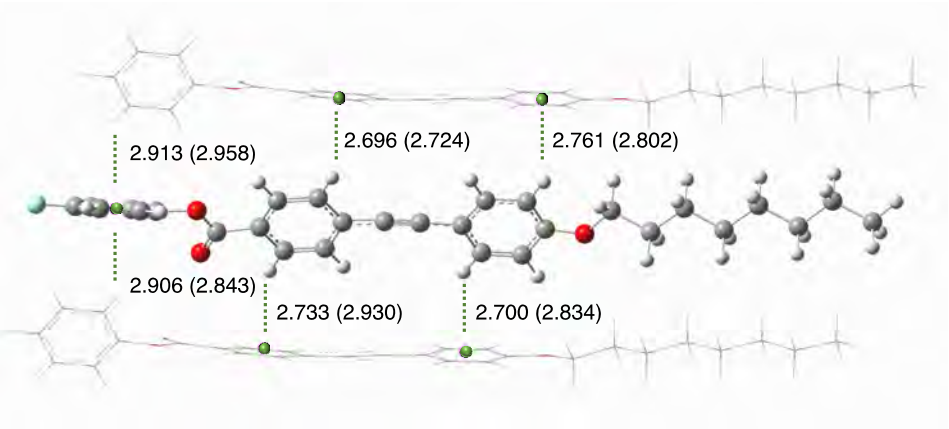

FIGURE 2.16 – Molecular packing of **FOEB** [94]. Weak interactions (CH-π) and the corresponding calculated (experimental) distances are also given in Angtroms.

We have then investigated the impact on the optical properties of two different parameters which are (1) the chosen model (monomer or dimer) and (2) the environment. We thus compared the calculated absorption values of a monomer and a dimer with or without the environment (*i.e.* the other molecules within the crystal treated at the QM' level with the ONIOM model). The results are given in Table 2.8. We can say that (i) there is almost no variation of the λ_{max} value if the absorption properties are computed for a dimer cluster embedded in the crystal, indeed one can observe an expected splitting of the absorption band of the monomer and (ii) there is a slight impact of the environment on the λ_{max} value (+7 nm when the environment is not considered). Hence, while maintaining the environment is important, we can consider only a monomer when calculating the optical properties of **FOEB** in the crystal.

This model choice can also be justified by the calculation of the possible energy transfer between the two molecules within the dimer. To do so, we have relied on the model proposed in Gaussian 16, namely the Electronic Energy Transfer (EET) model [58, 59]. The value of the exciton coupling V_{12} between the two monomers (1 and 2) within the dimer, is equal to 29 meV which indicates a small coupling between the two **FOEB** moieties. This can be rationalized by the molecular packing as illustrated in Figure 2.20.

Excited state study: structure, emission properties and CIE effect

Due to the close environment, the molecular structure of the S_1 is slightly modified upon optimization. It appears that the S_1 optimized structure is close to the TLN one: the

TABLE 2.8 – Calculated maximum absorption wavelengths (λ_{max}) in nm, oscillator strengths (f) and major contributions in the electronic excitations for **FOEB** in different environments.

Model	State	λ_{max}	f	Assignment
			Crystal	
Mono. ONIOM	S_1	310	1.605	HOMO → LUMO
Mono. No env.	S_1	317	1.564	HOMO → LUMO
Dim. ONIOM	S_1	319	0.327	HOMO → LUMO+1
	S_2	305	2.561	HOMO-1 → LUMO
			Aggregate	
Mono. ONIOM	S_1	286	0.692	HOMO → LUMO
Mono. No env.	S_1	286	0.709	HOMO → LUMO
Dim. ONIOM	S_1	290	0.799	HOMO → LUMO/LUMO+1

structure tends to be planar in a non-polar solvent (TLN) but also in the crystalline environment (α decreases). The calculated emission energy for the S_1 state is reported in Table 2.5. As pointed out by Tang *et al*, the emission value in the crystalline environment is close to the one obtained in TLN (388 and 386 nm). We nicely reproduce both the position of this emission band in the crystal ($\Delta E_{exp-calc}$ = 0.08 eV) but also the small difference with the emission value in TLN ($\Delta\lambda_{em,TLN-CRY}$ = 2 and 4 nm experimentally and calculated respectively).

To explain the strong emissive behavior in the crystalline phase with Φ_F=60% (Table 2.5), the calculation of the vibrational spectrum of the S_1 structure was performed. Then, a careful comparison of the molecular vibrational modes at low frequencies was made between the crystal and the solution. One should note that it was not possible to calculate the HR factors within the ONIOM framework. In solution, the largest HR factors were found for two different types of motions. As previously described, the first one (HR = 0.70 and 0.23 in TLN and ACN respectively) corresponds to a global motion of the molecule out of the plane. The second one mainly implies movements of the lateral substituents (HR = 0.93 and 0.19 in TLN and HR = 2.37 in ACN). A third motion, only observable in THF (HR = 0.26), implies stretching motions in the plane of the molecule. Due to the packing and especially to the orientation of the phenyl rings, vibrations involving the lateral parts

of the molecules are no longer possible and thus it was not possible to identify the modes we pointed out in solution.

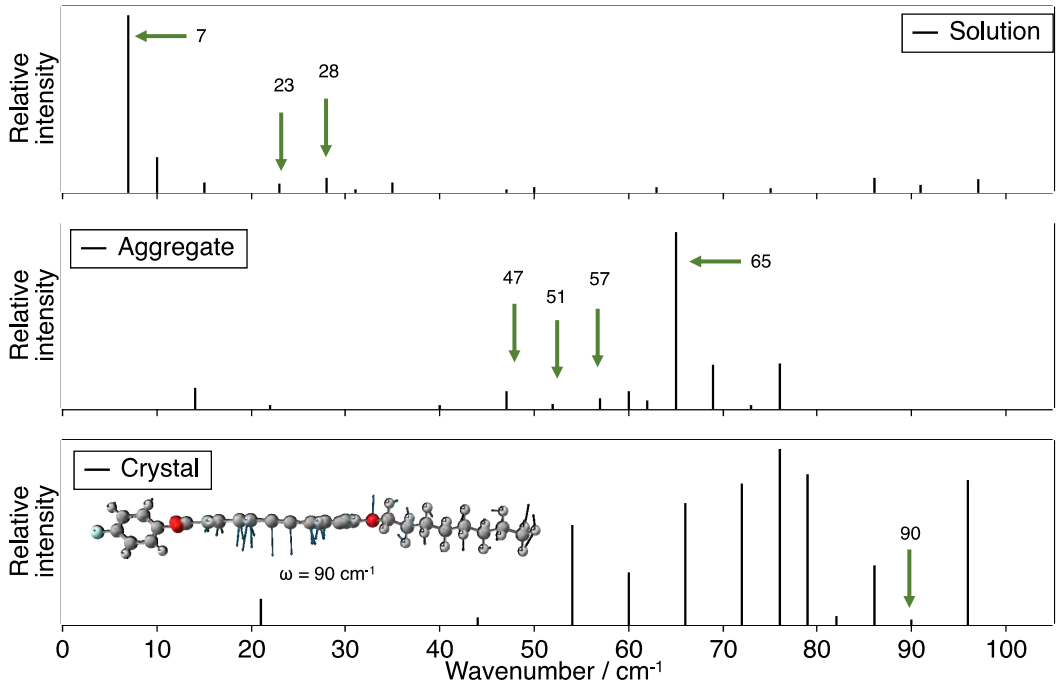

FIGURE 2.17 – Low-frequency vibrational modes (0-100 cm^{-1} region) calculated for the S_1 state of **FOEB** in TLN solution (top), aggregate (middle), and crystal (bottom). All the vibrational modes corresponding to large HR values in solution and the modes presenting similarities in the crystal or in the aggregate are depicted in Appendix A-4.

For the vibrational modes involving the entire molecule, similar motions could be identified in the crystal ($\omega = 90cm^{-1}$, see Figure 2.17 and $\omega = 105\ cm^{-1}$, see Appendix A-4). In brief, vibrational modes involving only the lateral parts are no longer possible within the crystalline environment while the motion in and out of the plane of the molecule can still occur. Thus, we expect the fluorescence quantum yield to increase when going from solution to crystal. To go beyond, we expect the increase of Φ_F to be stronger when going from TLN/ACN to crystal than going from THF to crystal. In the first case there is a vanishing of vibrational modes involved in a non-radiative decay process while in the second case there is only a decrease of the amplitude of the vibration involved in the non-radiative decay process. Experimental data are in line with this hypothesis with an

increase of the emission efficiency in the crystalline phase with a Φ_F value of 60% (see Table 2.5).

2.3.3 They also formed aggregates.

Ground state study: structural and absorption properties

The aggregate encompassing 25 **FOEB** molecules represented in Figure 2.18 is stable during the 10 ns simulation, no splitting is observed along the trajectory.

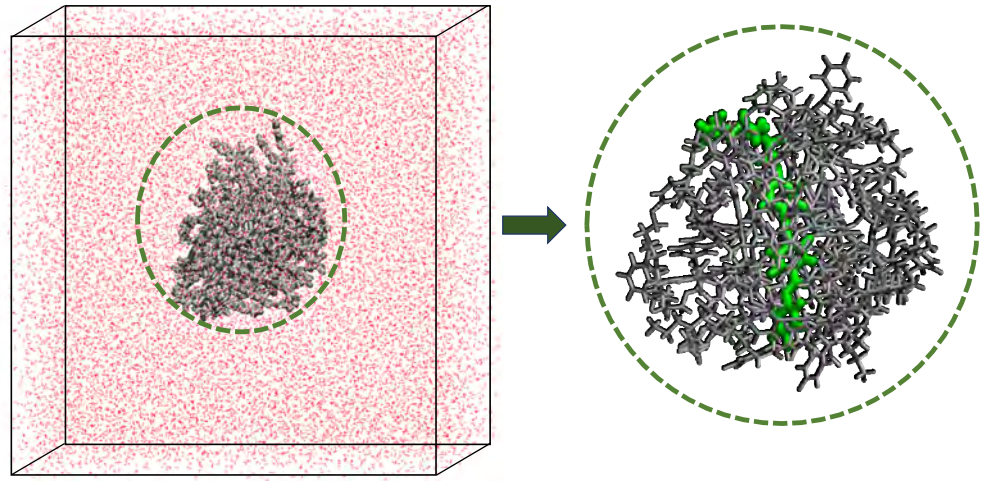

FIGURE 2.18 – QM/QM' model for the **FOEB** aggregate sampled with MD simulations. On the left, conformation of the **FOEB** aggregate extracted from a MD simulation with a representation of the water box and on the right, QM/QM' model for the aggregate: one embedded molecule is defined as the QM region (in green) and the others (24) are described with the QM' model.

On Figure 2.19 we have reported the evolution along the simulation time of some structural parameters for a central molecule. The main conclusion concerns ϕ, the dihedral angle between the two phenyl groups close to the ethylenic bond.

While in solution the tolane moiety is planar with a dihedral angle close to 180°, its value reaches -70° within the aggregate and the two phenyl rings close to the ethylenic bond are nearly perpendicular. The molecule being less planar and thus less conjugated in the aggregate, the λ_{max} value is experimentally blue-shifted (-0.61 eV) compared to solution and we reproduce this blue-shift with our calculation (-0.52, -0.41, -0.45 eV with respect

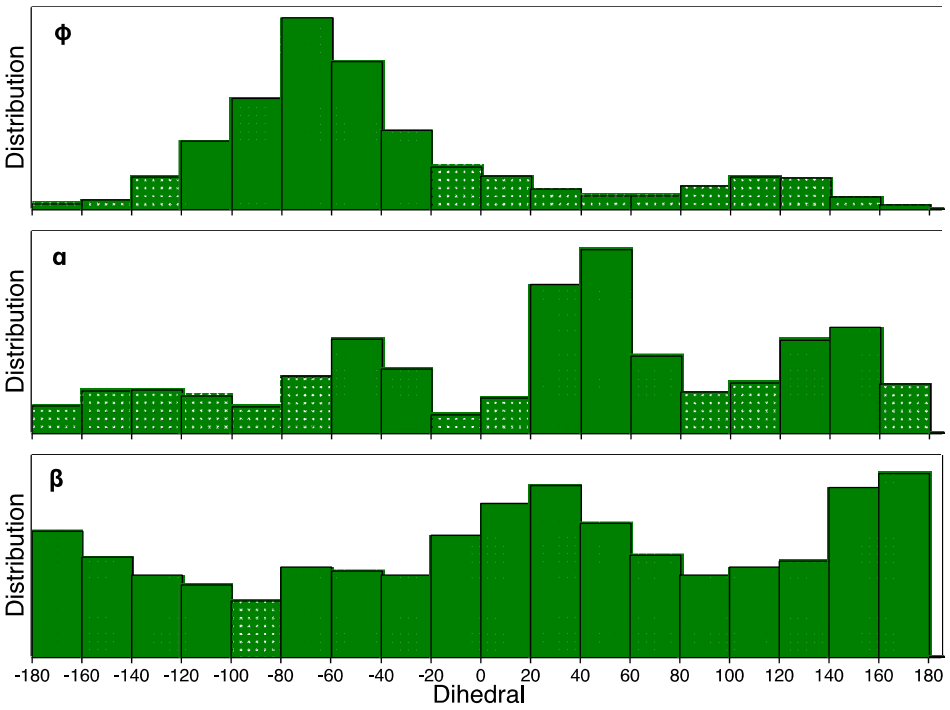

FIGURE 2.19 – Distribution of the ϕ, α and β dihedral angles along the 10 ns trajectory of a central **FOEB** molecule within the aggregate.

to λ_{max} calculated in TLN, THF and ACN respectively). Hence, the constraints imposed by the other **FOEB** molecules and the solvent has a direct impact on the structure and the optical properties of the central **FOEB** molecule.

We have also investigated the electronic impact of the environment on the absorption properties by comparying the λ_{max} values of a monomer and a dimer with or without environment (Table 2.8). It indicates that (i) there is no impact of the environment on the λ_{max} and (ii) there is a negligible variation of the λ_{max} value if the absorption properties are computed for a dimer cluster embedded in the aggregate. Hence, the modification of the absorption spectrum is only due to strong structural deformations within the aggregate.

Excited state study: structure, emission properties and ACQ effect

We first calculated the vibrational spectrum of the first excited state optimized structure. We carefully investigated the low-frequency vibrational modes and compared them with the ones obtained in solution. This comparison reveals that the mode contributing to the energy dissipation in solution can be retrieved in the aggregated environment (vibrational

mode in and out of the plane of the molecule involving whether the entire molecule or mainly the fluorophenyl of alkyl lateral moieties). Despite the presence of other **FOEB** molecules in the neighboring, vibrational motions that we identified as responsible for the moderate emissive behavior in solution are still possible in the aggregate.

Another process can be added to explain the small value of Φ_F in the aggregate, namely the possible energy loss through excitation energy transfers between two molecules in the aggregate. The value of the largest exciton coupling V_{ij} between two monomers i and j in a dimer (Figure 2.20) reaches 62 meV and this is a typical value of a "medium" coupling.

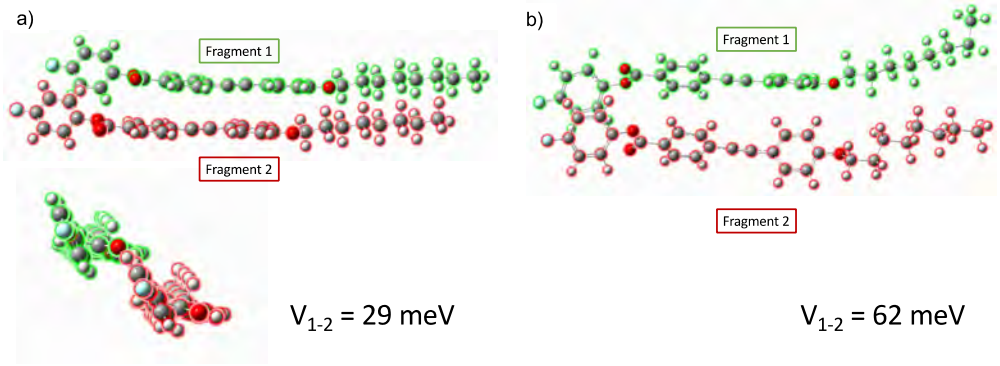

FIGURE 2.20 – Representation of a possible stacked dimer within (a) the crystalline phase (lateral and side views) and (b) the aggregate along with the calculated coupling value (in meV) between the two molecules.

This value is twice as large as the one calculated in the crystal. Indeed, in the crystal, the small value of the exciton coupling is due to the particular molecular packing that, unlike the aggregate, prevents any π-π stacking. The excitonic coupling always enhances the non-radiative decay constants [113], the molecular arrangement within the aggregate should promote the non-radiative relaxation pathway through excitonic couplings. This phenomenon combined with the energy dissipation during the internal conversion process through the low-frequency vibration mode identified in solution should be at the origin of the observed ACQ.

2.4 AIE or CIE ? Choose the right DPYDPE isomer

As developed in Section 2.2.1 we selected the cLR-PCM(TD-ωB97X-D//ωB97X-D) computational scheme to study the isomers of **DPYDPE** (see Figure 2.7) and their corresponding AIE or CIE behavior.

2.4.1 Solution: a dark beginning.

Ground state: structure and absorption properties

The absorption properties were calculated for both isomers (see Table 2.9). It appeared that the maximum absorption band corresponded to the first excited state ascribed as an HOMO $\rightarrow$ LUMO transition. The HOMO is located on the pyrrole rings while the LUMO is delocalized on the phenyl rings. The transition thus presents a charge transfer (CT) character. The following transitions (S_2 and S_3) are nearly degenerated and have smaller values of oscillator strength. The corresponding transitions (HOMO to LUMO+1 and LUMO+2) have a more pronounced CT character. All the mentioned molecular orbitals are represented in Figure 2.21.

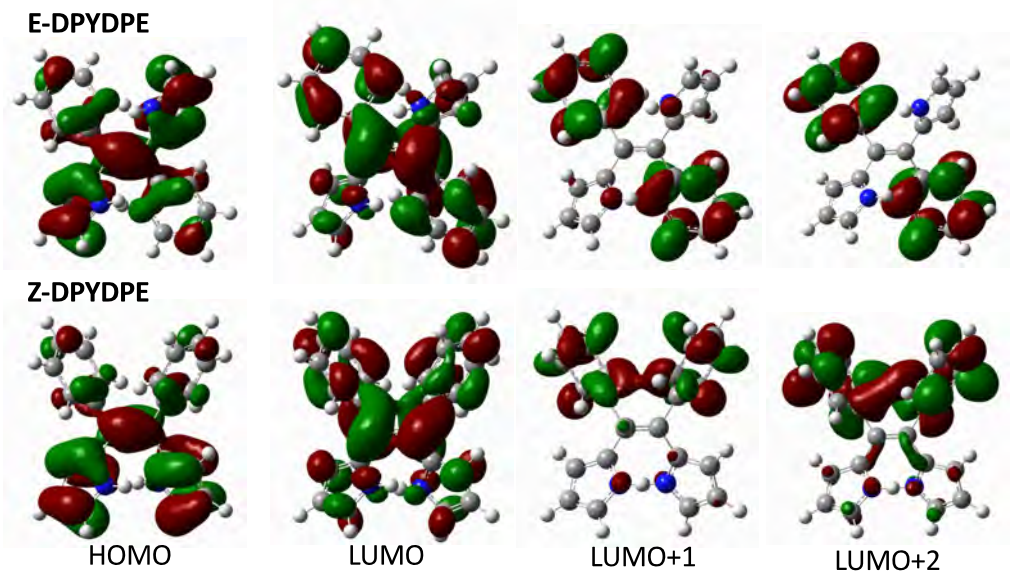

FIGURE 2.21 – Molecular orbitals of **E-DPYDPE** (top) and **Z-DPYDPE** (bottom) calculated at the PCM(THF)-ωB97X-D level (isodensity = 0.025 au).

Because of the well-known large flexibility of TPE-like molecules, we investigated the

TABLE 2.9 – Calculated absorption (λ_{max}) and emission (λ_{em}) wavelengths in nm, oscillator strengths (f) and electronic excitation assignments for **E-DPYDPE** and **Z-DPYDPE** in different surroundings. Both experimental λ and Φ_F are also provided [95].

		Absorption				Emission			
	State	λ_{max}	f	Assignment	$\lambda_{max,exp}$	λ_{em}	f	Φ_F	$\lambda_{em,exp}$
					Solution				
E	S_1	337	0.569	HOMO → LUMO		755	0.240		
	S_2	264	0.001	HOMO → LUMO+1	357	358	0.041	0.2	461
	S_3	263	0.371	HOMO → LUMO+2		-	-		
Z	S_1	341	0.467	HOMO → LUMO		779	0.224		
	S_2	258	0.003	HOMO → LUMO+1	340	303	0.012	6	470
	S_3	255	0.142	HOMO → LUMO+2		311	0.250		
					Crystal				
E	S_1	304	0.762	HOMO → LUMO	-	396	0.488	10	483
Z	S_1	333	0.430	HOMO → LUMO	-	427	0.375	89	489
					Aggregate				
E	S_1	354	0.363	HOMO → LUMO	-	504	0.313	69	475
Z	S_1	305	0.764	HOMO → LUMO	-	409	0.525	37	450

impact of the possible rotations of one pyrrole ring, illustrated through χ_1 angle (see Figure 2.7 for the definition of the angle), on the energetics and the absorption properties (Figure 2.22).

It was found that the rotation barrier is equal to 4.3 (4.8) kcal.mol^{-1} with ΔG= 3.4 (3.8) kcal.mol^{-1} for **E-DPYDPE** (**Z-DPYDPE**). Both systems are thus flexible. To go further, the intramolecular hydrogen bond of **Z-DPYDPE** induces a slight rigidification of the structure with a higher rotation barrier (+0.5 kcal.mol^{-1}). The hydrogen bond lengths (2.891 and 2.862 Å) and the angles formed by the N-H—N atoms (almost 90°), indicate a weak to moderate hydrogen bond. Upon a complete rotation of the pyrrole ring, two stable isomers are found for both isomers. The relative Boltzmann population of the two conformers are 72:28 and 63:37 for **E-DPYDPE** and **Z-DPYDPE** respectively. No impact on the optical properties upon rotation is observed with a $\Delta\lambda$ smaller than 5 nm between the two stable conformers. Going from one conformer to the second one induce a loss of planeity of the molecule that is illustrated through the optical properties of the

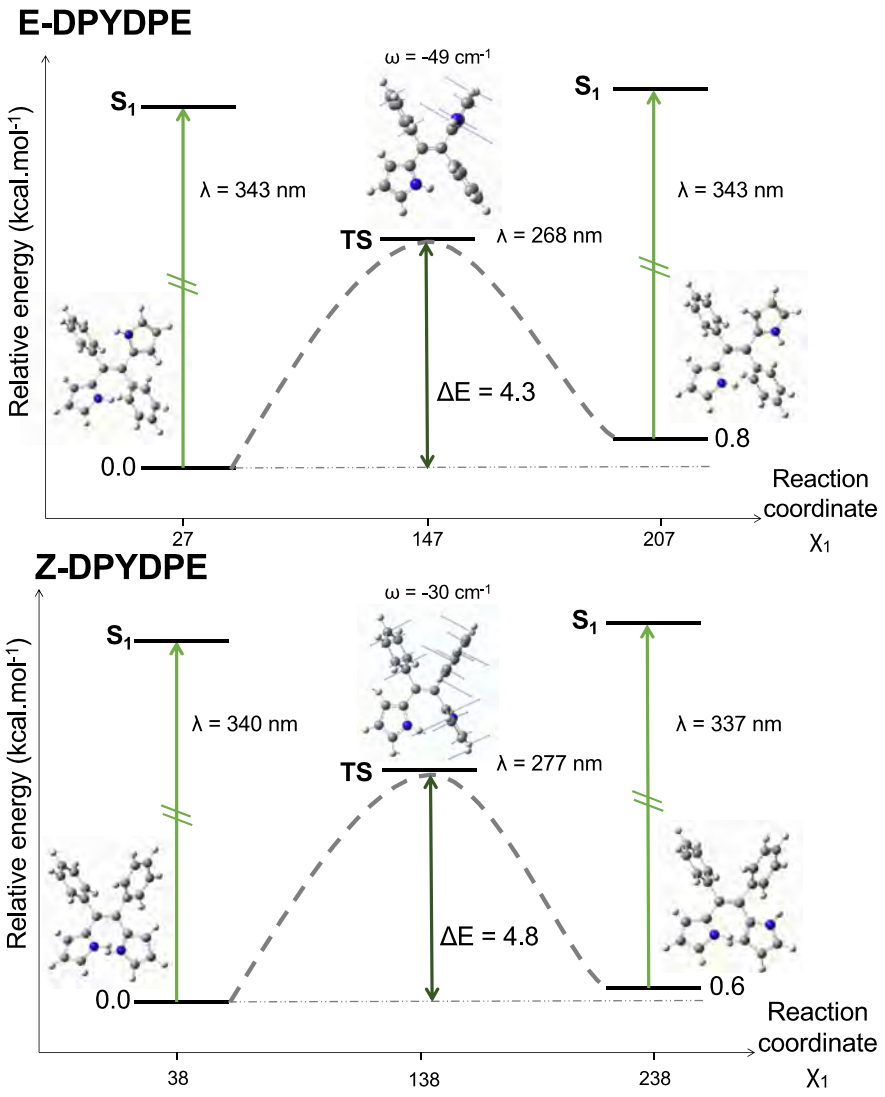

FIGURE 2.22 – Impact of the rotation of one pyrrole ring on the energetics and absorption properties (maximum absorption wavelengths λ in nm). The relative energies are given with respect to the most stable conformer, either for **E-DPYDPE** or **Z-DPYDPE**. At the Transition State (TS), the vibration mode with an imaginary frequency is represented.

transition state (TS). Indeed, the calculated λ_{max} of the TS is smaller than the ones of the conformers with a value of 268 (277) nm for **E-DPYDPE** (**Z-DPYDPE**). The rotation of a phenyl ring was also investigated (See Appendix A-5). The calculated rotation barrier was equal to 10.8 (5.4) kcal.mol^{-1} with a ΔG of 11.1 (6.9) kcal.mol^{-1} for **E-DPYDPE** (**Z-DPYDPE**). Because of the steric constraints, it is more difficult for a phenyl ring to rotate than for a pyrrole one and it thus requires more energy.

Excited state: structure and emission properties

The low-lying excited states for both isomers were optimized. In the following, the different considered excited states are denoted as S_n with n=1...3. One has to notice that the S_3 could not be obtained for **E-DPYDPE**.

The strongest structural modifications upon excited state optimizations are globally the same for **E-DPYDPE** and **Z-DPYDPE**:

- A torsion of the phenyl groups illustrated through the evolution of ξ_1 and ξ_2 is observed. For example ξ_1 moves from -121° for S_0 to -156 and -88° for the S_1 and S_2 of **E-DPYDPE** respectively.

- More particularly, for S_1, a global "opening" of the structure is observed. ϕ and ψ, which account for the torsion against the central vinyl moiety and thus the flatness of the structure, move from 12 and -170° for the GS structure to 61 and -121° for the S_1 geometry for **E-DPYDPE**.

- The S_2 structure, except for the torsion of the phenyl group, undergoes less structural modification when compared to the S_0 geometry.

For both isomers, the strong structural modifications between S_0 and S_1 lead to large Stokes shifts with calculated emission wavelengths of 755 and 779 nm for **E-** and **Z-DPYDPE**, respectively. There is a large discrepancy between these values and the experimental emission data (461 nm for **E- DPYDPE**, 470 nm for **Z- DPYDPE**), and we can conclude that S_1 is not the emissive state. The poorly emissive character (Φ_F=0.2% for **E-** and 6% for **Z-DPYDPE**) may be due to an emission process involving excited states that are higher in energy. Indeed, in Table 2.9, the comparison of emission wavelengths calculated for the S_2 and S_3 structures shows a better agreement than the emission wavelength calculated for the S_1 state with experiment. However one can still observe a blue-shift. This hypsochromic shift is partially related to the single-excitation nature of TD-DFT. To test this hypothesis with an affordable computational strategy, we have performed configuration interaction singles (CIS) and CIS(D) calculations for the emission energy of each isomer in vacuum [114]. We have found that the difference in calculated emission energies ΔE_{CIS}-$\Delta E_{CIS(D)}$ is 0.48 eV for **E-DPYDPE** (S_2 state). For **Z-DPYDPE**, this difference is about 0.51 eV for the S_2 state and 0.45 eV for S_3. Therefore, CIS overestimates

the emission energies compared to CIS(D) and we can thus conclude that the neglecting of double excitations in CIS yields to the overestimation of the value of the emission energy. Of course, this result, based on the comparison of CIS and CIS(D) methods, provides an indication of the role of the double excitations but does not allow to definitely rule on this effect. CCSD calculations, that could not be performed on our system, would provide a definitive conclusion.

As previously mentioned in the introduction, the origin of the non-emissive behavior of AIE molecules in solution can be attributed to the presence of an energetically accessible conical intersection (CI) leading to an ultrafast internal conversion from the excited to the ground state [115, 116, 55]. We thus plotted along the S_1 relaxation path (Figure 2.23), the energy of the ground and first excited state versus the rotation angle of the two phenyl rings ξ. We can conclude that there is no S_1/S_0 crossing along this relaxation path which strengthens our conclusion that the fluorescence quenching in solution is assigned to the photophysical energy dissipation caused by scissoring motions.

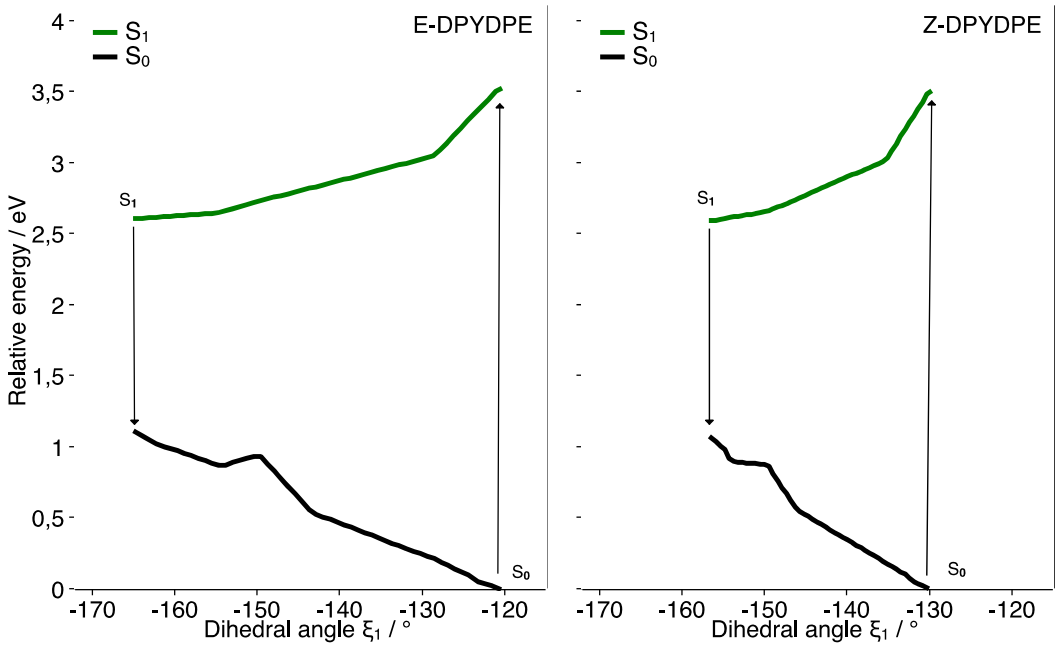

FIGURE 2.23 – Relative energy (eV) along the S_1 geometrical relaxation path of the two states S_0 and S_1 for (a) **E-** and (b) **Z-DPYDPE**. The potential energy surfaces are plotted versus the rotation angle of one phenyl ring ξ_1. For both isomers, the reference energy corresponds to the energy of the GS optimized structure.

We have then investigated the possible photophysical energy dissipation from these higher-energy excited states. For **E-DPYDPE**, as shown by Figure 2.24, the HR factors calculated for the S_2 state are much smaller than those calculated for S_1. This finding supports the conclusion the S_2 is more emissive than S_1. However, experimentally, the irradiation wavelength is set to 350 nm and this excitation is not sufficiently energetic to populate S_2 (λ=263 nm in Table 2.9). After irradiation, a complex relaxation pathway is thus necessary to induce an emission phenomenon from the S_2 state and this should result in a small value of the fluorescence quantum yield. One should also expect a wavelength effect: the fluorescence quenching phenomenon might be modulated by using different irradiation wavelengths. One can draw exactly the same conclusion for **Z-DPYDPE**. We have provided in Figure 2.24 the HR factors for the S_3 state since the oscillator strength f computed for this state is much larger than the S_2 one (see Table 2.9). Therefore, S_3 is potentially the emissive state which is comforted by the values of the HR factors that are much smaller than the S_1 ones.

Why is the value of the fluorescence quantum yield Φ_F larger for **Z-DPYDPE** than for **E-DPYDPE** in solution? Indeed, Figure 2.24 shows that the reorganization energy for **E-DPYDPE** is larger than **Z-DPYDPE**. Hence, the photophysical energy dissipation caused by vibrational motions might induce a stronger fluorescence quenching for **E-DPYDPE**. We want to stress out that we do not compare the same state for the two isomers since it was not possible to characterize the S_3 structure for **E-DPYDPE**. A modification of the electronic structure for the E isomer might lead to a dissociative S_3 potential energy surface (with no minimum) and thus impede the radiative relaxation process from this more emissive state (the comparison of the oscillator strength value in Table 2.9 also shows that S_3 is more emissive than S_2). An investigation of the topology of the excited state potential energy surfaces with multi-configurational approaches, which goes beyond the scope of the present study, should be necessary to clarify this point.

2.4.2 Crystal: one chance out of two

Ground state: structure and absorption properties

We first validated our structural model as explained in Section 2.2.2 and found a negligible difference between our optimized structure and the X-ray crystallographic data. We then

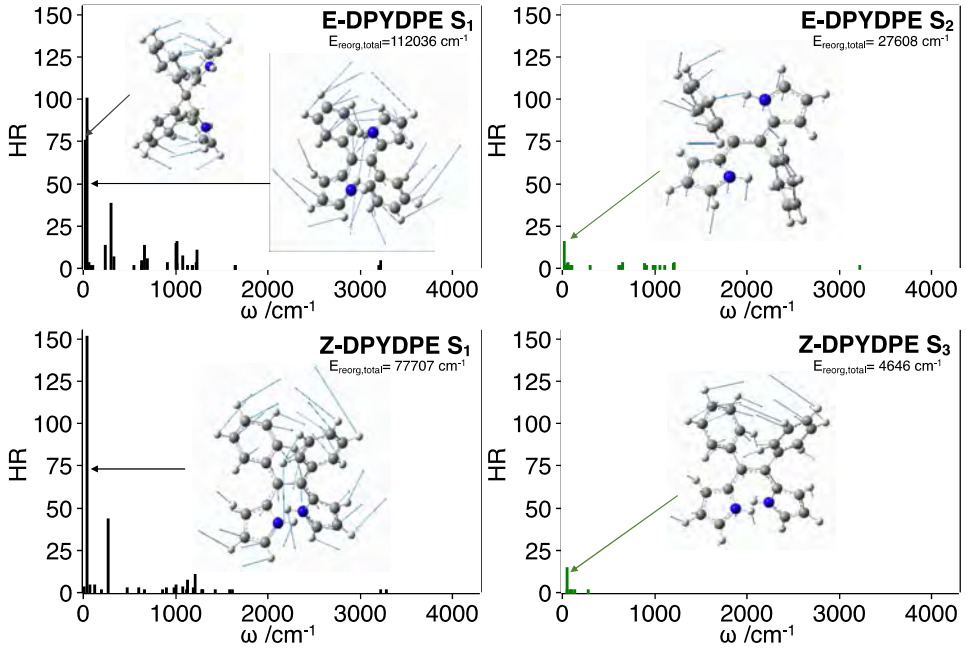

FIGURE 2.24 – Calculated HR factors for **E-DPYDPE** (top) and **Z-DPYDPE** (bottom) versus the normal mode wave numbers in the S_1 state (left) and S_2 state or S_3 state (right). The representation of the vibration modes yielding the largest HR factors is given.

looked carefully at the molecular packing. As represented on Figure 2.25, it appears that there is no π-π stacking. It leads to a not so-tight packing of the molecules for both isomers. Some CH-π interactions are also observed for both isomers (Figure 2.25) along with intermolecular NH-π interactions for **Z-DPYDPE** only.

As reported in Table 2.9, the λ_{max} value of **E-DPYDPE** (304 nm) is blue-shifted with respect to the solution value (337 nm). The same conclusion holds to a smaller extent for **Z-DPYDPE**, with calculated λ_{max} values of 341 and 333 nm in solution and the crystal phase, respectively. In order to understand if this hypsochromic shift arises from an electronic or a steric effect, we have performed TD-DFT calculations on the crystalline optimized structure without any surrounding. The values obtained for λ_{max} are very close to those obtained with the environment, namely 305 nm for **E-** and 330 nm for **Z-DPYDPE** (Table 2.10). Finally, we have calculated the absorption properties of a central dimer within the ONIOM framework and the calculated λ_{max} values are 305 and 327 nm for **E-DPYDPE** and **Z-DPYDPE** respectively. Therefore, the effect of excimer formation on the calculated absorption spectrum is negligible. These results show

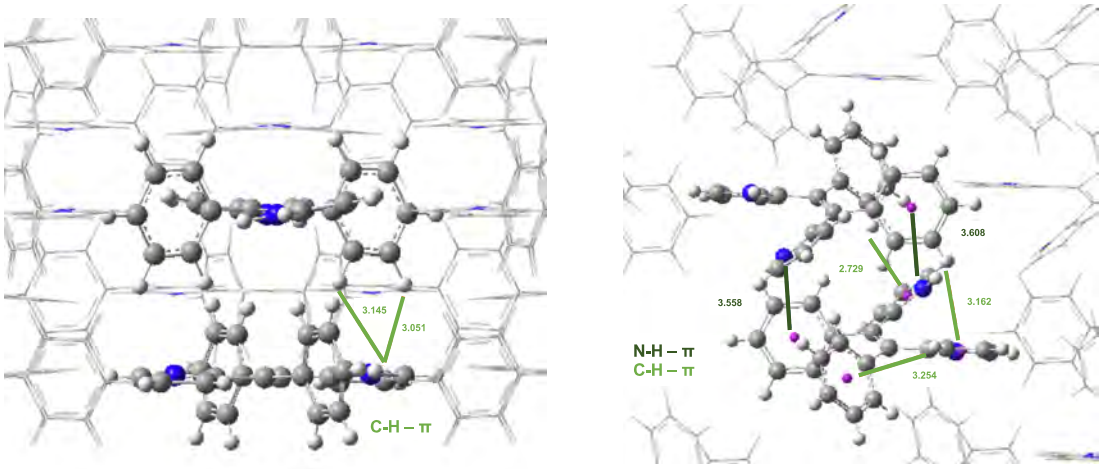

FIGURE 2.25 – Molecular packings of **E-DPYDPE** (left) and **Z-DPYDPE** (right). Weak interactions (CH-$\pi$and NH-π) and the corresponding distances (in Angstroms) are given.

that the modification of the absorption properties while going from solution to the crystal phase mainly arises from the structural deformations and that, with this loose packing, the electronic intermolecular couplings are not sufficient to alter the observed photophysical properties.

Excited state: structure and emission properties

The first excited state (S_1) has been optimized for both isomers. Because of the close environment, the structures remain similar as the ones of the ground state. However, the S_1 structures of the crystalline phase are very different from the S_1 structures of the solution. At the same time, the electronic structure of S_1 in the crystal is directly comparable since this state still arises from a HOMO $\rightarrow$ LUMO electronic excitations at the S_1 optimized geometry with comparable frontiers orbitals. The calculated emission energies from the S_1 state are given in Table 2.9 and we can observe a blue shift compared to experiments (deviation of 0.5 and 0.3 eV for **E-DPYDPE** and **Z-DPYDPE** respectively) and this could be due to the single-excitation character of TD-DFT calculations. Contrary to the isolated molecule in solution, we believe that the emission band can be attributed to radiative

TABLE 2.10 – Calculated maximum absorption wavelengths (λ_{max}) in nm, oscillator strengths (f) and major contributions in the electronic excitations for **E-DPYDPE** and **Z-DPYDPE** in different environments.

	E-DPYDPE			**Z-DPYDPE**		
	λ_{max}	f	Assignment	λ_{max}	f	Assignment
			Solution			
Mono.	337	0.569	HOMO → LUMO	341	0.467	HOMO → LUMO
			Crystal			
Mono. ONIOM	304	0.762	HOMO → LUMO	333	0.430	HOMO → LUMO
Mono. No env.	305	0.745	HOMO → LUMO	330	0.420	HOMO → LUMO
Dim. ONIOM	305	0.679	HOMO-1 → LUMO	327	0.766	HOMO-1 → LUMO
			Aggregate			
Mono. ONIOM	359	0.356	HOMO → LUMO	307	0.740	HOMO → LUMO
Mono. No env.	355	0.363	HOMO → LUMO	306	0.770	HOMO → LUMO
Dim. ONIOM	358	0.298	HOMO-1 → LUMO+1	302	0.887	HOMO-1 → LUMO

emission from the S_1 state since (i) the comparison between experiments and calculations is more favorable than the solution and (ii) the experimental-calculated deviation is in the line of previous TDDFT calculations carried out on the emission phenomena in molecular crystals [102]. We can also conclude that for the S_1 state, the role played by the molecular environment on the emission process is much more important than those in the absorption. Indeed, for the absorption (Table 2.9), while going from the solution to the crystal phase, there is a small difference on the excitation energies and corresponding transition dipoles. On the opposite, for the emission (Table 2.9), there is a large blue shift of the emission band corresponding to the radiative relaxation from the S_1 state which is due to a strong structural deformation of the ES minimum. At the same time, the oscillator strength value is multiplied by 2.0 and 1.7 for **E-DPYDPE** and **Z-DPYDPE** respectively (for instance, the value of f for the **E** isomer is 0.240 in solution and 0.488 in crystal). Therefore, the crystalline environment should enhance the molecular emissive efficiency by increasing the transition dipole moment of the corresponding state.

Finally, after calculating the vibrational spectrum of the S_1 structure, we have looked over the molecular vibrational modes showing pronounced rotation motions at low

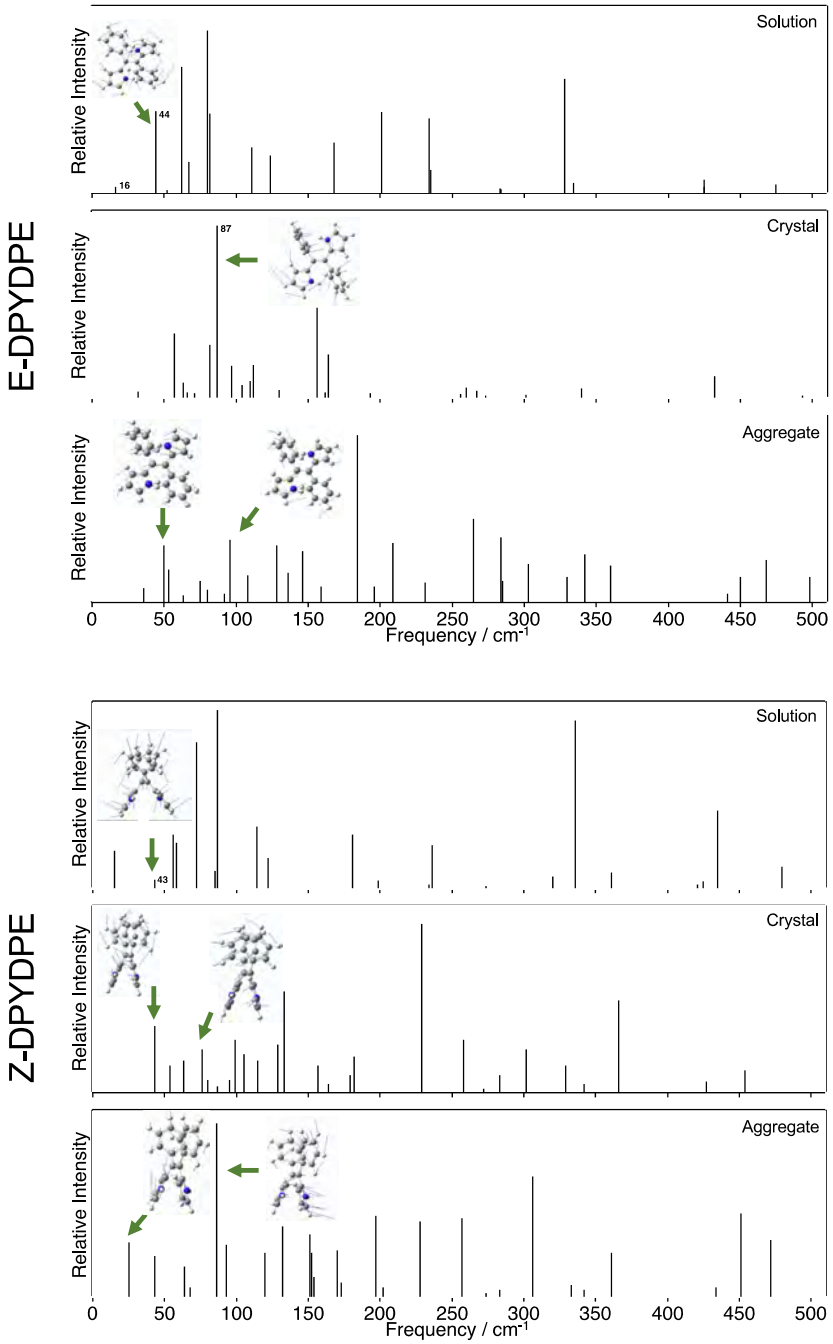

FIGURE 2.26 – Low frequencies vibrational modes (0-500 cm^{-1} region) calculated for the S_1 state of **E-DPYDPE** (top) and **Z-DPYDPE** (bottom) in solution (top), crystal (middle) and aggregate (bottom). The vibrational modes corresponding to large HR value in solution are given and the modes presenting similarities in the crystal or in the aggregate are represented.

frequencies and compared them with the ones obtained in solution. For **E-DPYDPE** in solution, the mode with the largest HR factor (44 cm^{-1} mode) is ascribed to a scissoring motion and can be directly compared to the 87 cm^{-1} in the crystal (see Figure 2.26). However, the other mode presenting a large HR factor (16 cm^{-1} mode) could not be identified in the crystal. Consequently, for **E-DPYDPE**, the fluorescence quantum yield increases from 0.2 % in solution to 10 % in the crystal since over the two scissoring vibrational modes greatly contributing to the nonradiative decay process, one still exists in the crystal and could participate to the energy dissipation. For **Z-DPYDPE**, a comparison with the solution reveals that the mode contributing to the energy dissipation in solution (43 cm^{-1} mode) is no longer present in the crystal. On Figure 2.26, we have represented some modes presenting some similarities but the scissoring motion is limited to the phenyl rings. We thus expect that there is no vibrational mode involved efficiently in the nonradiative decay process and this should explain the strong increase of Φ_F in the crystal (89 %).

2.4.3 Aggregation: stairway to AIE

In the course of the Molecular Dynamics simulation, among the 10 randomly selected snapshots, we have chosen the system with the largest Boltzmann factor to analyze the calculated absorption and emission wavelengths (Table 2.9), analyze the geometry of the GS and ES and the low frequencies vibrational modes. The absorption and emission properties calculated for the other snapshots are given as comparative data in Appendix A-6. We have focused our attention on one embedded molecule as displayed on Figure 2.27).

Ground state: structure and absorption properties

In the course of the MD simulation, the large aggregate represented in Figure 2.27 revealed to be stable and there was no splitting into smaller clusters. The radial distribution function (RDF) between water molecules and **E-DPYDPE** or **Z-DPYDPE** molecules is given in Figure 2.28. The RDF actually corresponds to an average value (considering all the solute molecules within the aggregate) and presents a typical evolution behavior [55, 114]. The analysis of these RDF curves reveals for both isomers two peaks around 5 and 7 Å. A detailed analysis revealed that the peak at 5 nm corresponds to a hydrogen bond between the water molecules and the nitrogen of the pyrrole groups while the peak at 7 nm corresponds to an interaction between water and the phenyl groups. For

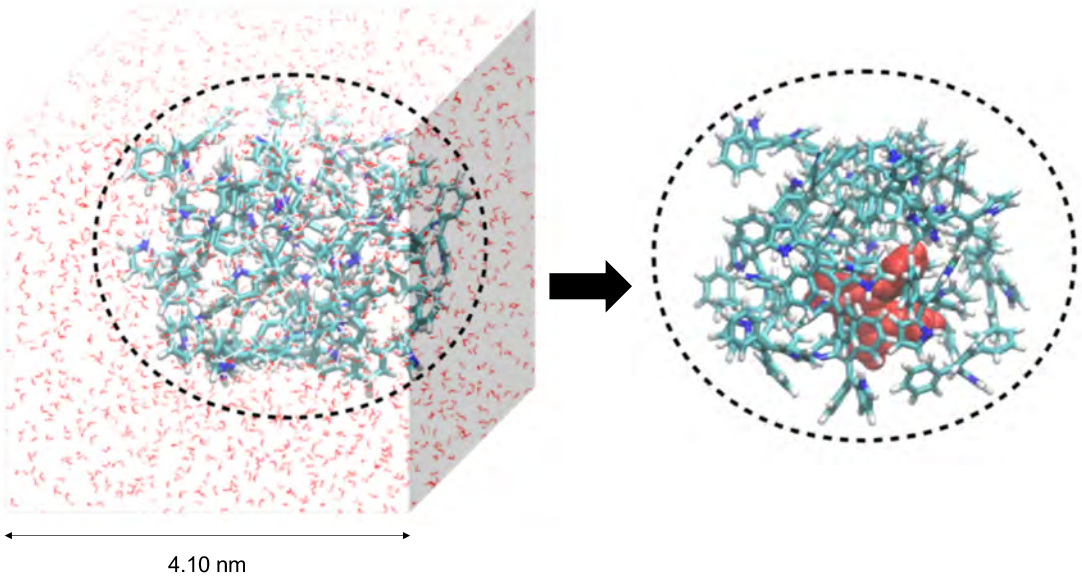

FIGURE 2.27 – QM/QM' model for **DPYDPE** aggregates sampled with MD simulations. Conformation for E-DPYDPE aggregates extracted from MD simulations with a representation of the water box (left) and QM/QM model for each aggregate: The embedded molecule is defined as the QM region (in red), and the other molecules are defined as the QM' region (right).

E-DPYDPE, the first peak shows larger intensity compared to **Z-DPYDPE** since the N-H group of the pyrrole rings are not involved into intramolecular interactions and can more easily form H bonds with water. Figure 2.28 provides the RDF as a function of the mass-center distance between two **E-DPYDPE** or **Z-DPYDPE** molecules. These distributions show large disorders but we can identify three peaks in the 0-10 nm range for the two isomers at circa 5.0, 6.5 and 9.5 Å. The peak intensities are not the same for the two isomers and we can see that for **Z-DPYDPE**, the shortest distance interactions (5 nm) are prominent.

We have then compared the structures of the GS optimized within the aggregate with the ones obtained in solution. Due to the anisotropic constraints imposed by the other **DPYDPE** molecules and by the solvent, strong distortions are observed for both isomers. A superposition of the structures is provided in Appendix A-5. Due to these large structural modifications compared to the solution, we can observe a variation of the maxi-

mum absorption wavelength λ_{max} in Table 2.9. Indeed, for **E-DPYDPE**, the λ_{max} value is red-shifted (-0.62 eV) while for **Z-DPYDPE**, there is a blue shift (+0.40 eV). One can draw the same conclusions for the λ_{max} of the ten different snapshots (Appendix A-6). Table 2.10 also shows that (i) there is no impact of the environment on the λ_{max} value and (ii) there is no variation of the λ_{max} value if we compute the absorption properties of a dimer cluster embedded in the aggregate. Hence, the modification of the absorption spectra is only due to strong structural deformations within the aggregate.

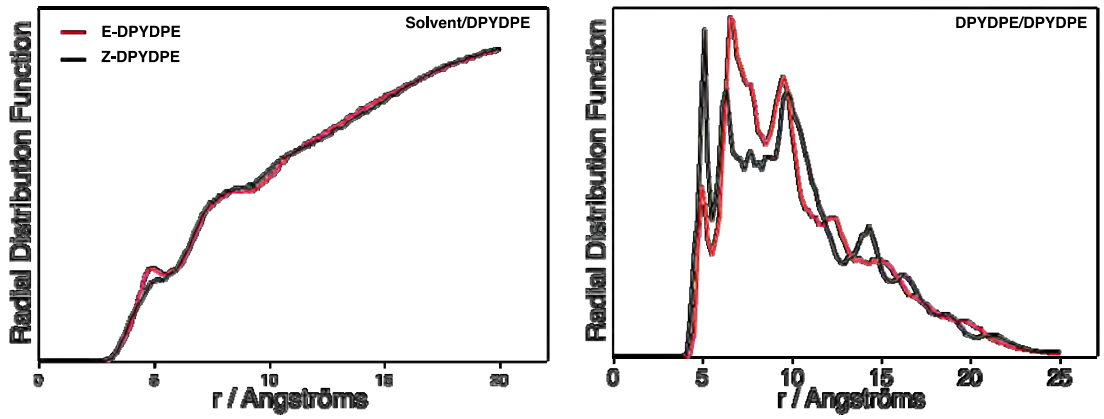

FIGURE 2.28 – Radial distribution functions between water molecules and DPYDPE molecules (left) and radial distribution functions between two DPYDPE molecules (right).

Excited state: structure and emission properties

If we compare the GS and S_1 geometries in the aggregate, the structural modifications obtained in the course of the relaxion process implies mainly the torsion of the phenyl rings for **E-** and the pyrrole groups for **Z-DPYDPE**. The calculated emission wavelengths λ_{em} are given in Table 2.9. A nice agreement is found with a deviation from experimental data of -0.12 eV and 0.28 eV for **E-DPYDPE** and **Z-DPYDPE** respectively.

To understand the AIE effect, we can first compare the oscillator strength value of the emission process arising from the S_1 state in solution and in aggregate. This value is respectively multiplied by 1.3 and 2.3 for **E-DPYDPE** and **Z-DPYDPE** which shows that the environment should enhance the molecular emissive efficiency. Then, we have calculated the vibrational spectrum of S_1 and looked over the molecular vibrational modes that were involved in the nonradiative decay process in solution. In Figures 2.26, we have

represented some modes presenting some similarities with the modes presenting large HR factors in solution. However, these modes do not correspond to scissoring motion. Therefore, for both **E-DPYDPE** and **Z-DPYDPE**, there is no vibrational mode potentially contributing to the energy dissipation and this should explain the strong increase of Φ_F in aggregates.

Why is the value of the fluorescence quantum yield Φ_F larger for **E-DPYDPE** than **Z-DPYDPE** in aggregates? This can be explained by the restriction of the motion of the different rings in the aggregates due to three types of interactions:

- Type (1): Intermolecular interactions with the solvent.
- Type (2): Intermolecular interactions with DPYDPE molecules.
- Type (3): Intramolecular interactions between the pyrrole rings, only observed **Z-DPYDPE**.

For **Z-DPYDPE**, there is a subtle competition between these three effects and the analysis of MD simulations shows that the interactions of types (2) and (3) are predominant. On the opposite, for **E-DPYDPE**, there is no intramolecular hydrogen bonding and Figure 2.28 has shown that the intermolecular interactions with the solvent prevail. The large AIE effect for **E-DPYDPE** might thus arise from stronger interactions with the solvent.

2.5 ACQ and CIE: let's play with substituents of the TTP family.

The study of the **TTP** family (see Figure 2.29) is here presented with the aim to understand whether the ACQ or CIE effect for the derivatives of a molecule. After a benchmark study performed with PBE0, B3LYP and CAM-B3LYP XC functionals as developed in Section 2.2.1, we relied on the LR-PCM-(TD-B3LYP//B3LYP) computational scheme along with the 6-311+G(d,p) basis set. The results of the benchmark is provided in Appendix A-8.

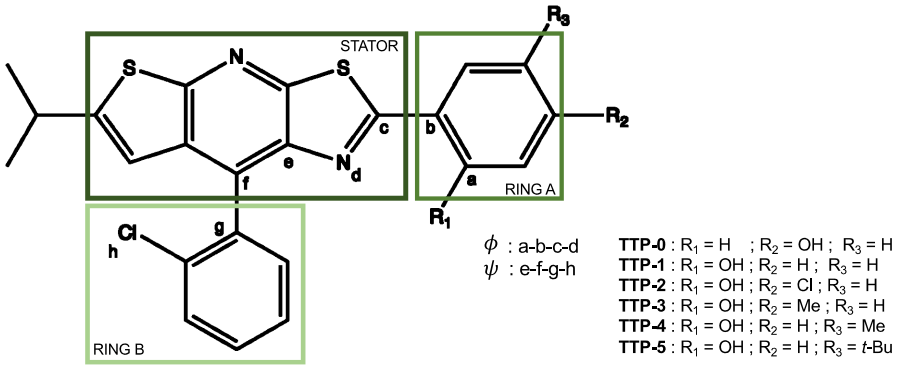

FIGURE 2.29 – Representation of the structures of the **TTP** family. The atom denomination along with the definition of important dihedrals are also provided.

2.5.1 Solution: on the dark side

Structural parameters and absorption properties.

Key structural parameters are given in Table 2.11. For **TTP-0**, the stator and the A-ring are not coplanar: the value of the dihedral angle ϕ between these two rings is 19°. Moving the *para* -OH (R_2 in Figure 2.29) to the *ortho* position of A-ring (R_1 in Figure 2.29) leads to the formation of a strong intramolecular H-bonding between the N_d atom of the stator and the -OH substituent. For instance, the N_d..HO distance for **TTP-1** is 1.761 Å and the value of the N_d-H-O angle is 146°. For the molecules **TTP-1**-**TTP-5**, the introduction of this intramolecular H bond rigidifies the structure. It is more planar (ϕ equal or close to zero) and thus more conjugated. The conjugation can be illustrated via the length of

the C_b-C_c bond between the stator and the A-ring. The length of this bond is decreasing (around -0.1 Å) for **TTP-1** to **TTP-5** compared to **TTP-0**. As a consequence, the value of the maximum absorption wavelength (λ_{max}, given in Table 2.12), which is directly linked to the importance of the electronic conjugation, is impacted. Indeed, there is a bathochromic shift from **TTP-0** ($\lambda_{max} = 349$ nm) to **TTP-1**-**TTP-5** (360 nm $\leq \lambda_{max} \leq$ 368 nm). For all the molecules a good agreement between calculations and experimental data is found with the largest excitation energy difference, $\Delta E_{calc-exp}$, obtained for the molecule **TTP-3** (0.13 eV). The calculated λ_{abs} systematically corresponds to the $S_0 \rightarrow S_1$ transition and can be ascribed to an electronic excitation from the Highest Occupied Molecular Orbital (HOMO) to the Lowest Unoccupied Molecular Orbital (LUMO). Figure 2.30 shows that there is no charge transfer for this electronic transition, the frontier orbitals being mainly located both on the stator and the A-ring.

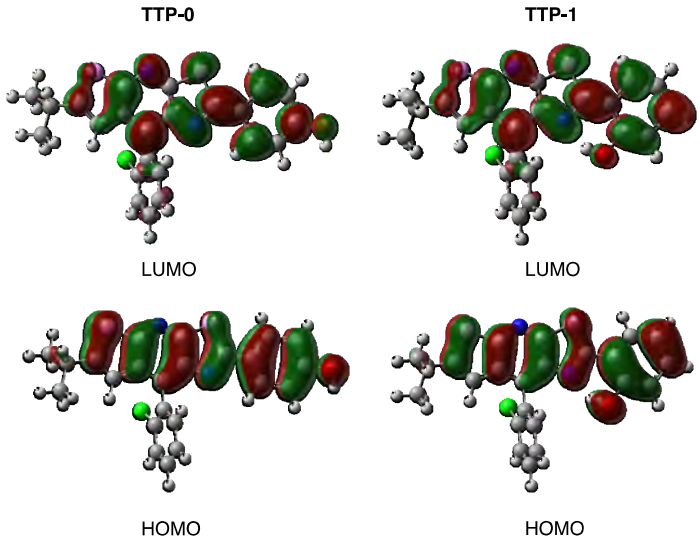

FIGURE 2.30 – Molecular Orbitals (MO) of **TTP-0** and **TTP-1** calculated at the PCM(benzene)-B3LYP level (isodensity = 0.025 au).

Emission properties and description of the Excited State Intramolecular Proton Transfer phenomenon.

Experimentally, except for **TTP-0**, a large Stokes shift is observed with a value of 173 nm, 155 nm, 171 nm, 193 nm and 189 nm for **TTP-1**, **TTP-2**, **TTP-3**, **TTP-4** and **TTP-5** respectively [96, 97]. These Stokes shift are in the range of typical Excited State

TABLE 2.11 – Selected geometrical parameters calculated for the **TTP** family for both S_0 and S_1 optimized geometries in benzene and in the crystalline phase. For **0**, the S_1 geometry corresponds to the enol (E) form and for **TTP-1**-**TTP-5** to the keto (K) form (see Figure 2.31). Distances and angles are in Angstroms and in degrees respectively. The atom numbering and the dihedral angles ϕ and ψ are defined on Figure 2.29. The values reported in parenthesis correspond to the X-Ray structure [96, 97].

Molecule	**TTP-0**	**TTP-1**	**TTP-2**	**TTP-3**	**TTP-4**	**TTP-5**
Solution				**S_0**		
ϕ	-19	0	0	0	0	1
ψ	-117	-101	-77	-103	-103	-81
C_b-C_c	1.466	1.457	1.457	1.454	1.456	1.456
N_d...HO	-	1.761	1.754	1.764	1.766	1.767
	S_1(E)			**S_1(K)**		
ϕ	-8	4	-21	3	2	11
ψ	-125	-121	-65	-121	-121	-59
C_b-C_c	1.465	1.460	1.457	1.459	1.460	1.462
N_d...HO	-	1.810	1.909	1.818	1.790	1.821
Crystal				**S_0**		
ϕ	-17(-19)	6(6)	-2(1)	-4(-5)	-1(-1)	4(4)
ψ	-114(-117)	-115(-116)	-67(-63)	-118(-116)	-112(-112)	-63(-63)
C_b-C_c	1.468(1.465)	1.455(1.452)	1.457(1.460)	1.449(1.451)	1.452(1.453)	1.451(1.458)
N_d...HO	-	1.781(1.951)	1.724(1.892)	1.749(1.898)	1.753(1.874)	1.781(1.900)
	S_1(E)			**S_1(K)**		
ϕ	-11	6	-1	-6	-8	4
ψ	-120	-120	-64	-126	-119	-58
C_b-C_c	1.422	1.451	1.464	1.471	1.476	1.474
N_d...HO	-	1.852	1.880	1.935	1.807	1.943

Intramolecular Proton Transfer (ESIPT) fluorescence [117, 118, 85, 119]. A schematic representation of this phenomenon is provided in Figure 2.31 for the parent molecule **TTP-1**.

TABLE 2.12 – Calculated absorption (λ_{max}) and emission (λ_{em}) wavelengths in nm, oscillator strengths (f) and electronic excitation assignments for **TTP** family in solution and within the crystalline environment. Both experimental λ_{max} and Φ_F are also provided [96, 97].

	Absorption				Emission			
	λ_{max}	f	Assignment	$\lambda_{max,exp}$	λ_{em}	f	Φ_F	$\lambda_{em,exp}$
				Solution				
TTP-0	349	0.983	HOMO → LUMO	360	411	0.984	10	387
TTP-1	360	0.740	HOMO → LUMO	373	525	0.321	2	545
TTP-2	361	0.919	HOMO → LUMO	375	533	0.331	12	530
TTP-3	361	0.850	HOMO → LUMO	374	534	0.292	4	545
TTP-4	369	0.648	HOMO → LUMO	377	557	0.295	4	570
TTP-5	368	0.681	HOMO → LUMO	376	559	0.295	4	565
				Crystal				
TTP-0	338	0.557	HOMO → LUMO	394	415	0.182	1zz	452
TTP-1	360	0.313	HOMO → LUMO	374	567	0.141	26	550
TTP-2	360	0.625	HOMO → LUMO	393	486	0.303	55	530
TTP-3	361	0.557	HOMO → LUMO	400	601	0.124	60	532
TTP-4	366	0.433	HOMO → LUMO	400	605	0.134	60	550
TTP-5	365	0.481	HOMO → LUMO	402	611	0.152	62	555

The most stable tautomer in the GS is found to be the enol one, the potential energy barrier TS_{E-K} being too high (7.3 kcal mol^{-1}) to reach the keto (K) form. Upon irradiation and excitation of the enol form S_0(E), one reaches the first Franck-Condon excited state S_1^{FC}(E). The relaxation on the first ES leads to the S_1(E) geometry. However, the computed emission wavelength for this structure (λ_{em} = 408 nm) is not in agreement with the experimental value (545 nm) [96]. At the same time, the decrease of the energetic barrier on the ES TS^*_{E-K} (1.5 kcal mol^{-1}) allows the proton transfer and the formation of the corresponding keto form, S_1(K). For this structure, the computed emission wavelength is 525 nm and the energy difference between experimental and computed λ_{em} values becomes negligible (see Table 2.12). One can note that experimentally, in benzene, no dual emission

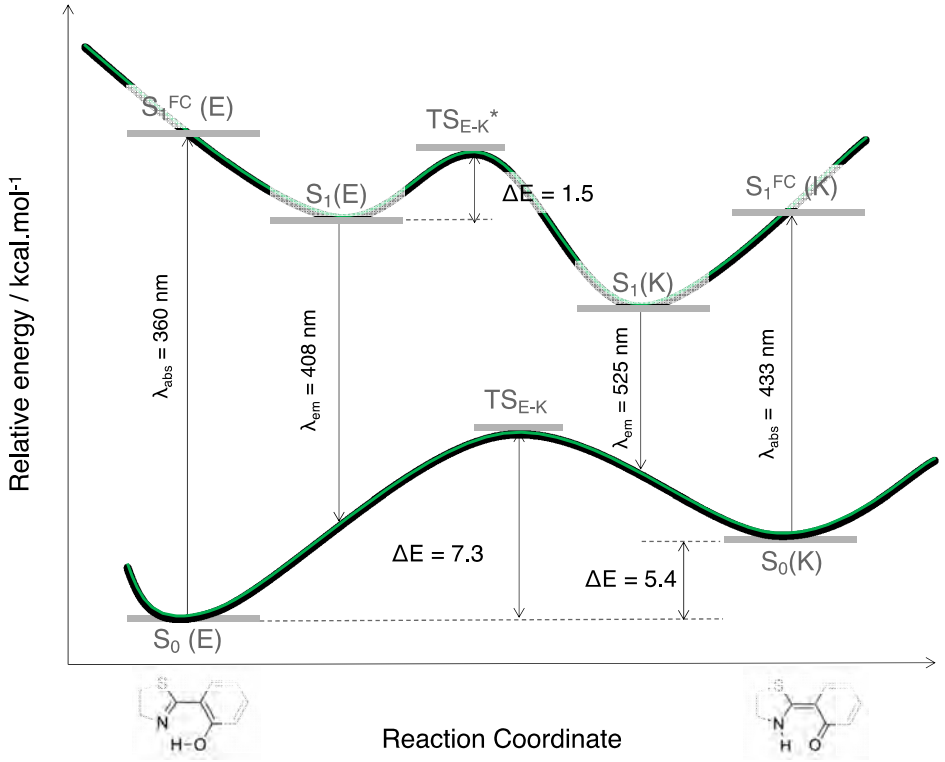

FIGURE 2.31 – Impact of the proton transfer, from an enol to a keto form of **TTP-1**, on the calculated energetics and optical properties (absorption and emission wavelengths in nm).

could be observed and this shows that the ESIPT phenomena is fast and quantitative. The same conclusions hold for compounds **TTP-2**-**TTP-5** and the large experimental Stokes shift observed for these molecules is nicely reproduced by our calculations, as shown in Table 2.12.

For the molecule **TTP-0**, due to the *para* position of the hydroxyle moiety, there is no ESIPT phenomenon. The emission signal arises from a relaxation from the enol form S_1(E), thus leading to a small Stokes shift (exp: 27 nm, calculated: 62 nm). To explain the non-radiative behavior of **TTP-0** in solution, Huang *et al.* proposed (i) the formation of intermolecular hydrogen bonding and (ii) the participation of photo-induced proton transfer [96]. However, the formation of intermolecular hydrogen bonds between the solvent and the solute is unlikely in an aprotic solvent. In the same vein, the concentration of the solution (2.10^{-5} M) should not promote the formation of H bonds between solute molecules. The same conclusions hold for the intermolecular photo-induced proton transfer:

the concentration of the solution as well as the nature of the solvent should not favor this phenomenon. Hence, the existence of non-radiative energy-dissipating paths should not arise from intermolecular interactions, as originally stated in the experimental study, but from intramolecular-scale processes.

In this framework, as previously stated and studied for the two other systems, the non-emissive behavior of AIE/CIE molecules in solution can be explained by different phenomena [55, 116, 115]. In some cases, the weak photoluminescence (PL) efficiency is due to the presence of an energetically accessible conical intersection (CI) leading to an ultrafast internal conversion from the excited state to the ground state. The identification of conical intersections for the considered systems is far from trivial since (i) the molecules are large, (ii) the electronic structure is thus described within the TD-DFT framework and (iii) the environment should be properly described to account for the emission modulation phenomena. At that stage, the partial characterization of the fundamental and first excited potential energy surfaces (minima and transition states as shown in Figure 2.31 for **TTP-1**) has not revealed the existence of S_1/S_0 crossing. The role of photophysical energy dissipation caused by vibrational motions was then investigated to rationalize the weak emission signal in solution. To this purpose, the HR factors were computed and used as an indicator of the contribution of vibrational modes in the non-radiative relaxation pathways. Indeed, we remind here that the non-radiative decay rate is influenced by the internal conversion (IC) rate which directly relies on these factors [55]. Calculated HR factors are represented on Figure 2.32 for **TTP-0** and **TTP-1** and also in Appendix A-9 for the four others molecules.

For all the compounds, one vibrational mode is of major importance and is always associated to one of the lowest frequencies (ω=20 cm^{-1} for **TTP-0** and 21 cm^{-1} for **TTP-1**). A large HR factor is found for this mode, HR = 5 and 12 for **TTP-0** and **TTP-1** respectively (the complete list of HR factors and corresponding reorganization energies is given in Appendix A-9. One can notice that for all the structures, this mode corresponds to the same motion (see Figure 2.33 for a schematic representation of this vibration mode).

One can notice that **TTP-0** is more emissive than **TTP-1**, with PL efficiency of 10% and 2% respectively. For **TTP-1**, the intramolecular hydrogen bond was originally

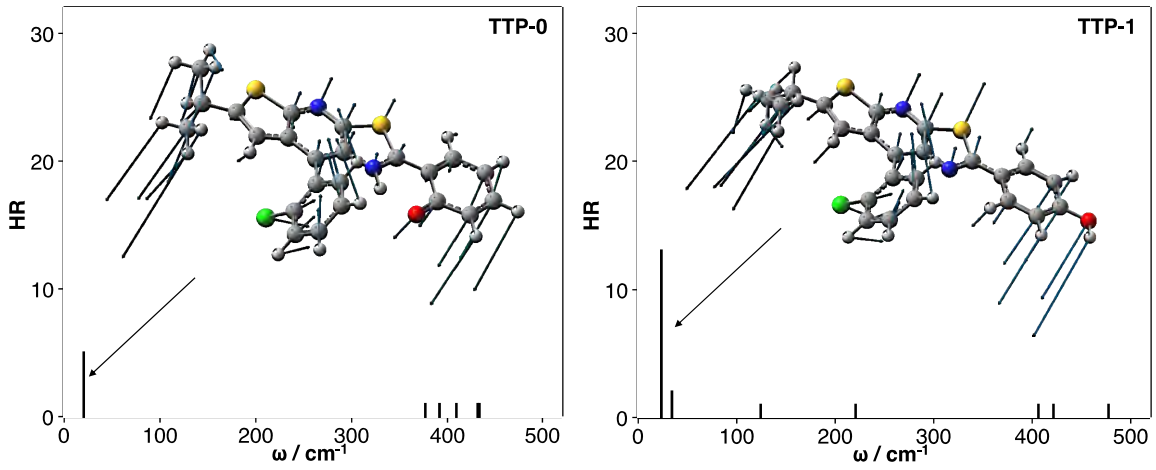

FIGURE 2.32 – Calculated HR factors versus the normal-mode wave numbers (ω) in the S_1 state for **TTP-0** (left) and **TTP-1** (right). Vibration modes yielding the largest HR factors are also represented.

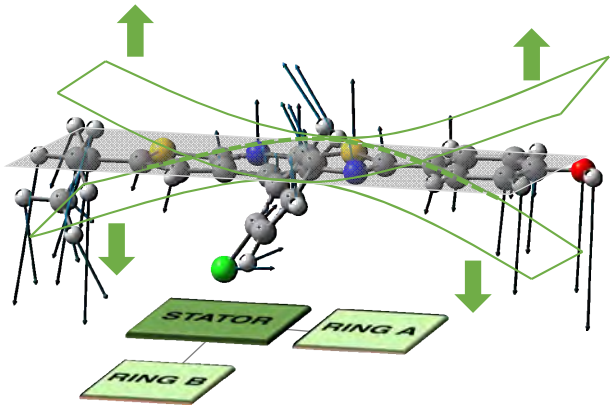

FIGURE 2.33 – Schematic representation of the vibrational mode corresponding to the large HR value (ω=20 cm^{-1}, HR = 5 for molecule **TTP-0**).

introduced to rigidify the molecular structure, activate the Restriction of Intramolecular Motion (RIM) and enhance PL efficiency. The counter-intuitive behaviour observed for **TTP-1** can be rationalized by the identification of the vibrational mode contributing to the energy dissipation: this mode implies a bending of the conjugated core (stator and A-ring) above and under the molecular plane (Figure 2.33). For the molecule 1, the "stator-

ring A" moiety becomes more conjugated. The rigidification of the structure thus induces an enhancement of the HR factor and an increase of the reorganization energy (105 cm^{-1} for **TTP-0** and 275 cm^{-1} for **TTP-1**). As a matter of fact, the intramolecular H-bond induces less structural reorganization while relaxing on the S_1 potential energy surface and this should enhance the value of the HR value according to Eq. 2.7. The same conclusion holds for the molecules **TTP-3**, **TTP-4** and **TTP-5**. They exhibit a relatively small fluorescence quantum yield which is due to the participation of the same low-frequency vibration mode (Figure A-7), with a high HR factor (HR = 12, 12 and 23 for **TTP-3**, **TTP-4** and **TTP-5** respectively), to the IC and thus the non-radiative desexcitation processes. We can also deduce that for alkyl susbtituents, neither the substitution position (4-Me for **TTP-3** and 5-Me for **TTP-4**), nor the bulkiness of the group (5-Me for **TTP-4** and 5-*t*-Bu for **TTP-5**) influence the emission properties. For the compound **TTP-2** with a 4-Cl substituent, there is not only one low-frequency vibration mode with a high HR factor but two (HR= 7 and 6 for ω=20 cm^{-1} and ω=30 cm^{-1}). One can notice that these frequencies correspond to the same nearly degenerate vibrational mode. One frequency mainly implies the stator (ω=20 cm^{-1}) while for the second one (ω=30 cm^{-1}), the A-ring is mainly involved (Figure A-7). This different behavior and the decrease of the HR values compared to molecules **TTP-3-TTP-5** might be rationalized by the twist of the A-ring with respect to the stator for the S_1(K) structure of **TTP-2**. Therefore, one can observe a slight modulation of PL efficiency between **TTP-2** (Φ_F = 12%) and **TTP-3**, **TTP-4** and **TTP-5** (Φ_F = 4% for the three molecules).

2.5.2 Crystal: and there was light !

Investigation of the ACQ observed for molecule TTP-0

In their experimental study, Huang *et al.* have justified the decrease of the PL efficiency of **TTP-0** in the crystalline phase by the energy dissipation through intramolecular rotations (3 rotors) and the intermolecular π-π interactions [96]. We thus propose to investigate these hypotheses by computing the energy transfer couplings between the molecules in the crystal, and characterizing the possible contribution of other non-radiative decay routes. The experimental crystalline structure is given in Figure 2.34. The molecular packing is characterized by a π-π stacking leading to the identification of a possible trimer as depicted

on Figure 2.35.

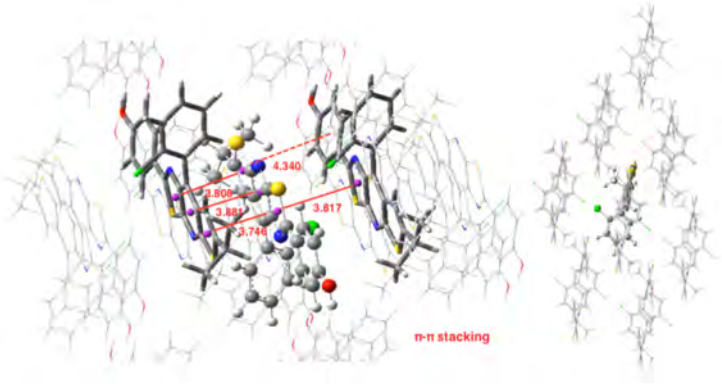

FIGURE 2.34 – Left: Representation of the packing of system **TTP-0**. Distances (in Angstroms) between the two (three) monomers that are involved in the dimer (trimer) are also indicated. Right: Representation of the cluster of 26 molecules used in the QM/QM' calculations.

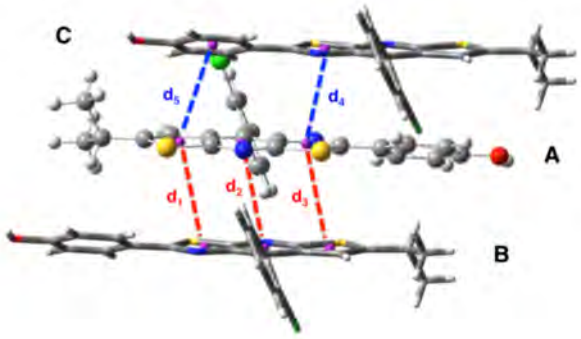

FIGURE 2.35 – Crystal structure of compound **TTP-0** with the three monomers A, B and C represented. The intermolecular distances d_1 to d_5 are defined.

On the one hand, for the monomers **A** and **B**, the two stators are superimposed and present a head-to-tail arrangement. On the other hand, for the monomers **A** and **C**, also arranged in an antiparallel configuration, there is an intermolecular π-π interaction between one ring of each stator (distance d_4 in Figure 2.35). Starting from a cluster of 26 molecules (see Figure 2.36 for a representation of the complete system), we have considered three different ONIOM models that vary in the definition of the QM region:

(i) **0-M**: the central monomer **A**

(ii) **0-D**: the dimer chromophore **A**-**B**

(iii) **0-T**: the trimer chromophore **C**-**A**-**B**.

In the course of the geometry optimizations, we have optimized the positions of respectively one, two and three molecules for the **TTP-0-M**, **TTP-0-D** and **TTP-0-T** models, the positions of the other molecules (respectively 25, 24 and 23 molecules) being frozen.

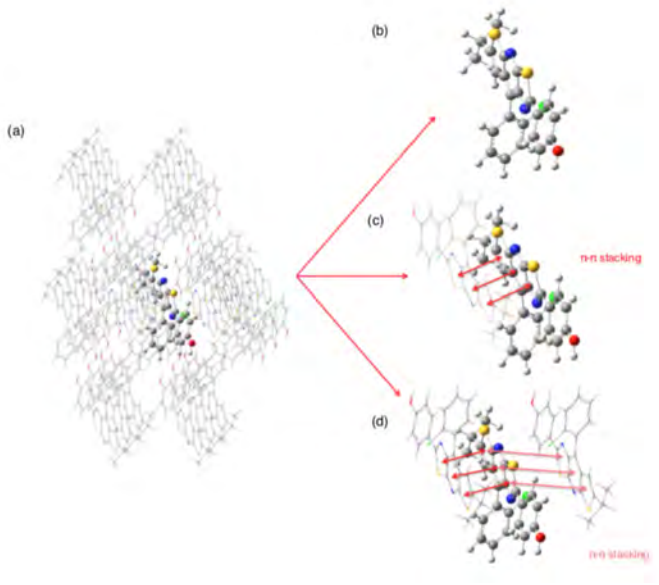

FIGURE 2.36 – Representation of the QM/QM' model based on the crystalline packing (example of molecule **TTP-0**). Different high-level regions, namely (b) a monomer, (c) a dimer or (d) a trimer can be considered.

In Table 2.13, selected optimized geometrical parameters obtained with the three models are compared to experiments. For the intramolecular structural parameters, namely the two dihedral angles and the C_b-C_c bond distance, one can conclude that (i) the three different models provide the same results and (ii) there is no major difference between the experimental and calculated values. The same conclusions hold for the intermolecular π-π interactions that are described by the distances between two ring centers (d_1 to d_5 in Figure 2.35). The small intermolecular distances d_1 to d_3 ($\sim$ 3.75 Å) show that the two monomers **A** and **B** are close enough to allow the emergence of short range interactions [120]. The interaction between **A** and **C** are weaker with only one π-stacking distance (d_4) shorter than 4 Å. We can also note that our computational strategy, that does not include dispersion corrections, provides intermolecular distances in agreement with experiments. The crystal packing is thus controlled by steric effects rather than dispersion. To explore

TABLE 2.13 – Selected geometrical parameters calculated for **TTP-0** in the ground state in the crystalline environment. The three ONIOM models **TTP-0-M**, **TTP-0-D** and **TTP-0-T** are compared with experiments [96]. The intramolecular (intermolecular) parameters are given on Figure 2.29 (Figure 2.35). For **TTP-0-D** (**TTP-0-T**), the two (three) different values given for ϕ, ψ and the distance C_b-C_c correspond to the two molecules A and B (three molecules A, B and C). Distances are in Angstroms and dihedral angles in degrees.

	X-Ray	**TTP-0-M**	**TTP-0-D**	**TTP-0-T**
ϕ	-19	-17	-18, -18	-18, -18, -19
ψ	-117	-114	-116, -115	-114, -115, -114
C_b-C_c	1.465	1.468	1.467, 1.467	1.466, 1.467, 1.466
d_1	3.784	3.782	3.779	3.781
d_2	3.768	3.766	3.762	3.691
d_3	3.690	3.778	3.606	3.667
d_4	3.766	4.022	3.695	3.703
d_5	4.424	4.256	4.091	4.054

the possible excitonic coupling, we have computed the absorption spectra for the three different models (Table 2.14 for **TTP-0** and **TTP-1** and in Appendix A-10 for the four other molecules).

For the monomer **0-M**, compared to the isolated molecule in solution (Tables 2.12), the maximum absorption band is also ascribed to a HOMO→LUMO electronic excitation, with the frontier orbitals identical to the solvated monomer ones. The crystal environment shifts this state to the blue (λ_{max}=338 nm) compared to the absorption in solution (λ_{max}=349 nm). Experimentally, a red-shift of the absorption band is observed (λ_{max}=360 and 400 nm in solvated and crystalline phase respectively).

A global broadening of the spectrum ($\lambda_{max} \geq$ 350 nm), red-shifted, is observed when moving from the monomer to the dimer and the trimer due to the presence of numerous low-energetic transitions with low to medium oscillator strength (f) values. Those transitions may arise from excitonic coupling. Further understanding can be achieved by calculating the excitonic couplings between the three chromophores. In Table 2.15, the

TABLE 2.14 – Calculated absorption wavelength (λ_{max} in nm), oscillator strengths (f) and dominant molecular contributions in $S_0 \rightarrow S_n$ transitions for the different ONIOM models considered for the **TTP-0** and **TTP-1** molecules.

System	State	λ_{max}	f	Assignment
TTP-0-M	S_1	344	0.116	HOMO-1→LUMO
	S_2	338	0.557	HOMO→LUMO
TTP-0-D	S_3	351	0.221	HOMO-1→LUMO
	S_7	335	0.586	HOMO-2→LUMO+1
TTP-0-T	S_3	362	0.127	HOMO-1→LUMO
	S_6	349	0.553	HOMO-2→LUMO
	S_1	338	0.508	HOMO-3→LUMO+1
TTP-1-M	S_1	360	0.312	HOMO→LUMO
	S_2	355	0.225	HOMO-1→LUMO
TTP-1-D	S_4	359	0.257	HOMO→LUMO+1
	S_5	351	0.133	HOMO-2→LUMO

largest coupling, on the order of -100 meV, corresponds to the **A-B** interaction and the negative sign shows the existence of J-aggregates at the origin of the bathochromically shifted bands [121]. The $V_{\mathbf{A-C}}$ coupling is also negative and reaches ∼-60 meV. A recent work has demonstrated that excitonic coupling always enhances the non-radiative decay constants, regardless the sign of V [113]. Therefore, for **TTP-0**, in going from the solution to the crystal environment, the complex molecular packing with two different π-stacking arrangements promotes non-radiative relaxation pathway through excitonic couplings and this phenomenon is at the origin of the observed ACQ.

TABLE 2.15 – Coupling values (eV) between two chromophores in trimers (models **0-T** and **2-T**) and dimers (models **1-D**, **3-D**, **4-D** and **5-D**).

Molecule	**TTP-0**	**TTP-1**	**TTP-2**	**TTP-3**	**TTP-4**	**TTP-5**
$V_{\mathbf{A-B}}$	-0.097	-0.024	-0.021	0.015	0.015	0.001
$V_{\mathbf{A-C}}$	-0.057	-	0.017	-	-	-

Contribution of other non-radiative decay routes.

To gain further understanding on the origin of the very low emissive efficiency (λ_{em}=452 nm, Φ_F=1%), the geometry of the S_1(E) excited state has been determined for the **TTP-0-M** model. The structural parameters are given in Table 2.11. The S_1(E) structure is more planar than the GS and the comparison with the solvated monomer shows that the rotation of the B-ring is restricted in the crystal. The comparison of the calculated emission energy, in Table 2.12, with experiments reveals a reasonable blue-shift deviation (-0.25 eV). After calculating the vibrational spectrum of the S_1(E) structure, we have carefully investigated the low-frequency vibrational modes and compared them with the ones obtained in solution. This comparison reveals that the mode contributing to the energy dissipation in solution (20 cm^{-1}) can be retrieved in the crystalline environment. As illustrated on Figure 2.34, despite the intermolecular interactions arising from the π-π stacking, the packing structure for **TTP-0** does not restrict this vibrational motion.
We can thus conclude that the ACQ phenomenon arises from the combination of two processes: the energy loss through excitation energy transfers between the molecules in the crystal, as proposed by Huang *et al* in their experimental work [96, 97], and through vibrational motions (rather than intramolecular rotations).

Investigation of the CIE effect observed for molecules TTP-1-TTP-5

For the molecule **TTP-1**, as shown in Figures 2.37, the molecular packing is characterized by a π-π stacking between two monomers. The two stators are on top of each other and arranged in an antiparallel configuration, with an intermolecular distance of 3.75 Å. The molecular packings of the molecules **TTP-3**-**TTP-5** reveal the existence of the same type of head-to-tail arrangement between two monomers while for the system **TTP-2**, a trimer structure can be identified (Appendix A-11). Globally, for all the molecules, there is no major difference between the experimental and optimized structures (Table 2.11). Our calculation are for example able to provide a quite accurate description of the C_b-C_c bond distance, that accounts for the conjugation between the stator and the A-ring. There is small variation of the H-bonding between the N_d atom of the stator and the hydroxyl group: our calculations systematically provide shorter bonds than the experimental ones, with an average underestimation of 0.15 Å. We have then investigated the absorption

properties of the different systems. For **TTP-1**, we considered both the **1-M** and **1-D** models with respectively the monomer **A** and the dimer **A-B** defining the QM region. In going from a monomer chromophore to a dimer system, the brightest state shifts from S_1 to S_4 as shown in Table 2.14 but there is no modification of the maximum absorption wavelength ($\sim$ 360 nm). This finding is in agreement with the experimental data collected in Table 2.12.

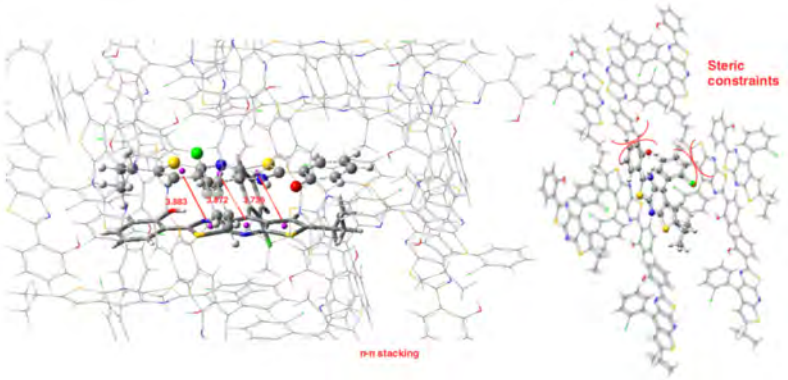

FIGURE 2.37 – Left: Representation of the packing of system **TTP-1**. Distances (in Angstroms) between the two (three) monomers that are involved in the dimer (trimer) are also indicated. Right: Representation of the cluster of 26 molecules used in the QM/QM' calculations.

To investigate the possible impact of the excitonic coupling on the non-radiative decay constant we calculated the J coupling. We found that the values (Table 2.15) are divided by at least four when compared to the ones calculated for **TTP-0**. Therefore, an impact on the k_{nr} is expected but in a lesser extent than **TTP-0**. For the systems ***i*=TTP-3**...**TTP-5**, the absorption energies calculated for the different model systems (monomers ***i*-M** and dimers ***i*-M**) are given in Table 2.14. The value of the J coupling in Table 2.15 is positive, which might indicate the formation of H-aggregate. More importantly, these values are close to zero. As a consequence, the non-radiative decay constant should not be impacted by the intermolecular interactions for these systems. For the system **TTP-2**, the excited-state properties of the trimer model **2-T** in Table 2.14 combined with the value of the J coupling reveals a more complicated situation with a larger modification of the spectrum compared to the **2-M** model (there is a large decrease of the oscillator strength

value) and two J coupling values, one positive and one negative.

The first excited states were optimized for all the molecules. Calculated emission energies for **TTP-1** to **TTP-5** are reported in Table 2.12. Either a hypso- (0.21 eV for **TTP-2**) or a bathochrome shift (0.07, 0.27, 0.20 and 0.29 for **TTP-1**, **TTP-3**, **TTP-4**, **TTP-5** respectively) with respect to experiments is found. The $\Delta E_{calc-exp}$ values in the crystalline environment are globally larger than the ones obtained in solution. Nevertheless, they remain in the range of values obtained with similar approaches (that is to say a central molecule with a frozen crystalline environment) considering molecular crystals within TDDFT calculations [122, 123]. A carefull investigation of the low-frequency vibrational modes of the S_1(K) structure was performed. For **TTP-1**, we identified one vibrational mode that can be responsible for the non-emissive behavior in solution. In the crystalline environment, this vibrational mode could not be identified. As illustrated on Figure 2.37, the particular packing of **TTP-1** leads to strong restrictions of molecular motions previously allowed in solution. Therefore, for **TTP-1**, there are two opposing phenomena:
- The small but non negligible value of the exciton coupling J that should enhance the non-radiative decay rate.
- The hindrance in the molecular plane bending motions that should lead to a decrease of the same non-radiative decay rate through reducing the IC rate.
This competition is in favor of the second effect thus leading to an enhancement of the PL efficiency: experimentally, Φ_F increases from 2% to 26% and **TTP-1** presents a moderate CIE effect. This conclusion is in agreement with a recent study that has demonstrated that for CIE luminogens, the excitoning coupling effect has not a major effect on the non-radiative decay rate [55]. It can enhance this rate by about 12-33% but does not modify the order of magnitudes of this constant. Finally, one should note that these two competitive effects both arise from the molecular packing of **TTP-1** in the crystalline phase. Contrary to the hypotheses of Huang *et al* [97], the intramolecular H-bonding is not directly responsible for the increase of the PL efficiency.
In the same vein, we have calculated the vibrational spectrum of S_1(K) for **TTP-2**-**TTP-5** and inspected the low-frequency vibrational modes. Due to the crystal packing, the vibrational mode potentially contributing to the energy dissipation in solution is no longer

present in the crystal phase. Since the excitonic coupling effects are negligible for these systems, this finding can rationalize the observed emission modulation and should explain the strong increase of Φ_F.

2.6 Conclusion

For the three cases that have been studied, namely **FOEB**, the two isomers of **DPYDPE** and the **TTP** family, a tailored computational scheme has been set up by relying on (TD-)DFT, QM/QM' and MD to study structural and optical (absorption and emission) properties in various environments (solvated, crystalline and aggregated phases).
The first step systematically consisted in the investigation of the optical properties in solution. The aim was either to propose an explanation of the modulation of emission when changing the polarity of the solvent (**FOEB**) or when considering different isomers (**E-DPYDPE** and **Z-DPYDPE**) or derivatives (**TTP** family). We have shown that for the three systems under investigation, the strong to moderate fluorescence quenching observed in solution was due to the photophysical energy dissipation caused by low-frequency vibrational modes, illustrated through the calculation of HR factors. Other features were investigated. For example for **DPYDPE** isomers, because of strong structural reorganization along the relaxation path on the S_1 PES, we looked for the existence of a possible conical intersection but no S_0/S_1 PES crossing was found. We did not faced RACI during our studies. We also proposed an explanation for the modulation of Φ_F for a series of molecules. For example for the **TTP** family, the rigidification of the structures by adding an intramolecular H-bond increases the fluorescence quenching (**TTP-1** and **TTP-3** to **TTP-5**) which is illustrated by larger HR factor values. Therefore, rigidifying the arch-bridge-like type stator with other rotors via weak bond (H-bonding for example) should be considered as a risky strategy since it can induce energy dissipation through vibrational motion of the newly rigidified stator. The calculated HR factors provide useful qualitative information that has allowed us to always find a correlation between the calculated total reorganization energy and the experimental Φ_F.
Then, the second step consisted in the study of more condensed phases namely the crystalline (for all the molecules) and/or the aggregated phase when necessary (**FOEB** and **DPYDPE** only). We had to face to different effect like ACQ (**FOEB** and **TTP-0**), AIE (**E-DPYDPE**) or CIE (**FOEB**, **Z-DPYDPE** or **TTP** derivatives). We showed that the ACQ phenomenon founds its origin in the combination of two processes contributing to the non-radiative decay:

- The energy loss through excitonic couplings that is due to the particular π-π stacking arrangement.
- The energy dissipation during the internal conversion process through the low-frequency vibration mode identified in solution. Indeed, the particular packing of both **FOEB** and **TTP-0** molecules does not restrict those vibrations.

On the other hand, AIE and CIE behavior were explained by the fact that the aggregate and/or the crystalline phase block the vibrational mode involved in the quenching of the emission process in solution thus opening the radiative decay channels. Nevertheless, a subtle competition has been highlighted for some molecules. For the molecule **TTP-1**, the non-radiative relaxation pathway through excitonic coupling is also possible and the competition between these two antagonist effects (RIV and excitonic coupling) finally leads to a moderate CIE effect. An other example of subtle effects occuring in the aggregate has been demonstrated for the **DPYDPE** molecule. For both isomers, all the non-radiative decay channels are blocked so the quantum efficiency rises compared to the isolated molecules in solution. There is though a difference between the two isomers which is due to a competition between intermolecular interactions with the solvent, with other **DPYDPE** molecules and intramolecular interactions between the pyrrole rings.

Therefore, combining adequate theoretical strategies enables a careful investigation of the different photophysical processes at the origin of the ACQ, AIE and CIE effects and a qualitative understanding of the experimental observations. The development of new AIEgens and their use in high-tech innovative devices can thus take advantage of state-of-the-art theoretical investigation studies. The appropriate modeling of the environmental effects is crucial to pave the way towards the development of novel CIE functional materials. In this thesis we have particularly been interested in the description of the environment and this has avoided, because of the currently available models, a further exploration of more quantitatives descriptions involving for example the calculation of k_{nr} or the calculations of HR factors within the ONIOM model. However, those qualitatives approaches always allowed us to rationalize the relative behaviors of molecules belonging to the same family. Those studies permitted to publish three articles [124, 125, 126].

CHAPTER 3

To be colorful or not to be ?

3.1 Introduction: Photochromism

3.1.1 Definition

Photochromism is a reversible transformation between two isomers, A and B, of the same chemical species. As represented on Figure 3.2, one can go from A (the thermodynamically stable form) to B by absorbing light. A and B can be differentiated by their structural and electronic properties and this can lead to different absorption spectra.

One can notice that the reverse reaction, B→A, is possible. It can be achieved thermally, the phenomenon is thus known as photochromism of type T, or photochemically giving rise to photochromism of type P. In most of the cases, the photochromic process involves only one molecule (unimolecular reaction). Bimolecular reactions are sometimes also encountered, as for the photocycloaddition reaction. When the A form is colorless or pale yellow and the B form is colored (from blue to red), that is to say that $\lambda_{max}(\mathrm{B}) > \lambda_{max}(\mathrm{A})$, the phenomenon is known as *positive* photochromism. On the contrary, when $\lambda_{max}(\mathrm{A}) > \lambda_{max}(\mathrm{B})$, it is a *negative* or *inverse* photochromic phenomenon.

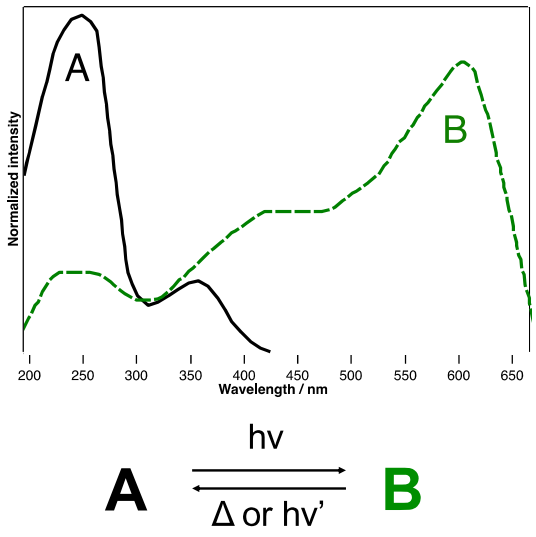

FIGURE 3.1 – Absorption spectra of the A and B isomers of a photochromic compound.

3.1.2 History

The term photochromism comes from the Greek words *phos*, which means light, and *chroma*, color. It was proposed in 1950 by Hirshberg [127]. However, the phenomenon was coined many years before. Indeed, the first reported case of photochromism was reported in 1867 [128]. Fritzsche noticed that an orange-colored solution containing tetracene molecules was losing its color during the day and was recovering it during the night, as illustrated in Figure 3.2.

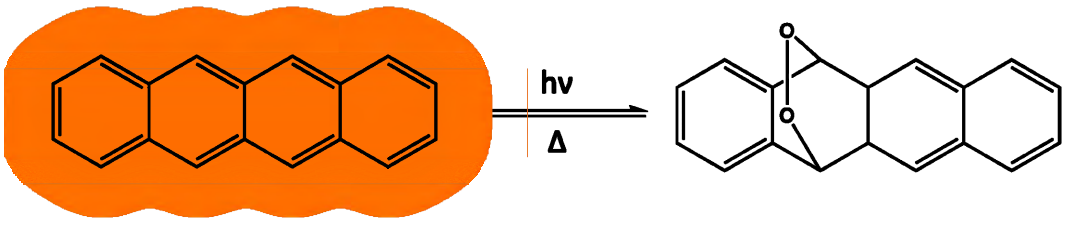

FIGURE 3.2 – Representation of the first reported photochromic molecule [128].

Following this first observation, studies on solutions and materials exhibiting the same behavior were undertaken. One can for example cite the work performed by Wislicenus [129] and Blitz [130, 131, 132] who coined the color change of some organic molecules

(Figure 3.3).

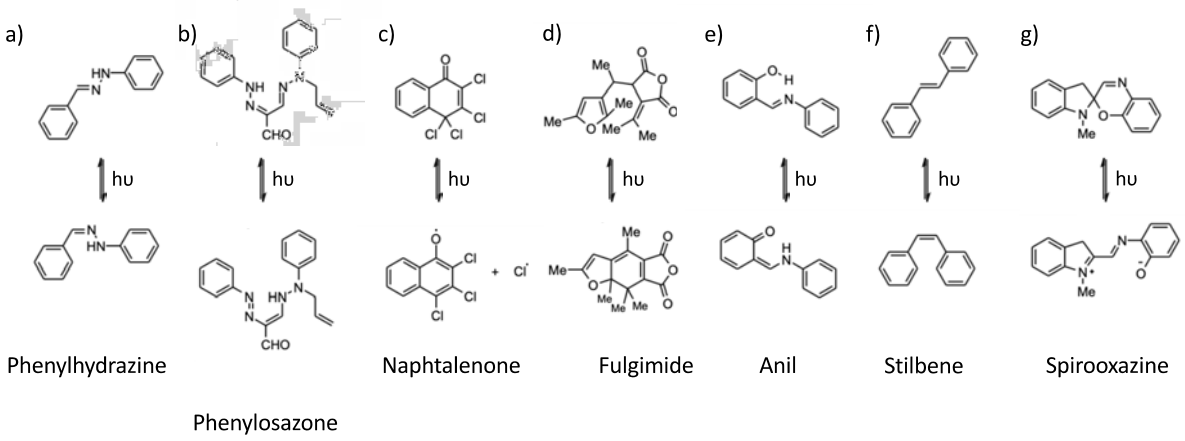

FIGURE 3.3 – Representation of some photochromic molecules families.

In 1899, Markwald discovered the first solid-state photochromic organic compound (Figure 3.3.c) [133]. Other families, studied during this period, were also pointed out such as fulgides [134], anils [135, 136] and stilbenes [137] (Figure 3.3.d-f). Until the 1920s, most of the studies consisted in the description of the observed phenomena rather than in a deep comprehension of the mechanisms. It is only during the 1930s, when the interest in photochromism was not at its highest level, that Harris and Gheorghiu undertook mechanistic studies [138, 139]. In the 1960s with the development of physical methods (NMR, X-ray, UV-Vis, IR and time-resolved spectroscopies) and the organic synthesis capabilities, the photochromism gained more attention. However the poor photoresistance (that is to say the photochemical reaction A $\rightleftarrows$ B is becoming less efficient or can totally disappear due to photodegradation issues) of the molecules was one major drawback for further development involving photochromic molecules. It is in the 1980s, with the work on spirooxazines [140, 141] (Figure 3.3.g), that molecules with high fatigue resistance were considered leading to a breakthrough for practical applications involving photochromism mechanism. Glasses using photochromism of type T as working mechanism were developed [142]. The A$\rightarrow$B reaction being controlled by the UV/Visible light irradiation while the reverse reaction is thermally induced. At the same time, regarding the photochromism of type P, molecules were developed for data storage applications and molecular switches [143, 144].

3.1.3 Photochromic molecule: DTE derivatives

Among the wide variety of photochromic molecules, we have been particularly interested in the dithienylethene (DTE) family. Indeed, DTE derivatives have shown a good fatigue resistance, a high sensitivity and a thermal irreversibility. For all this reasons, they are considered as good candidates for practical applications such as optical devices and date storage/recording [145, 146, 147]. We have represented on Figure 3.4 the photochromic behavior of a DTE derivative with two different isomers, the most stable isomer being the open form (OF) and the photoinduced form being the closed form (CF).

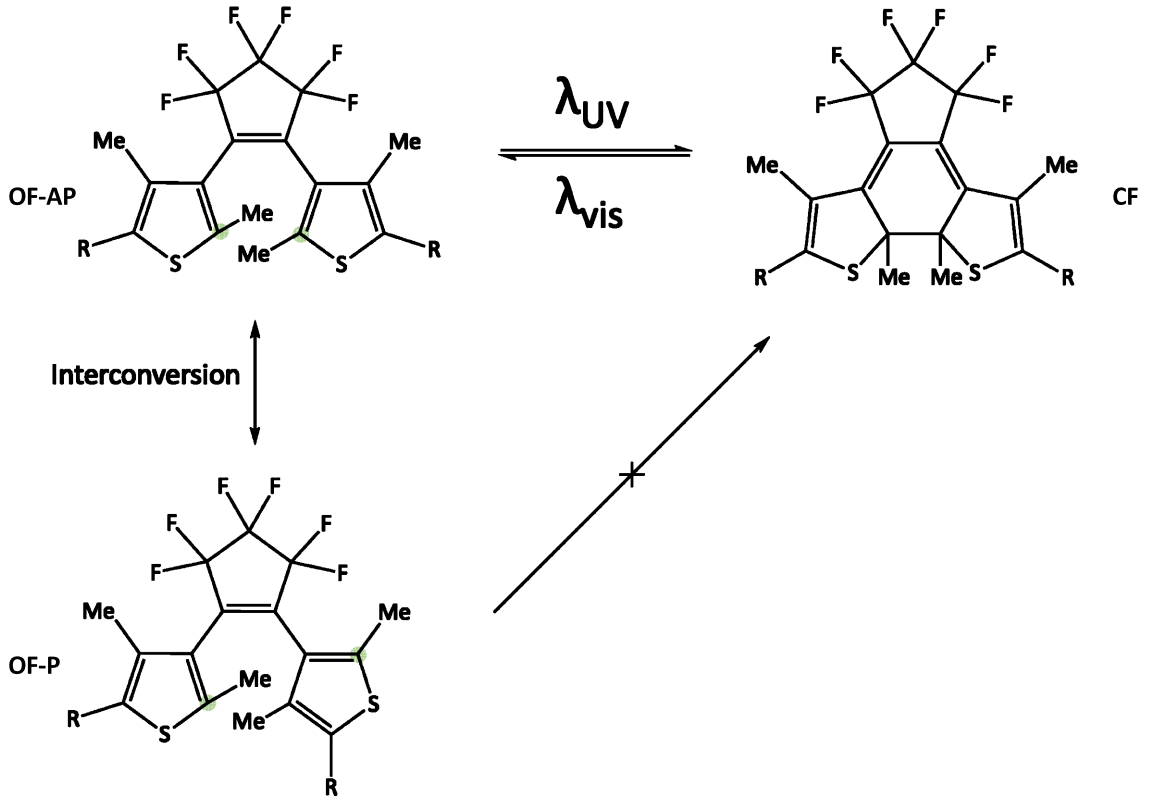

FIGURE 3.4 – Representation of the structures of a DTE derivative The three forms are represented, namely the closed form (**CF**) and the two open forms, the anti-parallel (**OF-AP**) and the parallel (**OF-P**) ones. The reactive carbons, indicating an anti-parallel or parallel form, are highlighted with green dots.

One can notice that a second open form can be found. The difference between the two open forms arises from the orientation of the reactive carbons (see Figure 3.4), they can

be oriented in the same direction (giving rise to the parallel form, **OF-P**) or in opposite directions (giving rise to the anti-parallel form, **OF-AP**). Nevertheless, **OF-P** is not photoactive, the photochemical reaction being only possible between **OF-AP** and **CF**. The transformation between **CF** and **OF** is achieved *via* the light absorption, UV light for **OF-AP**→**CF** and visible light trigger the **CF**→**OF-AP** reaction. The photochemical reaction between **OF-AP** and **CF** is thermally irreversible.
If one wants to use DTE as molecular switch for data storage and recording as previously mentioned, one needs to be able to easily differenciate the different forms, to consider them as "on/off" states. For the DTE molecules, it appears that the two absorption spectra are different. Indeed, **OF** absorbs in the UV domain and it is thus colorless, while **CF** is absorbing in the visible domain, leading to a colored **CF** (the color depends on the substituents R, represented on Figure 3.4).

3.1.4 Lucky dip! DTE-Upy

The system that has been considered throughout this study (Figure 3.5) has been synthesized by Pr. M. Takeshita [148, 149] from the University of Saga in Japan. This DTE derivative is functionalized by ureidopyrimidinone (Upy) moieties at its extremities. The **Upy** groups are used and known for their capability to form quadruple hydrogen-bonding blocks allowing supramolecular assemblies [150, 151] as illustrated on Figure 3.5.c). Lateral alkyl chains ($C_{11}H_{23}$) have been added for solubility purposes [149].

The photochromic behavior of the **DTE-Upy** molecules is the same as the one described in Section 3.1.3, that is to say that the **OF-AP** form (the most stable one) can be isomerized into **CF** upon UV light irradiation (the cycloreversion reaction is activated by visible light) [152, 153] and is in thermal equilibrium with the non-photoactive **OF-P** form [154, 155, 156].

Experimental features

Due to the presence of the **Upy** functionalization, some inter and intramolecular interactions are possible. One can thus imagine the formation of small oligomers or supramolecular assemblies involving the **Upy** groups.

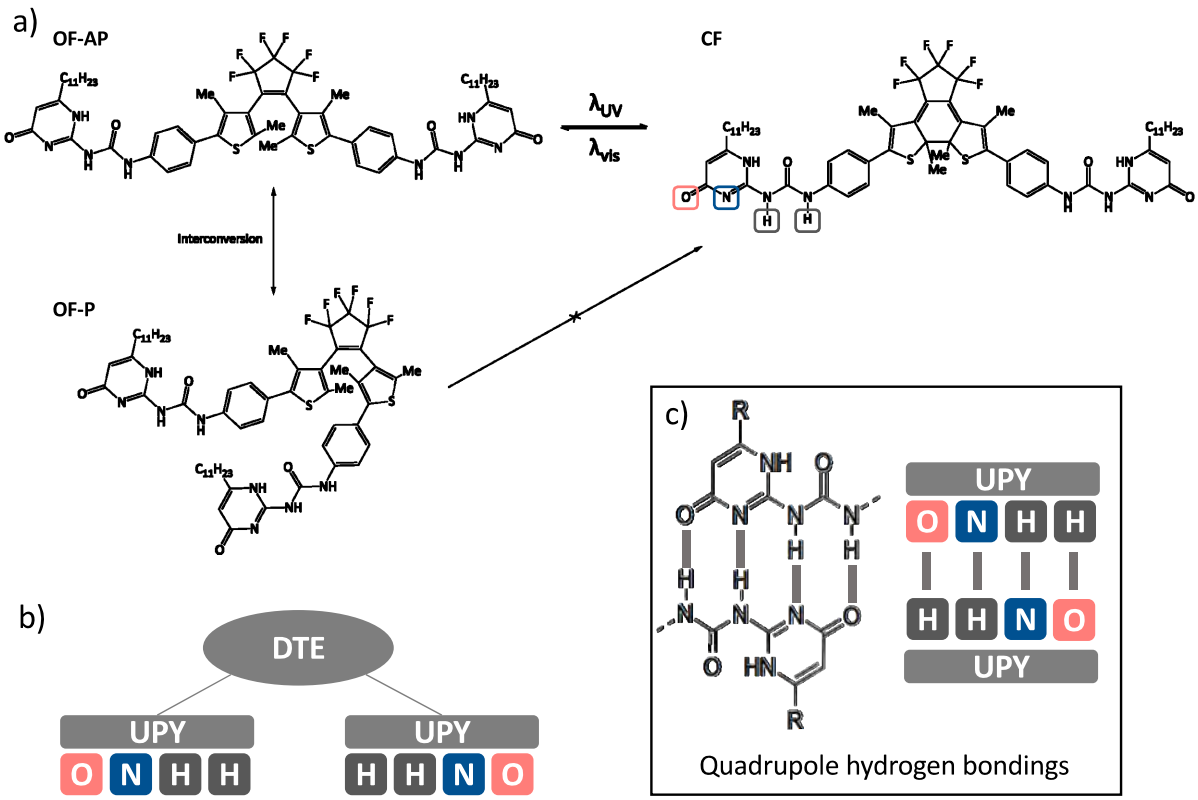

FIGURE 3.5 – a) Photochromic reaction for **DTE-Upy** between **OF-AP** and **CF** isomer (the **OF-P** is not photoactive). b) Schematic representation of the **DTE-Upy** molecule. c) Schematic representation of the hydrogen-bonding patterns betweeen two **Upy** groups.

In chloroform, for the **OF**, only small particles less than 10 nm were detected by dynamic light scattering (DLS), showing that there is no formation of large supramolecular assemblies for these isomers. Besides, from ^{1}H NMR study of the **OF** isomers in $CDCl_3$, Takeshita *et al* have assumed that the protons of the **Upy** moieties are involved in intramolecular hydrogen bonding [148]. UV irradiation of the **OF** solution (100 μM in $CHCl_3$) resulted in an increase of the original particle size which reaches 650 nm after three hours, thus indicating the slow formation of supramolecular assemblies from the photogenerated **CF** isomer. For initial concentations over 200 μM, the aggregation process is so efficient that a strong blue precipitate is observed. Subsequent visible light irradiation decreased the particle size (down to 400 nm) and some additional heating is necessary to disassemble the aggregates into the original small particles ($\approx$10 nm).

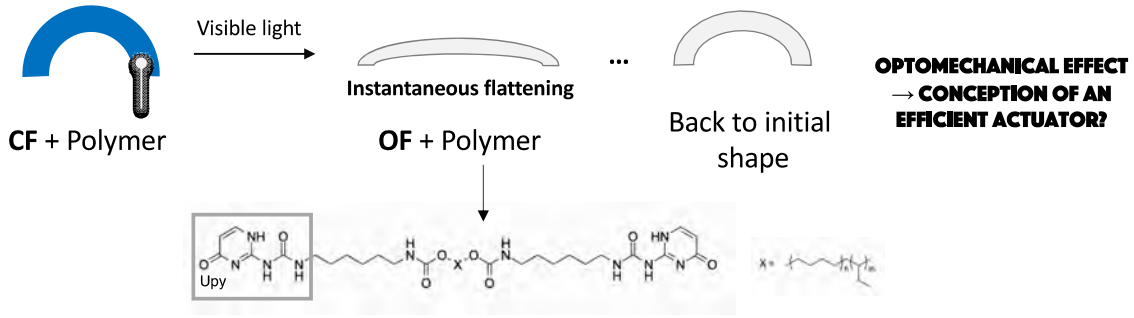

FIGURE 3.6 – Schematic representation of the behavior of **DTE-Upy** molecules in a polymer thin film.

Moreover, the photochromic molecules have been studied within a polymer matrix (the structure of the polymer is provided in Figure 3.6). Before any irradiation, films made from the **CF** form are curved and colored in blue. Under irradiation in the visible, a pre-stage instantaneous flattening of the film is observed followed by a slow return to a curved shape as the photochromic transformation propagates in the thickness of the thin film (see Figure 3.6 for a schematic representation of the phenomenon). This macroscopic optomechanical effect is attributed to a molecular-scale phenomenon, i.e the photochromic reaction (Takeshita *et al*, to be published).

Previous study

Recently, the excited state dynamics of **DTE-Upy** has been investigated with the help of NMR experiments, ultrafast spectroscopy and preliminary density functional theory (DFT) calculations [157]. The structures of the three isomers, **OF-AP**, **OF-P** and **CF**, have been determined with the help of DFT geometry optimizations. To do so, two identical **DTE-Upy** molecules were connected to each other by one quadruple hydrogen-bonding block (see Figure 3.7 for a schematic representation of a dimer involving four hydrogen bonds, **DIM-4H**).

The following structures were obtained, a linear **DIM-4H** conformation for **OF-AP** (and **CF**) and a cyclic conformation, **DIM-8H**, with two Upy-Upy assemblies for **OF-P**. This cyclic conformation can avoid the formation of larger assemblies for the **OF** isomer.

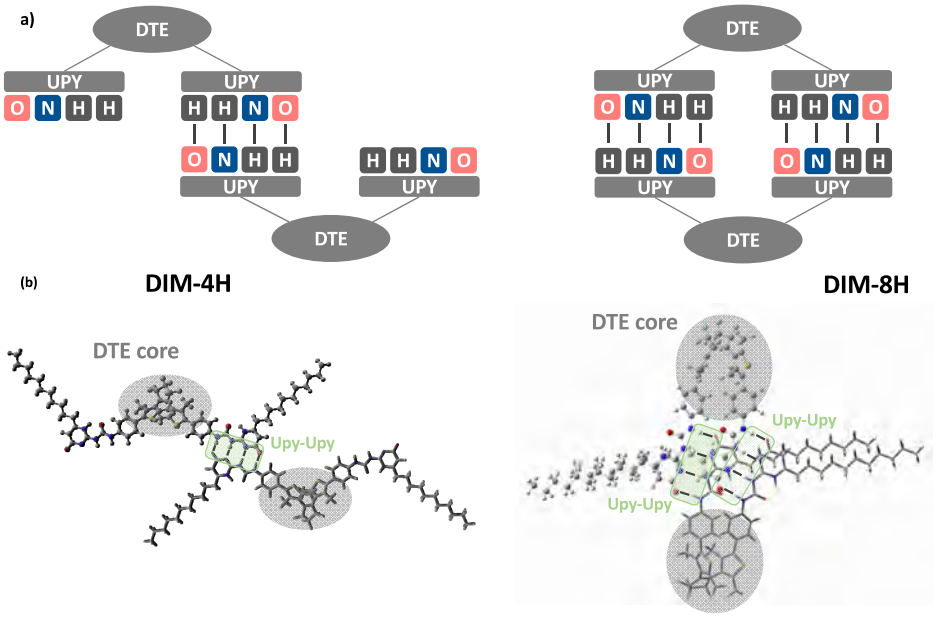

FIGURE 3.7 – Schematic representation of the **DTE-Upy** dimer with two possible arrangements: linear (DIM-4H) and cyclic (DIM-8H). (b) **OF-AP** and **OF-P** dimer structures optimized at the ωB97X-D/6-31G(d) calculation level in $CHCl_3$ [157].

Since no dynamical effects were taken into account with DFT calculations, further studies have to be considered to confirm the formation and the stability of this cyclic dimer. Since no studies have been initiated for a **DTE-Upy** molecule embedded in a polymer matrix, all the protocols and the tools have to be developed before to consider the study of the optomechanical effect.

3.2 DTE-Upy in solution

In this first part, we aim at filling the lack of investigation including dynamical effetcs by studying (i) the stability of the dimers and larger oligomers (hexamers and π-stacked dimers) in solution at room temperature and (ii) the impact of the **DTE-Upy** flexibility on both the photochromic properties and the formation of the supramolecular assemblies. Our purpose is to justify the formation of the supramolecular assembly only for the **CF** isomers. The general strategy and the different steps of this chapter are illustrated on Figure 3.8.

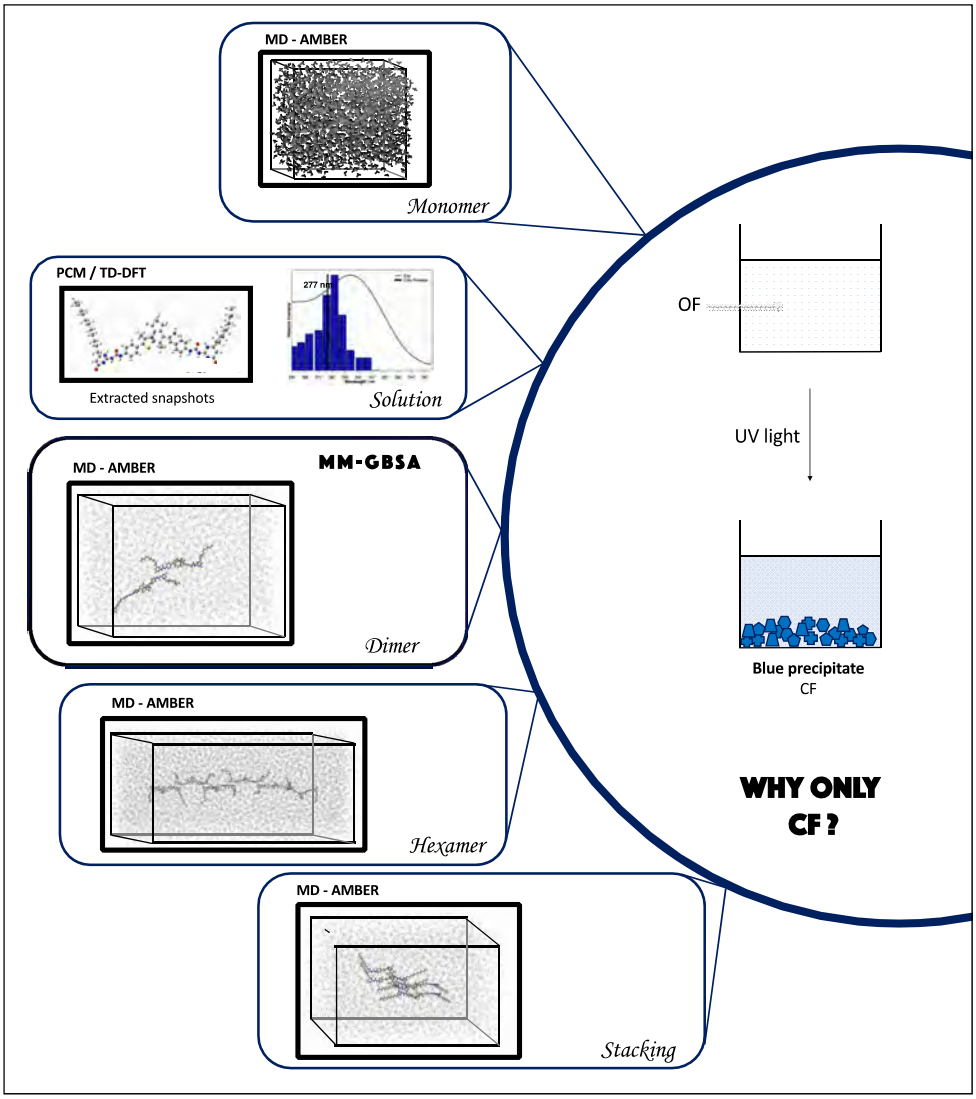

FIGURE 3.8 – Schematic representation of the strategy of the study of **DTE-Upy** molecules in solution.

3.2.1 Computational details

3.2.1.1 Molecular Dynamics

Molecular Dynamics (MD) simulations are run with the generalized AMBER force field (GAFF) [29] as implemented in the AMBER16 package [105]. For each isomer, the atomic charges were derived following the parametrization procedure in the generalized AMBER force field, that is to say using HF/6-31G(d) RESP charges. Throughout our study, we have considered monomers, dimers, stacked dimers and hexamers in our simulation box containing, on average, 1800, 2400, 6500 and 30000 solvent molecules (chloroform). For π-stacked dimers and hexamers, only the **OF-AP** and **CF** conformers have been considered.

To describe the electrostatic interactions, periodic boundary conditions are imposed, a cut-off of 8 Å is considered and the Particle Mesh Ewald (PME) method is used [108, 109]. For each simulation, the system was heated from 0 to 300 K in 100 ps in the NVT ensemble. NVT was followed by an equilibration step of 100 ps in the isothermal-isobaric NPT ensemble and a subsequent production run was performed within the same NPT ensemble during 10 ns for the monomers and dimers, and 50 ns for the tetramers and the hexamers, with a time step of 1 fs. The reference pressure (1 Bar) and temperature (300 K) are incorporated with the Berendsen method [110]. The binding energy is computed with the help of the Molecular Mechanics/Generalized Born Surface Area (MM/GBSA) method [158]. For dimers, this approach is based on the difference between the free energies of the dimer and each isolated monomer in solution. At that stage, we have considered 1000 conformations.

Validation of GAFF parameters

Hereafter is explained the procedure we have followed to validate the use of GAFF for the study of **DTE-Upy** molecules. We compared the structures of the three forms obtained after:

- A minimization process in vacuum with GAFF with AMBER16 (without PBC).
- An optimization process at a QM level (ωB97X-D/6-31G(d)) in vacuum.

In Table 3.1 we have gathered some important structural parameters (defined on Figure

3.9) used for the comparison.

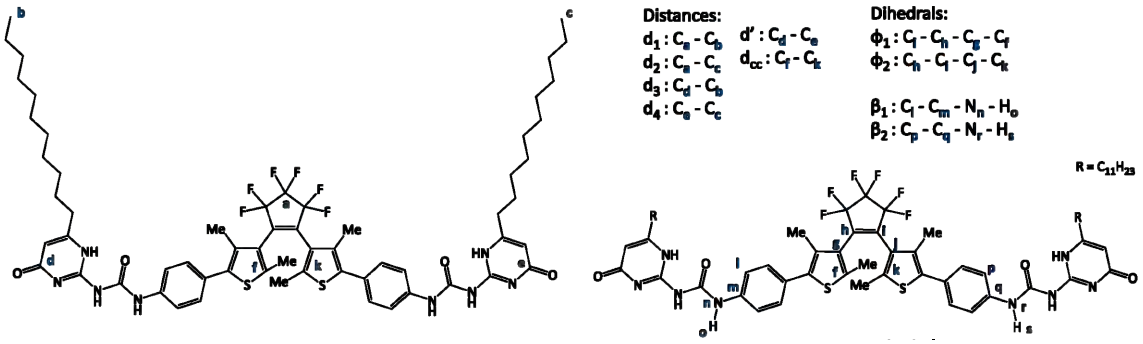

FIGURE 3.9 – Definition of the key structural parameters.

TABLE 3.1 – Selected geometrical parameters calculated for the isomers **CF**, **OF-AP** and **OF-P** calculated in vacuum with the ωB97X-D/6-31G(d) level with G16 and with the GAFF force field with AMBER16. The distances are in Angstroms, the dihedral angles are in degrees. The structural parameters are defined on Figure 3.9.

	CF		**OF-AP**		**OF-P**	
	ωB97X-D	GAFF	ωB97X-D	GAFF	ωB97X-D	GAFF
Bonds						
d_{cc}	1.54	1.57	3.71	3.66	3.97	4.11
d_1	18.34	17.24	26.52	25.34	14.38	13.66
d_2	27.43	28.20	22.21	23.26	13.82	14.48
d_3	16.20	16.47	12.63	12.65	16.26	15.75
d_4	15.76	15.57	13.28	13.30	17.24	15.65
d'	27.02	26.79	26.11	27.37	19.58	20.69
Dihedral						
Φ_1	-4	-1	-61	-22	61	22
Φ_2	-12	-13	-60	-58	-115	-126

(1) For the **CF** conformer no major deviations are observed.

(2) For both **OF-AP** and **OF-P** we check the impact of both process on the **DTE** core (responsible of the experimental observed optical properties). To do so, we calculated

the values of the BLA, that is an indicator of the conjugation path of the **DTE** core. We found values equal to 0.087 (0.091) Å and 0.088 (0.092) Å for respectively a QM optimization process and a GAFF minimization for **OF-AP** (**OF-P**). The **DTE** core and more particularly its conjugation is preserved whether using a QM optimization or a GAFF minimization.

(3) If one looks further at the structural parameters, one can observed deviations. For the **OF-AP** conformer, the distance between the two reactive carbons, d_{cc}, is shorter with GAFF minimization than with a QM optimization (3.60 Å *vs* 3.76 Å). Small deviations are also found for the distances d_i (i=1 to 4) that correspond to the distances between the **DTE** core and the extremities of the alkyl chains (i=1,2) and the distances between the **Upy** groups and the extremities of the alkyl chains (i=3,4). Finally for the distance d', the QM optimization leads to a more "compact" structure (d'= 26.11 and 27.37 Å for QM and GAFF optimization respectively). The main difference arises from the two dihedral ϕ_1 and ϕ_2. Indeed, the QM optimization provides a symmetric structure with the same values for both dihedral angles (-60°) while with GAFF, there is a disymmetry (-58°;-22°).

(4) For the **OF-P** conformer, as for the **OF-AP** conformer, small deviations are observed for d_i distances between the two structures. Once again the main differences concern d_{cc} and the two dihedral angles, ϕ_1 and ϕ_2.

As a conclusion we have seen that even if structural differences are observed between the two processes, there is a global negligible impact on the structure as the conjugation path is maintained in both cases. We then confirmed this statement by computing the optical properties (absorption) of the corresponding structures. The results are gathered in Table 3.2).

As expected thanks to the previous conclusion, there is no difference between the optical properties of a structure optimized *via* QM methods or minized with GAFF.

3.2.1.2 QM calculations

All the calculations have been performed using the Gaussian 16 package [36] within the (time-dependent) density functional theory, (TD-)DFT, framework. For some test calculations, we have optimized the structures of the isolated and self-assembled **DTE-Upy** with the ωB97X-D range-separated hybrid functional [101] combined with the 6-31G (d)

TABLE 3.2 – Impact of the geometries on the maximum absorption wavelength (λ_{max}) calculated at the CAM-B3LYP/6-311+G(2d,p) for the isomers **OF-AP**, **OF-P** and **CF**. Two different geometries are considered for each isomer: the one optimised with the GAFF force field with AMBER16 and the one optimized with the ωB97X-D/6-31G(d) level with G16 in vacuum.

	OF-AP		**OF-P**		**CF**	
	ωB97X-D	GAFF	ωB97X-D	GAFF	ωB97X-D	GAFF
λ_{max}	280	282	271	270	515	522

atomic basis set. This computational scheme was used in a previous study to investigate the structural properties of **DTE-Upy** and its parent molecule (the DTE core without **Upy** groups) [156, 157]. Among DFT including dispersion corrections methods, ωB97X-D functional is actually one of the most accurate methodology to describe the geometrical parameters and interaction energy of systems presenting hydrogen-bonding interactions [159].

The optical properties have been systematically determined using vertical TD-DFT calculations with the CAM-B3LYP functional [100] in combination with the 6-311+G(2d,p) basis set. We have previously demonstrated that this computational scheme is able to reproduce accurately the maximum absorption wavelength, λ_{max}, of DTE molecules [156, 157].

We have then tested three different computational schemes to compute the UV-Vis absorption properties:

- Scheme (1) the full **DTE-Upy** molecule(s) are treated at the CAM-B3LYP/6-311+G(2d,p) level (hereafter referred to as the "QM" model).
- Scheme (2) the **DTE-Upy** molecule(s) is (are) described with the ONIOM QM/QM' model: the optical properties of the DTE core functionalized with the **Upy** groups are described with the "QM" approach while the lateral alkyl chains (R = $C_{11}H_{23}$ Figure 3.9) are treated at the QM' level (HF/3-21G). The link atom approach has been used to take into account the boundary between the QM and the QM' regions.
- Scheme (3) the lateral alkyl chains are removed and replaced with methyl groups.

TABLE 3.3 – Impact of the computational scheme on the maximum absorption wavelenght λ_{max} (in nm) and the oscillator strenght (f) calculated for the isomers **OF-AP**, **OF-P** and **CF**: scheme (1) the full **DTE-Upy** molecule(s) are treated at the CAM-B3LYP/6-311+G(2d,p) "QM" level; scheme (2) the **DTE-Upy** molecule is described with the ONIOM QM/QM' model: the optical properties of the DTE core functionalized with the **Upy** groups are described with the "QM" approach while the lateral alkyl chains (R = $C_{11}H_{23}$, Figure 3.9) are treated at the QM' level (HF/3-21G); scheme (3) the lateral alkyl chains are removed and replaced with methyl groups. The PCM($CHCl_3$) approach has been systematically considered.

	Scheme 1		Scheme 2		Scheme 3	
	λ_{max}	f	λ_{max}	f	λ_{max}	f
OF-AP	278	1.709	278	1.623	278	1.640
OF-P	276	0.955	275	1.081	276	0.975
CF	516	0.433	516	0.417	516	0.420

A comparison of these three approaches, presented in Table 3.8, shows that these three methods lead to the same value of the maximum absorption wavelength λ_{max}. We have then decided to use the less computational-demanding approach, namely the scheme (3). For each system under study, we have randomly selected snapshots from MD simulations, removed all the explicit solvent molecules and relied on the Polarizable Continuum Model (IEF-PCM, solvent: chloroform) in the equilibrium limit using the linear-response (LR) PCM scheme to quantify the impact of the environment [160].

3.2.2 Results

3.2.2.1 Monomer

We have selected key structural parameters represented on Figure 3.9. For the DTE core, the d_{cc} distance, corresponding to the distance between the two carbon atoms involved in the photocyclisation reaction, and the two dihedral angles, ϕ_1 and ϕ_2, enable to discriminate the **OF** and **CF** isomers as well as the **OF-AP** and **OF-P** conformers. Starting either from the **OF-AP** or the **OF-P** isomer, the representation of the dihedral angles ϕ_1 and ϕ_2 (defined on Figure 3.9) along the 10 ns trajectory reveals an interconversion between the **OF-AP** and **OF-P** conformers as shown by Figure 3.10.

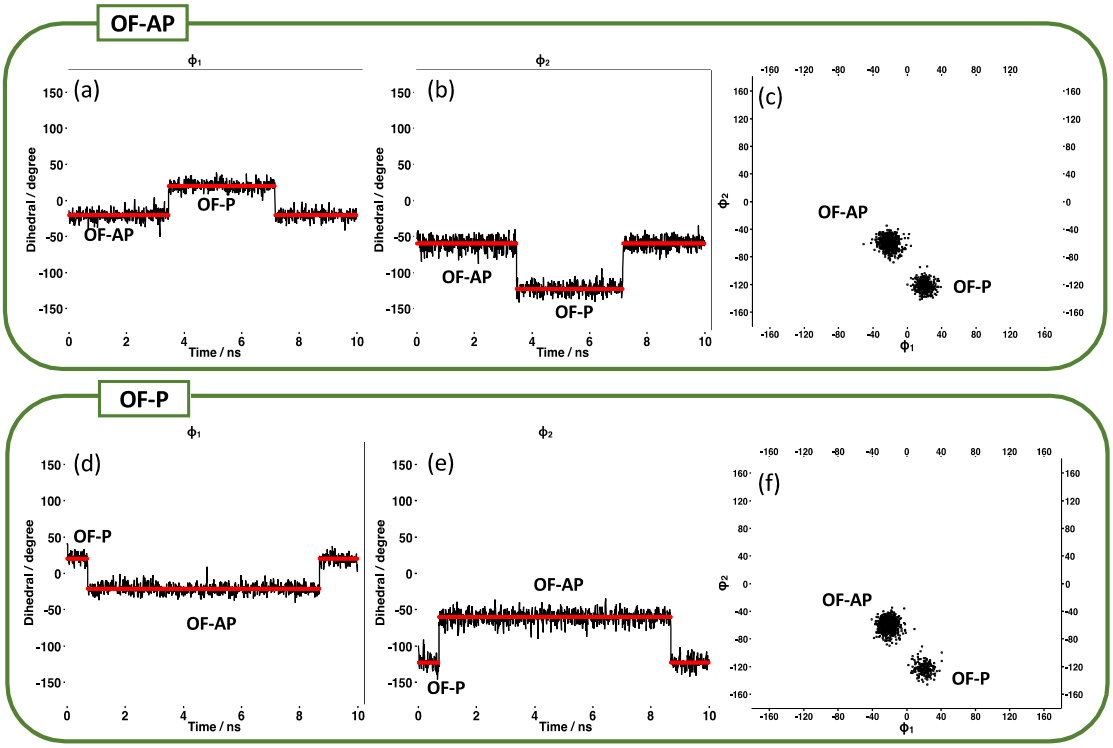

FIGURE 3.10 – Time evolution of the dihedral angles ϕ_1 and ϕ_2 along the 10 ns trajectory for an initial conformation corresponding to **OF-AP** (a and b) and **OF-P** (d and e). Representation of value couples (ϕ_1;ϕ_2) for **OF-AP** (c) and **OF-P** (f).

The average values of the (ϕ_1;ϕ_2) dihedral angles for **OF-AP** and **OF-P** are respectively (-20.0°;-60.0°) and (20°;-120°). Those values are close to the values reported previously

in Table 3.1, that is to say that the same isomers are found. ^{1}H NMR measurements have previously demonstrated the existence of an equilibrium between these two isomers with an **OF-P**:**OF-AP** ratio in favor of **OF-P** (63:37 at ambient temperature in $CDCl_3$). Our MD simulations are thus in qualitative agreement with experimental features. At this point it is necessary to say that our aim is not to provide quantitative analysis of the observed phenomena. This interconversion can also be highlighted by monitoring the evolution of the d_{cc} distance along the MD simulation as shown by Figure 3.11. The average value of d_{cc} is 3.65 Å for **OF-AP** and 4.10 Å for **OF-P**.

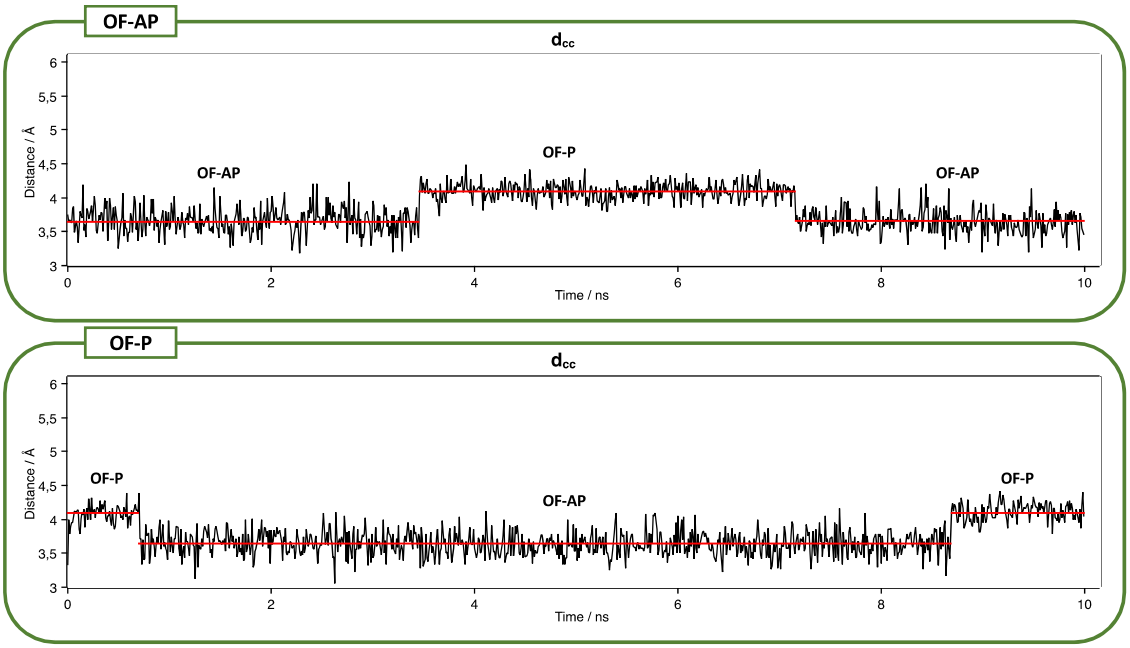

FIGURE 3.11 – Evolution of the d_{cc} bond distance (see Figure 3.9) as a function of the simulation time for the **OF-AP** and **OF-P** conformers.

After photocyclization, for the **CF** isomer, the dihedral angles (ϕ_1;ϕ_2) and the d_{cc} distance (with an average value of 1.57 Å) are much less flexible as illustrated on Figure 3.12.

We have then investigated the flexibility of the **Upy** groups. Indeed, the distance d' (Figure 3.9) characterizes the global expansion of the molecule: for large d' values, the two **Upy** groups are far apart for each other while for smaller d' values, there is a folding

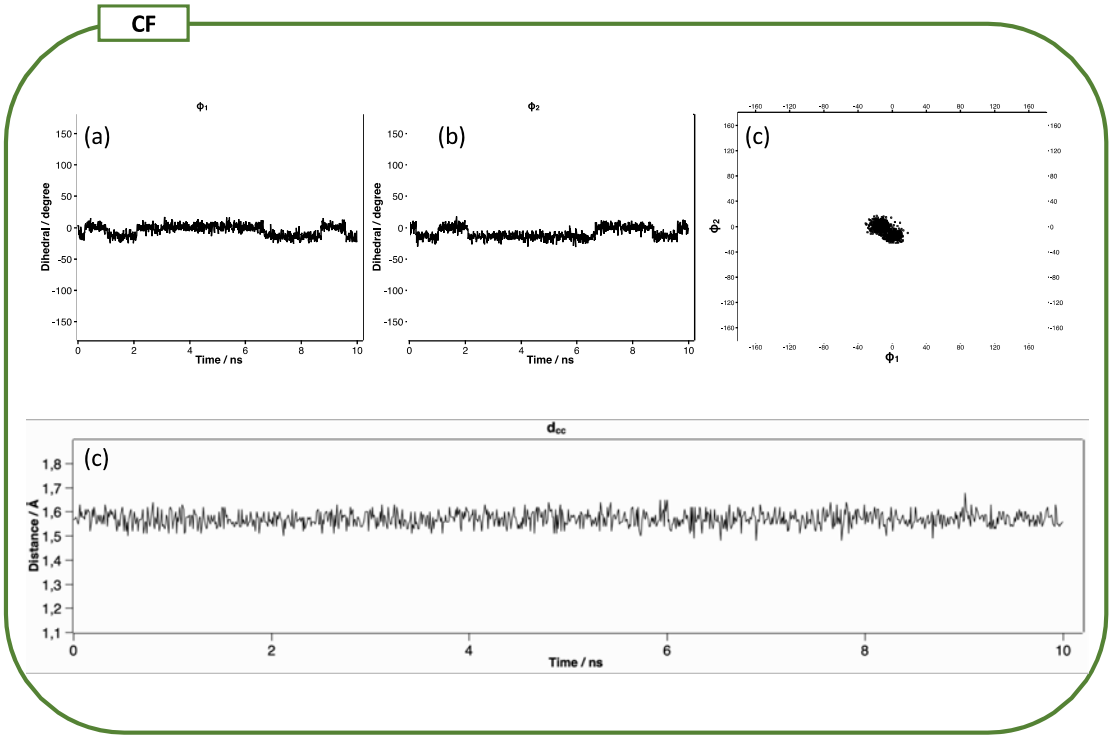

FIGURE 3.12 – Structural data for **CF** conformer. Time evolution of the dihedral angles ϕ_1 (a) and ϕ_2 (b) along the 10 ns trajectory. c) Representation of value couples (ϕ_1;ϕ_2). c) Evolution of the d_{cc} bond distance (see Figure 3.9) as a function of the simulation time.

of the molecule and the two groups get closer. The evolution of d' along the trajectory is given on Figure 3.13 for an initial conformation corresponding either to the **OF-AP**, **OF-P** or **CF** isomer.

For the **OF-AP** isomer, two different conformers can be identified, one presenting a d' value of (27.21 ± 1.11) Å and the other one with d'=(21.13 ± 2.38) Å. These two conformers actually respectively correspond to **OF-AP** and **OF-P**: the distance d' also enables to characterize the **OF-AP**-**OF-P** interconversion. The same conclusion holds for the MD simulation carried out with an **OF-P** initial configuration. For the **CF** isomer, the system is less flexible with d'=(25.79 ± 0.80) Å, there is a rigidification of the structure for this more conjugated isomer.

Furthermore, one should note that for the **OF-P** conformer, which is characterized by the smaller d' value, there is no Upy-Upy intramolecular interactions, the value of d' reaching

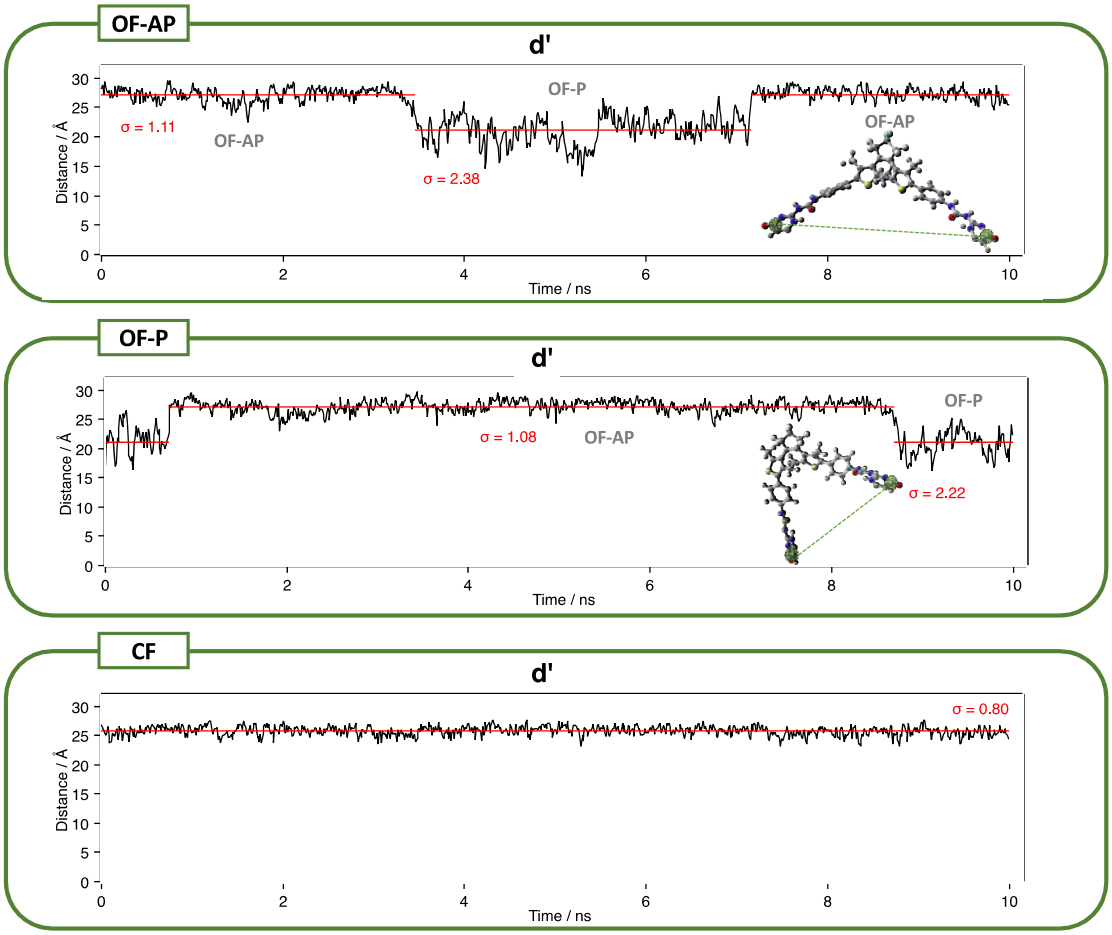

FIGURE 3.13 – Time evolution of the d' distance (in Å) along the 10 ns trajectory for the isomers **OF-AP**, **OF-P** and **CF**. Some representative conformations are provided for the **OF-AP** conformer (for the sake of clarity, the lateral alkyl chains are not represented).

21 Å. We can compare these results with the work of Li *et al* [161]. For another DTE functionalized with two **Upy** units, with the help of ^{1}H NMR and DOSY, they have shown that the two **Upy** groups can dimerize intramolecularly to form a cyclic monomer with the two thienyl rings fixed in a **OF-P** conformation, which prohibits its photocyclization and limits the formation of supramolecular assemblies. For **DTE-Upy**, contrary to the hypothesis of Takeshita and coworkers in their pioneering experimental study [148], there is no intramolecular Upy-Upy interactions.

The orientation of the **Upy** groups is characterized by the β_1 and β_2 dihedral angles defined on Figure 3.9 and some representative conformations are provided on Figure 3.14.

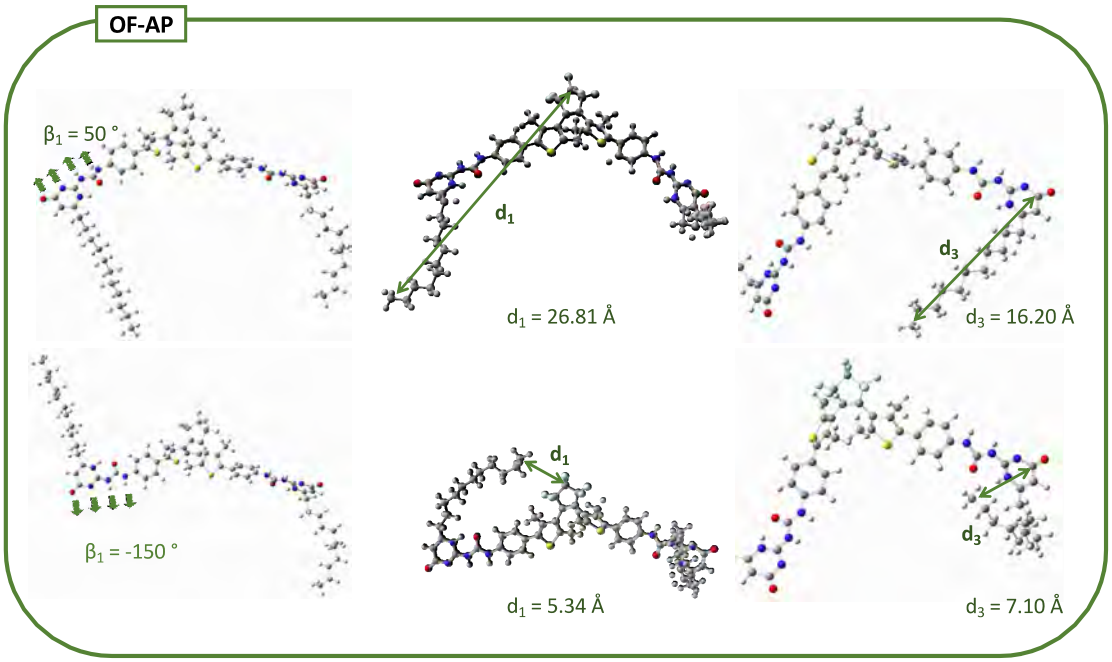

FIGURE 3.14 – Illustration of the flexibility of the lateral chains. Left: **OF-AP** structures with β_1=50° (up) and β_1 =150° (bottom); Middle: **OF-AP** structures with a large d_1 value (up) and a small d_1 value (bottom). Right: **OF-AP** structures with a large d_3 value (up) and a small d_3 value (bottom).

One should note that the β_1 and β_2 present some preferential values: $\sim$ 50° and $\sim$ 150° for **OF-AP** and **OF-P** ($\sim$ -10° and $\sim$ -5° for **CF**).

Finally, the flexibility of the lateral alkyl chain has been studied by monitoring the values of d_1 and d_2 that correspond to the distance between the perfluorocyclopentene ring of the DTE and the alkyl chain extremity, and d_3 and d_4 that characterize the alkyl chain folding. For the three different isomers, the system is highly flexible as shown by the time evolutions of the d_i distance (with i=1 to 4) and the large range of values accessible for each distance (see Figure 3.15). Some representative conformations are given on Figure 3.14.

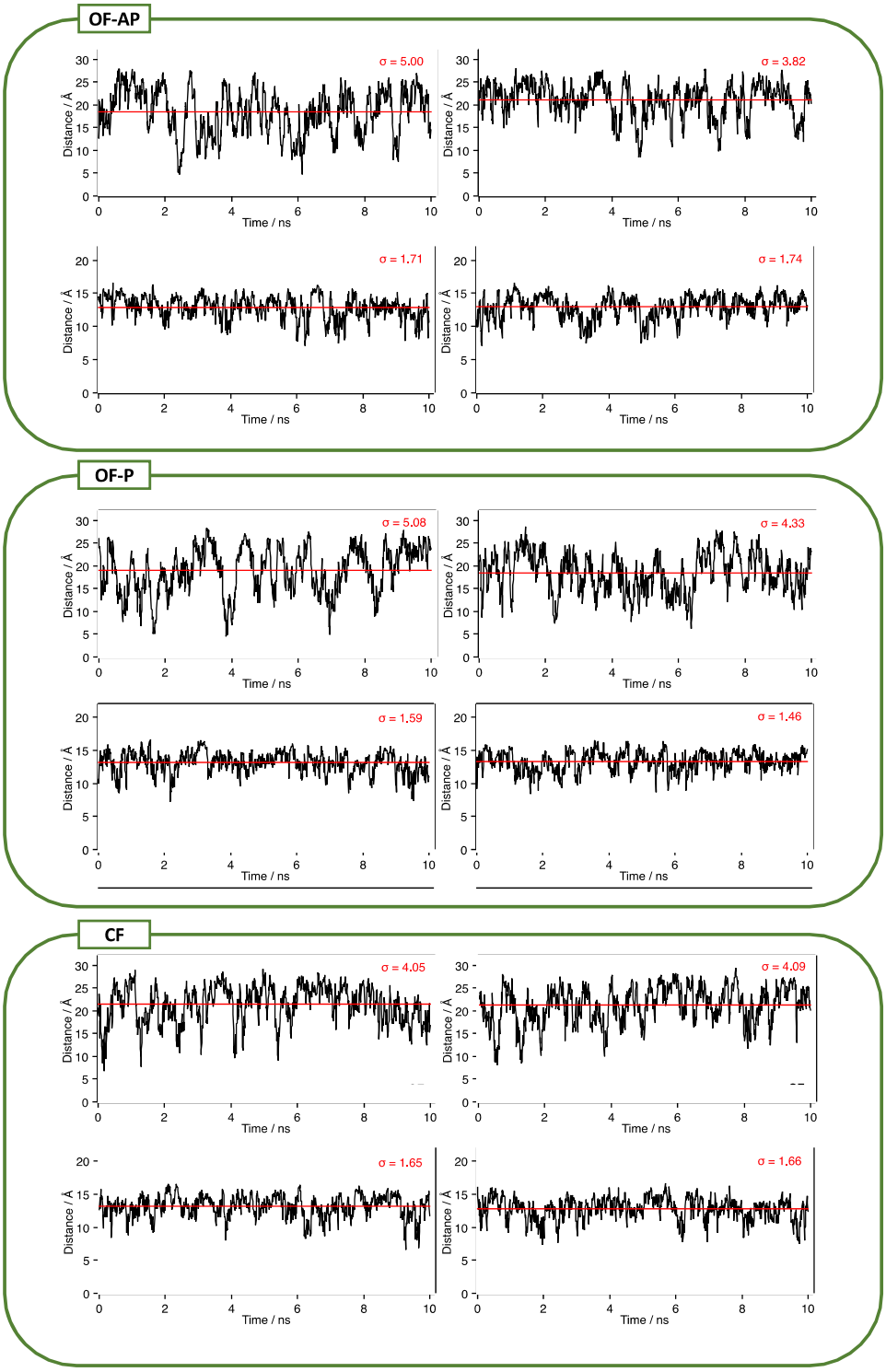

FIGURE 3.15 – Time evolution of the distances d_1, d_2, d_3 and d_4 along the 10 ns trajectory for the **OF-AP** (top), **OF-P** (middle) and **CF** (bottom) isomers. These parameters are defined on Figure 3.9.

The high flexibility of the systems has an incidence on the UV-Vis absorption properties. For each MD trajectory, we have randomly selected 100 snapshots and calculated the excitation energies for each structure following the computational strategy described in the methodology Section 3.2.1.2. Figure 3.16 provides the distribution of the maximum absorption wavelength λ_{max} calculated from the 100 snapshots extracted from the MD trajectory.

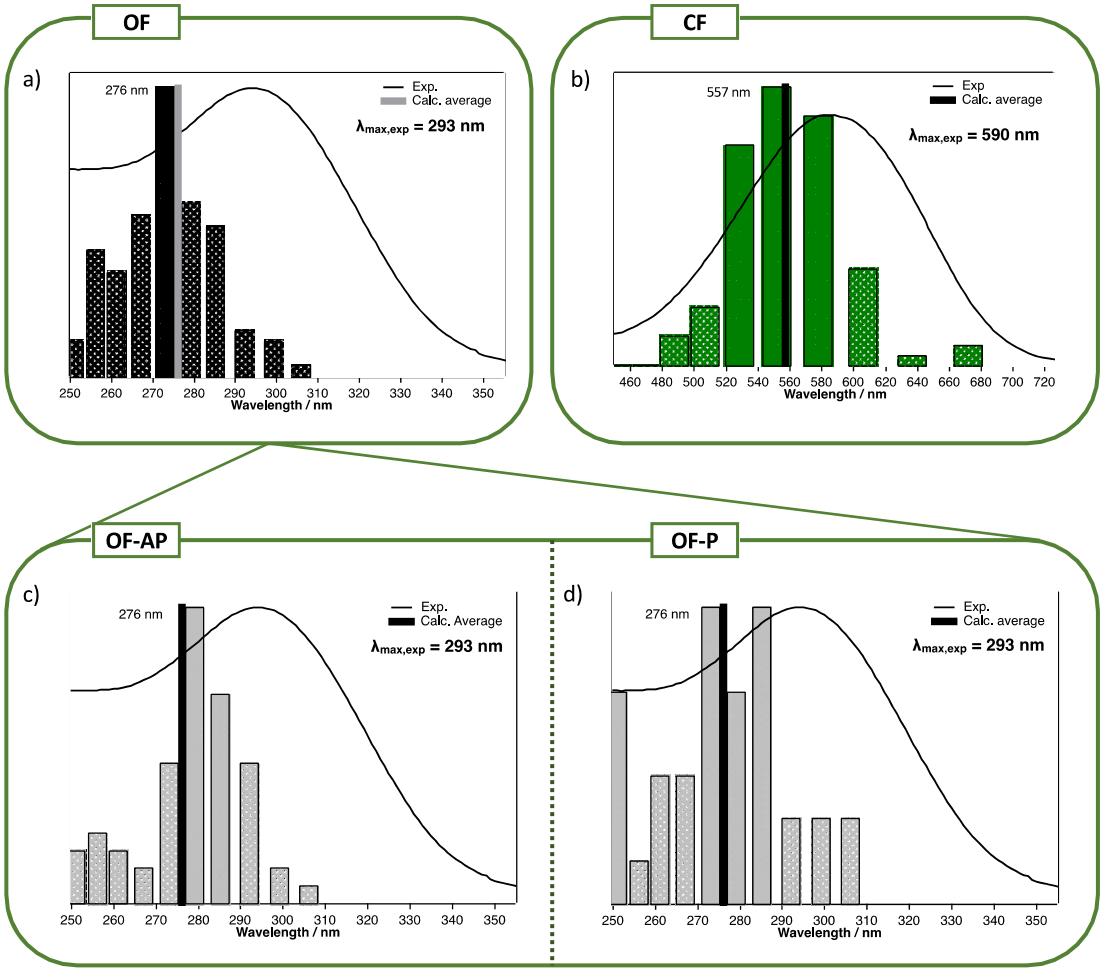

FIGURE 3.16 – Histograms of the distribution of the maximum absorption wavelength λ_{max} in nm (bin sizes: 0.10 eV). (a) and (b): distributions calculated for 100 snapshots extracted from the MD trajectory corresponding respectively to an initial **OF-AP** or **CF** conformation; (c) and (d) distributions calculated for the snapshots extracted from the OF trajectory corresponding respectively to the **OF-P** and **OF-AP** conformations. For each histogram, the average value of the λ_{max} is given and the experimental UV-Vis absorption spectrum is provided [157].

In Figure 3.16.a, for the trajectory corresponding to an initial **OF-AP** conformation, the calculated distribution is large with λ_{max} ranging from 250 to 310 nm and this result arises from the flexibility of the system and highlights the impact of the molecular structure on the optical properties. The average maximum absorption wavelength is in nice agreement with experimental features with an energy difference of 0.21 eV between calculated and experimental values [157]. We have then separated the pool of extracted structures into two categories, corresponding either to the **OF-AP** or the **OF-P** structures. For the **OF-AP** structures, the calculated distribution (Figure 3.16.c) is more peaked than the one obtained for **OF-P** (Figure 3.16.d). This result is in agreement with the relative flexibility of the **OF-AP** and **OF-P** conformers, the **OF-P** structures being much more flexible as illustrated for example on Figure 3.13.

3.2.2.2 Dimer

We have then investigated the properties of the dimers in solution. We have considered three initial structures with the following combinations of isomers: **OF-AP/OF-AP**, **OF-P/OF-P** and **CF/CF**. For each dimer, the starting geometry corresponds to linear arrangement (Figure 2(a)) with one block of four hydrogen bonds (DIM-4H). We will first focus our attention on the MD results obtained for the **OF-AP/OF-AP** dimer. Hereafter, the corresponding MD trajectory will be referred to as **DIM-AP-4H-linear** (the **OF-P/OF-P** and **CF/CF** trajectories will be respectively referred to as **DIM-P-4H-linear** and **DIM-CF-4H-linear**).

Analysis of the DIM-AP-4H-linear trajectory.

We have first checked the stability of this dimer in solution by plotting the distances corresponding to the intermolecular hydrogen-bonding block (x_1 to x_4). Figure 3.17 shows that the H-bond network is stable along the whole trajectory with bond distances ranging from 1.5 to 3.2 Å.

We have then investigated, for each **DTE-Upy** molecule within the dimer, the **OF-AP/OF-P** interconversion by plotting the (ϕ_1;ϕ_2) value couples as illustrated on Figure 3.18. We can conclude that this interconversion is still possible within the dimer. Indeed,

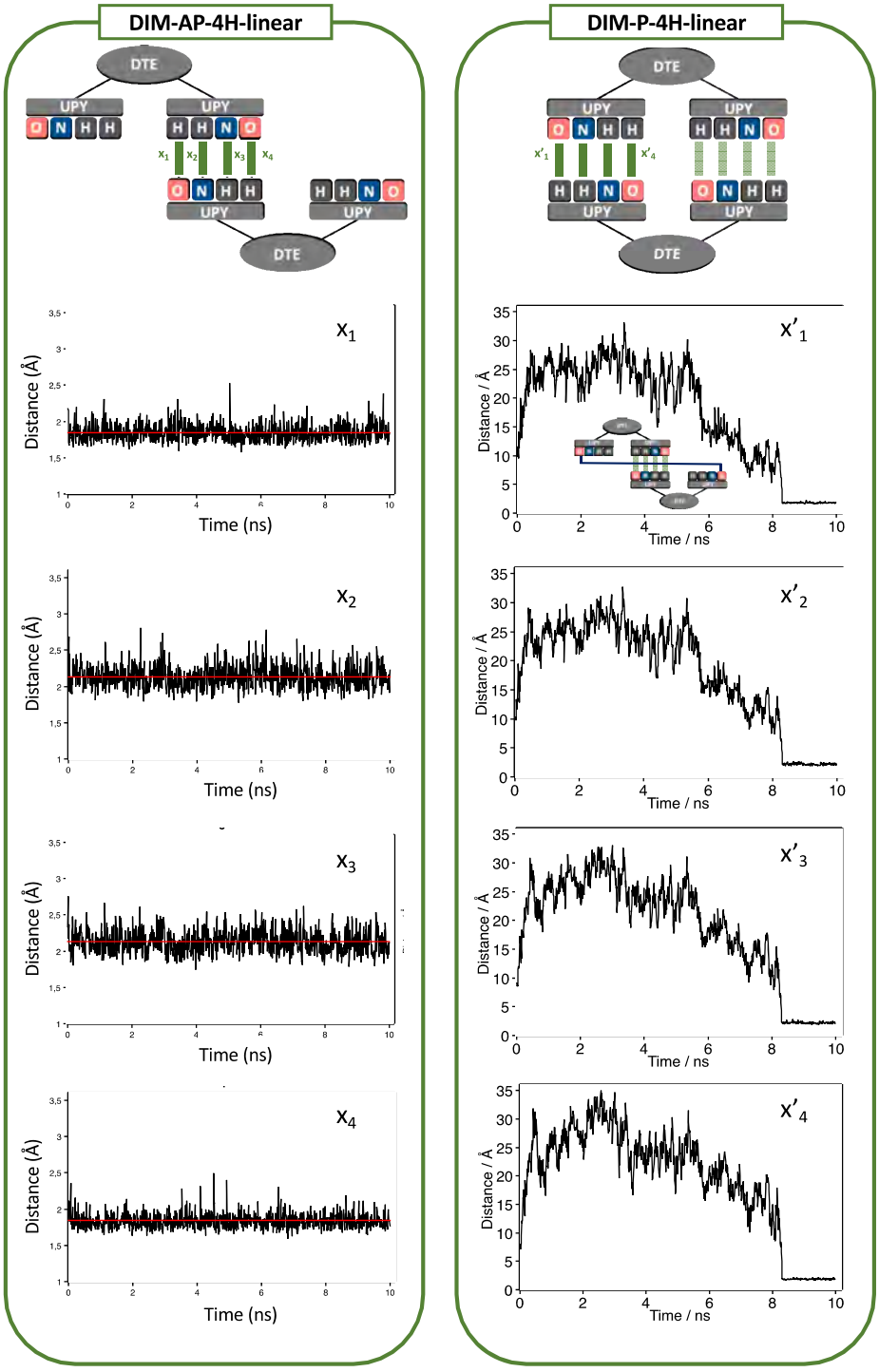

FIGURE 3.17 – (left) Schematic representation of the distances x_1 to x_4 and the time evolution of these distance (in Å) for the **DIM-AP-4H-linear** trajectory and (right) time evolution of the x'$_1$ to x'$_4$ distance (in Å) for the **DIM-P-4H-linear** trajectory.

for one monomer, there is a **OF-AP** $\rightarrow$ **OF-P** isomerization after 0.01 ns of the MD production phase and no further interconversion could be observed along the trajectory. For the second monomer, the **OF-AP**/**OF-P** interconversion can be observed throughout the trajectory. This interconversion can also be monitored with the evolution of the distance d' (Appendix A-9). Like the monomer, the large value of d' corresponds to the **OF-AP** isomer and the smaller one to the **OF-P** structure.

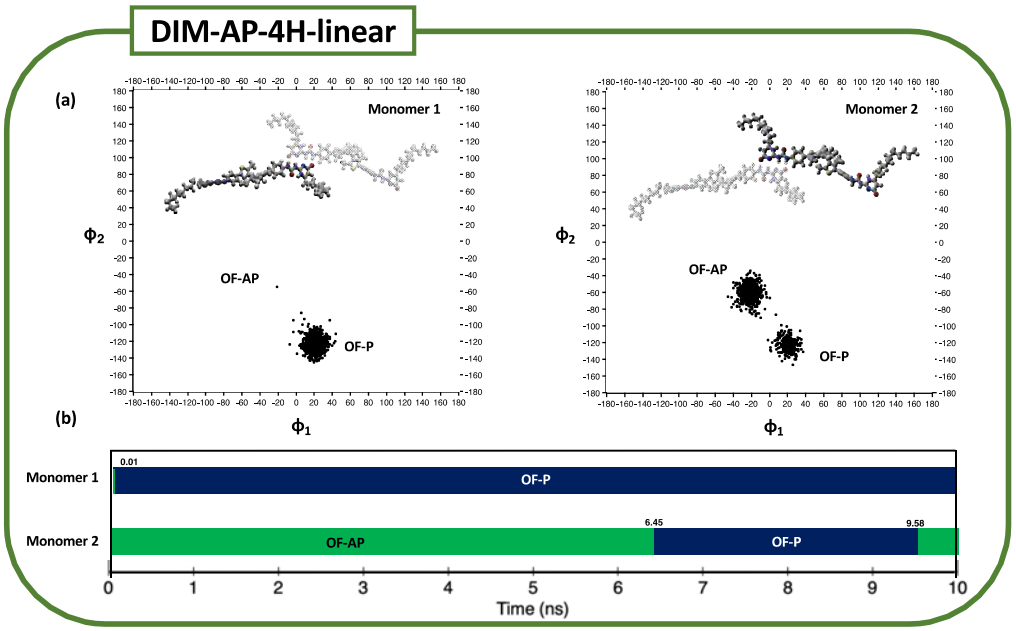

FIGURE 3.18 – **(a)** Representation of the (ϕ_1;ϕ_2) value couples for the two monomers along the **DIM-AP-4H-linear** trajectory. **(b)** Schematic representation of the **OF-AP**/**OF-P** interconversion along the **DIM-AP-4H-linear** trajectory.

Finally, the optical properties of the dimer have been investigated and compared to the monomer. To this purpose, we have extracted one structure and compared the calculated UV-Vis absorption properties with the ones calculated for a monomer. As shown by Figure 3.19(a), there is no impact of the dimerization on the absorption properties with a λ_{max} value of respectively 283 nm and 281 nm for the monomer and dimer respectively. Indeed, for the dimer, the maximum absorption wavelength arises from a HOMO $\rightarrow$ LUMO+2 electronic excitation with these orbitals localized on a single **DTE-Upy** moiety (Figure 3.19(b)).

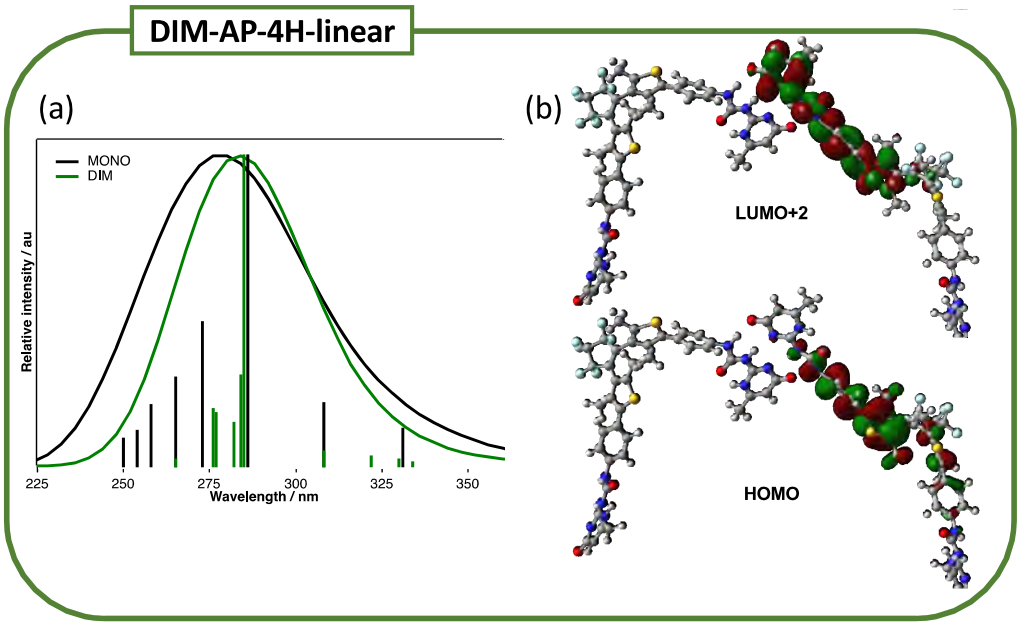

FIGURE 3.19 – **(a)** Calculated normalized absorption spectra (stick and convoluted with a Gaussian function with a FWHM=0.33 eV) for a **OF-AP** monomer and a **OF-AP/OF-P** dimer (solvent: chloroform). **(b) OF-AP/OF-P** dimer: orbitals involved in the electronic transition corresponding to the maximum absorption wavelength.

Analysis of the DIM-P-4H-linear MD trajectory.

For the **DIM-P-4H-linear** trajectory, we have followed the same strategy and the following conclusions can be drawn:

- The quadruple hydrogen bonding is stable with H-bond distances ranging from 1.5 to 3.4 Å (Figure 3.17).

- There is no modification of the UV-Vis absorption properties upon dimerization with λ_{max} values of respectively 279 nm and 281 nm for the monomer and dimer.
- Contrary to the **DIM-AP-4H-linear** trajectory, there is no **OF-P/OF-AP** isomerization (Appendix A-13) but a conversion to another parallel isomer denoted **OF-P'**. Indeed, this new isomer appears after the formation of a cyclic dimer whose schematic representation is given on Figure 3.7(a).

The time evolution of the x'$_1$ to x'$_4$ distances, corresponding to the H-bond distances for the Upy-Upy block that is not involved in a quadruple hydrogen bondings at the beginning of the dynamics, shows a suddent decrease as depicted on Figure 3.17. The cyclic dimer, that has been previously identified after DFT optimization [157], can thus be spontaneously formed from a linear dimer at room temperature. This dimer cyclization could not be observed for the **DIM-AP-4H-linear** trajectory nor for the **DIM-CF-4H-linear** one, the particular arrangement of the **DTE-Upy** in the **OF-P** conformation is a necessary condition to trigger the formation of the second H-bond block.

A new MD trajectory (10 ns), denoted as **DIM-P-8H-cyclic**, has thus been launched for the cyclic **OF-P** dimer that shows 8 H-bonds (two quadruple hydrogen bondings). The two blocks of Upy-Upy interactions are stable along the trajectory (Appendix A-14) and there is no further **OF-P/OF-AP** isomerization. The system is locked in the cyclic dimer conformation which is particularly stable as shown by the computed values of the binding energies (Table 3.4). Indeed, the calculated free energy of binding for the cyclic dimer is (-21.6 $\pm$ 2.1) kcal.mol^{-1} that is to say twice as large as the value computed for the corresponding **OF-P** linear dimer, (-12.4 $\pm$ 1.9) kcal.mol^{-1} . This increase of stability logically corresponds to the formation of a second block of quadruple hydrogen bondings. Table 3.4 also shows that for the **OF-AP** and **CF** linear dimers, the binding energy due the dimer formation is comparable to the **OF-P** linear case.

To conclude, for the **OF** dimers, after formation of the first block of quadruple H bonds, the **OF-P/OF-AP** isomerization is still possible. Once a **OF-P** linear dimer is formed, a cyclic dimer, which is particularly stable, can be obtained. Due to the constrained structure of this dimer, the **OF-P/OF-AP** isomerization is then impeded. Since the **OF-P** isomer is not photoactive, this structure is a bottleneck that prevents the forma-

TABLE 3.4 – Free energy of binding calculated with the MM/GBSA approach in kcal.mol^{-1}.

	DIM-4H-linear	**DIM-8H-cyclic**
OF-AP	-10.1 ± 1.4.	-
OF-P	-12.4 ± 1.9	-21.6± 2.1
CF	-10.7± 1.6	-

tion of larger assemblies. The existence of such a dimer is thus a first explanation for the non-formation of large supramolecular assemblies for **OF** isomers.

3.2.2.3 Hexamer

In the case where the **OF-P** cyclic dimer is not formed, we assume that larger oligomers are present in solution and we have investigated the behaviour of **OF-AP** and **CF** linear hexamers in solution. The corresponding trajectories will be respectively denoted as **HEXA-AP-linear** and **HEXA-CF-linear**.

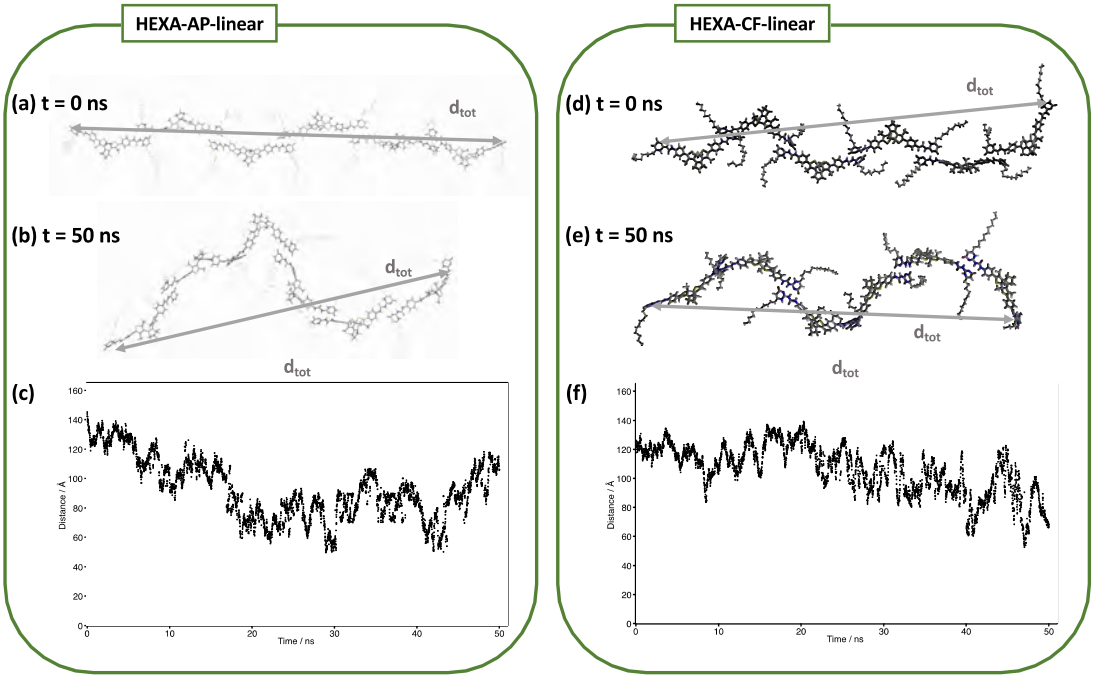

FIGURE 3.20 – **(a)** and **(b)** Representation of the **OF-AP** hexamer at t=0 ns and t = 50 ns respectively; (c) Time evolution of the d_{tot} distance along the 50 ns trajectory. **(d)**, **(e)** and **(f)** same information for the **CF** hexamer.

Figure 3.20 shows the time evolution of the distance d_{tot} between the two extremities of the hexamer for the **HEXA-AP-linear** and **HEXA-CF-linear** trajectories. For both systems, large variations of d_{tot} could be observed along the trajectories with a distance ranging from ∼50 to ∼140 Å. There is a global decrease of this distance along the trajectory which is due to a folding of the hexamer. This can be illustrated by the comparison of a snapshot extracted from the MD at t =0 ns and t = 50 ns (respectively Figure 3.20 (a) and (b) for **HEXA-AP-linear** and (d) and (e) for **HEXA-CF-linear**).

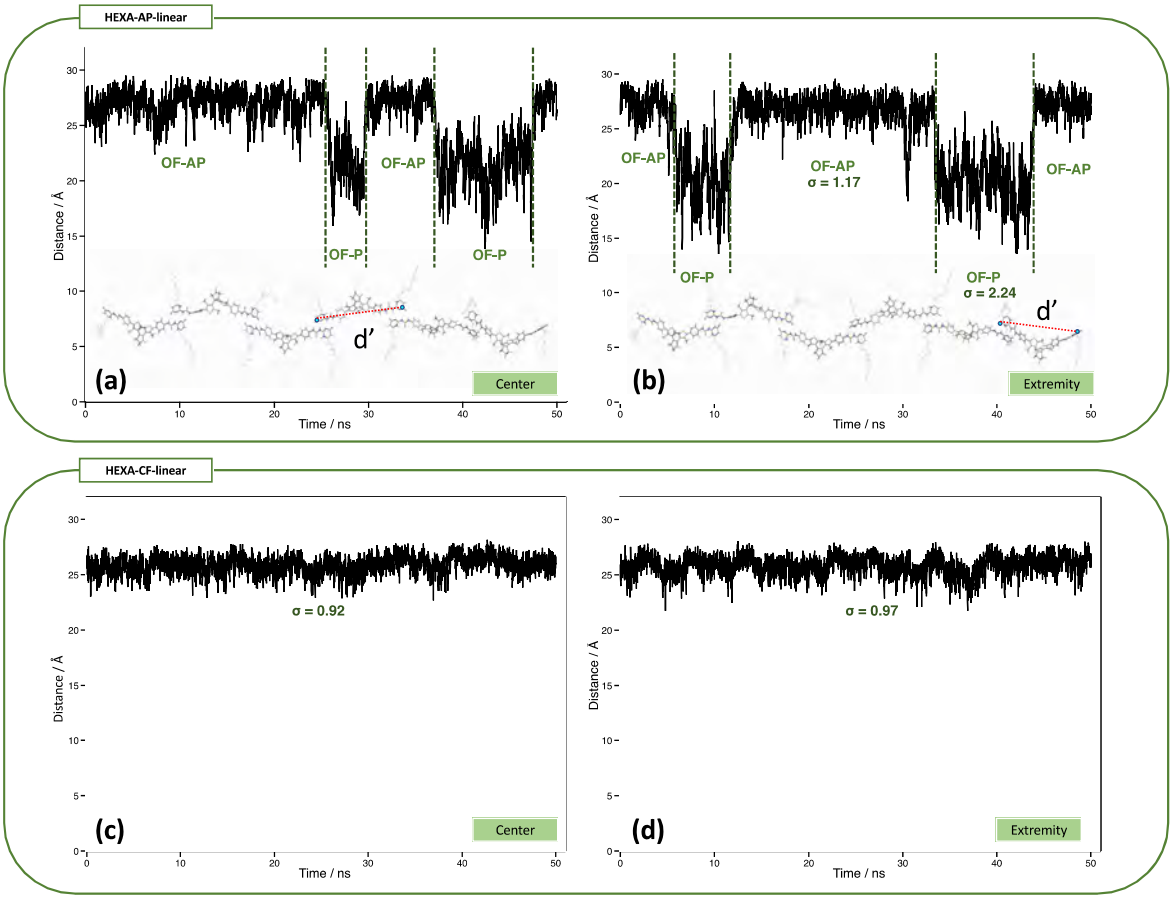

FIGURE 3.21 – **HEXA-AP-linear** trajectory: Time evolution of the d' distance (in Å) along the 50 ns trajectory for a **OF-AP** molecule localized at the center of the hexamer **(a)** and at the extremity **(b)**. **HEXA-CF-linear** trajectory: same information for a **CF** isomer on **(c)** and **(d)**.

On Figure 3.21, the time evolution of the distance d' defined on Figure 3.9 is provided for a **OF** molecule localized at the center (Figure 3.21(a)) and at the extremity (Figure 3.21(b)) of the hexamer. As previously shown, this distance discriminates between the **OF-AP** and **OF-P** isomers. For the **HEXA-AP-linear** trajectory, at t = 0 ns, both molecules correspond to the **OF-AP** isomer and present a large d' distance. Then, in the course of the trajectory, an **OF-AP**/**OF-P** interconversion can be identified. This observation can be made whatever the position of the **DTE-Upy** molecule within the hexamer. Figures 3.21(a) and (b) also show that the **OF** molecules within the hexamer are highly flexible with standard deviation σ for the distance d' of 1.17 and 2.24 Å for respectively the **OF-AP** and **OF-P** isomers. We can compare this flexibility to the **CF**

isomers. As shown on Figures 3.21(c) and (d), there is much less variation in the distance d' for the **CF** isomers localized either at the center of at the extremity of the hexamer chain. The oligomer is thus more rigid after photocyclization. The high flexibility of the **OF** hexamer compared to the **CF** should have an impact on the supramolecular assembly formation. Actually, due to entropic contributions, it should be easier for a new monomer to form a quadruple H-bond blocks with a **CF** molecule localized at the extremity of the chain rather than with a highly flexible **OF** localized in the same position. The difference of flexibility between the **OF** and **CF** oligomers can thus be a second argument to rationalize the non-formation of supramolecular assemblies for **OF** isomers.

3.2.2.4 π-Stacked dimers

A $\pi - \pi$ stacking interaction between two dimerized **Upy** motif has previously been characterized in supramolecular assemblies [162, 163]. π stacking was shown to strengthen the hydrogen bonds in multiple H-bonded dimers thanks to the increase of charge-transfer interactions between the H-bonding partners [163]. For both **OF-AP** and **CF** isomers, we have thus considered π-stacked dimers, *i.e.* four molecules with two H-bonded linear dimer presenting a stacking interaction (Figure 3.22(a)). The corresponding trajectories are respectively denoted as **TETRA-AP-STACK** and **TETRA-CF-STACK** and a representation of the π-stacked dimers before equilibration is provided on Figure 3.22(b).

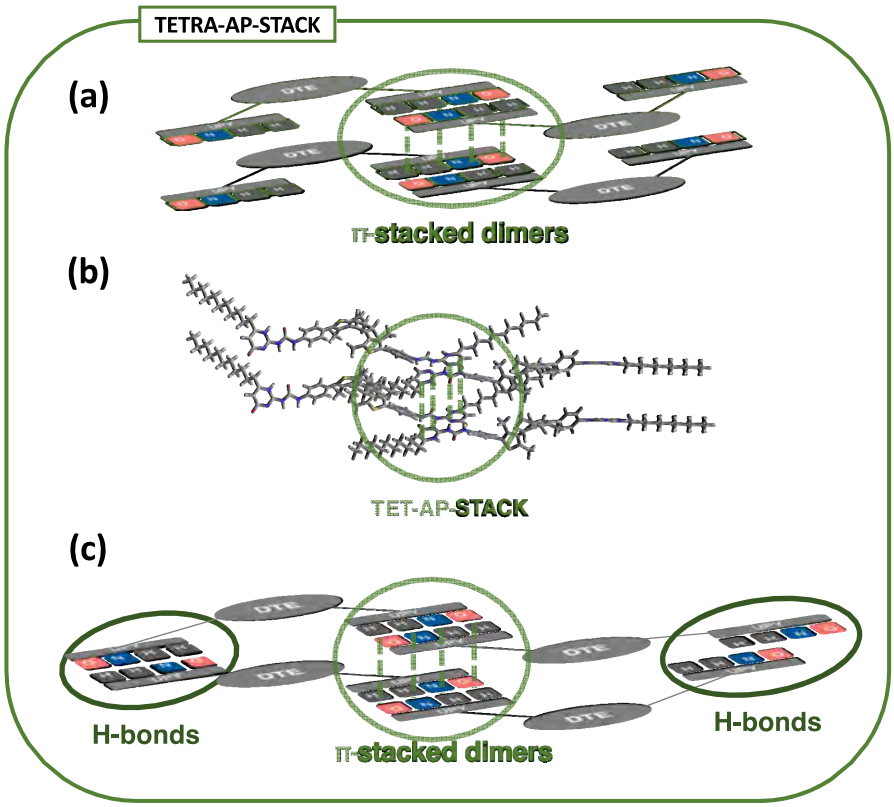

FIGURE 3.22 – **(a)** Schematic representation of the π-stacked dimers before equilibration; **(a)** Representation of the **OF-AP** π-stacked dimers before equilibration for the **TETRA-AP-STACK** trajectory; **(c)** Schematic representation of the π-stacked dimers at t = 50 ns.

Along both trajectories, one can observe that (1) for the two dimers, the H-bond network is stable and (2) the average π-stacking distance is 3.60 Å, a value that can be

directly compared to the experimental value of 3.55 Å and to the DFT value of 3.56 Å for model stacked dimers [163, 164]. The π-stacked dimers are thus stable for both the **OF** and **CF** isomers along the MD simulation.

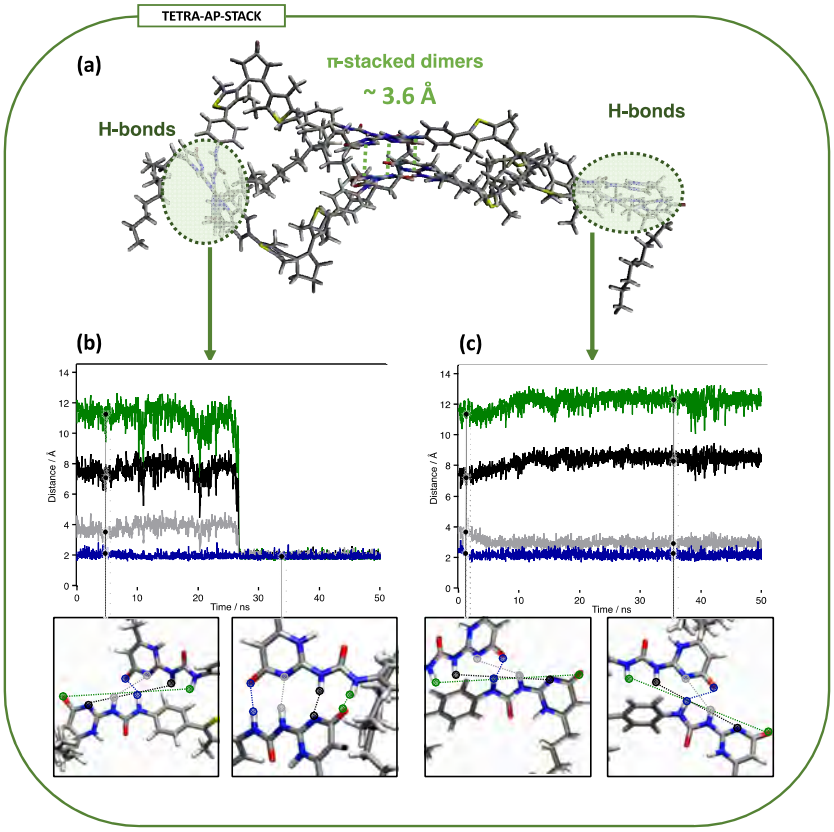

FIGURE 3.23 – **TETRA-AP-STACK** trajectory: (a) Representation of the π-stacked dimers at t= 50 ns; **(b)** and **(c)** Time evolution of the H-bond distances characterizing the Upy-Upy interactions for the two blocks localized at the extremity of the π-stacked dimers.

Interestingly, for the **TETRA-AP-STACK** system, after the equilibration step (t= 0 ns), there is formation of one hydrogen bond between the two **Upy** groups localized at the extremity of the π-stacked dimers (Figure 3.23(b) and (c)). At t$\simeq$ 26 ns, Figure 3.23(b) shows a rearrangement of one Upy-Upy block and the formation of quadruple hydrogen bondings. This H-bond network is stable until the end of the trajectory (t=50 ns). One should note that a prerequisite to trigger the formation of the quadruple hydrogen bondings is the formation of an **OF-P** isomer for at least one monomer. Indeed, the **OF-AP/OF-P** isomerization is always possible for the four molecules forming the π-stacked

dimers (Figure A-15). At t$\simeq$ 26 ns, there is a **OF-AP** $\rightarrow$ **OF-P** isomerization for one monomer which enables a structural rearrangement and the alignment of the two **Upy** moieties.

For the second block (Figure 3.23(c)), there is a weaker interaction between the two **Upy** groups with two hydrogen bonds. There is some **OF-AP**/**OF-P** isomerization, as shown by Figure A-15, but no structural rearrangement allowing the formation of quadruple hydrogen bondings. Even if the two **Upy** groups are not perfectly aligned for this second block, the π-stacked dimers are completely locked as schematically represented on Figure 3.22(c): there is no free **Upy** group that could participate to the formation of H-bonds with incoming **DTE** molecule. The existence of such very stable π-stacked dimers can thus limit the formation of supramolecular assemblies for **OF** isomers.

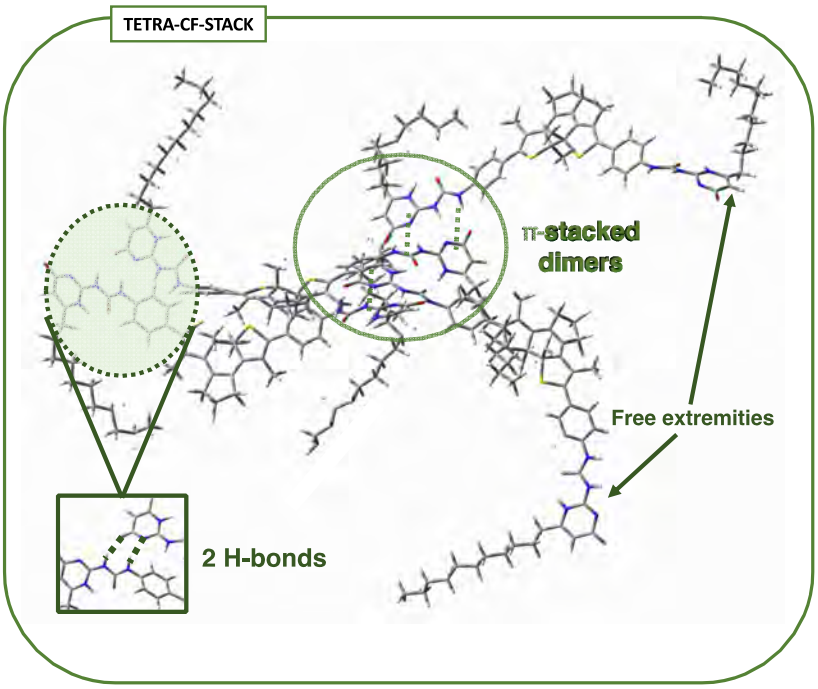

FIGURE 3.24 – **TETRA-CF-STACK** trajectory: representation of the π-stacked dimers at t=50 ns.

On the opposite, for the **TETRA-CF-STACK** trajectory, Figure 3.24 shows that at t=50 ns, there are only two H-bonds between two **Upy** moieties. Due to the rigidity of the system, the two **Upy** groups are not correctly aligned and cannot form quadruple hydrogen bondings. At the same time, at the other extremity of the π-stacked dimers, the two **Upy** groups are free and can thus participate to the formation of larger assemblies

through H-bond interactions.

3.2.3 Conclusion

With the help of MD simulations, we have investigated the behavior of **OF** and **CF** monomers, dimers, hexamers and π-stacked dimers in solution. Our purpose was to explain the formation of supramolecular assemblies only for the **CF** isomers. We have shown that this behavior can be rationalized by (i) the possible formation of a very stable cyclic dimer for the **OF-P** isomers; (ii) the relative flexibility of the **OF** oligomers compared to their **CF** counterparts, as shown by the study of the hexamers in solution; (iii) the possible existence of π-stacked dimers that do not present free **Upy** groups for the **OF** system. These results systematically show that the progression of the supramolecular assembly will be more complicated or even completely impeded for the **OF** oligomers. In particular, the existence of very stable cyclic structures, with no free **Upy** groups, constitutes bottlenecks that block the supramolecular self-assembly. The formation of such stable cyclic structures is systematically triggered by the **OF-AP**/**OF-P** isomerization: the presence of at least one **OF-P** isomer within the considered system is a necessary condition to form these cyclic aggregates. The functionalization of the **DTE** core in order to impede the **OF-AP**/**OF-P** isomerization [153] should thus promote the formation of supramolecular assemblies for the **OF** isomers.

3.3 DTE-Upy in polymer

In this second part, we aim at initiate the study of the **DTE-Upy** molecules within a complex environment that is a polymer by (1) proposing a protocol able to set up a system involving a molecule embedded in a polymer matrix, (2) studying the impact of the polymer matrix on the **DTE-Upy** molecules and (3) studying the impact of the photochromic reaction on the polymer matrix. This general strategy is illustrated on Figure 3.25.

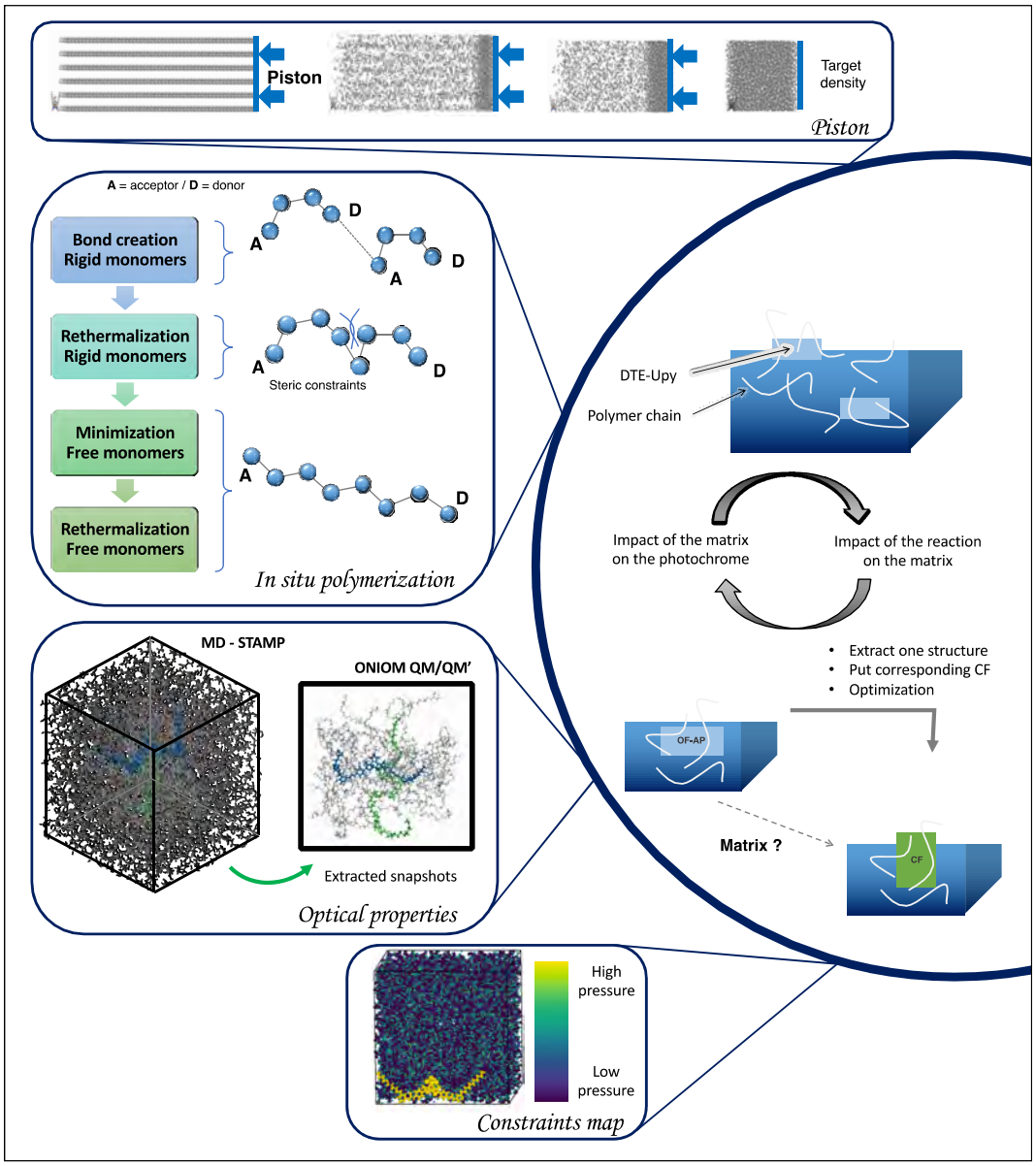

FIGURE 3.25 – Schematic representation of the strategy of the study of **DTE-Upy** molecules in a polymer matrix.

3.3.1 Computational details

3.3.1.1 Molecular Dynamics

For the molecule embedded in a polymer matrix the MD simulations were carried out using the code developed at Commissariat à l'Energie Atomique et aux Energies Alternatives (CEA/DAM/DIF), STAMP. This code was designed to simulate very large systems of atoms (surfaces, materials) [165, 166] and was adapted to take into account molecular systems. A recent development of this code has also been used throughout this study, allowing the *in situ* polymerization around a molecule [167]. This feature is a novelty as usually, one does not perform polymerization around a molecule but create a hole in a polymeric system in order to insert a molecule [168]. One then needs to carefully define the FF [169, 170] of the embedded molecules as in most of the case, one will be interested in the optical properties of the embedded molecule, that are dependent of the structure. The procedure to run MD simulations with STAMP being not straightforward, we propose here to describe the different steps from the set up of the initial box to the production step.

Initial box

The starting system is built by stacking boxes containing one **DTE-Upy** molecule or one butadiene (**BTDN**) molecule. The box containing one **BTDN** monomer is replicated 60 times along x and 6 times along y and z leading to a global system containing one box with one **DTE-Upy** molecule and 2160 boxes of **BTDN** monomer. The resulting simulation box is not realistic, (1) it is not a homogeneous media and (2) the total number of molecules in a simulation box of this size does not allow the reproduction of a realistic density for such a system.

Piston

To homogenize the system and to retrieve a realistic density, we applied a piston. We considered the canonical ensemble (NVT, T=300K), with a Langevin thermostat (caracterized by a friction coefficient, hereafter denoted as γ), γ, of 10^{13} s^{-1}. PBC were applied along y and z while the piston was applied along x. The **DTE-Upy** molecule has been kept frozen. The piston stopped when the desired density (0.828 $g.cm^{-3}$) was reached.

Before to move over the polymerization step, a transition step has to be performed to (1) consider the new size of the simulation box that corresponds to right density and (2) apply PBC along x, y and z.

Polymerization

The polymerization process starts with a system (**DTE-Upy+ BTDN** monomers) at the right density (0.828 g.cm^{-3}), at the desired temperature (T=300K). For each monomer in the simulation box, an extremity is defined as a donor and the other one is defined as an acceptor. Moreover, at the beginning, 100 monomers are randomly and uniformly ascribed as initiator. It means that the polymerization process can start only from those initiators. It also defines the final number of polymer chains that will be created. To perform a polymerization step one needs to add a monomer to a growing chain and to relax the created bond. The time during which this process will occur has to be chosen. The different steps are described hereafter.

1- Bond creation

Each initiator will create a new bond with another monomer (acceptor) that is close enough. If an acceptor is chosen for the creation of a bond with two different initiators, the one that will effectively create a bond is randomly chosen and the bond with the other initiator is not created. As soon as the new bond is created, both the initiator and the acceptor are no more reactive. The donor extremity of the acceptor that has just reacted and created a bond becomes the new initiator. The previous initiator will thus be the end of the growing polymer chain. This phase is instantaneous.

2- Bond relaxation

- The previously created bond may not be chemically reasonable with for example a carbon-carbon distance that is too long. It is thus necessary to bring closer the two monomers involved in the newly created bond. This phase is carried out in the canonical (NVT) ensemble with a Langevin thermostat. Throughout this process, the monomers are rigid. It means that only translation and rotation are possible while internal deformation are not allowed. Moreover, the force that is necessary to bring closer the acceptor (free monomer) and the initiator (chain end) is only applied to the free monomer. It prevents the deformation (stretch) of the polymer chain that was previously created. During this

phase, the interactions due to bending and dihedral angles involving the created bonds are cancelled. As the non-bonded potential are continuously considered, the free monomer is brought close to the chain ends without creating inter or intramolecular overlap. The bond relaxation is only partial during this phase because monomers are rigid and hydrogen atoms can be located between the two newly bonded atoms. The end of this phase is reached when the distance between the initiator and the acceptor has a value that has been previously defined (a typical simple carbon-carbon distance, 1.54 Å).

- It is then necessary to relaxe the angles of the newly created bond. A reorientation of the free monomer with respect to the initiator is possible. This phase is similar to the previous one (bond relaxation). All monomers are still rigid and the NVT ensemble with a Langevin thermostat is used. The only difference is that the interactions due to bending angles involving the new bonds are considered.

- Once the distance and the bending angle of the created bond has been achieved, the dihedral angles can be relaxed. This is the last step of the formation of the polymer chain backbone. It is similar to the two previously steps. The only difference is that the full intramolecular potential is now considered.

3- Minimization

During this phase, the hydrogen atoms will be correctly positioned around the created bond, according to the parameters of the force field. As the monomers are fully flexible during this step, the new positions of the hydrogen atoms may induce a further relaxation of the bond, bending and dihedral angles previously relaxed. This step will end when the value of the force on each atom reaches the given criteria.

4- Relaxation

This phase allows the system to relax efficiently any far for equilibrium local configuration left after the previous phases have occurred. This phase is carried out in the NVT ensemble with a Langevin thermostat, whose friction coefficient is higher than before. The monomers are fully flexible. The final polymer chains contain between 20 and 25 monomers.

Equilibration and production

During the equilibration phase, the system is gently equilibrated. It is performed in the NVT ensemble with the usual Langevin friction coefficient (1.10^{12}) and no frozen atoms,

during 0.1 ns. It is followed by the production phase, carried out with the same parameters, during 1 ns.

In Table 3.5 we have gathered all the parameters used during the simulation of the different previously mentioned steps.

TABLE 3.5 – Important parameters used during the simulations in STAMP.

	Piston[a]	Polymerization	Production[b]
Ensemble		LNVT	
DTE-Upy[c]	Frozen	Frozen	Free
BTDN[d]	Free	Free	Free
T (K)		300	
PBC	y,z	x,y,z	x,y,z
γ (s^{-1})	10^{12}	10^{12}[e]	10^{12}

[a] An intermediate step between the piston and the polymerization is performed to get back the PBC along the three axis.

[b] The same parameters are used for the equilibration step.

[c] **DTE-Upy** molecules are described by GAFF.

[d] **BTDN** are described by OPLS. It has already been demonstrated that it was suitable for the description of **BTDN**.

[e] Within the polymerization process, for the relaxation step, a higher value of γ is used (10^{14} s^{-1}).

The interaction between **DTE-Upy** and **BTDN** are ruled by Van der Waals interactions and electrostatic interactions. Van der Waals interactions are defined by a Lennard-Jones potential which is dependent of ϵ and σ (mixing rules are then used to account for all the crossed interactions). For the electrostatic interactions, the Coulomb potential is expressed using the HF/6-31G(d) RESP charges for all the atoms (**DTE-Upy** + **BTDN**).

Validation of GAFF parameters in STAMP

We have presented in Section 3.2.1.1 the procedure we have followed to validate the use of GAFF parameters for the study of **DTE-Upy** molecules in solution. Initially, as STAMP was not able to deal with organic molecules, GAFF was not implemented in it. Before any calculation, the implementation of GAFF in STAMP has been done. We present here the test we performed to check the validity of the implementation of the GAFF parameters in STAMP. To do so, we performed:

- A minimization process in vacuum with GAFF with AMBER.
- A minimization process in vacuum with GAFF in STAMP.

In both cases, the steepest descent algorithm was considered. In Table 3.6 we have gathered some important structural parameters used for the comparison.

TABLE 3.6 – Selected geometrical parameters calculated for the isomers **OF-AP**, **OF-P** and **CF** calculated in vacuum with the GAFF force field with STAMP with the GAFF force field with AMBER16. The distances are in Angstrom, the dihedral angles are in degrees. The structural parameters are defined on Figure 3.9.

	OF-AP		**OF-P**		**CF**	
	GAFF@STAMP	GAFF	GAFF@STAMP	GAFF	GAFF@STAMP	GAFF
Bonds						
d_{cc}	3.44	3.44	4.18	4.12	1.54	1.57
d_1	19.38	19.30	28.20	28.28	28.71	28.56
d_2	23.15	23.07	26.67	26.56	24.94	24.87
d_3	14.22	13.90	15.36	15.55	15.54	15.58
d_4	14.12	14.29	15.46	15.69	15.48	15.58
d'	28.34	27.86	19.38	19.41	26.68	26.10
Dihedral angles						
Φ_1	-61	-54	26	22	-20	-14
Φ_2	-14	-14	-122	-124	5	1

For the three conformers the difference between the structures obtained after a minimization with STAMP or AMBER are trifling. For each structural parameter (distance), slight deviations are observed between GAFF and GAFF@STAMP structures, represen-

ting each time less than 2 %. After the structural comparison, we also investigated the optical properties of the resulting structures (Table 3.7).

TABLE 3.7 – Impact of the geometries on the maximum absorption wavelength (λ_{max}) calculated at the CAM-B3LYP/6-3111+G(2d,p) for the isomers **OF-AP**, **OF-P** and **CF**. Two different geometries are considered for each isomer: the one optimized with the GAFF force field with AMBER16 and the one optimized with GAFF in STAMP.

	OF-AP		**OF-P**		**CF**	
	GAFF@STAMP	GAFF	GAFF@STAMP	GAFF	GAFF@STAMP	GAFF
λ_{max}	265	267	274	272	538	530

As it was expected due to the structures that are really similar, the optical properties are also similar for the two structures obtained whether after a minimization process in AMBER or in STAMP, each time with GAFF.

3.3.1.2 Absorption properties: set up of the computational strategy

The calculation scheme has to be defined for the calculation of the optical properties within the polymer matrix. We extracted a snapshot from the MD simulation in STAMP and defined a layer of 4 Å around the **DTE-Upy** molecule (see Figure 3.26).

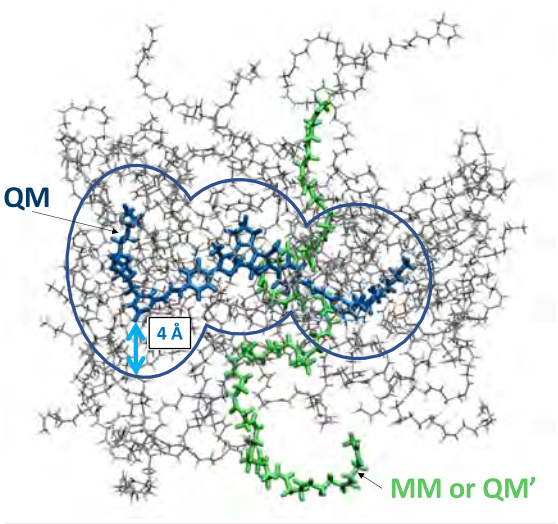

FIGURE 3.26 – Representation of the extracted snapshot with the definition of the QM and MM or QM' level.

For each atom located within this layer, its corresponding complete polymer chain was considered. The calculation protocols we tested are described hereafter:

- Scheme (1) the **DTE-Upy** molecule + the polymer chains are described with the ONIOM QM:MM model: the optical properties of the **DTE-Upy** is described with the "QM" approach (CAM-B3LYP/6-311+G(2d,p)) while the lateral alkyl chains of **DTE-Upy** and the polymer chains are treated at the MM level (UFF) with a charge embedding scheme.
- Scheme (2) the **DTE-Upy** molecule without its alkyl chains + the polymer chains are described with the ONIOM QM:QM' model: the optical properties of the **DTE-Upy** is described with the "QM" approach while the lateral alkyl chains of **DTE-Upy** and the polymer chains are treated at the QM' level (HF/3-21G) with an electrostatic embedding scheme.
- Scheme (3) the polymer chains and the alkyl chains are removed and the **DTE-Upy** molecule is treated at a QM level.

TABLE 3.8 – Impact of the computational scheme on the maximum absorption wavelength λ_{max} (in nm) and the oscillator strenght (*f*) calculated for the isomers **OF-AP**, **OF-P** and **CF**: scheme (1) ; scheme (2) ; scheme (3) .

	Scheme 1		Scheme 2		Scheme 3	
	λ_{max}	f	λ_{max}	f	λ_{max}	f
OF-AP	265	0.383	266	0.377	265	0.400
OF-P	267	0.294	268	0.276	266	0.302
CF	536	0.331	536	0.331	536	0.341

Once again, for the sake of finding the best compromise between the cost of the calculation and its accuracy, we relied on scheme 3 that is the "cheapest" one while providing results as good as more expensive methods (scheme 3: $\lambda_{max} = 266$ nm and scheme 1 and 2 λ_{max}= 267 and 268 nm respectively for **OF-P**). One can conclude by saying that the **BTDN** polymer has no electronic impact on the optical properties of the **DTE-Upy**.

3.3.2 Impact of the matrix on the DTE-Upy properties

In this part we will systematically study the effect of the polymer matrix on the structural properties and then on the UV-Vis properties of the three **DTE-Upy** isomers, namely **OF-AP**, **OF-P** and **CF**.

3.3.2.1 Structural analysis

For each isomer, 10 simulations of 1 ns were performed. The 10 simulations of each conformer have different starting structures that were extracted from the simulations presented in Section 3.2.2. As the structures are different, 10 different polymerization steps were performed for each structure. It allowed us to sample efficiently the structural flexibility of the **DTE-Upy** conformers and avoid to keep "blocked" in a unique potential well. The different structures that have been considered are represented on Figure 3.27. It allows especially to sample the d_i distances and the β dihedral angles. The simulations we performed only last 1 ns as the effective simulation time is really long. To achieve 1 ns of simulation, it requires one month on one node of eight processors.

The structural parameters we have looked at are the same as in Section 3.2.2 and are represented on Figure 3.9. The results are presented as follows:
- For each conformer (**OF-AP**, **OF-P** and **CF**) the evolution along the 1 ns simulation time of only 1 simulation has been represented graphically. All the average values for all the structural parameters along with their standard deviations are also gathered in Table 3.9.
- For the 9 other simulations of each conformer, only the average value of each parameter along with the standard deviation value are presented in Appendices A-16, A-17 and A-18. Nevertheless, all the results and the conclusions are similar for the simulations presented in Appendix and the ones that will be presented in this part.

Starting either from **OF-AP** or **OF-P** isomer, the representation of the (ϕ_1;ϕ_2) dihedral angles on Figure 3.28 reveals that no interconversion is occurring. The average values of the (ϕ_1;ϕ_2) dihedral angles for **OF-AP** and **OF-P** are respectively (-20°;-60°)

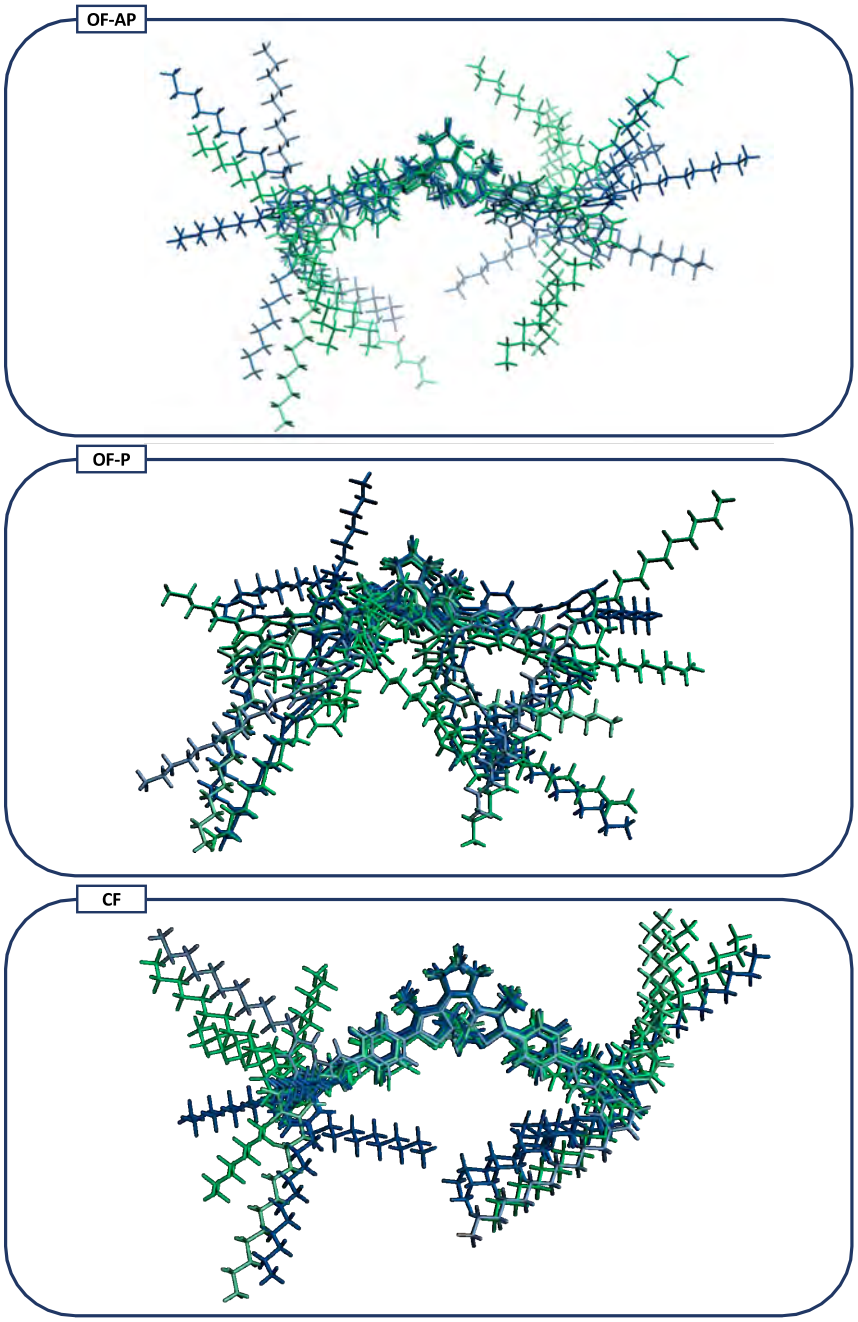

FIGURE 3.27 – Representation of the 10 structures used as starting point for the 10 simulations for each conformer.

and (20°;-120°). In solution, for a 10 ns simulation time, the interconversion process was always observed (see Section 3.2.2.1). To allow a reasonable comparison between simulations in solution and within a polymer matrix, we launched 10 simulations of 1 ns for **OF-AP** and **OF-P**. For **OF-AP**, we observed an interconversion in 4 simulations while

TABLE 3.9 – Average values for different distances (in Angstroms, Å) and dihedral angles (in degrees, °) for the three selected trajectories launched for the **OF-AP**, **OF-P** and **CF** conformers in STAMP. The standard deviation are provided between parenthesis under each value. These parameters are defined on Figure 3.9. The values obtained for each conformer, in solution (Section 3.2), are also provided to ease the comparison.

	d_{cc}	d_1	d_2	d_3	d_4	d'	ϕ_1	ϕ_2
Polymer matrix								
OF-AP	3.61	19.70	24.78	15.30	14.63	27.73	-16	-64
	(0.13)	(1.55)	(1.64)	(0.66)	(1.25)	(0.80)	(8)	(8)
OF-P	4.10	16.52	20.62	13.16	13.03	21.38	20	-123
	(0.11)	(1.62)	(1.71)	(0.99)	(1.65)	(1.58)	(6)	(8)
CF	1.56	23.29	21.16	14.53	15.07	28.11	-20	6
	(0.03)	(1.50)	(1.65)	(1.01)	(0.80)	(0.47)	(6)	(6)
Solution								
OF-AP	3.65	18.39	20.99	12.89	12.99	27.18	-21	-60
	(0.18)	(5.01)	(3.82)	(3.12)	(1.74)	(1.09)	(6)	(9)
OF-P	4.09	18.98	18.46	13.26	13.37	21.50	20	-121
	(0.15)	(5.08)	(4.33)	(1.59)	(1.46)	(2.29)	(10)	(12)
CF	1.57	21.37	21.25	13.21	12.82	25.79	-9	5
	(0.03)	(4.05)	(4.09)	(1.65)	(1.66)	(0.80)	(9)	(9)

for **OF-P**, the interconversion process was occurring in 5 simulations over the total 10 simulations. For a shorter simulation time, the interconversion process is not systematic but there is almost 1 chance over 2 to observe it. Within the polymer environment, the presence of the polymer chains around the **DTE-Upy** seems to avoid this interconversion process. This is confirmed by the evolution of the d_{cc} that does not show any characteristic variation corresponding to the interconversion process, either for **OF-AP** or **OF-P** with average values of (3.61 ± 0.13) Å and (4.10 ± 0.11) Å respectively (Figure 3.28).

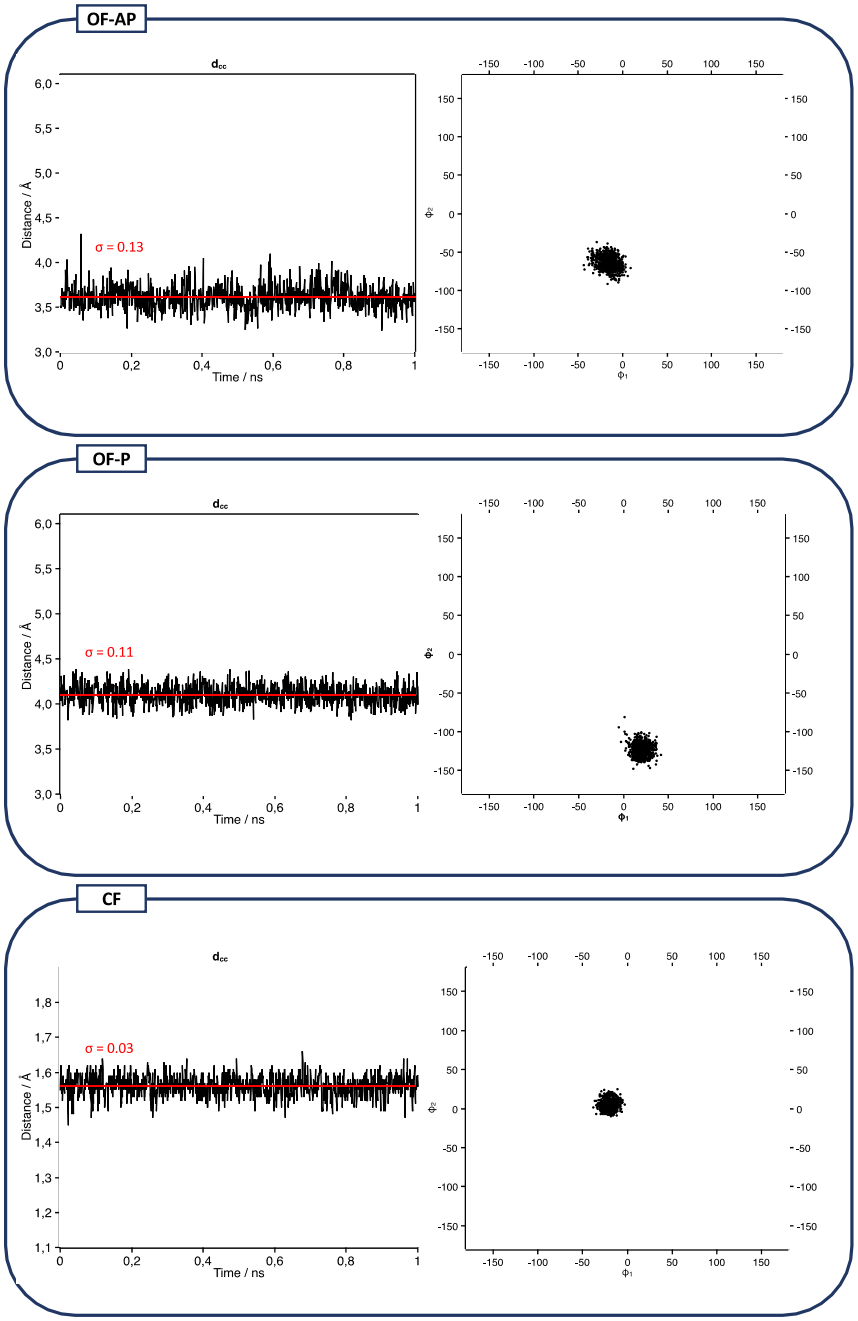

FIGURE 3.28 – Time evolution of the d_{cc} distance and representation of value couples (ϕ_1,ϕ_2) for the isomers **OF-AP** (top), **OF-P** (middle) and **CF** (bottom).

Is the photochemical reaction still possible within the polymer environment ?

From an empiric point of view, it has been demonstrated that it was necessary to fulfill two conditions to say that the photocyclization reaction (**OF-AP** $\rightleftarrows$ **CF**) is possible [171]:
- The d_{cc} distance has to be lower than 4.2 Å.
- The LUMO orbital has to present a bonding character between the two reactive carbons to ensure the possibility to have the photochromic reaction, **OF-AP** $\rightleftarrows$ **CF**.

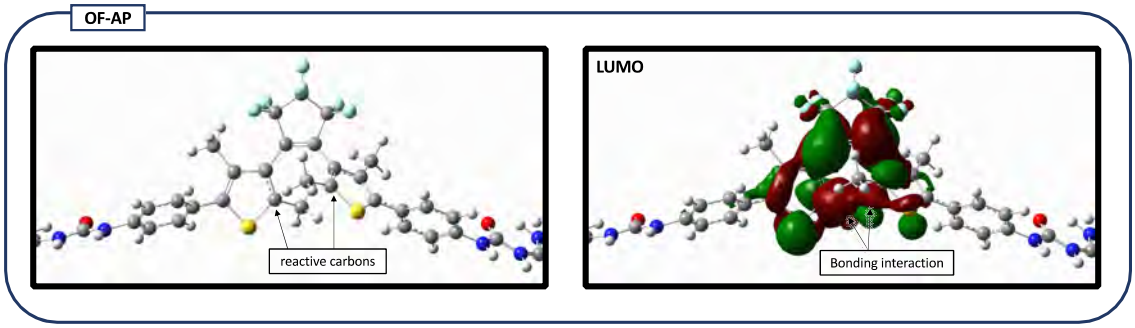

FIGURE 3.29 – Representation of the LUMO molecular orbital (isodensity=0.025 ua) of **OF-AP**.

We can see that the d_{cc} distance is always lower than 4.2 Å (Figure 3.28). Moreover, we represented on Figure 3.29, for a structure extracted from **OF-AP** simulation and for which the molecular orbitals have been computed, the LUMO orbital. One can observe that, indeed, there is a bonding interaction between the two reactive carbons. The fact that the two empirical conditions (d_{cc} distance and nature of the LUMO orbital) are fulfilled indicates that the photochemical reaction in the polymer matrix may be possible.

For the **CF** conformer, the (ϕ_1;ϕ_2) dihedral angles and the d_{cc} distance (with an average value of 1.56 Åand a standard deviation of σ=0.03 Å) are less flexible (Figure 3.28) than what is observed for the **OF-AP** and **OF-P** (See Table 3.9). The flexibility of the systems is also due to the presence of the lateral alkyl chains, illustrated through the d_i distances (the definition of the distances are provided on Figure 3.9). In solution, those chains were really flexible with standard deviations going up to 5 Å (see Table 3.28). The evolution of the d_i distances for the three conformers are represented on Figure 3.30 while

the average value and the standard deviations are gathered in Table 3.28.

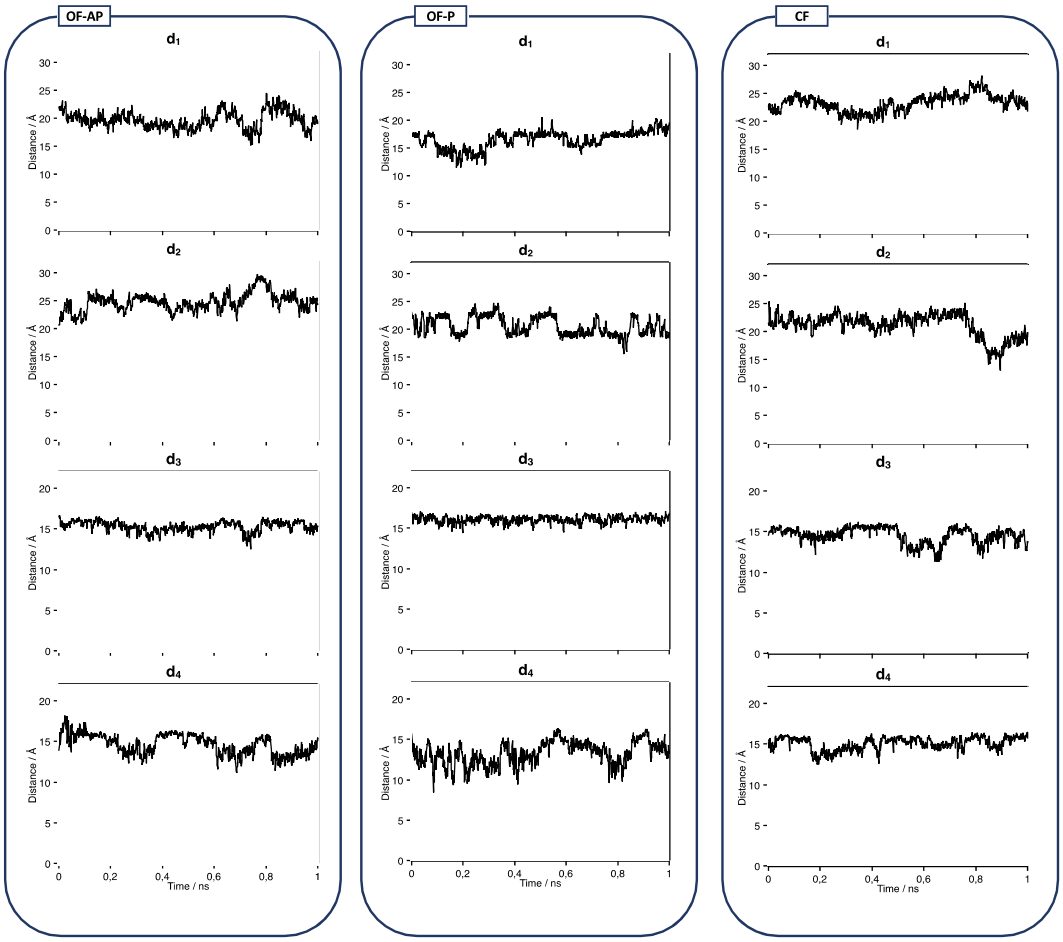

FIGURE 3.30 – Time evolution of the distances d_i (i=1 to 4) along the 1 ns trajectory for the **OF-AP** (top), **OF-P** (middle) and **CF** (bottom) isomers. These parameters are defined on Figure 3.9.

For the three conformers, the d_i distances show a moderate flexibility with a fluctuation around the average value between 1 and 2 Å. In solution, the flexibility of the systems was also illustrated through the evolution of the d' distance (it is also an indicator of the isomerization process as a small value of d' characterizes an **OF-P** isomer while a larger one corresponds to an **OF-AP** isomer). Its time evolution for each conformer is represented on Figure 3.31.

Along the 1 ns simulation of one isomer, only one isomer is observed, confirming once again that no interconversion is observed.

As a conclusion of the structural analysis of the three conformers within the polymer ma-

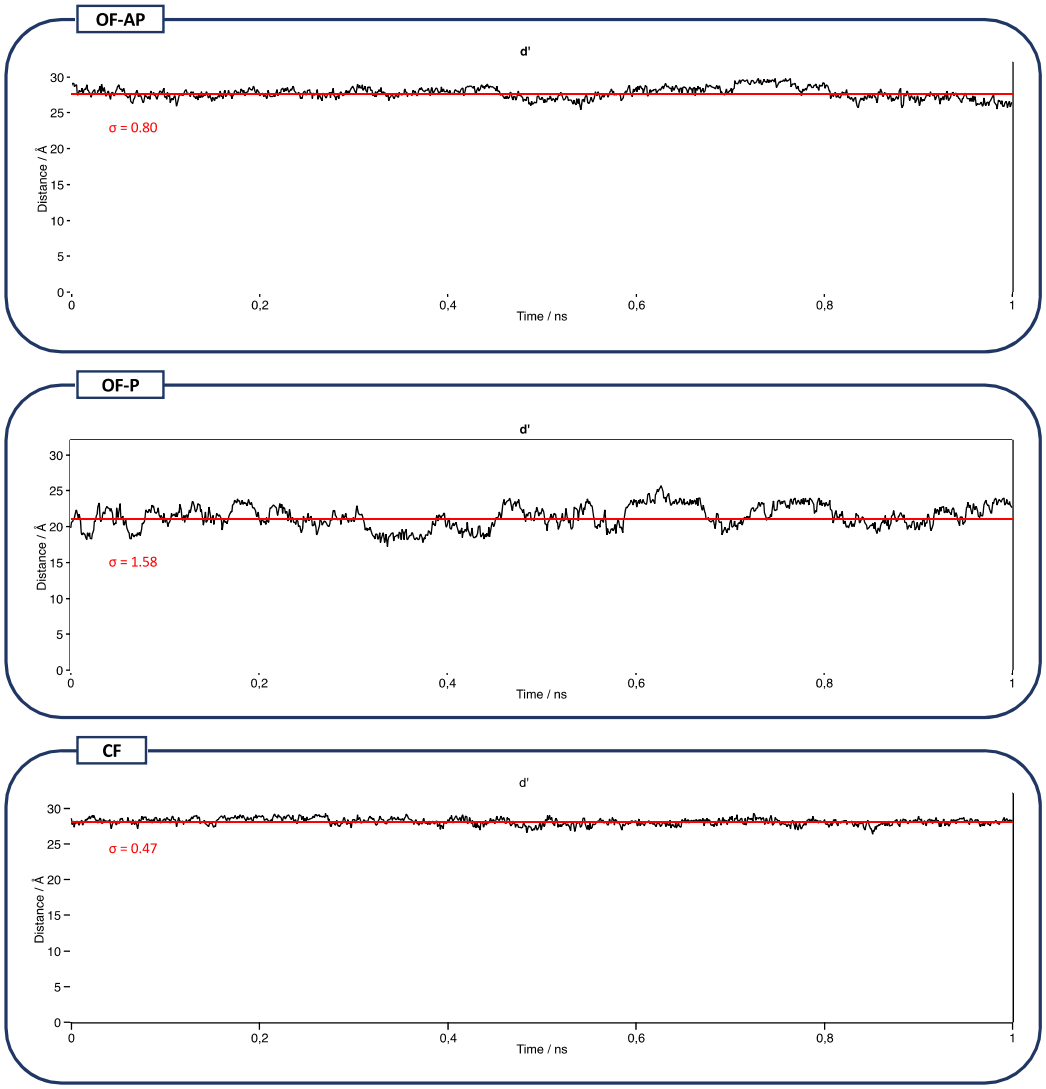

FIGURE 3.31 – Time evolution of the d' distance (in Å) along the 1 ns trajectory for the isomers **OF-AP** (top), **OF-P** (middle) and **CF** (bottom).

trix, one can say that:

- All the standard deviations of all the structural parameters are lower for the **CF** conformer. This is particularly the case for the d_{cc} distance (σ= 0.03 Å for the **CF** conformer *vs* σ= 0.13 and 0.11 Å for the **OF-AP** and **OF-P** conformers respectively) and the d' one (σ0.47 Å for the **CF** conformer *vs* σ= 0.80 and 1.58 Å for the **OF-AP** and **OF-P** conformers respectively).

- The same relative flexibility as the one in solution is found within the polymer matrix. The **CF** conformer is the less flexible, followed by **OF-AP** conformer while **OF-P** confor-

mer is the most flexible one.

To go further in the analysis of the evolution of the different structural parameters within the polymer matrix, one can make a comparison with what was observed in solution (see Table 3.28). It appears that globally and logically, the **DTE-Upy** molecules are less flexible within the polymer. Indeed, for each structural parameter, the standard deviation, that measures the fluctuation with respect to the average value, is lower within the polymer matrix. Even if a relative flexibility is allowed (d_i distances still have large variations) the **DTE-Upy** molecules and more particularly the **DTE** core, are constrained by the polymer chains. The polymer chains thus have a mechanical effect on the photochromic molecules. As a final remark, all the statements that have been made for each trajectory chosen for each conformer are also valid for the 9 other simulations presented in Appendices A-16, A-17 and A-18.

Simulation of 5 ns of the OF-AP conformer.

As it has been said before, for a short time simulation (1ns), even in solution, the interconversion is not systematic. Necessarily, in a really dense environment and due to the slow reorganization time of the polymer, the interconversion process may not be seen. To overcome this potential issue, we performed a longer simulation (5ns). We followed the time evolution of the two dihedrals ϕ_1 and ϕ_2 (see Figure 3.32).

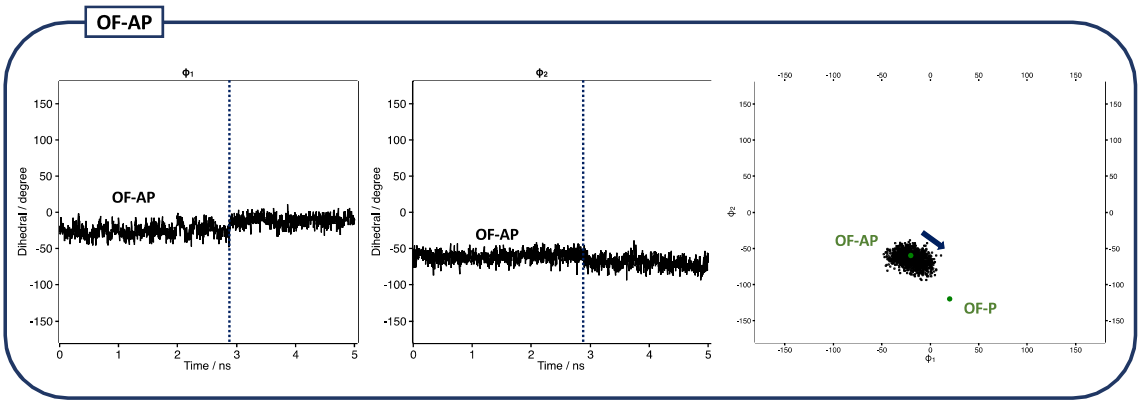

FIGURE 3.32 – Time evolution (5ns) of the ϕ_1 and ϕ_2 dihedrals for the **OF-AP** isomer (right). The values couple (ϕ_1,ϕ_2) are also represented (right). The average values the value couple (ϕ_1,ϕ_2) obtained in solution are represented with green dots.

The first conclusion is that we do not see a proper interconversion process. Nevertheless, we observe a conformational change. Indeed, the average values of the first 3 ns are (-20°;-60°). At 3 ns we observed a transition and the new couple values is (-10°;-70°). The values are thus slowly moving towards the characteristic values of the **OF-P** conformer. It illustrates that the interconversion process may be possible within the polymer matrix but on a longer time scale.

3.3.2.2 Optical properties

We have already shown in Section 3.2 that the flexibility of the systems had an impact on the UV-Vis absorption properties. It was found that the flexibility was inducing a large distribution of the maximum absorption wavelength (λ_{max}). In this part, we aim at investigating the impact of the loss of flexibility (and thus of the polymer matrix) on the absorption properties. To do so, for each simulation of 1 ns, we have randomly selected 10 snapshots and calculated their optical properties using the protocol explained in Section 3.3.1.2. Finally, 100 snapshots are considered for each conformer.

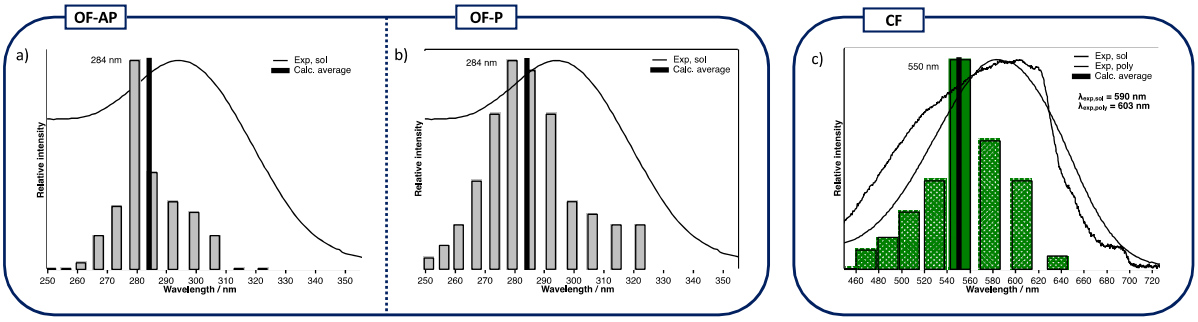

FIGURE 3.33 – Histograms of the distribution of the maximum absorption wavelength λ_{max} in nm (bin sizes: 0.10 eV). (a), (b) and (c): distributions calculated for 100 snapshots extracted from the MD trajectories corresponding respectively to an initial **OF-AP**, **OF-P** and **CF** conformation respectively. For each histogram, the average value of the λ_{max} is given and the experimental UV-Vis absorption spectrum in solution [157] and for the polymer matrix are provided.

Figure 3.33 provides the distribution of the maximum absorption wavelength, λ_{max}, calculated from the 100 snapshots extracted from the MD trajectory for the three confor-

mers.

(1) For **OF-AP** (**OF-P**) the minimum and the maximum wavelength, λ_{max}, were ranging from 250 nm to 310 nm with a standard deviation of the λ_{max} of 10 (15) nm. Within the polymer matrix the results are similar with calculated λ_{max} values between 260 nm and 310 nm and a standard deviation of 12 (14) nm. Nevertheless, within the polymer matrix, the distribution of the maximum absorption wavelength is red-shifted with respect to what was observed in solution. This is illustrated *via* the value of the average λ_{max}. In solution the average value was equal to 276 nm while in the polymer, the average value reaches 284 nm.

(2) For **CF** the minimum and the maximum wavelength, λ_{max}, were ranging from 480 nm to 680 nm with a standard deviation of 35 nm. Within the polymer matrix the results are similar with calculated values between 460 nm and 640 nm and a standard deviation of 30 nm. Nevertheless, within the polymer matrix, the distribution of the maximum absorption wavelength is slightly blue-shifted with respect to what was observed in solution. This is illustrated *via* the value the average λ_{max}. In solution the average value was equal to 557 nm while in the polymer, the average value reaches 550 nm.

The polymer matrix, by avoiding the large flexibility that was observed in solution, has a slight impact on the optical properties as: (1) the average λ_{max} are respectively red-shifted for the **OF** isomers and blue-shifted for the **CF** and (2) it appears that the distribution of the maximum absorption wavelength is narrower within the polymer matrix. This is in line with the loss of flexibility that is observed in polybutadiene matrix.

3.3.3 Impact of the photochemical reaction on the matrix

In this part, we aim at studying the impact of the photochemical reaction on the polymer matrix. The photochemical reaction, **OF-AP** $\rightleftarrows$ **CF**, implies a large structural modification. Indeed the **DTE** core of the **CF** isomer is planar (this is illustrated by the small values of ϕ_1 and ϕ_2) while the **OF-AP** is not. Going from one isomer to the other may induce constraints on the surrounding polymer chains. One has to notice that this photochemical reaction is really fast (≈fs) [172] while the the reorganization time of the polymer is much more longer. By considering the polymer time scale, one can say that the photochemical reaction is instantaneous. We will thus induce a brutal **OF**→**CF** or **CF**→**OF** geometrical change and study the relaxation of the polymer around the **DTE-Upy** molecule. The hypothesis that is made is that the photochromic reaction (cyclization and cycloreversion) is possible within the polymer environment that is to say that the d_{cc} distance is lower than 4.2 Å and the nature of the LUMO orbital of the **DTE-Upy** has the desired photochromic characteristic (bonding interaction between the two reactive carbons) [171].

3.3.3.1 Embedded photochemical reaction: How ?

First, one need to perform the polymerization around whether the **OF-AP** or **CF** conformer. Let's consider the example of the cycloreversion **CF**→ **OF-AP**. To mimic this photochemical reaction, one need to fulfill the following tasks:

- Consider the **CF** structure along with its surrounding polymer chains.
- Change the connectivity between the two reactive carbons that should not be bonded anymore.
- Change the atom types when necessary.
- Change the charges in order to consider the charges of an **OF-AP** conformer instead of the **CF** charges.
- Change the force field in order to consider the one appropriate to describe an **OF-AP** isomer and no longer the **CF** conformer.

Once this step is done, one has an input containing the geometry of the **CF** conformer with all the parameters (connectivity, charges, force field, atom type) corresponding to the **OF-AP** conformer.

Obviously, this structure is really constrained. The first step thus consisted in a minimization process of the **DTE-Upy** with fixed **BTDN** chains (the details of the parameters used to perform this step are gathered in Table 3.10). The steepest descent algorithm is used. Once this step is achieved, a production step is performed in the NVE ensemble. One has to notice that a preliminary step to the production may be necessary if the structure obtained after minimization is really constrained. One can perform a LNVT production, with frozen **BTDN** chains, in order to further relax the structure of the **DTE-Upy** that may have been trapped in a potential well.

TABLE 3.10 – Important parameters used during the simulations in STAMP. For each ensemble that has been used, MIN (minimization), LNVT (NVT ensemble + friction coefficient) and NVE, the parameters have been listed.

	MIN	LNVT	NVE
DTE-Upy	Free	Free	Free
BTDN	Frozen	Frozen	Free
T (K)	300	300	300
PBC	Yes	Yes	Yes
γ	-	10^{12}	-
Simulation time (ns)	-	0.2	1

3.3.3.2 Minimization

For both reactions that we are trying to mimic (**OF-AP**$\rightarrow$ **CF** and **CF**$\rightarrow$ **OF-AP**) a minimization process has been performed, with frozen **BTDN** chains.

In the following, we will represent, for both reactions (**OF-AP**$\rightarrow$ **CF** and **CF**$\rightarrow$ **OF-AP**), the local pressures before and after a minimization process. The Viriel methods is used to calculate the pressure [173]. It allows to retrieve individual pressure values, for each atom. The corresponding "pressure map" is visualized thanks to Ovito software [174]. Although pressure should ideally be considered for a volume element and not for individual atoms, the STAMP code does not currently have the functionality that will allow us to average the pressure over a given volume and get rid of its strong local fluctuations (this

is work in progress). For these technical reasons, we will thus represent the qualitative evolution of the atomic pressure without specifying the pressure scale (Figures 3.35, 3.37, 3.38).

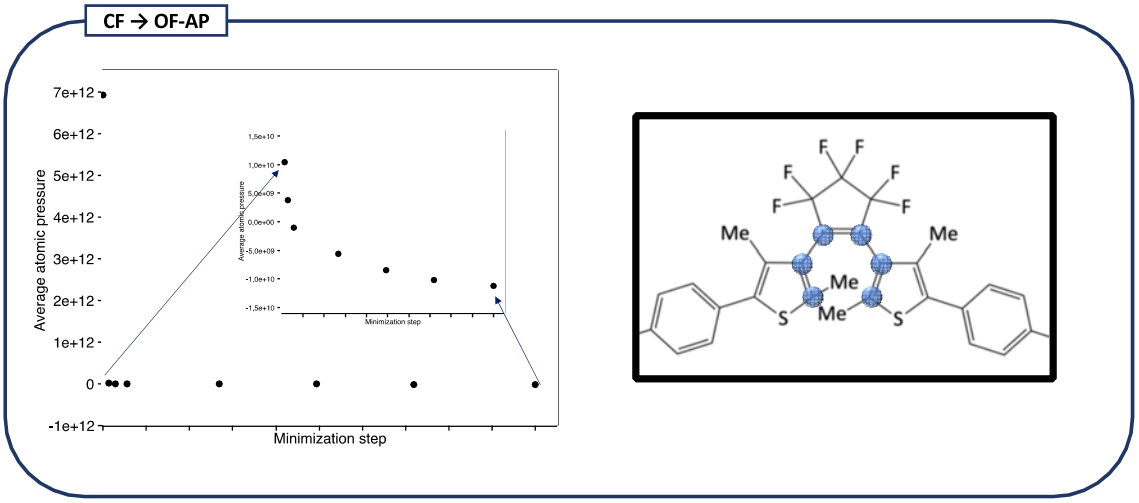

FIGURE 3.34 – Evolution of the average pressure of the six atoms that are involved in the photochemical reaction (right).

The color scale has been chosen so as to highlight the local pressure variations. In order to justify this representation, we have represented the average atomic (local) pressure for the atoms involved in the reverse photochromic reaction, that is to say **CF**→ **OF-AP** (see Figure 3.34). One can observe that the average pressure for the six atoms involved in the cycloreversion reaction (see the right part of Figure 3.34) is decreasing upon minimization. On Figure 3.35 it can be seen that before the minimization, the pressure for the atoms of the **DTE-Upy** is high (yellow/light green colors for most of the atoms of the **DTE-Upy** core).

It was expected as the force field and the charges that are used to describe this molecule are the ones of the **CF** while the structure, before minimization, is the one of **OF-AP**. Upon minimization, the pressure on each atom is decreasing as the structure is moving toward a proper **CF** isomer. To control the nature of the obtained final structure we looked at some key parameters that characterize each conformer, namely d_{cc} distance (Figure 3.36) and (ϕ_1;ϕ_2) dihedrals. The starting point, corresponding to **OF-AP**, has a d_{cc} equal to 3.70 Å and couple values of (-23°;-58°).

The final structure has a d_{cc} equal to 1.68 Å and couple values of (-15°;3°). The

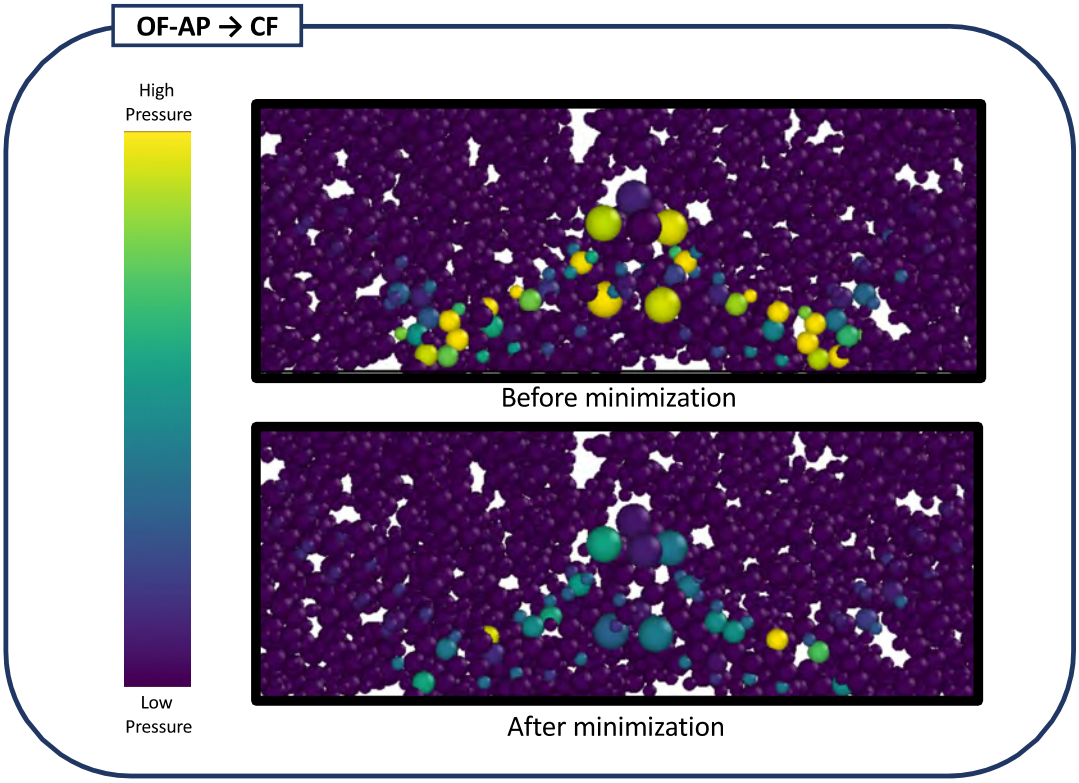

FIGURE 3.35 – Representation of the pressure before (top) and after (bottom) the minimization process for the **OF-AP**→ **CF** structural modification. Atoms with a high pressure are yellow and atoms with lower pressure are represented in purple.

minimization process thus provides a proper **CF** conformer. As indicated in Table 3.10, during this step, all the **BTDN** chains are frozen and are not impacted by the pressure induced by the atoms of the **DTE-Upy**.
On Figure 3.37 we have represented the values of the atomic pressure before and after the optimization process of the **DTE-Upy** for the opening reaction, that is to say **CF**→ **OF-AP**.

Once again it can be seen that before the minimization process, all the atoms of the **DTE-Upy** core are under pressure (yellow color for almost all of them) while after the minimization process the pressure of each atom has decreased. The final structure was analyzed to ensure the presence of **OF-AP**. The d_{cc} distance is thus equal to 3.66 Å while the two dihedrals are (-18°;-63°) for initial values of 1.54 Å for the d_{cc} and couple values of (-14°;4°) for the initial structure. The minimization process thus permits to obtain a

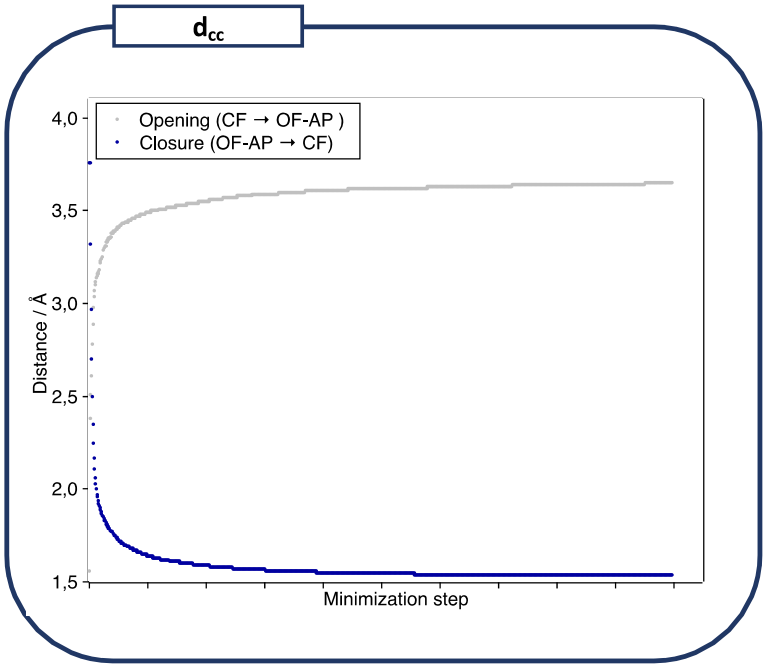

FIGURE 3.36 – Evolution of the d_{cc} distance upon minimization for cyclization (**OF-AP**→ **CF**) and cycloreversion (**CF**→ **OF-AP**) reactions.

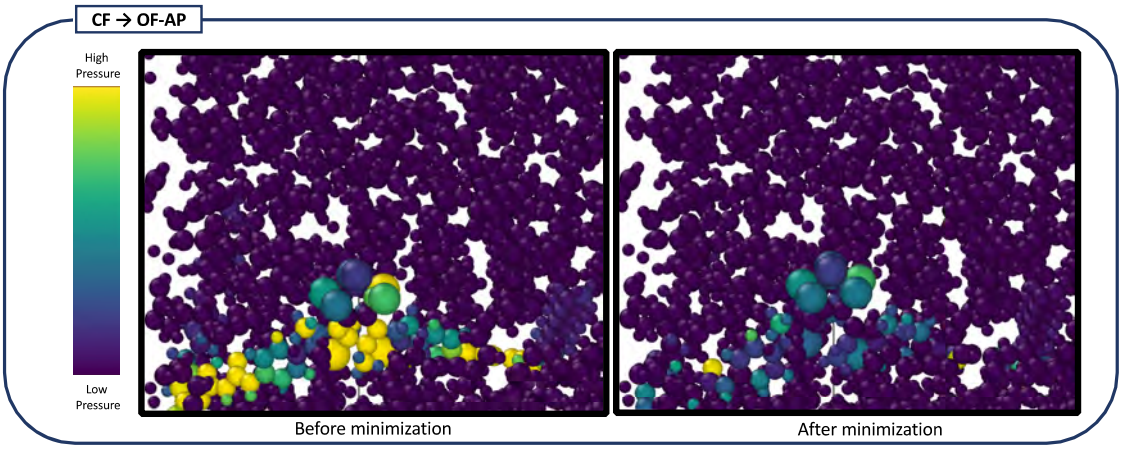

FIGURE 3.37 – Representation of the pressure before (left) and after (right) the minimization process for the **CF**→ **OF-AP** structural modification. Atoms with a high pressure are yellow and atoms with lower pressure are represented in purple.

proper **OF-AP** conformer starting from **CF** conformer.

One remark concerning both mimicked reaction, the lateral alkyl chains are not affected, in terms of pressure, by the nature of the conformer (**OF-AP** or **CF**). Indeed, the atoms of those lateral chains have more or less the same pressure as the surrounding polymer chains

in which they are embedded. It means the minimization process particularly involves the **DTE** core and the **Upy** moieties.

As already mentioned, all the polymer chains were frozen during the minimization process. In the next step (NVE production), all the molecules (**DTE-Upy** and **BTDN** polymer chains) will be free. The aim will be to investigate the impact of this brutal structural modification of **DTE-Upy** on the surrounding polymer chains and more generally on the polymer matrix.

3.3.3.3 NVE production

Starting from what was obtained in the previous step we performed NVE simulation for both mimicked photochemical reaction. The NVE ensemble lets the forces drive the entire dynamics of the system and is not perturbed by any spurious effect or artefact on the equations of motion: therefore it is the most natural ensemble to study the time evolution of strongly dynamic processes. The results in terms of pressure for each atoms are represented on Figure 3.38.

If one look at the **OF-AP**$\rightarrow$ **CF** mimicked reaction, one can observe that at a time t_0, few constraints are imposed on the polymer matrix by the newly minimized **CF** conformer. Indeed, some of the atoms around the **DTE-Upy** are tinted in yellow/light green, indicating a high pressure for this atoms. Upon increasing the simulation time, one can observe that the pressure is progressively decreasing (yellow/light green atoms are vanishing to give rise to more green/light blue one, indicating a lower pressure). At a time t= 1 ns, almost all of the constraints that were imposed by the **DTE-Upy** on the polymer matrix have disappeared.

For the **CF**$\rightarrow$ **OF-AP** mimicked reaction, at a time t=0 ns, one can observe strong constraints around the **OF-AP** molecule. Indeed, a lot of atoms are yellow-colored around the **OF-AP** molecule, indicating a high pressure. As the simulation goes on (t=0.5 ns), it appears that this high pressure is "communicated" to the neighboring atoms. This is illustrated on Figure 3.38 by the red dotted circle which is wider at t=0.5 ns than at t=0 ns. At t=1 ns, the red dotted circle is even wider, indicating more atoms with a

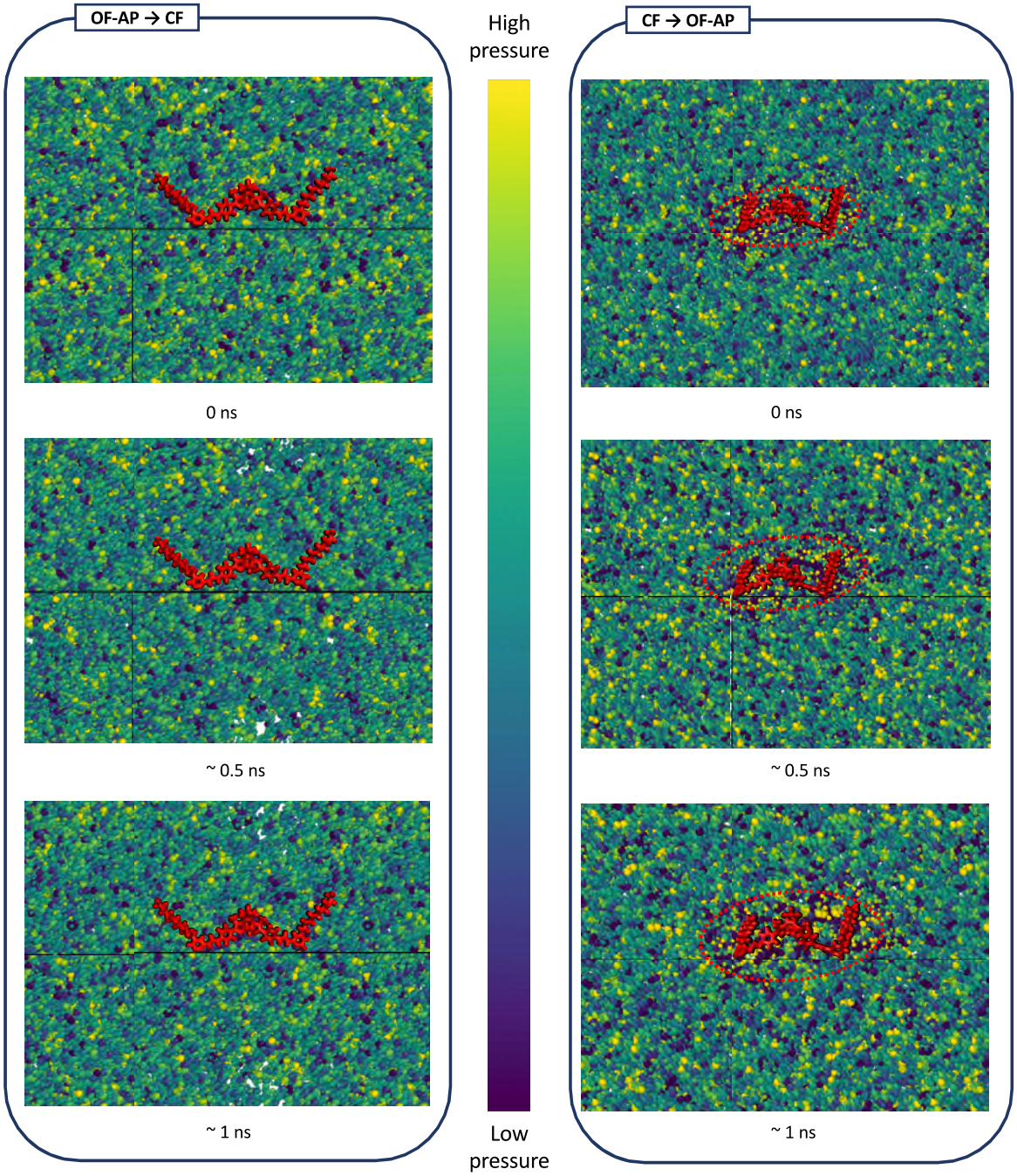

FIGURE 3.38 – Representation of the pressure at time t=0, 0.5 and 1 ns of NVE simulation for **OF-AP**→ **CF** (left) and **CF**→ **OF-AP** structural modification. To highlight the position of the **DTE-Upy** molecule within this really dense environment, we have superposed its structure, colored in red, on the pressure map. Atoms with a high pressure are yellow and atoms with lower pressure are represented in purple.

high pressure, meaning that the pressure is being "dissipated", step by step, all over the polymer matrix.

As a conclusion of this part, it appears that:

- For the closure reaction (**OF-AP**→ **CF**) no strong constraints are imposed on the polymer matrix. Indeed, after less than 1 ns, the pressure of each atom of the polymer matrix has an average low value and no "constrained" points (atoms or area with high pressure) are observed. This can be explained by the fact that, for the **OF-AP**→ **CF** reaction, the initial structure has its two parts that are staggered (illustrated *via* the values of ϕ_1 and ϕ_2), the polymer is thus adapted to this staggered configuration for the two arms of the **OF-AP**. The **CF** structure is more planar (due to the bond between the two reactive carbons that rigidifies the all structure) and may have less structural impact on the surrounding polymer chains that were adapted to **OF-AP**. In a simpler way, for the same cavity size, if one replaced **OF-AP** by **CF**, the boundary of this cavity will not be strongly impacted by this change as the **CF** conformer occupy less volume than **OF-AP**.
- For the opening reaction (**CF**→ **OF-AP**), the constraints imposed by the **DTE-Upy** on the polymer matrix are strong. One can define a "constraint layer" in which the atoms seem to be affected (the pressure for each atom is thus high) by the presence of the brutally formed **OF-AP** conformer. This constraint layer is getting larger upon increase of the simulation time. Contrary to the **OF-AP**→ **CF** reaction, the **CF**→ **OF-AP** reaction induces large structural modification as described in the previous point. The polymer matrix which was adapted to the **CF** has now to adapt itself to a new conformer, occupying more volume due to its two staggered parts. Finally, due to this strong constraint, it appears that 1 ns is not enough for the polymer matrix to "absorb" this constraint. After 1 ns, this constraint is still spreading around the **DTE-Upy** molecule. Indeed, the characteristic relaxation time of a polymer is dependent of the size of the polymer chains. Even if in our case the polymer chains are relatively short, the relaxation time can easily reaches the millisecond. The opening reaction has thus more impact on the polymer matrix than the closure reaction.

3.4 Conclusion

In this chapter we have proposed to study a photochromic molecule, namely the **DTE-Upy** photoswitch. This molecule has been considered in different environments as its behavior has been experimentally characterized in both solution (chloroform) and polymer matrix.

The aim of our theoretical investigations was to provide answers or indications concerning the observed experimental features:

- In solution, why the supramolecular assembly was only possible for **CF** conformers ?

- In polymer matrix, can we explain the optomechanical effect ? How can a reaction occurring at a molecular level has an impact at a macroscopic level and modify the morphology of the material ?

Of course, the experimental systems were really complex to model and the first step we had to do was to simplify those systems to develop first the code and the methodology in collaboration with the CEA and to make them easier to simulate. This is why for example for the behavior in the polymer matrix, a simpler polymer was considered, namely the polybutadiene. Another important point was to define a strategy able to provide answers to the experimental questions. For the behavior in solution, we designed a strategy that consisted in studying successively monomers, dimers, hexamers and π-stacked dimers.

In solution we provided a beam of evidences allowing the comprehension of the differences that were observed between **OF** and **CF**, especially why supramolecular assemblies were only possible for **CF**.

In the polymer matrix, we studied first the impact of a polybutadiene matrix on the **DTE-Upy** molecules (**OF-AP**, **OF-P** and **CF**) and secondly the impact induced by the cyclization/cycloreversion reactions (**OF-AP**$\rightarrow$ **CF** and **CF**$\rightarrow$ **OF-AP**) on the polymer matrix. We showed that, logically, the polymer matrix has a mechanical impact on the **DTE-Upy** molecules. Indeed, the flexibility, specially the one of the **DTE** core and in a lesser extent of the lateral alkyl chains is lower within the polymer. Concerning the impact of the photochemical reaction on the polymer matrix, we have seen that the cycloreversion has more impact than the cyclization. Some of the perspectives that are currently in progress are to consider (1) longer simulation time, especially for the **CF**$\rightarrow$ **OF-AP**

as we saw that after 1 ns the polymer was still trying to spread the locally high pressure generated by the brutal change of **DTE-Upy** conformer and (2) be able to plot maps with average pressures.

General conclusion and perspectives

In this manuscript we have presented several investigations dealing with photoinduced processes that are impacted by the environment that can be seen as a constraint. The main goals of this thesis were to (1) propose different calculation protocols able to take into account the wide range of environments that are experimentally considered (solution, aggregate, crystal, polymer matrix) and (2) rationalize the effect of a particular environment on the photoinduced processes (absorption, emission, photochemical reactions). Throughout those studies we mainly used DFT and TD-DFT but also classical molecular dynamics (with AMBER and STAMP codes) and hybrid approaches (ONIOM).

In Chapter 2, we presented the theoretical studies we performed concerning the rationalization of *Aggregation Caused Quenching*, *Aggregation Induced Emission* and *Crystallization Induced Emission* phenomena. Three systems have been considered (**FOEB** molecule, isomers of **DPYDPE** and derivatives of **TTP**) and each time an effort has been made to propose an accurate calculation protocol able to reproduce the optical properties (absorption and emission) but also to take into account the different environments. Once the calculation scheme was set up, we systematically provide an explanation of the poorly or strongly emissive behavior within a given environment by investigating one non-radiative desexcitation pathway, namely the vibrational desexcitation. One has to notice that throughout our study the RACI (Restricted Access to Conical Intersection) mechanism has never been highlighted to account for the emission modulation. It was demonstrated by the calculation of the Huang Rhys factors and the careful study of the

vibrational modes at low frequencies. Using the same concepts, we have been able to explain the modulation that existed, for one given molecule, between different environments and thus to propose an explanation for ACQ/AIE/CIE phenomena.

In Chapter 3 we presented the theoretical studies that have been carried out in collaboration, first with Dr. S. Aloïse from University of Lille 1 and secondly with Dr. C. Lemarchand and Dr. N. Pineau from CEA DAM/DIF. The molecules under study were the **DTE-Upy** photoswitches. The experimental questions were numerous. Why a supramolecular assembly (large enough to observe a blue precipitate in solution) was possible only for the closed form isomers ? Is computational chemistry able to rationalize the optomechanical effect observe for a system involving both **DTE-Upy** molecules and polymer chains ? The first challenge to answer those questions was to be able to reproduce the experimental conditions or at least to propose a reasonable approximation of those environments.

In a first part, to study the behavior of the **DTE-Upy** molecules in solution we adopted a systematic study of the three conformers (the two open forms and the closed form) as monomers, dimers, hexamers and π-stacked dimers. The study of the monomers has allowed us, among other conclusions, to highlight the systematic interconversion process occurring between the antiparallel and parallel open forms isomers but also the large flexibility of the open forms compared to the closed form. Going toward larger assemblies has lead to different observations:

- For dimers of the parallel open form isomer, a limiting form involving 8 hydrogen bonds has been found. This limiting form avoids the formation of larger assemblies and can be found even when starting from two antiparallel open form isomers due to the systematic antiparallel/parallel interconversion.
- For hexamers, the flexibility is higher for systems involving open form isomer compared to the closed form. This flexibility is unfavorable to the progression of the supramolecular assembly.
- A limiting structure, avoiding larger assemblies, has also been found for π-stacked dimers involving open form isomers.

All those evidences allow us to provide some answers to the experimentalists concerning

the difference between open and closed form conformers and to the limited supramolecular assembly process for the open form. Aside the problem of the relative flexibility of the open and closed isomers, the existence and the properties of the parallel conformer are of high importance to account for the experimental observations.
In a second part we have considered the **DTE-Upy** conformers in a polymer matrix. We used, in collaboration with CEA, classical molecular dynamics with the STAMP molecular dynamics code. Developments have been implemented in the STAMP code by our collaborators in CEA in the course of this PhD project so as to study such photoactive systems. Contrary to previous studies dedicated to the study of photoactive molecules embedded in a polymer matrix, it allows *in situ* polymerization. We have rationalized the effect of the polymer matrix on the structural parameters and by extension on the optical properties. We also started the investigation of the effect of the photochemical reaction on the matrix. Once again, we designed an appropriate computational protocol to mimic this photochemical reaction.

Concerning the perspectives associated to Chapter 2 and the study on ACQ, AIE and CIE, the objective is now to adopt a more quantitative approach with for example the calculation of the HR factors within an ONIOM approach (for aggregates, crystals and polymer matrices). From a technical point of view it was not possible to achieve this type of calculation with Gaussian16. One can also mention the calculation of the non-radiative decay constant, k_{nr}, that will give an objective parameter concerning the emissive behavior of the molecules within the different environments. It can be achieved by using MOMAP software [175, 176]. It is a suite of codes that allows the calculation of photophysical properties.
In Chapter 3, the main work that remains to do concerns the polymer. Indeed, in our work we considered a model polybutadiene matrix.

Even if it was a reasonable starting point to set up the computational approach and to develop all the analysis tools, it is not the experimental one (the structure is represented on Figure C.1). One possible development can thus be to consider for example:
- A functionalization, with **Upy** moieties, of the polymer chains. The idea is to create a H-bond network between **DTE-Upy** molecules and polymer chains that can amplify the

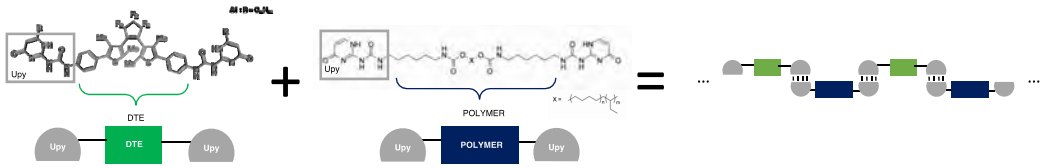

FIGURE C.1 – Representation of experimental polymer structure with the **Upy** functionalization (middle). Schematic representation of the possible supramolecular assembly involving **DTE-Upy** molecules and polymer molecules (right).

photoinduced structural modifications of the thin film (Figure C.1).

- The kinetics of the polymer relaxation being slow, longer simulations may be useful. For the moment we systematically performed 1 ns of simulation.

Another project has already been initiated in order to describe AIEgens in polymeric environments. This study thus combines the two "aspects" that have been developed in this PhD project. This type of system combining emissive molecules and a polymer embedding are particularly used for applications such as Luminescent Solar Concentrators (LSC) [177, 178]. We combined the protocol we have developed in the two previous chapters, that is to say the study of the modulation of the emission efficiency along with the environment and the new *in situ* polymerization scheme. We have studied the Triphenylamine-(Z)-4-benzylidiene-2-methyloxazol-5 (4H)-one (**TPA-BMO**), represented on Figure C.2.

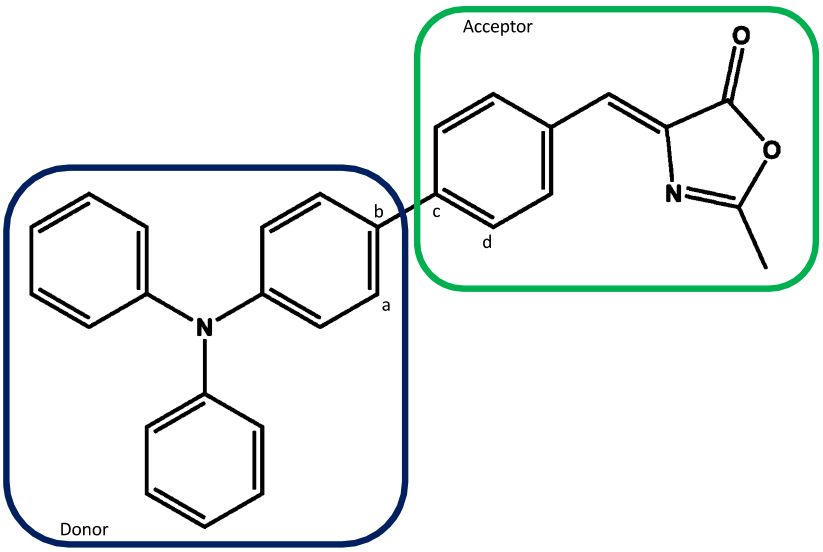

FIGURE C.2 – Representation of the structure of the **TPABMO** molecule.

This molecule can be divided into two parts, the **TPA** constitutes the donor part while the **BMO** is the acceptor part. The way the **TPA** and the **BMO** moieties are connected to each other, creates a conjugation path all over the molecule.
The interest of this molecule lies in the modulation of its fluorescence efficiency as a function of the environment under consideration (Table C.1).

One can observe a modulation of the fluorescence quantum yield (Φ_F) and of the emission wavelength (λ_{em}) with the solvent polarity [179]. It appears that, contrary to what is usually observed for ACQ molecules, the emission of **TPA-BMO** is not quenched in aggregate [180]. Moreover, the crystalline structure seems to have a low CIE phenomenon compared with non polar solvents (Φ_F=46% and 62% in the crystal and in DXN solution respectively). Finally, within a polymer matrix of whether polybutadiene, poly (methyl

TABLE C.1 – Experimental properties of the **TPA-BMO** molecules in various solvents [179], aggregate [180], crystalline phase [181] and in different polymer matrix [182]. The optical (absorption and emission) properties are given in nm. The fluorescence quantum yield, Φ_F, is also provided.

	Solution			Aggregate	Crystal	Polymer		
	DXN[a]	THF[b]	ACN[c]	-	-	PB[d]	PMMA[e]	PEG[f]
λ_{max}	406	407	408	425	-	-	-	-
λ_{em}	530	576	580, 700	574	635	499	525	567
Φ_F	0.62	0.51	0.03	-	0.46	-	-	-

[a] Dioxane. [b] Tetrahydrofuran. [c] Acetonitrile. [d] Polybutadiene. [e] Poly(methyl methacrylate). [f] Polyethylene glycol.

methacrylate) or polyethylene glycol, the position of the emission band shifts to longer wavelengths as the polarity of the polymer chains increases. This feature is a really important experimental parameter as it can be used to differentiate and to unravel the nature of mixed polymer phases [182]. Following the procedure we have developed and described in the two previous chapters, calculations have been performed to study the **TPA-BMO** in all the mentioned environments that is to say:

- In solution and in different solvents. The aim is to explain the modulation of Φ_F along with the variation of λ_{em} with the polarity of the solvent.
- In aggregate, to explain the variation of λ_{max} and λ_{em}.
- In the crystalline phase, to explain the λ_{em} variation and the slight CIE effect.
- In the polymer matrix, to explain the modulation of λ_{em} in different polymers. For the moment, only PB polymer is considered. The aim is thus to be able to explain the blue-shift with respect to non-polar solvents (DXN).

The novelty of this work regarding what has been done previously lies in the consideration of the emission properties and thus of the study of excited states in complex environments. We have represented on Figure C.3 some preliminary results.

The main conclusion of those preliminary results is that, even if we are not able to predict precisely the position of the different absorption and/or emission bands our careful choice of computational protocol is able to reproduce the trend that is observed

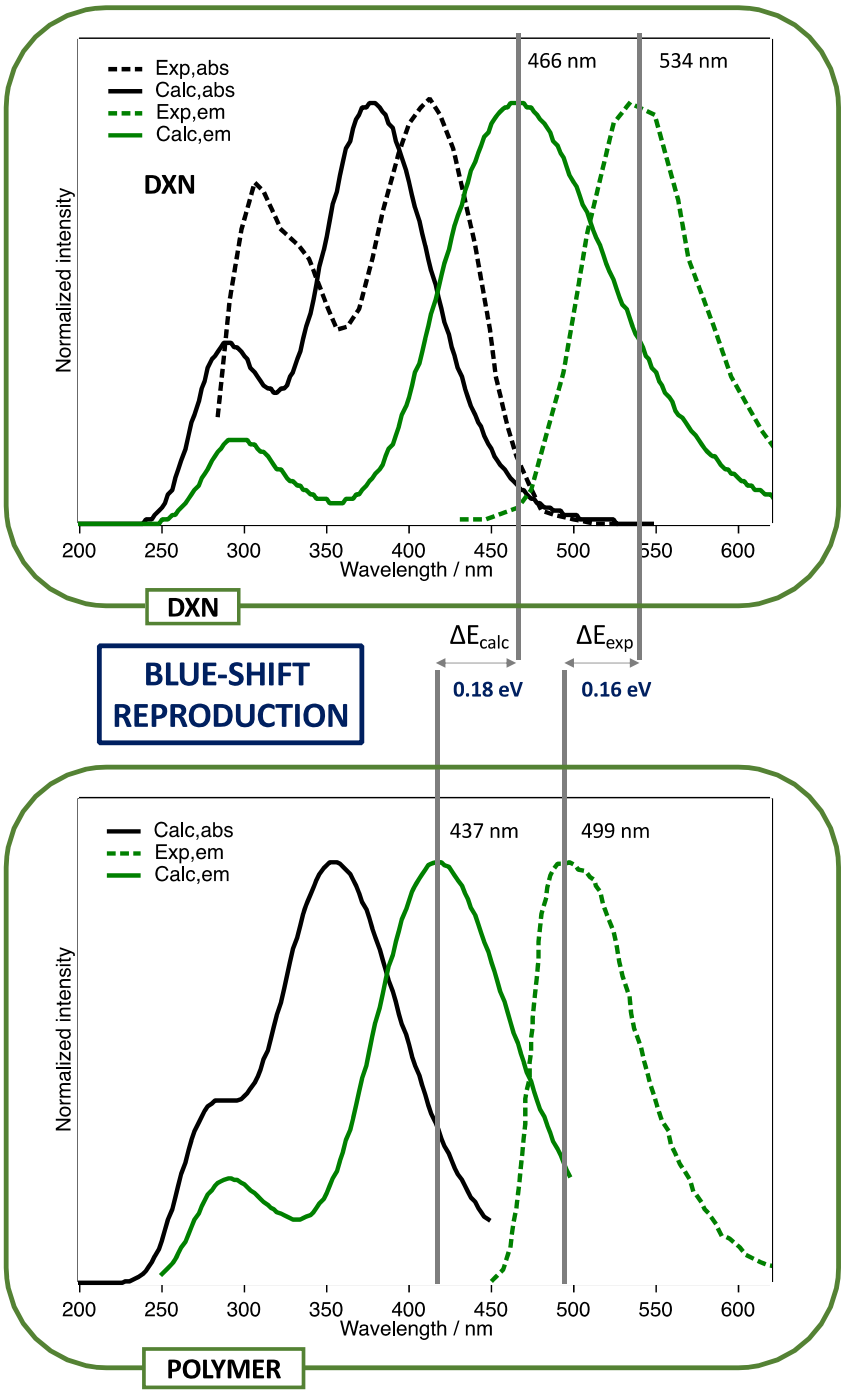

FIGURE C.3 – Calculated normalized absorption and emission spectra (convoluted with a gaussian function, FWHM=0.33 eV) for a **TPA-BMO** molecule in a DXN solvent (top) and within a PB polymer matrix (bottom). The experimental spectra, when available, are also provided [179, 182].

between DXN solution and PB polymer matrix (all the calculations have been performed using M06-2X functional and 6-311+G(d,p) basis set). Indeed, experimentally, a blue shift of 0.16 eV is observed between the λ_{em} in DXN (534 nm) and in PB matrix (499 nm). With our calculations, we obtain a blue shift of 0.18 eV. As previously said, one can find fluorophores embedded in polymer matrix in LSC. LSC are transparent layers containing fluorophores and allowing to concentrate the sun light on a small surface. As the refraction index of the material is higher that the one of the environment, the LSC will trap some of the incident photons thanks to a total intern reflexion. The LSC allows to decrease the amount of photovoltaic materials to use. The main issue to circumvent for this kind of system is the possible aggregation process of the fluorophores that may lead to ACQ phenomenon. AIEgen are thus good candidates for LSC applications. The methodologies that have been developed throughout this study can be used to help the design of new materials.

As it is now possible to (1) consider organic molecules within a polymer matrix and (2) quantify the impact they have on each other, one can imagine to impose external constraints (compression, stretching, shearing) and go towards mechanochromism or mechanofluorochromism.

Mechanochromism is actually the change of color of a material upon application of an external force. The change of emission properties upon application mechanical force is known as mechanofluorochromism, luminescent molecules see their optical properties modified (intensity and/or color) upon application of external mechanical forces. The latest are particularly used as mechanosensors [183]. In this case, the mechanofluorochromic molecules are used as "evidences" of the constraints that can be applied to a material. Indeed, if the material is stressed in a particular way, the mechanofluorochromic molecule will emit light or not and evidence the mechanical constraint. The approaches that have been developed within the framework of this thesis can naturally be applied in the context of designing new mechanochromic materials.

Bibliography

[1] T. R. Kelly, H. De Silva, and R. A. Silva. *Nature*, **1999**, 401(6749):150–152.

[2] N. Koumura, R. W. J. Zijlstra, R. A. van Delden, N. Harada, and B. L. Feringa. *Nature*, **1999**, 401(6749):152–155.

[3] B. L. Feringa, R. A. van Delden, N. Koumura, and E. M. Geertsema. *Chem. Rev.*, **2000**, 100(5):1789–1816.

[4] P. C. Knipe, S. Thompson, and A. D. Hamilton. *Chem. Sci.*, **2015**, 6:1630–1639.

[5] R. A. Bissell, E. CÃ³rdova, A. E. Kaifer, and J. F. Stoddart. *Nature*, **1994**, 369(6476):133–137.

[6] D.-H. Qu, Q.-C. Wang, J. Ren, and H. Tian. *Org. Lett.*, **2004**, 6(13):2085–2088.

[7] J. Delaire, J. Piard, R. Méallet-Renault, and G. Clavier. *Photophysique et photochimie: Des fondements aux applications.* QuinteSciences. EDP Sciences, 2017.

[8] M. Yamada, M. Kondo, J.-i. Mamiya, Y. Yu, M. Kinoshita, C. Barrett, and T. Ikeda. *Angewandte Chemie International Edition*, **2008**, 47(27):4986–4988.

[9] E. Schrödinger. *Phys. Rev.*, **1926**, 28:1049–1070.

[10] M. Born and R. Oppenheimer. *Ann. Phys. (Berlin)*, **1927**, 389(20):457–484.

[11] J. C. Slater. *Phys. Rev.*, **1929**, 34:1293–1322.

[12] R. Ditchfield, W. J. Hehre, and J. A. Pople. *J. Chem. Phys.*, **1971**, 54:724–728.

[13] P.-O. Löwdin. *Rev. Mod. Phys.*, **1962**, 34:80–87.

[14] P. Hohenberg and W. Kohn. *Phys. Rev.*, **1964**, 136:B864–B871.

[15] W. Kohn and L. J. Sham. *Phys. Rev.*, **1965**, 140:A1133–A1138.

[16] J. P. Perdew, A. Ruzsinszky, L. A. Constantin, J. Sun, and G. I. Csonka. *J. Chem. Theory Comput.*, **2009**, 5(4):902–908.

[17] A. Savin. On degeneracy, near-degeneracy and density functional theory. In J. Seminario, editor, *Recent Developments and Applications of Modern Density Functional Theory*, volume 4 of *Theoretical and Computational Chemistry*, pages 327 – 357. Elsevier, 1996.

[18] D. Jacquemin, E. A. Perpète, G. E. Scuseria, I. Ciofini, and C. Adamo. *J. Chem. Theory Comput.*, **2008**, 4(1):123–135.

[19] D. Jacquemin, A. Planchat, C. Adamo, and B. Mennucci. *J. Chem. Theory Comput.*, **2012**, 8(7):2359–2372.

[20] A. D. Becke. *Phys. Rev. A*, **1988**, 38:3098–3100.

[21] C. Lee, W. Yang, and R. G. Parr. *Phys. Rev. B*, **1988**, 37:785–789.

[22] S. H. Vosko, L. Wilk, and M. Nusair. *Can. J. Phys.*, **1980**, 58(8):1200–1211.

[23] J. P. Perdew, K. Burke, and M. Ernzerhof. *Phys. Rev. Lett.*, **1996**, 77:3865–3868.

[24] J. P. Perdew, K. Burke, and M. Ernzerhof. *Phys. Rev. Lett.*, **1997**, 78:1396–1396.

[25] J.-D. Chai and M. Head-Gordon. *J. Chem. Phys.*, **2008**, 128(8):084106.

[26] M. Casida. *Time-Dependent Density Functional Response Theory for Molecules.* World Scientific, 1995.

[27] M. Casida and M. Huix-Rotllant. *Annu. Rev. Phys. Chem.*, **2012**, 63(1):287–323.

[28] A. D. Laurent and D. Jacquemin. *Int. J. Quantum Chem.*, **2013**, 113(17):2019–2039.

[29] J. Wang, R. M. Wolf, J. W. Caldwell, P. A. Kollman, and D. A. Case. *J. Comput. Chem.*, **2004**, 25:1157–1174.

[30] L. Verlet. *Phys. Rev.*, **1967**, 159:98–103.

[31] H. C. Andersen. *J. Chem. Phys.*, **1980**, 72(4):2384–2393.

[32] R. Berraud-Pache and I. Navizet. *Phys. Chem. Chem. Phys.*, **2016**, 18:27460–27467.

[33] D. Bakowies and W. Thiel. *J. Phys. Chem.*, **1996**, 100(25):10580–10594.

[34] S. Caprasecca, S. Jurinovich, L. Viani, C. Curutchet, and B. Mennucci. *J. Chem. Theory Comput.*, **2014**, 10(4):1588–1598.

[35] Q. Li, B. Mennucci, M. A. Robb, L. Blancafort, and C. Curutchet. *J. Chem. Theory Comput.*, **2015**, 11(4):1674–1682.

[36] M. J. Frisch, G. W. Trucks, H. B. Schlegel, G. E. Scuseria, M. A. Robb, J. R. Cheeseman, G. Scalmani, V. Barone, G. A. Petersson, H. Nakatsuji, X. Li, M. Caricato, A. V. Marenich, J. Bloino, B. G. Janesko, R. Gomperts, B. Mennucci, H. P. Hratchian, J. V. Ortiz, A. F. Izmaylov, J. L. Sonnenberg, D. Williams-Young, F. Ding, F. Lipparini, F. Egidi, J. Goings, B. Peng, A. Petrone, T. Henderson, D. Ranasinghe, V. G. Zakrzewski, J. Gao, N. Rega, G. Zheng, W. Liang, M. Hada, M. Ehara, K. Toyota, R. Fukuda, J. Hasegawa, M. Ishida, T. Nakajima, Y. Honda, O. Kitao, H. Nakai, T. Vreven, K. Throssell, J. A. Montgomery, Jr., J. E. Peralta, F. Ogliaro, M. J. Bearpark, J. J. Heyd, E. N. Brothers, K. N. Kudin, V. N. Staroverov, T. A. Keith, R. Kobayashi, J. Normand, K. Raghavachari, A. P. Rendell, J. C. Burant, S. S. Iyengar, J. Tomasi, M. Cossi, J. M. Millam, M. Klene, C. Adamo, R. Cammi, J. W. Ochterski, R. L. Martin, K. Morokuma, O. Farkas, J. B. Foresman, and D. J. Fox. Gaussian 16 Revision A.03, 2016. Gaussian Inc. Wallingford CT.

[37] H. P. Hratchian, A. V. Krukau, P. V. Parandekar, M. J. Frisch, and K. Raghavachari. *J. Chem. Phys.*, **2011**, 135(1):014105.

[38] N. J. Mayhall, K. Raghavachari, and H. P. Hratchian. *J. Chem. Phys.*, **2010**, 132(11):114107.

[39] P. V. Parandekar, H. P. Hratchian, and K. Raghavachari. *J. Chem. Phys.*, **2008**, 129(14):145101.

[40] N. C. Handy and H. F. Schaefer. *J. Chem. Phys.*, **1984**, 81(11):5031–5033.

[41] H. P. Hratchian, P. V. Parandekar, K. Raghavachari, M. J. Frisch, and T. Vreven. *J. Chem. Phys.*, **2008**, 128(3):034107.

[42] B. Mennucci. *Wiley Interdisciplinary Reviews: Computational Molecular Science*, **2012**, 2(3):386–404.

[43] R. Cammi and B. Mennucci. *J. Chem. Phys.*, **1999**, 110(20):9877–9886.

[44] M. Cossi and V. Barone. *J. Chem. Phys.*, **2001**, 115(10):4708–4717.

[45] M. Caricato, B. Mennucci, J. Tomasi, F. Ingrosso, R. Cammi, S. Corni, and G. Scalmani. *J. Chem. Phys.*, **2006**, 124(12):124520.

[46] R. Improta, V. Barone, G. Scalmani, and M. J. Frisch. *J. Chem. Phys.*, **2006**, 125(5):054103.

[47] C. A. Guido, D. Jacquemin, C. Adamo, and B. Mennucci. *J. Chem. Theory Comput.*, **2015**, 11(12):5782–5790.

[48] J. Franck and E. G. Dymond. *Trans. Faraday Soc.*, **1926**, 21:536–542.

[49] E. Condon. *Phys. Rev.*, **1926**, 28:1182–1201.

[50] M. Kasha. *Discuss. Faraday Soc.*, **1950**, 9:14–19.

[51] M. Kasha and S. P. McGlynn. *Annu. Rev. Phys. Chem.*, **1956**, 7(1):403–424.

[52] R. S. Sánchez-Carrera, M. C. R. Delgado, C. C. Ferrón, R. M. Osuna, V. Hernández, J. T. L. Navarrete, and A. Aspuru-Guzik. *Org. Electron.*, **2010**, 11(10):1701–1712.

[53] C. Deng, Y. Niu, Q. Peng, A. Qin, Z. Shuai, and B. Z. Tang. *J. Chem. Phys.*, **2011**, 135(1):014304.

[54] Q. Wu, C. Deng, Q. Peng, Y. Niu, and Z. Shuai. *J. Comput. Chem.*, **2012**, 33(23):1862–1869.

[55] Y.-C. Duan, Y. Wu, J.-L. Jin, D.-M. Gu, Y. Geng, M. Zhang, and Z.-M. Su. *ChemPhysChem*, **2017**, 18(7):755–762.

[56] T. Förster. *Radiation Research Supplement*, **1960**, 2:326–339.

[57] D. L. Dexter. *J. Chem. Phys.*, **1953**, 21:836–850.

[58] C. Curutchet and B. Mennucci. *J. Am. Chem. Soc.*, **2005**, 127(47):16733–16744.

[59] V. Russo, C. Curutchet, and B. Mennucci. *J. Phys. Chem. B*, **2007**, 111(4):853–863.

[60] M. F. Iozzi, B. Mennucci, J. Tomasi, and R. Cammi. *J. Chem. Phys.*, **2004**, 120(15):7029–7040.

[61] J. Huang, J.-H. Su, and H. Tian. *J. Mater. Chem.*, **2012**, 22:10977–10989.

[62] Z. Zhao, S. Chen, C. Y. K. Chan, J. W. Y. Lam, C. K. W. Jim, P. Lu, Z. Chang, H. S. Kwok, H. Qiu, and B. Z. Tang. *Chem. Asian J.*, **3 2012**, 7(3):484–488.

[63] T. Förster and K. Kasper. *Z. Phys. Chem. (Muenchen, Ger.)*, **1954**, 1:275–277.

[64] T. Förster and K. Kasper. *Z. Elektrochem.*, **1955**, 59(10):976–980.

[65] J. B. Birks. *Photophysics of aromatic molecules*, volume 74. Ed. Wiley: London, 1970.

[66] J. Liang, Q. L. Nguyen, and S. Matsika. *Photochem. Photobiol. Sci.*, **2013**, 12:1387–1400.

[67] J. Yang, L. Li, Y. Yu, Z. Ren, Q. Peng, S. Ye, Q. Li, and Z. Li. *Mater. Chem. Front.*, **2017**, 1:91–99.

[68] J. Luo, Z. Xie, J. W. Y. Lam, L. Cheng, H. Chen, C. Qiu, H. S. Kwok, X. Zhan, Y. Liu, D. Zhu, and B. Z. Tang. *Chem. Commun.*, **2001**, 18:1740–1741.

[69] B. Z. Tang, X. Zhan, G. Yu, P. P. Sze Lee, Y. Liu, and D. Zhu. *J. Mater. Chem.*, **2001**, 11:2974–2978.

[70] J. Chen, C. C. W. Law, J. W. Y. Lam, Y. Dong, S. M. F. Lo, I. D. Williams, D. Zhu, and B. Z. Tang. *Chem. Mater.*, **2003**, 15(7):1535–1546.

[71] X. Fan, J. Sun, F. Wang, Z. Chu, P. Wang, Y. Dong, R. Hu, B. Z. Tang, and D. Zou. *Chem. Commun.*, **2008**, 26:2989–2991.

[72] Z. Li, Y. Dong, B. Mi, Y. Tang, M. Häussler, H. Tong, Y. Dong, J. W. Y. Lam, Y. Ren, H. H. Y. Sung, K. S. Wong, P. Gao, I. D. Williams, H. S. Kwok, and B. Z. Tang. *J. Phys. Chem. B*, **2005**, 109(20):10061–10066.

[73] E. Zhao, J. W. Y. Lam, Y. Hong, J. Liu, Q. Peng, J. Hao, H. H. Y. Sung, I. D. Williams, and B. Z. Tang. *J. Mater. Chem. C*, **2013**, 1:5661–5668.

[74] B. Chen, H. Nie, P. Lu, J. Zhou, A. Qin, H. Qiu, Z. Zhao, and B. Z. Tang. *Chem. Commun.*, **2014**, 50:4500–4503.

[75] G. Liang, J. W. Y. Lam, W. Qin, J. Li, N. Xie, and B. Z. Tang. *Chem. Commun.*, **2014**, 50:1725–1727.

[76] S. Li, S. M. Langenegger, and R. HÃ¤ner. *Chem. Commun.*, **2013**, 49:5835–5837.

[77] J. Shi, N. Chang, C. Li, J. Mei, C. Deng, X. Luo, Z. Liu, Z. Bo, Y. Q. Dong, and B. Z. Tang. *Chem. Commun.*, **2012**, 48:10675–10677.

[78] J. Luo, K. Song, F. l. Gu, and Q. Miao. *Chem. Sci.*, **2011**, 2:2029–2034.

[79] N. L. C. Leung, N. Xie, W. Yuan, Y. Liu, Q. Wu, Q. Peng, Q. Miao, J. W. Y. Lam, and B. Z. Tang. *Chem. Eur. J.*, **2014**, 20(47):15349–15353.

[80] K. Sharma nee Kamaldeep, S. Kaur, V. Bhalla, M. Kumar, and A. Gupta. *J. Mater. Chem. A*, **2014**, 2:8369–8375.

[81] Q. Peng, Y. Yi, Z. Shuai, and J. Shao. *J. Am. Chem. Soc.*, **2007**, 129(30):9333–9339.

[82] Y. Niu, W. Li, Q. Peng, H. Geng, Y. Yi, L. Wang, G. Nan, D. Wang, and Z. Shuai. *Mol. Phys.*, **2018**, 116(7-8):1078–1090.

[83] Y. Niu, Q. Peng, C. Deng, X. Gao, and Z. Shuai. *J. Phys. Chem. A*, **2010**, 114(30):7817–7831.

[84] M. G. S. Londesborough, J. Dolanský, L. Cerdán, K. Lang, T. Jelínek, J. M. Oliva, D. Hnyk, D. Roca-Sanjuán, A. Francés-Monerris, J. Martinčík, M. Nikl, and J. D. Kennedy. *Adv. Opt. Mater.*, **2017**, 5(6):1600694.

[85] M. Dommett, M. Rivera, and R. Crespo-Otero. *J. Phys. Chem. Lett.*, **2017**, 8(24):6148–6153.

[86] R. Crespo-Otero and M. Barbatti. *Chem. Rev.*, **2018**, 118(15):7026–7068.

[87] P.-I. Shih, C.-Y. Chuang, C.-H. Chien, E.-G. Diau, and C.-F. Shu. *Adv. Funct. Mater.*, **2007**, 17(16):3141–3146.

[88] Z. Zhao, P. Lu, J. W. Y. Lam, Z. Wang, C. Y. K. Chan, H. H. Y. Sung, I. D. Williams, Y. Ma, and B. Z. Tang. *Chem. Sci.*, **2011**, 2:672–675.

[89] Z. Zhao, S. Chen, C. Y. K. Chan, J. W. Y. Lam, C. K. W. Jim, P. Lu, Z. Chang, H. S. Kwok, H. Qiu, and B. Z. Tang. *Chem. Asian J.*, **2012**, 7(3):484–488.

[90] J. Huang, X. Yang, J. Wang, C. Zhong, L. Wang, J. Qin, and Z. Li. *J. Mater. Chem.*, **2012**, 22:2478–2484.

[91] C. Y. K. Chan, J. W. Y. Lam, Z. Zhao, S. Chen, P. Lu, H. H. Y. Sung, H. S. Kwok, Y. Ma, I. D. Williams, and B. Z. Tang. *J. Mater. Chem. C*, **2014**, 2:4320–4327.

[92] B. Yang, X. Niu, Z. Huang, C. Zhao, Y. Liu, and C. Ma. *Tetrahedron*, **2013**, 69(38):8250 – 8254.

[93] C.-A. Chou, R.-H. Chien, C.-T. Lai, and J.-L. Hong. *Chem. Phys. Lett.*, **2010**, 501(1):80 – 86.

[94] J. Tong, Y. J. Wang, Z. Wang, J. Z. Sun, and B. Z. Tang. *J Phys. Chem. C*, **2015**, 119(38):21875–21881.

[95] K. Garg, E. Ganapathi, P. Rajakannu, and M. Ravikanth. *Phys. Chem. Chem. Phys.*, **2015**, 17:19465–19473.

[96] M. Huang, R. Yu, K. Xu, S. Ye, S. Kuang, X. Zhu, and Y. Wan. *Chem. Sci.*, **2016**, 7:4485–4491.

[97] M. Huang, S. Ye, K. Xu, J. Zhou, J. Liu, X. Zhu, and Y. Wan. *J. Mater. Chem. C*, **2017**, 5:3456–3460.

[98] M. J. Frisch, G. W. Trucks, H. B. Schlegel, G. E. Scuseria, M. A. Robb, J. R. Cheeseman, G. Scalmani, V. Barone, G. A. Petersson, H. Nakatsuji, X. Li, M. Caricato, A. V. Marenich, J. Bloino, B. G. Janesko, R. Gomperts, B. Mennucci, H. P. Hratchian, J. V. Ortiz, A. F. Izmaylov, J. L. Sonnenberg, D. Williams-Young, F. Ding, F. Lipparini, F. Egidi, J. Goings, B. Peng, A. Petrone, T. Henderson, D. Ranasinghe, V. G. Zakrzewski, J. Gao, N. Rega, G. Zheng, W. Liang, M. Hada, M. Ehara, K. Toyota, R. Fukuda, J. Hasegawa, M. Ishida, T. Nakajima, Y. Honda, O. Kitao, H. Nakai, T. Vreven, K. Throssell, J. A. Montgomery, Jr., J. E. Peralta, F. Ogliaro, M. J. Bearpark, J. J. Heyd, E. N. Brothers, K. N. Kudin, V. N. Staroverov, T. A. Keith, R. Kobayashi, J. Normand, K. Raghavachari, A. P. Rendell, J. C. Burant, S. S. Iyengar, J. Tomasi, M. Cossi, J. M. Millam, M. Klene, C. Adamo, R. Cammi, J. W. Ochterski, R. L. Martin, K. Morokuma, O. Farkas, J. B. Foresman, and D. J. Fox. Gaussian 09 Revision I.09, 2016. Gaussian Inc. Wallingford CT.

[99] C. Adamo and V. Barone. *J. Chem. Phys.*, **1999**, 110(13):6158–6170.

[100] T. Yanai, D. P. Tew, and N. C. Handy. *Chem. Phys. Lett.*, **2004**, 393(1):51–57.

[101] J.-D. Chai and M. Head-Gordon. *Phys. Chem. Chem. Phys.*, **2008**, 10:6615–6620.

[102] D. Presti, F. Labat, A. Pedone, M. J. Frisch, H. P. Hratchian, I. Ciofini, M. C. Menziani, and C. Adamo. *J. Chem. Theory Comput.*, **2014**, 10(12):5577–5585.

[103] L. Wilbraham, C. Adamo, F. Labat, and I. Ciofini. *J. Chem. Theory Comput.*, **2016**, 12(7):3316–3324.

[104] D. Presti, L. Wilbraham, C. Targa, F. Labat, A. Pedone, M. C. Menziani, I. Ciofini, and C. Adamo. *J. Phys. Chem. C*, **2017**, 121(10):5747–5752.

[105] D. Case, D. Cerutti, T. I. Cheatham, T. Darden, R. Duke, T. Giese, H. Gohlke, A. Goetz, D. Greene, N. Homeyer, S. Izadi, A. Kovalenko, T. Lee, S. LeGrand, P. Li, C.

Lin, J. Liu, T. Luchko, R. Luo, D. Mermelstein, K. Merz, G. Monard, H. Nguyen, I. Omelyan, A. Onufriev, F. Pan, R. Qi, D. Roe, A. Roitberg, C. Sagui, C. Simmerling, W. Botello-Smith, J. Swails, R. Walker, J. Wang, R. Wolf, X. Wu, L. Xiao, D. York, and P. Kollman. Amber 2016, 2016. University of California, San Francisco.

[106] E. G. B. L. Martínez, R. Andrade and J. M. Martínez. *J. Comput. Chem.*, **2009**, 30(13):2157–2164.

[107] W. L. Jorgensen, J. Chandrasekhar, J. D. Madura, R. W. Impey, and M. L. Klein. *J. Comput. Chem.*, **1983**, 79(2):926–935.

[108] T. Darden, D. York, and L. Pedersen. *J. Chem. Phys.*, **1993**, 98(12):10089–10092.

[109] U. Essmann, L. Perera, M. L. Berkowitz, T. Darden, H. Lee, and L. G. Pedersen. *J. Chem. Phys.*, **1995**, 103(19):8577–8593.

[110] H. J. C. Berendsen, J. P. M. Postma, W. F. van Gunsteren, A. DiNola, and J. R. Haak. *J. Chem. Phys.*, **1984**, 81(8):3684–3690.

[111] D. R. Roe and T. E. Cheatham. *J. Chem. Theory Comput.*, **2013**, 9(7):3084–3095.

[112] P. J. Stephens, F. J. Devlin, C. F. Chabalowski, and M. J. Frisch. *J. Phys. Chem.*, **1994**, 98(45):11623–11627.

[113] W. Li, L. Zhu, Q. Shi, J. Ren, Q. Peng, and Z. Shuai. *Chem. Phys. Lett.*, **2017**, 683:507–514.

[114] G. Sun, Y. Zhao, and W. Liang. *J. Chem. Theory Comput.*, **2015**, 11(5):2257–2267.

[115] S. Ruiz-Barragan, K. Morokuma, and L. Blancafort. *J. Chem. Theory Comput.*, **2015**, 11(4):1585–1594.

[116] A. Prlj, N. Doslic, and C. Corminboeuf. *Phys. Chem. Chem. Phys.*, **2016**, 18:11606–11609.

[117] V. S. Padalkar and S. Seki. *Chem. Soc. Rev.*, **2016**, 45:169–202.

[118] V. S. Padalkar and S. Seki. *Bull. Korean Chem. Soc.*, **2013**, 34:465–469.

[119] L. Lin, J. Fan, L. Cai, and C.-K. Wang. *RSC Adv.*, **2017**, 7:44089–44096.

[120] N. J. Hestand and F. C. Spano. *Acc. Chem. Res.*, **2017**, 50(2):341–350.

[121] M. Kasha, H. R. Rawls, and A. M. El-Bayoumi. *Pure Appl. Chem.*, **1965**, 11(3-4):371–392.

[122] B. Wang, X. Wang, W. Wang, and F. Liu. *J. Phys. Chem. C*, **2016**, 120(38):21850–21857.

[123] Q. Wu, T. Zhang, Q. Peng, D. Wang, and Z. Shuai. *Phys. Chem. Chem. Phys.*, **2014**, 16:5545–5552.

[124] L. Le Bras, C. Adamo, and A. Perrier. *J. Phys. Chem. C*, **2017**, 121(45):25603–25616.

[125] L. Le Bras, K. Chaitou, S. Aloïse, C. Adamo, and A. Perrier. *Phys. Chem. Chem. Phys.*, **2019**, 21:46–56.

[126] L. Le Bras, C. Adamo, and A. Perrier. *ChemPhotoChem*, **2019**, accepted.

[127] Y. Hirshberg. *Compt. Rend. Acad. Sci.*, **1950**, 231:903.

[128] M. Fritzsche. *Compt. Rend. Acad. Sci.*, **1867**, 64:1035.

[129] W. Wislicenus. *Annu. Chem*, **1893**, 308:366.

[130] H. Blitz. *Annu. Chem*, **1899**, 305:170.

[131] H. Blitz. *Phys. Chem*, **1899**, 30:527.

[132] H. Blitz and A. Wienands. *Annu. Chem*, **1899**, 308:1.

[133] W. Markwald. *Annu. Chem*, **1899**, 30:140.

[134] H. Stobbe. *Ber Dtsch. Chem. Ges.*, **1905**, 38(3):3673–3682.

[135] A. Senier and F. G. Shepheard. *J. Chem. Soc., Trans.*, **1909**, 95:1943–1955.

[136] A. Senier, F. G. Shepheard, and R. Clarke. *J. Chem. Soc., Trans.*, **1912**, 101:1950–1958.

[137] H. Stobbe and H. Mallison. *Ber Dtsch. Chem. Ges.*, **1913**, 46(2):1226–1238.

[138] L. Harris, J. Kaminsky, and R. G. Simard. *J. Am. Chem. Soc.*, **1935**, 57(7):1151–1154.

[139] W. Georghiu, C.V. *Bull. Soc. Chim.*, **1934**, 1:97.

[140] N. Y. C. Chu. *Can. J. Chem.*, **1983**, 61(2):300–305.

[141] N. Chu. Chapter 10 - 4n+2 systems: Spirooxazines. In H. Dürr and H. Bouas-Laurent, editors, *Photochromism*, pages 493 – 509. Elsevier Science, Amsterdam, 2003.

[142] S. Higgins. *Chim. Oggi-Chem. Today*, **2003**, 21:63–67.

[143] A. Toriumi, S. Kawata, and M. Gu. *Opt. Lett.*, **Dec 1998**, 23(24):1924–1926.

[144] S. Kawata and Y. Kawata. *Chem. Rev.*, **2000**, 100(5):1777–1788.

[145] X. Yao, T. Li, J. Wang, X. Ma, and H. Tian. *Adv. Opt. Mater.*, **2016**, 4(9):1322–1349.

[146] K. Matsuda and M. Irie. *J. Photochem. Photobiol., C*, **2004**, 5(2):169 – 182.

[147] M. Irie, T. Fukaminato, K. Matsuda, and S. Kobatake. *Chem. Rev.*, **2014**, 114(24):12174–12277.

[148] M. Takeshita, M. Hayashi, S. Kadota, K. H. Mohammed, and T. Yamato. *Chem. Commun.*, **2005**, 6:761–763.

[149] M. Takeshita, M. Hayashi, and T. Miyazaki. *Chem. Lett.*, **2010**, 39(2):82–83.

[150] F. H. Beijer, R. P. Sijbesma, H. Kooijman, A. L. Spek, and E. W. Meijer. *J. Am. Chem. Soc.*, **1998**, 120(27):6761–6769.

[151] R. P. Sijbesma and E. W. Meijer. *Chem. Commun.*, **2003**, 1:5–16.

[152] J. C. Crano and R. J. Guglielmetti. *Organic Photochromic and Thermochromic Compounds: Physicochemical Studies, Biological Applications, and Thermochromism.*, volume 2. Springer Science and Business Media: New York, 1999.

[153] M. Irie. *Chem. Rev.*, **2000**, 100(5):1685–1716.

[154] A. Perrier, S. Aloïse, M. Olivucci, and D. Jacquemin. *J. Phys. Chem. Lett.*, **2013**, 4(13):2190–2196.

[155] S. Aloïse, R. Yibin, I. Hamdi, G. Buntinx, A. Perrier, F. Maurel, D. Jacquemin, and M. Takeshita. *Phys. Chem. Chem. Phys.*, **2014**, 16:26762–26768.

[156] I. Hamdi, G. Buntinx, A. Perrier, O. Devos, N. Jaïdane, S. Delbaere, A. K. Tiwari, J. Dubois, M. Takeshita, Y. Wada, and S. Aloïse. *Phys. Chem. Chem. Phys.*, **2016**, 18:28091–28100.

[157] I. Hamdi, G. Buntinx, O. Poizat, A. Perrier, L. Le Bras, S. Delbaere, S. Barrau, M. Louati, M. Takeshita, K. Tokushige, M. Takao, and S. Aloïse. *J. Phys. Chem. A*, **2018**, 122(14):3572–3582.

[158] H. Gohlke and D. A. Case. *J. Comput. Chem.*, **2004**, 25(2):238–250.

[159] K. S. Thanthiriwatte, E. G. Hohenstein, L. A. Burns, and C. D. Sherrill. *J. Chem. Theory Comput.*, **2011**, 7(1):88–96.

[160] J. Tomasi, B. Mennucci, and R. Cammi. *Chem. Rev.*, **2005**, 105(8):2999–3094.

[161] S.-L. Li, T. Xiao, W. Xia, X. Ding, Y. Yu, J. Jiang, and L. Wang. *Chem. Eur. J.*, **2011**, 17(38):10716–10723.

[162] L. Brunsveld, B. J. B. Folmer, E. W. Meijer, and R. P. Sijbesma. *Chem. Rev.*, **2001**, 101(12):4071–4098.

[163] D. Guo, R. P. Sijbesma, and H. Zuilhof. *Org. Lett.*, **2004**, 6(21):3667–3670.

[164] A. T. ten Cate, P. Y. W. Dankers, H. Kooijman, A. L. Spek, R. P. Sijbesma, and E. W. Meijer. *J. Am. Chem. Soc.*, **2003**, 125(23):6860–6861.

[165] J.-B. Maillet, M. Mareschal, L. Soulard, R. Ravelo, P. S. Lomdahl, T. C. Germann, and B. L. Holian. *Phys. Rev. E*, **2000**, 63:016121.

[166] R. Renou, L. Soulard, E. Lescoute, C. Dereure, D. Loison, and J.-P. Guin. *J. Phys. Chem. C*, **2017**, 121(24):13324–13334.

[167] C. A. Lemarchand, D. Bousquet, B. Schnell, and N. Pineau. *J. Chem. Phys.*, **2019**, 150(22):224902.

[168] G. Del Frate, F. Bellina, G. Mancini, G. Marianetti, P. Minei, A. Pucci, and V. Barone. *Phys. Chem. Chem. Phys.*, **2016**, 18:9724–9733.

[169] G. Prampolini, M. Campetella, N. De Mitri, P. R. Livotto, and I. Cacelli. *J. Chem. Theory Comput.*, **2016**, 12(11):5525–5540.

[170] V. Barone, I. Cacelli, N. De Mitri, D. Licari, S. Monti, and G. Prampolini. *Phys. Chem. Chem. Phys.*, **2013**, 15:3736–3751.

[171] A. Perrier, F. Maurel, and D. Jacquemin. *Acc. Chem. Res.*, **2012**, 45(8):1173–1182.

[172] I. Hamdi, G. Buntinx, O. Poizat, S. Delbaere, A. Perrier, R. Yamashita, K.-i. Muraoka, M. Takeshita, and S. Aloïse. *Phys. Chem. Chem. Phys.*, **2019**, 21:6407–6414.

[173] D. Frenkel and B. Smit, editors. *Understanding Molecular Simulation (Second Edition)*. Academic Press, San Diego, second edition edition, 2002.

[174] A. Stukowski. *Modelling and Simulation in Materials Science and Engineering*, **2009**, 18(1):015012.

[175] Q. Peng, Y. Yi, Z. Shuai, and J. Shao. *J. Am. Chem. Soc.*, **2007**, 129(30):9333–9339.

[176] Y. Niu, W. Li, Q. Peng, H. Geng, Y. Yi, L. Wang, G. Nan, D. Wang, and Z. Shuai. *Mol. Phys.*, **2018**, 116(7-8):1078–1090.

[177] R. Mori, G. Iasilli, M. Lessi, A. B. Muñoz-Garcia, M. Pavone, F. Bellina, and A. Pucci. *Polym. Chem.*, **2018**, 9:1168–1177.

[178] C. Papucci, T. A. Geervliet, D. Franchi, O. Bettucci, A. Mordini, G. Reginato, F. Picchioni, A. Pucci, M. Calamante, and L. Zani. *Eur. J. Org. Chem.*, **2018**, 2018(20-21):2657–2666.

[179] Y. Zhang, M. Jiang, G.-C. Han, K. Zhao, B. Tang, and K. S. Wong. *J. Phys. Chem. C*, **2015**, 119:27630–27638.

[180] M. Jiang, Z. He, Y. Zhang, H. Sung, V. Lam, Q. Peng, Y. Yan, K. Wong, I. Williams, Y. Zhao, and B. Tang. *J. Mater. Chem. C*, **2017**, 5:7191–7199.

[181] Y. Yilin Zhang, M. Jiang, T. Han, X. Xiao, W. Chen, L. Wang, K. Wong, R. Wang, B. Wang, K. Tang, and K. Wu. *ACS. Appl. Mater. Interfaces*, **2018**, 10:34418–34426.

[182] T. Han, C. Gui, J. . Lam, M. Jiang, N. Xie, R. . Kwok, and B. Z. Tang. *Macromolecules*, **2017**, 50:5807–5815.

[183] J. Zhao, J. Peng, P. Chen, H. Wang, P. Xue, and R. Lu. *Dyes Pigm.*, **2018**, 149:276–283.

Appendices

A-1 FOEB molecule: benchmark

For one solvated FOEB molecule in toluene (linear-response PCM scheme), the optimization of the S_0 state has been carried out with PBE0, CAM-B3LYP and ωB97X-D. Looking carefully at the key structural parameters in Table A-1 allows us to conclude that the differences between PBE0 and ωB97X-D geometries are minimal. In both cases, the tolane moiety is planar while the lateral part involving the fluorophenyl moiety is tilted with respect to the central part (α is equal to -66° and -67° after a geometry optimization with PBE0 and ωB97X-D respectively). For the geometry optimized with CAM-B3LYP, if the central part is also planar (ϕ = -180°), the fluorophenyl moiety is less tilted (α = -57°) with respect to the central core than the two others geometries. After an optimization process with three different XC functionals, namely PBE0, CAM-B3LYP and ωB97X-D, we computed the maximum absorption wavelength, λ_{max}, with the same three different XC functionals, thus considering nine different TD//Optimization calculation schemes. For each scheme, we have calculated the λ_{max} within the LR-PCM methodology. In Figure A-1, we have shown the difference $|\Delta E_{exp-calc}|$ in eV between experimental and calculated excitation energies. For the TD-CAM-B3LYP scheme, the values of the computed λ_{max} are the same if we consider PBE0 and CAM-B3LYP optimized structures. It leads in each case to a difference with the experiment of 0.06 eV. On the opposite, the ωB97X-D geometry provides a smaller λ_{max} and thus a larger excitation energy compared to the re-

TABLE A-1 – Selected geometrical parameters calculated for **FOEB** molecule.The distances are in Angstroms, the dihedral angles are in degrees. The bond numbering is provided on Figure 2.11.

	FOEB		
	PBE0	CAM-B3LYP	ωB97X-D
Bond			
d_{trip}	1.212	1.204	1.206
Dihedral angles			
ϕ	178	-180	-178
α	-66	-57	-67
β	-1	-1	0

sults obtained with the two others structures (0.15 eV). This is in agreement with the less conjugated (less planar) character of the ωB97X-D structure (Table A-1). We can therefore exclude computational strategy relying on a geometry optimization with the ωB97X-D functional. One can note that we obtain a different trend for TD-PBE0 with respect to

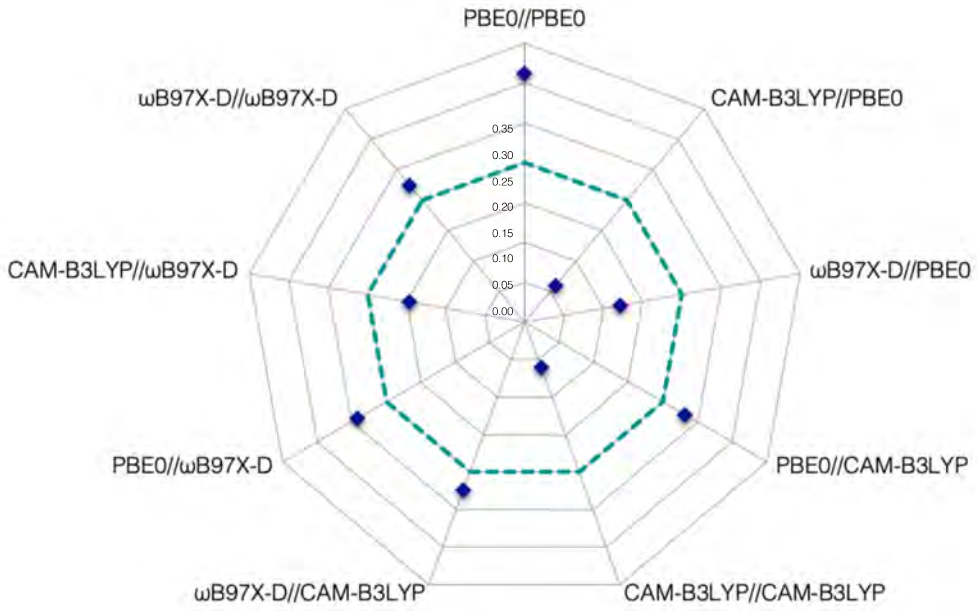

FIGURE A-1 – Representation of the energy difference between the experimental and calculated excitation energies $|\Delta E_{exp-calc}|$ in eV as a function of the TD//Optimization calculation scheme for **FOEB** molecule.

the other schemes. We systematically have a red-shift of the λ_{max} with a difference of 0.23 and 0.24 for CAM-B3LYP and ωB97X-D geometries respectively. The red-shift is even higher for PBE0 geometry (0.31 eV). The first conclusion is that PBE0 can be excluded of the possible XC functionals for the calculation of the optical properties. We can also not consider ωB97X-D functional for TD-DFT calculations. Indeed, for the same geometry, this functional systematically leads to a larger difference with experimental data than those obtained with the remaining TD-CAM-B3LYP functional (0.06 vs 0.12 and 0.06 vs 0.22 for PBE0 and CAM-B3LYP geometries respectively). Therefore, the calculation of the optical properties with CAM-B3LYP allows the most accurate reproduction of the experimental results. We thus have two possibilities left for the optimization process. The same results are obtained for CAM-B3LYP and PBE0 (the structures are also similar), with a blue-shift of 5 nm (0.06 eV) with respect to the experience. Hence, in order to lighten the computational burden, CAM-B3LYP will also be used for the optimization step.

A-2 FOEB molecule: HR factors

TABLE A-2 – Selected Huang-Rhys factors ($HR_j \geq 0.1$) with the corresponding reorganization energies $E_{reorg,j}$ and normal mode frequencies ω_j both in cm^{-1} for FOEB in TLN, THF and ACN in the first excited state.

TLN				**THF**				**ACN**			
mode	ω	HR	E_{reorg}	mode	ω	HR	E_{reorg}	mode	ω	HR	E_{reorg}
1	7	0.70	5	15	105	0.26	28	1	9	0.23	2
4	23	0.93	21	17	128	0.11	14	4	20	2.37	48
5	28	0.93	26					15	99	0.19	18
15	106	0.19	20								

A-3 FOEB molecule: superposition of the structures

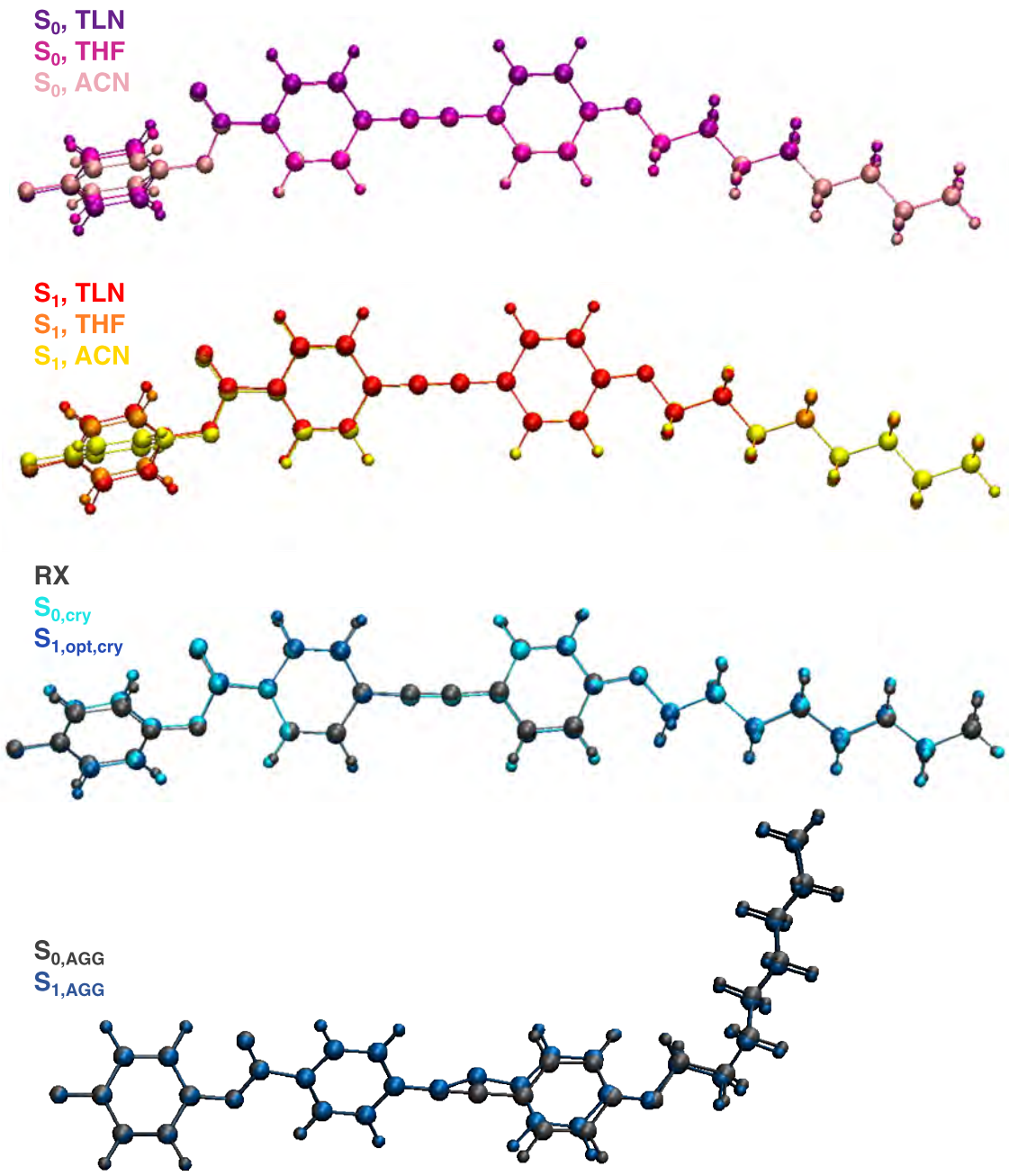

FIGURE A-2 – Different structure superpositions of **FOEB** molecule.

A-4 FOEB molecule: important vibrational modes

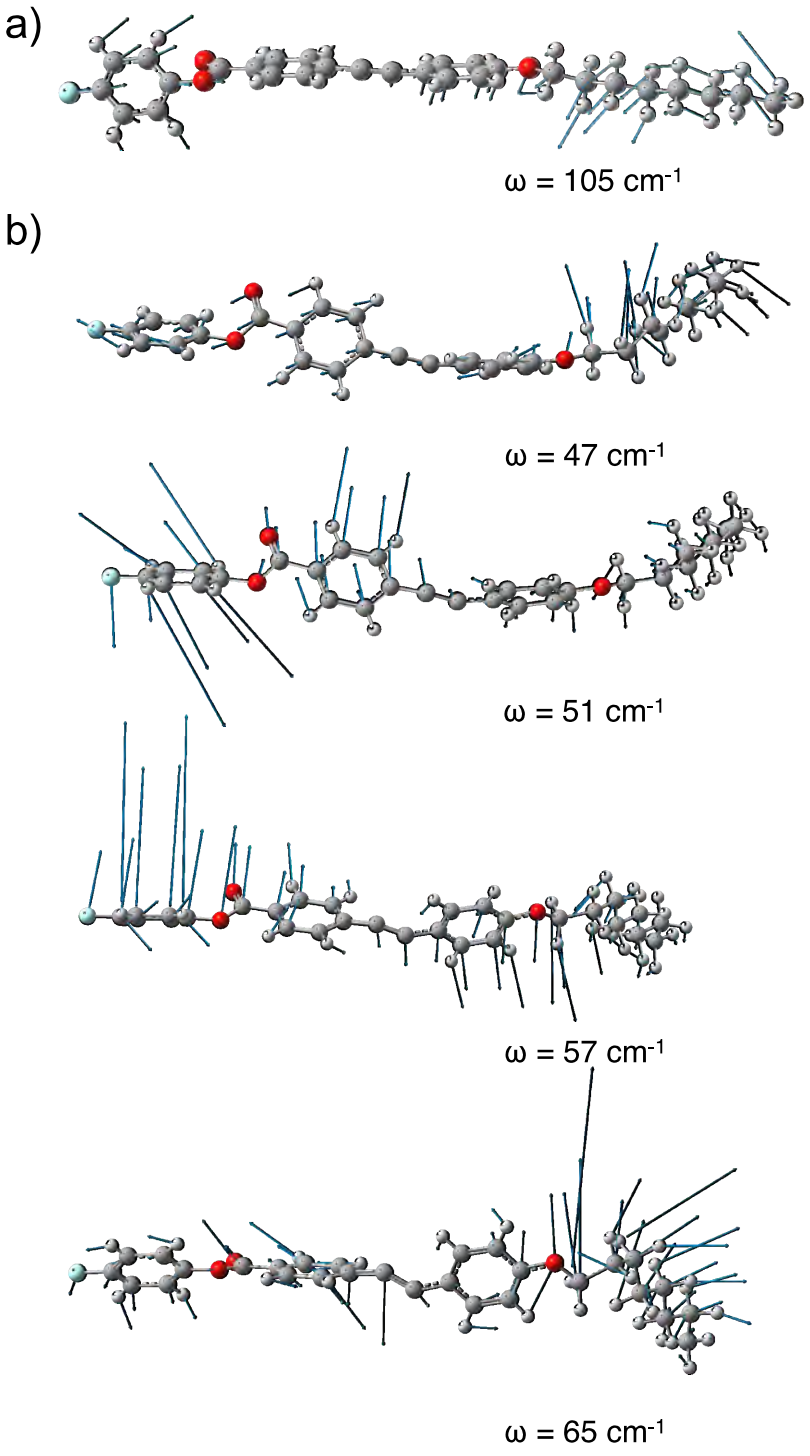

FIGURE A-3 – Vibrational modes of the **FOEB** molecule within (a) the crystalline and (b) the aggregated phase presenting simi-larities with the vibrational modes with large HR factors in solution.

A-5 DPYDPE isomers: phenyl rotation

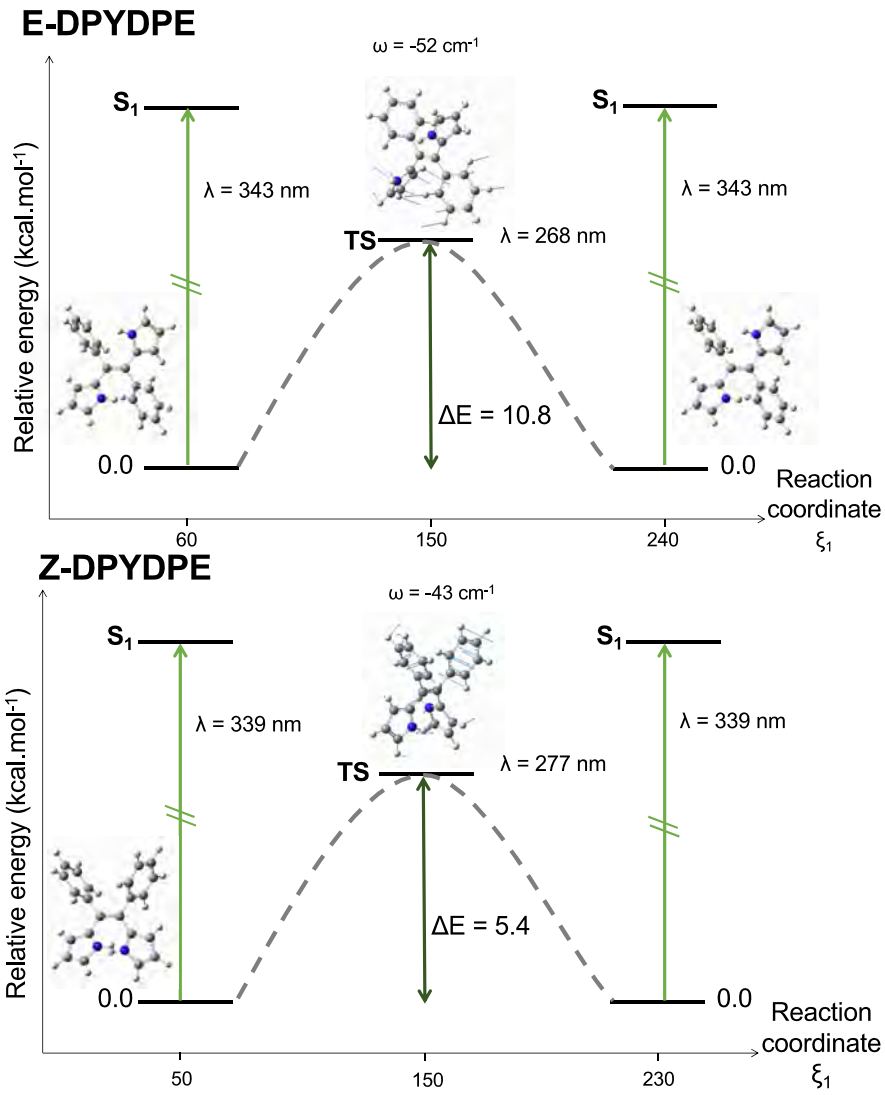

FIGURE A-4 – Impact of the rotation of one phenyl ring on the energetics and absorption properties (maximum absorption wavelengths λ in nm). The relative energies are given with respect to the most stable conformer, either for **E-DPYDPE** or **Z-DPYDPE**. At the Transition State (TS), the vibration mode with an imaginary frequency is represented.

A-6 DPYDPE isomers: optical properties of the aggregate

TABLE A-3 – **E-DPYDPE**: Relative energy (eV and J), maximum absorption wavelength λ_{max} in nm and emission wavelength λ_{em} computed for the ten different snapshots extracted from MD simulations. The oscillator strength f are also given.

Snapshot	1	2	3	4	5	6	7	8	9	10
ΔE (eV)	0.46	0.28	0.54	0.17	0.00	0.10	0.35	0.24	0.08	0.05
ΔE (10^{-20} J)	7.38	4.53	8.65	2.78	0.00	1.60	5.68	3.84	1.31	0.72
λ_{max}	336	345	344	346	354	363	353	384	384	386
f	0.416	0.403	0.431	0.374	0.363	0.340	0.417	0.331	0.341	0.328
λ_{em}	471	450	473	508	504	499	493	468	472	467
f	0.293	0.355	0.346	0.309	0.313	0.319	0.302	0.355	0.326	0.353

TABLE A-4 – **Z-DPYDPE**: Relative energy (eV and J), maximum absorption wavelength λ_{max} in nm and emission wavelength λ_{em} computed for the ten different snapshots extracted from MD simulations. The oscillator strength f are also given.

Snapshot	1	2	3	4	5	6	7	8	9	10
ΔE (eV)	0.09	0.02	0.03	0.02	0.15	0.00	0.03	0.16	0.22	0.24
ΔE (10^{-20} J)	1.38	0.37	0.54	0.27	2.48	0.00	0.44	2.6	3.59	3.81
λ_{max}	306	305	306	307	308	305	319	301	310	308
f	0.787	0.739	0.760	0.724	0.747	0.764	0.687	0.789	0.746	0.735
λ_{em}	441	408	425	389	374	409	432	433	394	389
f	0.387	0.527	0.460	0.637	0.763	0.525	0.417	0.422	0.583	0.628

A-7 DPYDPE isomers: structures superpositions

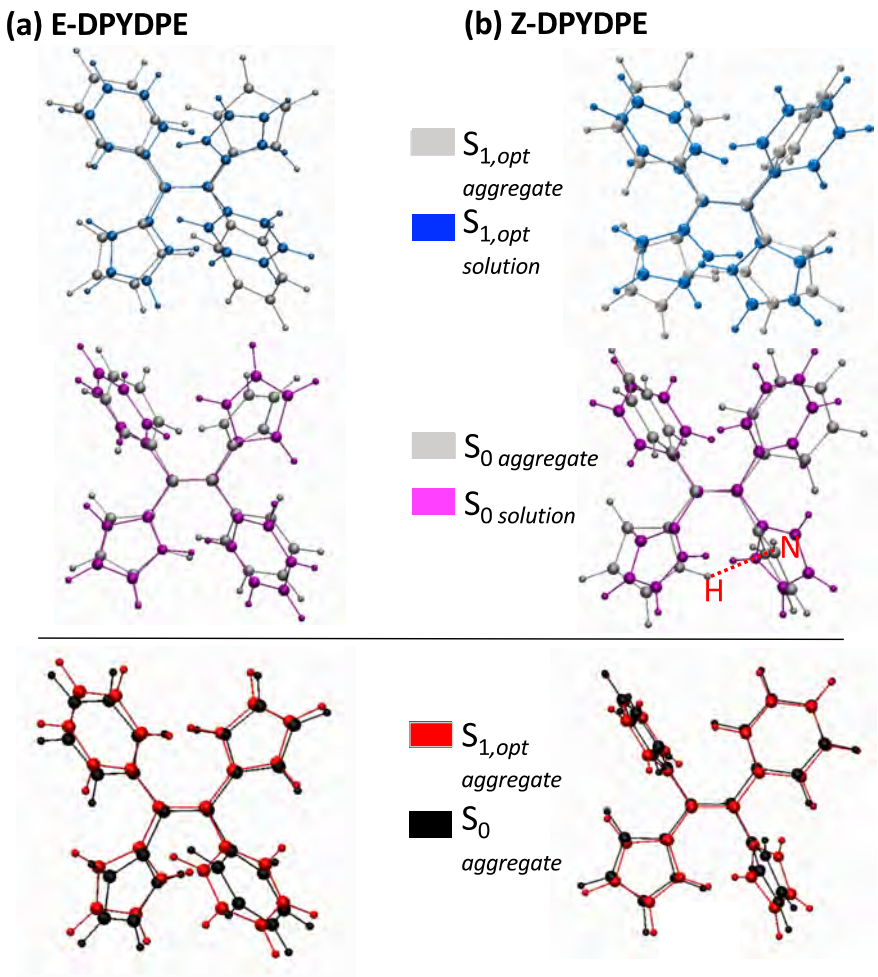

FIGURE A-5 – Structure superpositions. Top: Ground and excited states of (a) **E-DPYDPE** and (b) **Z-DPYDPE** optimized in solution and in the aggregate. Bottom: Ground- and excited-state structures optimized in the aggregate.

A-8 TTP family: benchmark

The absorption properties (λ_{max}) were calculated with 9 different combinations of TD//optimization computational schemes and compared to experimental data [96, 97]. One has to notice that the optimized structures are globally similar whatever the XC functional is used. Nevertheless, the choice of the XC functional has an impact on the calculated optical properties. Results, for the molecules **TTP-0** and **TTP-1**, are shown on Figure A-6. First, the energy difference $|\Delta E_{exp-calc}|$ between calculated and experimental values are very similar for **TTP-0** and **TTP-1**. Second, the CAM-B3LYP optimized structures systematically lead to a large $|\Delta E_{exp-calc}|$ value. This functional can thus be ruled out in the course of the geometry optimization. Thirdly, for TD-CAM-B3LYP calculation, there is also a larger $|\Delta E_{exp-calc}|$ value compared to TD-PBE0 and TD-B3LYP calculations for the same structure. For instance, the $|\Delta E_{exp-calc}|$ values are respectively 0.12 eV and 0.19 eV for the B3LYP//B3LYP and CAM-B3LYP//B3LYP schemes for the molecule **TTP-0**. At that stage, one can conclude that the B3LYP//B3LYP and PBE0//B3LYP strategies provide the same $|\Delta E_{exp-calc}|$ values. For the sake of simplicity, we decided to carry out geometry optimizations and TD-DFT calculations with the same XC functional, namely B3LYP. Indeed, with the B3LYP//B3LYP strategy, the $|\Delta E_{exp-calc}|$ value is equal to 0.12 eV for both **TTP-0** and **TTP-1**.

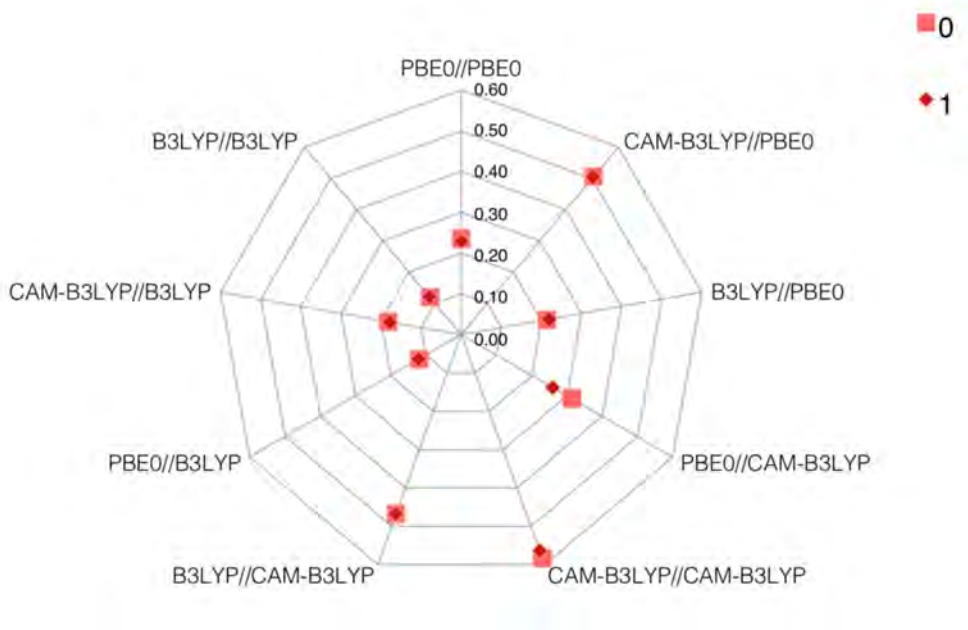

FIGURE A-6 – Representation of the energy difference between the experimental and calculated excitation energies $|\Delta E_{exp-calc}|$ in eV as a function of the TD//Optimization calculation scheme for **TTP-0** and **TTP-1** molecules.

A-9 TTP family: HR factors

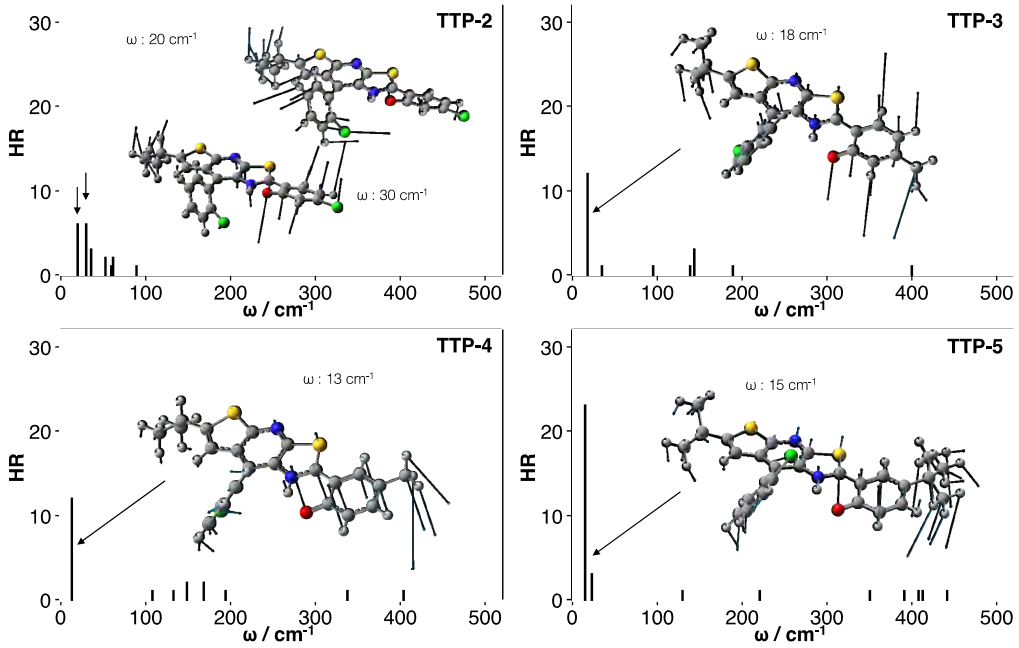

FIGURE A-7 – Calculated HR factors versus the normal-mode wave numbers (ω) in the S_1 state for **TTP-2** to **TTP-5**. Vibration modes yielding the largest HR factors are also represented.

TABLE A-5 – Selected Huang-Rhys factors (HRj $\geq$1) with the corresponding reorganization energies $E_{reorg,j}$ and normal mode frequencies ω_j both in cm^{-1} for **TTP-0**, **TTP-1**, **TTP-2**, **TTP-3**, **TTP-4** and **TTP-5** in the first excited state.

	mode	ω	HR	E_{reorg}		mode	ω	HR	E_{reorg}
TTP-0					**TTP-3**				
	1	20	5	105		1	18	12	218
	26	377	1	215		4	15	1	27
	28	392	1	296		10	95	1	56
	29	410	1	217		12	139	1	115
	32	432	1	522		13	144	3	498
	33	434	1	378		16	189	1	110
						31	400	1	428
TTP-1					**TTP-4**				
	1	23	13	275		1	13	12	152
	4	34	2	66		10	108	1	86
	10	124	1	98		12	133	1	149
	16	221	1	237		14	149	2	338
	28	406	1	260		15	168	2	322
	29	422	1	537		17	194	1	111
	34	478	1	405		27	338	1	187
						31	404	1	343
TTP-2					**TTP-5**				
	2	20	7	134		1	15	23	356
	4	30	6	188		3	23	3	60
	5	36	3	123		13	130	1	110
	6	52	2	90		19	221	1	223
	7	59	1	52		33	351	1	243
	8	61	1	77		36	391	1	236
	9	89	1	61		37	408	1	522
						41	442	1	432

A-10 TTP family: crystalline model

TABLE A-6 – Calculated absorption wavelength (λ_{max} in nm), oscillator strengths (f) and dominant molecular contributions in $S_0 \rightarrow S_n$ transitions for the different ONIOM models considered for **TTP2-TTP-5** molecules.

System	State	λ_{max}	f	Assignment
TTP-2-M	S_1	360	0.626	HOMO→LUMO
	S_4	303	0.181	HOMO→LUMO+1
TTP-2-D	S_2	370	0.188	HOMO-1→LUMO
	S_4	363	0.179	HOMO→LUMO+1
TTP-2-T	S_6	364	0.120	HOMO-1→LUMO+1
	S_7	360	0.103	HOMO-2→LUMO+1
TTP-3-M	S_1	361	0.558	HOMO→LUMO
	S_5	295	0.244	HOMO-1→LUMO
TTP-3-D	S_3	368	0.296	HOMO→LUMO+1
	S_6	356	0.562	HOMO-2→LUMO
TTP-4-M	S_1	366	0.434	HOMO→LUMO
TTP-4-D	S_2	363	0.273	HOMO→LUMO+1
TTP-5-M	S_1	365	0.482	HOMO→LUMO
TTP-5-D	S_2	367	0.885	HOMO-1→LUMO

A-11 TTP family: crystalline structures

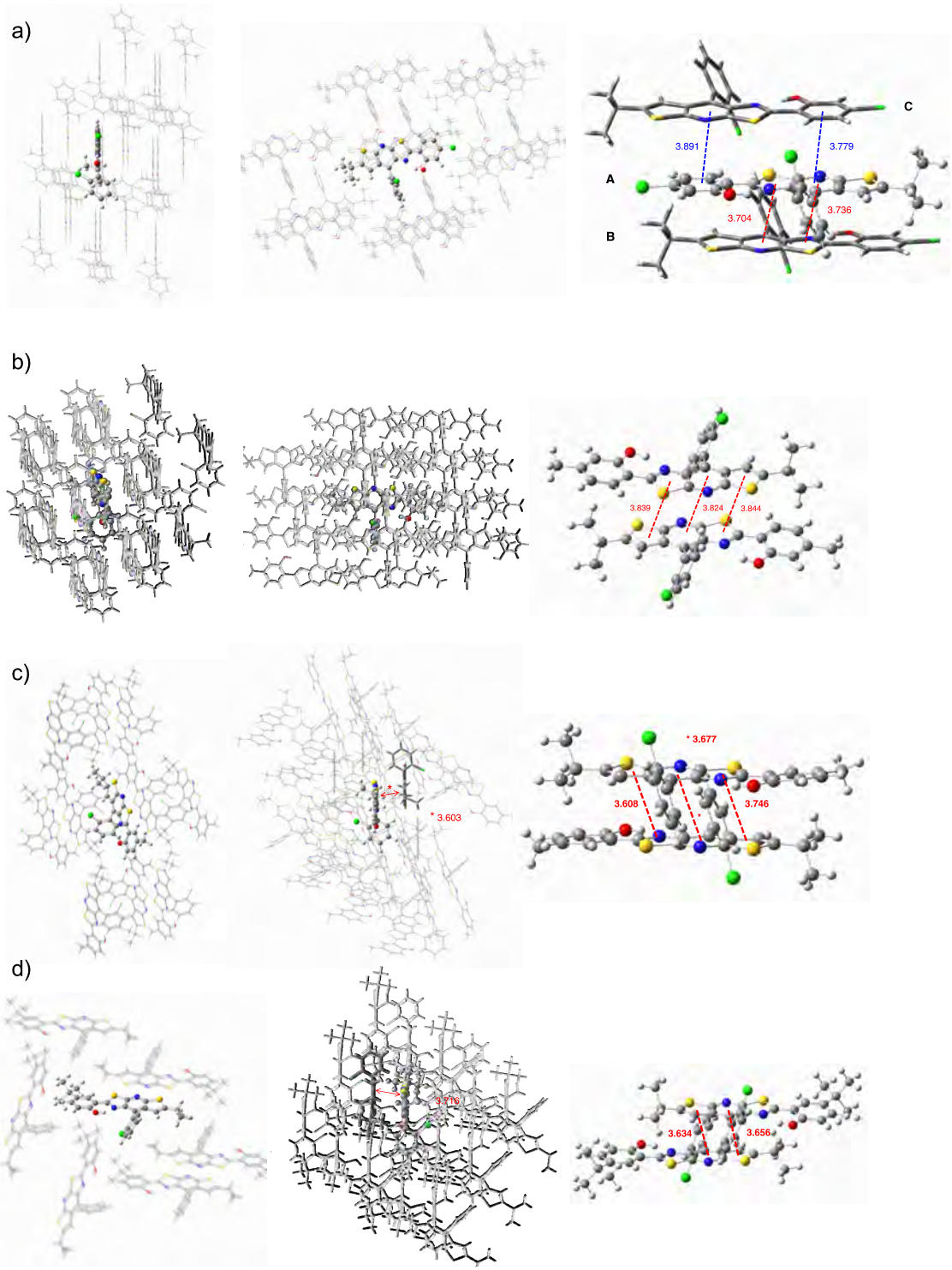

FIGURE A-8 – Representation of the packing of system (a) **TTP-2**, (b) **TTP-3**, (c) **TTP-4** and (d) **TTP-5**. The representations of possible dimers or trimers with intermolecular distances are also provided.

A-12 DTE-Upy: complementary analysis of the MD simulation of the dimers

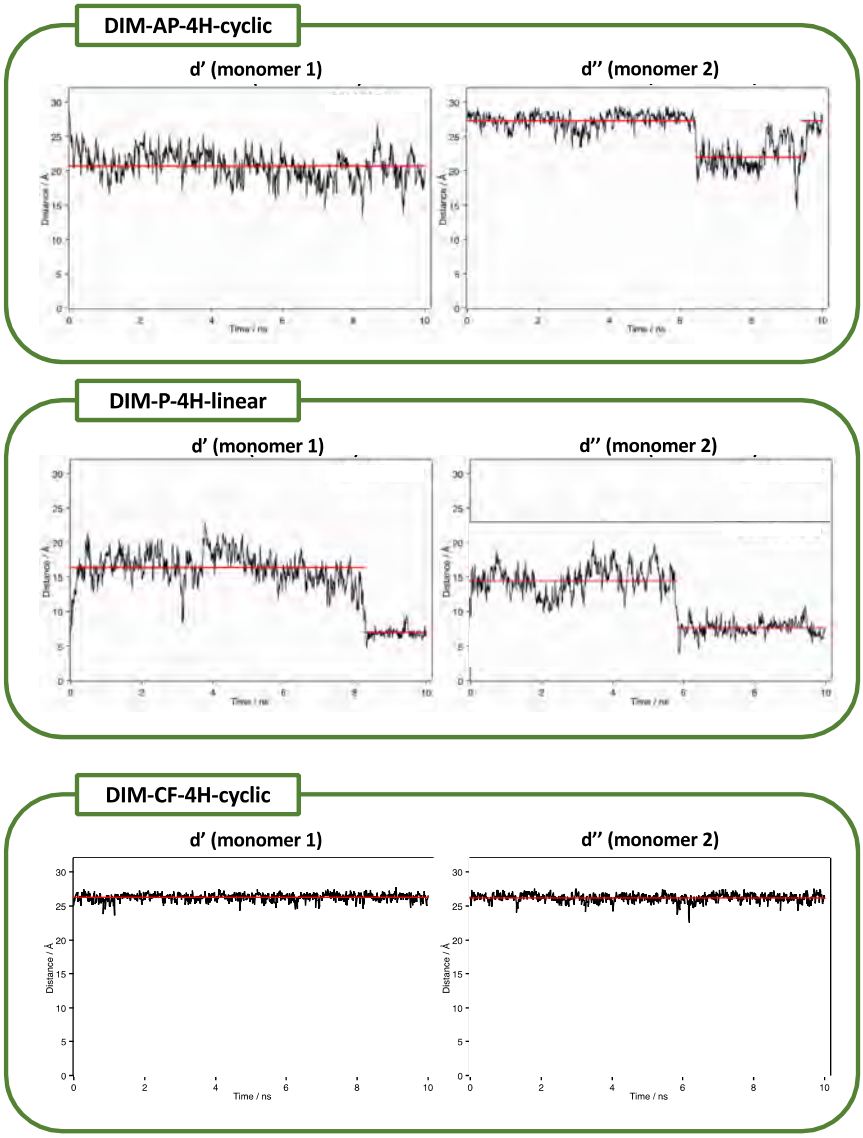

FIGURE A-9 – Evolution of the d' distances (Å) for the two monomers involved in a dimer of **DIM-AP-4H-linear**, **DIM-P-4H-linear** and **DIM-CF-4H-linear**. d' and d" correspond to the same distance but d' is for monomer 1 and d" is for monomer 2.

A-13 DTE-Upy: complementary analysis of the MD simulation of OF-P dimer

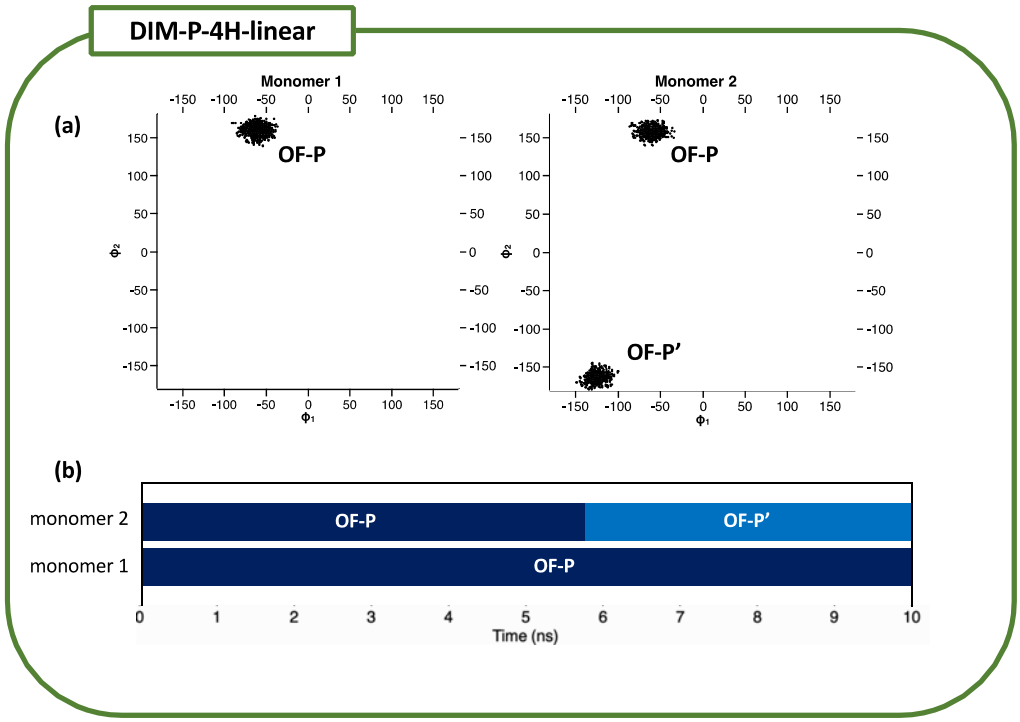

FIGURE A-10 – (a) Representation of the (ϕ_1,ϕ_2) value couples for the two monomers along the **DIM-P-4H-linear** trajectory. (b) Isomers in presence along the **DIM-P-4H-linear** trajectory.

A-14 DTE-Upy: complementary analysis of the MD simulation of OF-P cyclic dimer

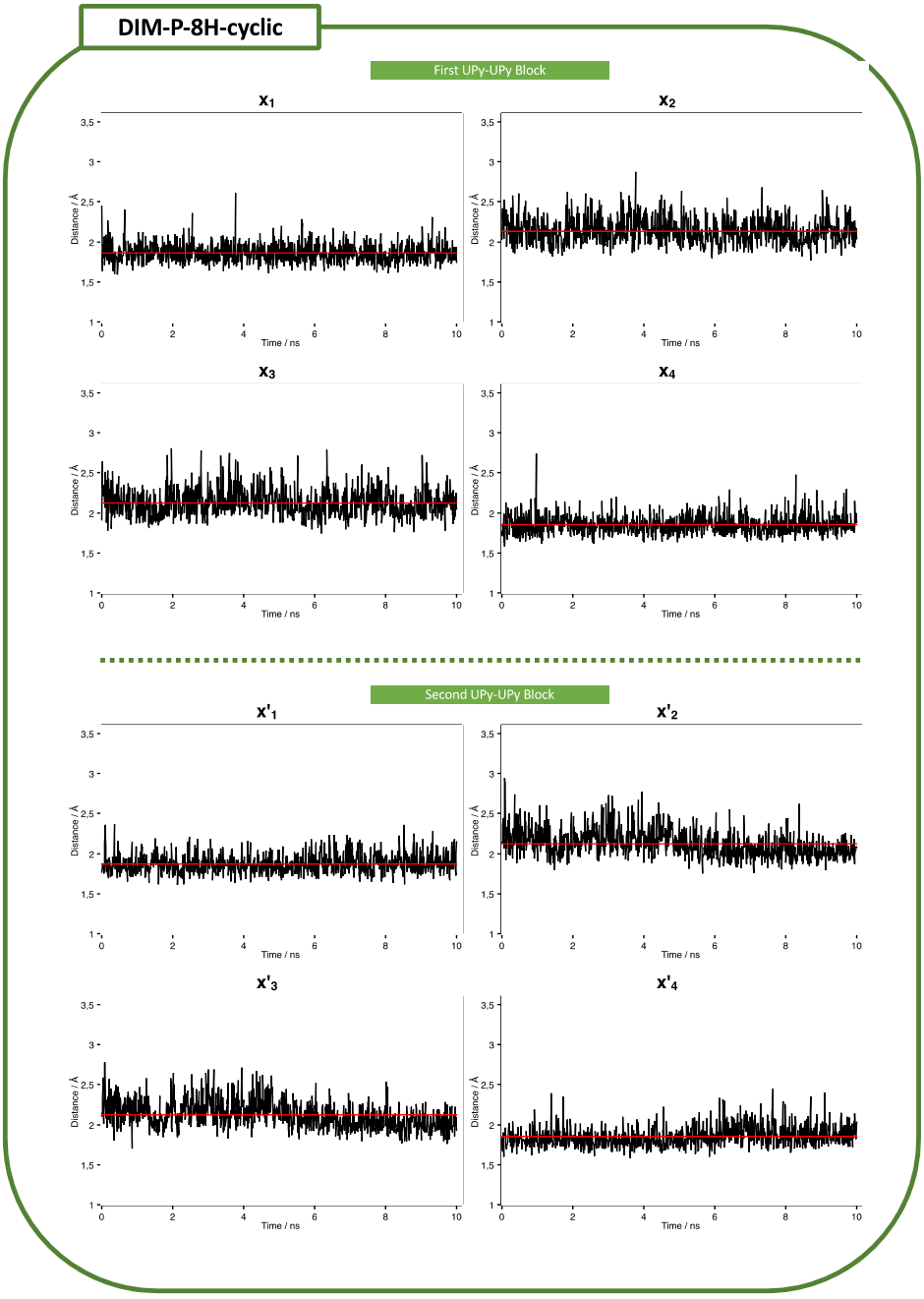

FIGURE A-11 – Time evolution of the x_1 to x_4 (first Upy-Upy quadrupole hydrogen bonding block, top) and x_1' to x_4' (second Upy-Upy quadrupole hydrogen bonding block, bottom) distance (in Å) for the **DIM-P-8H-cyclic** trajectory.

A-15 DTE-Upy: complementary analysis of the MD simulation of the π-stacked dimers

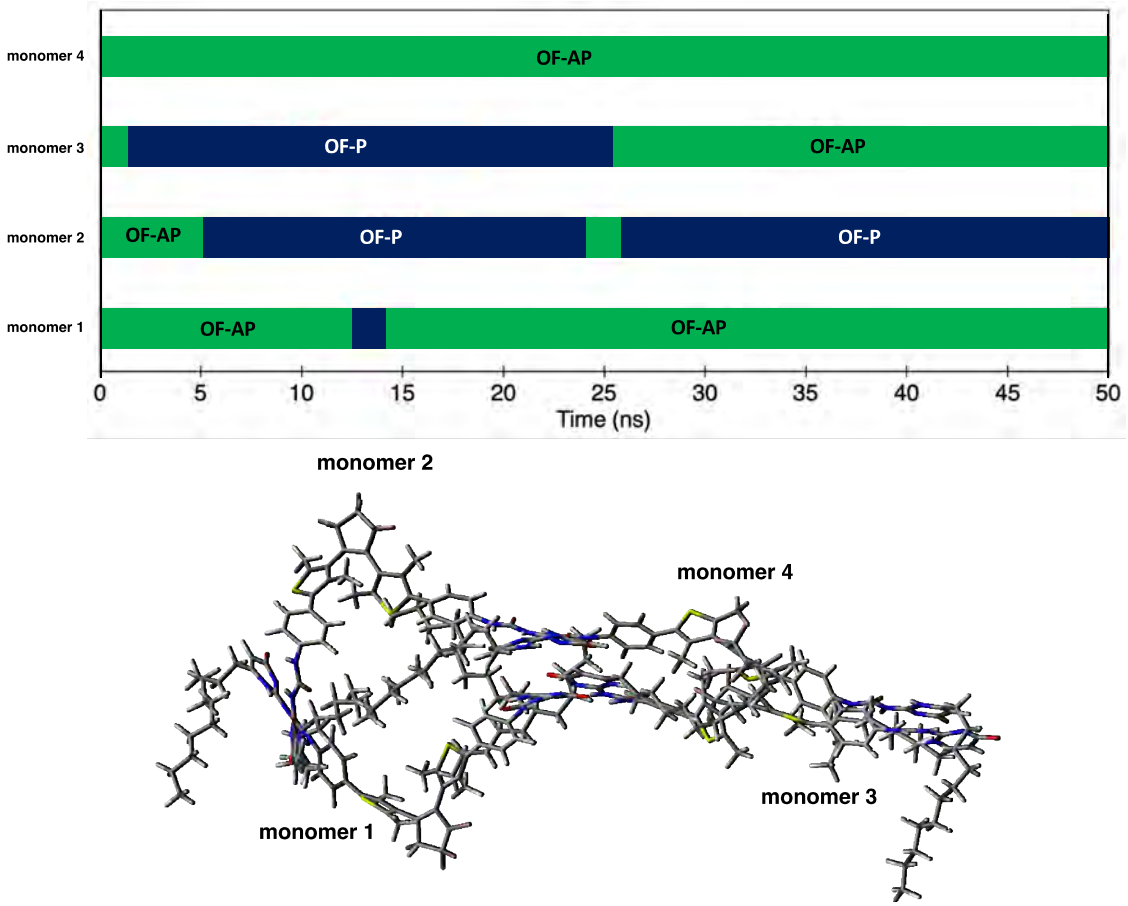

FIGURE A-12 – **TETRA-AP-STACK**: Isomers in presence along the trajectory for the four monomers forming the π-stacked dimers.

A-16 OF-AP: STAMP simulations

TABLE A-7 – Average values for different distances (in Angstroms, Å) and dihedral angles (in degrees, °) for the nine others 1 ns trajectories launched for the **OF-AP** conformer. These parameters are defined on Figure 3.9.

	d_{cc}	d_1	d_2	d_3	d_4	d'	ϕ_1	ϕ_2
OF-AP$_2$	3.76	22.90	22.81	15.13	14.83	28.48	-24	-61
OF-AP$_3$	3.78	26.13	20.44	15.24	14.59	26.09	-23	-64
OF-AP$_4$	3.66	23.21	24.99	15.81	15.66	28.43	-15	-65
OF-AP$_5$	3.71	24.04	14.81	13.58	16.08	29.31	-30	-57
OF-AP$_6$	3.70	19.38	15.03	15.94	15.53	27.93	-21	-63
OF-AP$_7$	3.79	19.02	17.73	15.82	16.82	26.69	-26	-59
OF-AP$_8$	3.71	16.24	13.36	15.23	15.36	29.35	-27	-62
OF-AP$_9$	3.77	29.90	24.24	15.89	14.08	27.04	-17	-51
OF-AP$_{10}$	3.77	27.44	25.70	14.25	14.78	28.57	-16	-66

A-17 OF-P: STAMP simulations

TABLE A-8 – Average values for different distances (in Angstroms, Å) and dihedral angles (in degrees, °) for the nine others 1 ns trajectories launched for the **OF-P** conformer. These parameters are defined on Figure 3.9.

	d_{cc}	d_1	d_2	d_3	d_4	d'	ϕ_1	ϕ_2
OF-P$_2$	4.07	18.15	19.68	13.16	13.03	22.99	20	-120
OF-P$_3$	4.10	21.84	23.13	12.06	13.35	21.72	20	-123
OF-P$_4$	4.12	22.64	21.66	14.09	13.21	22.00	20	-123
OF-P$_5$	4.01	22.92	21.68	12.49	14.19	22.21	20	-123
OF-P$_6$	4.07	21.20	18.53	13.96	12.96	20.30	22	-125
OF-P$_7$	4.09	17.06	18.67	12.37	12.94	21.17	24	-121
OF-P$_8$	4.09	22.08	19.91	14.60	13.66	20.66	21	-124
OF-P$_9$	4.04	20.55	19.35	19.71	13.52	23.21	19	-120
OF-P$_{10}$	4.09	20.39	19.64	12.73	12.90	21.92	20	-122

A-18 CF: STAMP simulations

TABLE A-9 – Average values for different distances (in Angstroms, Å) and dihedral angles (in degrees, °) for the nine others 1 ns trajectories launched for the **CF** conformer. These parameters are defined on Figure 3.9.

	d_{cc}	d_1	d_2	d_3	d_4	d'	ϕ_1	ϕ_2
$\mathbf{CF}_2$	1.56	16.55	22.16	15.18	15.39	27.42	-19	5
$\mathbf{CF}_3$	1.54	22.36	18.98	16.44	14.50	26.80	-15	-2
$\mathbf{CF}_4$	1.56	21.76	15.11	14.70	15.56	26.34	-18	5
$\mathbf{CF}_5$	1.55	23.49	15.18	14.22	16.80	26.92	-18	0
$\mathbf{CF}_6$	1.55	19.48	15.77	15.44	14.70	26.93	-18	4
$\mathbf{CF}_7$	1.55	18.21	22.23	15.47	15.20	25.18	-20	5
$\mathbf{CF}_8$	1.53	26.33	23.88	16.13	12.53	28.81	-18	1
$\mathbf{CF}_9$	1.56	22.30	26.54	15.66	14.63	25.82	-19	6
$\mathbf{CF}_{10}$	1.56	26.25	18.02	14.21	14.75	26.36	-19	4

RÉSUMÉ

Le contrôle des propriétés optiques des matériaux représente un défi considérable pour les applications de haute technologie. Outre le choix de molécules performantes (capables d'absorber ou d'émettre dans une région particulière du spectre avec une grande efficacité), il est important de tenir compte de l'effet de l'environnement (solution, agrégat, cristal ou matrice polymère) sur les propriétés visées. Lors de cette thèse nous nous proposons donc de rationaliser les interactions qui peuvent exister entre des processus photo induits (absorption/émission de lumière) et l'environnement qui peut être considéré comme une contrainte. Pour ce faire, un protocole de calcul permettant la prise en compte de divers environnements complexes ainsi que la modélisation des propriétés optiques a été mis en place, comprenant des calculs (TD-)DFT, de la dynamique moléculaire (solution et matrice polymère) ainsi que des approches hybrides QM/QM'.

MOTS CLÉS

TD-DFT, Dynamique Moléculaire, Spectroscopie UV-Vis, Fluorescence, Environnement

ABSTRACT

The control of the optical properties of molecules and materials represents a considerable challenge for high-tech applications. In addition to the choice of efficient molecules (able of absorbing/emitting in a particular region of the spectrum with high efficiency), it is important to take into account the effect of the environment (solution, aggregate, crystal, polymer matrix) on the desired properties. During this thesis, we propose to rationalize the interactions that can exist between photoinduced processes (absorption/light emission) and the environment, that can be considered as a constraint. To do this, a calculation strategy, appropriate to all the considered complex environments and allowing the modeling of the optical properties, has been set up. It includes (TD-)DFT calculations, molecular dynamics (solution and polymer matrix) as well as hybrid QM/QM' approaches.

KEYWORDS

TD-DFT, Molecular Dynamics, UV-Vis Spectroscopy, Fluorescence, Environment